The effect of manganese and chromium on the selective oxidation of low carbon strip steels for tinplate applications

Paton Ron Wilson
University of Wollongong

THE EFFECT OF MANGANESE AND CHROMIUM ON THE SELECTIVE OXIDATION OF LOW CARBON STRIP STEELS FOR TINPLATE APPLICATIONS

A thesis submitted in fulfilment of the requirements for the award of the degree

DOCTOR OF PHILOSOPHY

from

UNIVERSITY OF WOLLONGONG

by

PATON RON WILSON

Faculty of Engineering

2006

I, Paton Wilson, herby certify that the work embodied in this thesis is the result of original research and has not been submitted for a higher degree to any other University or Institution.

Paton Wilson

Acknowledgements

I would like to express the deepest gratitude to my supervisor, Dr Zhixin Chen for his guidance and support throughout the project. Much appreciation also goes to Professor Druce Dunne for his assistance. The support of my industrial supervisors, Chris Killmore and Stuart Laird is greatly appreciated.

Thanks also go to Dr David Wexler for TEM training and assistance, Phil Renwick for his assistance in TEM sample preparation techniques, Dr Charlie Kong for guidance in the use of FIB, Nick Mackie for SEM training and assistance, Greg Tillman for metallographic sample preparation and imaging, Mark Thompson for his support with industrial gas annealing experiments, and lastly final year students Greg Reece and Pierre Greig for there contribution to the project.

This project would have not been possible without the financial support of the Australian Research Council (ARC).

Importantly much appreciation goes to Bluescope Steel for their technical and financial support, supply of materials and use of equipment.

Finally I would like to thank Belinda, my family and friends for their continuous support.

Abstract

The ‘edge defect’ is a band of low reflectivity that occurs near the edge of batch annealed steels that have been tinplated. The tinplate product that contains this defect must be scrapped because of the poor aesthetical properties and the reduced corrosion resistance in the affected areas. This defect was known to be caused by surface precipitates formed during batch annealing of the steel strip substrate. This research aims to identify the surface precipitates and the factors that can be modified to reduce their formation in an effort to develop an alloying and/or processing strategy which eliminates the occurrence of the ‘edge defect’.

In this investigation the ‘edge defect’ was characterised using scanning electron microscopy (SEM) and transmission electron microscopy (TEM) which demonstrated that surface $MnCr_2O_4$ spinel precipitates were responsible for the ‘edge defect’ although two different oxides, (MnFe)O and $MnCr_2O_4$ spinel, were observed on the steel surface. The formation of the surface (MnFe)O and $MnCr_2O_4$ spinel was due to the selective oxidation of manganese and chromium during batch annealing. The effects of manganese, chromium and annealing temperature on selective oxidation were also investigated and it was found that the $MnCr_2O_4$ spinel precipitate size and distribution were directly affected by the content of the chromium in the steels. The higher the chromium content of the steel the coarser the surface $MnCr_2O_4$ spinel particles. The annealing temperature has a similar effect on the average size of the $MnCr_2O_4$ spinel. Within the range of this investigation the higher the annealing temperature the coarser the surface particle size.

The surface precipitates across the width of industrial batch annealed steel strip were characterised using SEM and TEM which established that the diameter of the surface oxide precipitates decreased from the edge to the centre of the steel strip. However, for the steel strip which exhibits the ‘edge defect’ the maximum size of the surface precipitates does not occur at the edge, rather about 20-100 mm from the edge. This has been interpreted as the result of the transition of internal selective oxidation to external selective oxidation suggesting that the steel sheet’s exhibiting the ‘edge defect’ are exposed to relatively higher oxygen potentials.

This investigation has identified that lowering the annealing temperature, reducing the chromium level in the steel and reducing the oxygen potential of the annealing environment will reduce the formation of the $MnCr_2O_4$ spinel. Therefore the 'edge defect' may be reduced by modifying these parameters during tinplate production. The minimisation of this defect will reduce production costs and improve product consistency for tinplate production.

Table of Contents

Acknowledgements iii
Abstract iv
Table of Contents vi
List of Abbreviations viii
Chapter 1 : Introduction 1
Chapter 2 : Review of the Literature 3
2.1 Introduction 3
2.2 Surface Graphitization 4
2.2.1 Morphology of Surface Graphite 9
2.2.2 Factors that Affect the Degree of Surface Graphitization 11
2.2.3 Effect of Steel Composition on Surface Graphitization 13
2.3 Selective Oxidation 19
2.3.1 Oxidation 19
2.3.2 Selective Oxidation 23
2.3.3 The Selective Oxidation of Steel 25
2.3.4 Effect of Temperature on Selective Oxidation of Steel 29
2.3.5 Effect of the Annealing Time on Selective Oxidation of Steel 31
2.3.6 Effect of Heating Rate on Selective Oxidation of Steel 31
2.3.7 Effect of Steel Composition on Selective Oxidation of Steel 31
2.3.8 Effect of Annealing Atmosphere on Selective Oxidation of Steel 32
2.3.9 Effect of Microstructure on Selective Oxidation of Steel 35
2.3.10 Oxides Commonly Found on the Surface of Steels after Annealing 35
2.4 Nitrogen Pick-up 40
2.5 Surface Characterisation Techniques 43
2.5.1 Scanning Electron Microscopy (SEM) 43
2.5.2 Transmission Electron Microscopy (TEM) 46
2.5.3 Auger Electron Spectroscopy (AES) 48
2.5.4 X-Ray (excited)-Photoelectron Spectrometry (XPS) 49
2.5.5 Secondary Ion Mass Spectrometry (SIMS) 50
2.5.6 Secondary Neutrals Mass Spectrometry (SNMS) 51
2.5.7 Ion Sputtering 52
2.6 Summary 53
Chapter 3 : Experimental 54
3.1 Materials 54
3.2 Annealing 56
3.2.1 Laboratory Annealing 56
3.2.2 Industrial Batch Annealing 58
3.3 Characterisation 61
3.3.1 Scanning Electron Microscopy (SEM) 61
3.3.2 Transmission Electron Microscopy (TEM) 62
3.3.3 X-Ray Diffraction (XRD) 65
3.3.4 Nitrogen Level Analysis 66
3.4 Image Analysis 67
3.5 Solid State Reaction between MnO and Cr_2O_3 68

Chapter 4 : Results 69
4.1 Characterisation of the Edge Defect 69
4.2 Steels Laboratory Annealed in Evacuated (Vacuum) Environment 82
4.2.1 SEM Characterisation 82
4.3 Characterization of (MnFe)O 86
4.3.1 XRD Characterisation 86
4.3.2 TEM Characterisation 87
4.4 Solubility of Oxides in Cleaning and Pickling Solutions 92
4.5 Steels Laboratory Annealed in 5% H_2 + 95% N_2 94
4.5.1 SEM Characterisation 94
4.5.2 TEM Characterisation 112
4.6 Surface Oxides across the Width of Steel Strip 137
4.6.1 Coil B1 137
4.6.2 Coil B2 144
4.7 Solid State Reaction of MnO and Cr_2O_3 146
Chapter 5 : Discussion 148
5.1 Formation of Oxides 148
5.1.1 Thermodynamic Consideration 148
5.1.2 Surface Spinel Oxides 153
5.1.3 The $MnCr_2O_4$ Spinel Formation Mechanism 154
5.1.4 Mixed Surface Manganese and Iron Oxide (MnFe)O 154
5.1.5 Surface Grain Boundary Oxides 155
5.2 Selective Oxidation of Chromium and Manganese 157
5.2.1 Effect of Annealing Temperature on Selective Oxidation 157
5.2.2 Effect of Steel Composition on Selective Oxidation 163
5.2.3 Effect of Annealing Atmosphere on Selective Oxidation 165
5.2.4 The 'Edge Defect' 165
Chapter 6 : Conclusions 176
Chapter 7 : Recommendations 178
Chapter 8 : References 179
Appendix 1: Associated Publications 185
List of Tables 186
List of Figures 187

List of Abbreviations

AES	Auger Electron Spectroscopy
BCC	Body Centred Cubic
EDS	Energy Dispersive X-Ray Spectroscopy
FCC	Face Centred Cubic
FIB	Focussed Ion Beam Miller
GDOES	Glow Discharge Optical Emission Spectroscopy
LHS	Left Hand Side
RHEED	Reflection High-Energy Electron Diffraction
RHS	Right Hand Side
SEM	Scanning Electron Microscopy
SIMS	Secondary Ion Mass Spectrometry
SNMS	Secondary Neutrals Mass Spectrometry
TEM	Transmission Electron Microscopy
XPS	X-Ray (excited)-Photoelectron Spectrometry
XRD	X-Ray Diffraction

Chapter 1 : Introduction

Tinplate is used to manufacture a wide range of products. This includes cans for food packaging, drums and pails for chemical, agricultural and industrial products, aerosol cans for both food and household products and even bakeware products and automotive components. Tinplate is considered to be a sophisticated and highly finished product made by the steel industry and a large number of specialist operations are necessary to convert the raw hot rolled strip into finished tinplate. Hot rolled strip is cold rolled to produce a thin steel strip with a thickness nominally less than 1 mm. This steel has been heavily deformed and as such has a low ductility. Re-crystallization annealing improves the steel sheet's formability. Batch annealing is a common re-crystallization annealing practice that is used to anneal steel strip for tinplate applications. Figure 1-1 demonstrates the operations that occur to convert the batch annealed steel coils to the finished tinplate product at Bluescope Steel's Port Kembla tinplate line. The steel strip is temper rolled to obtain the required mechanical properties and ensure a flat surface finish for tinplating. Next the strip is cleaned, pickled and then the strip is plated in a series of cells containing a complex electrolyte solution and pure tin anodes. A current is passed between the steel strip and the tin anodes to plate the underside of the strip. The strip is then turned over and passed through a second layer of cells to coat the other surface of the steel strip. The tinplate then passes through a reflow unit where the plated tin may be melted and then immediately quenched to produce a tinplate product with a bright lustre. Finally the tinplate undergoes a quality control process, oiling and cutting to produce the finished tinplate product.

The surface of the steel prior tinplating must be homogenous to ensure an even tin coating. Bluescope Steel (previously BHP, BHP Steel) have identified in the production and quality control room that a defect is observed in some tinplate coils. This defect was found to be caused by surface precipitates formed during batch annealing that reduced the wettability of the surface with respect to liquid tin. This caused uneven coatings of tin in local areas. This defect has been termed 'carbide edge' in the past due to the belief that these surface precipitates are carbides and the fact that this defect generally occurs near the coil edge. In this investigation the defect will be termed the 'edge defect'.

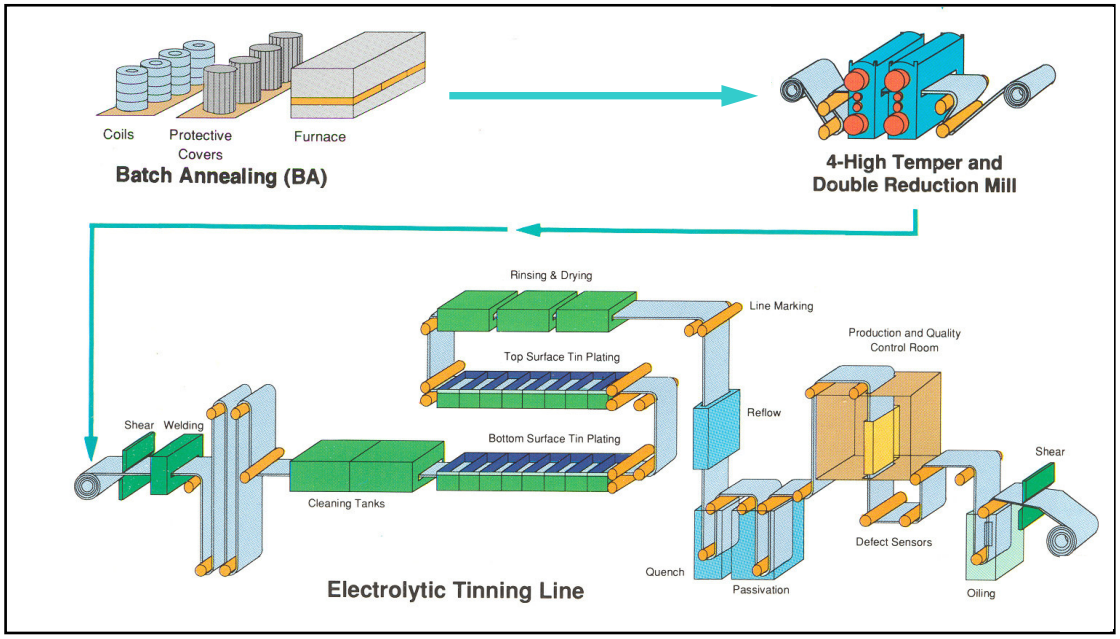

Figure 1-1: The tinplate production process for batch annealed steels

The 'edge defect' was first observed in the 1980's and coincided with the addition of chromium to batch annealed steel strip which was designed to reduce the formation of surface graphitization during batch annealing. The concentration of chromium in the steel is about 0.06 wt % and has been effective in reducing surface graphitization. This 'edge defect' is a continuous band of low reflectivity located near the edge of tinplated steel strip. This band is typically 20 to 50 mm wide and usually located 20 to 100 mm from strip edge. The first and last 1000 to 3000 m of coil is generally affected. Both edges of the strip and both the bottom and top surfaces are usually affected. The regions of low reflectivity are not aesthetically pleasing and result in a downgrading of the product. In addition, the affected areas exhibit a reduced corrosion resistance.

This thesis investigated the 'edge defect'. The steel surface was characterised and the surface precipitates were identified. Annealing experiments were carried out to develop a fundamental understanding of the effect chromium and manganese has on the formation of precipitates on the surface of low carbon sheet steel.

Chapter 2 : Review of the Literature

2.1 Introduction

Batch annealing is an important process in the production of tinplate steels. However, surface-related phenomena may arise during this process that can affect the finished tinplate product. Surface graphitization leaves a stain on the steel surface which is not easily removed and may affect the tinplating. Surface graphitization is reviewed in this chapter to understand fundamentally how this phenomenon occurs and the role of chromium in reducing this defect. This is followed by a comprehensive literature review on selective oxidation of steels. Chromium is often added to minimise surface graphitization during batch annealing which may lead to chromium being selectively oxidised as chromium has a much higher affinity for oxygen than iron.

As steels are annealed in nitrogen-rich environments, nitrogen pick-up may occur during batch annealing. Nitrogen pick-up can have a negative effect on the mechanical properties of the steel. Nitrogen competes with oxygen for surface active sites thus nitrogen pick-up is important to the selective oxidation process and a review on the literature on the relationship between nitrogen pick-up and oxidation is included in this chapter.

This chapter includes a section on techniques commonly used to characterise surfaces. The advantages and limitations of scanning electron microscopy (SEM), transmission electron microscopy (TEM), auger electron spectroscopy (AES), x-ray (excited)-photoelectron spectrometry (XPS), secondary ion mass spectrometry (SIMS) and secondary neutrals mass spectrometry (SNMS) are discussed.

2.2 Surface Graphitization

Surface graphitization is a phenomenon that forms when low carbon steel sheet is annealed in atmospheres reducing to iron. This defect appears as a black stain and is not removed by the cleaning or pickling operations that occur prior to coating [1]. The surface graphite reduces the wettability of the surface with respect to the liquid tin applied to the steel strip surface to produce tinplate. The bright lustre of the tin coating is affected and the surface has a mottled and matte appearance. This defect has also been termed frosty surface or graphite stain in the steel industry.

Surface graphitization occurs predominantly in batch annealed strip steels. There are two major sources of carbon in the batch annealing process, residual oil and the carbon in the steel. Residual oil present on the steel strip during batch annealing is caused by inadequate cleaning processes and may decompose and be carbonized on the steel sheet. It deposits as a soot near the edge of the strip [2] which is a different kind of staining to that of surface graphitization. This eliminates the residual oil as the source of carbon suggesting the source of carbon for surface graphitization is from within the steel itself.

Graphite is the stable phase of carbon in iron and carbon alloys at equilibrium states. Graphite is observed in cast irons and hyper-eutectoid steels held at high temperatures for long periods of time. However, the common form of carbon in steels is as the metastable phase cementite (Fe_3C) mainly because of the large volume expansion that is associated with the formation of graphite in a ferrite matrix and the slow kinetics of the cementite to graphite reaction. Surface graphitization in low carbon steels is quite unusual because of the very low amount of carbon present in the steel.

A mechanism for the formation of surface graphite was proposed by Inokuti [3] and refined by Nakamura and Sato [4]. It was assumed that the free energy of the iron at the surface of the steel is larger than that in the bulk and that the resistance for voluminous constituent arising from the graphite formation at the surface is less than that in the bulk. There is always a thin film of surface oxide about 10 nm thick [5] formed on cold rolled steel surface via reaction 2.a. The carbon in solution in the

steel reacts with the iron oxide layer to produce carbon monoxide (reaction 2.b) which then decomposes to form carbon dioxide and graphite as shown by reaction 2.c

$$Fe + ½O_2 \leftrightarrow FeO \quad (2.a)$$

$$FeO + \underline{C} \leftrightarrow Fe + CO \quad (2.b)$$

$$2CO \leftrightarrow CO_2 + C_{gr} \quad (2.c)$$

The C_{gr} denotes graphite. The $\underline{C}$ denotes the carbon in solid solution in the steel which becomes available for reaction by the decomposition of cementite as shown in reaction 2.d.

$$Fe_3C \leftrightarrow 3Fe + \underline{C} \quad (2.d)$$

The carbon dioxide in reaction 2.c can further react with iron as shown in reaction 2.e to generate carbon monoxide and iron oxide, which supply reactions 2.b and 2.c.

$$Fe + CO_2 \leftrightarrow FeO + CO \quad (2.e)$$

Other than reaction 2.c, carbon monoxide can react with iron to form cementite and carbon dioxide as shown in reaction 2.f depending on equilibrium constants.

$$3Fe + 2CO \leftrightarrow Fe_3C + CO_2 \quad (2.f)$$

The equilibrium constants for reaction 2.c and reaction 2.f are shown in equations 2.1 and 2.2 respectively.

$$K_{gr} = \left(\frac{P_{CO_2}}{P_{CO}^2} \right)_{gr} \quad (2.1)$$

$$K_{cem} = \left(\frac{P_{CO_2}}{P_{CO}^2} \right)_{cem} \quad (2.2)$$

The $\left(\frac{P_{CO_2}}{P_{CO}^2}\right)$ ratio must be maintained at an intermediate value between K_{gr} & K_{cem} in the clearance between the steel sheet's for graphite to form during batch annealing. This will cause reaction 2.c to tend to proceed to the right and reaction 2.f to tend to proceed to the left. The partial pressure of the carbon monoxide gas must be maintained above a certain critical level for graphite to be precipitated on the steel surface.

As the reactions proceed carbon is lost from within the steel. When the carbon in the steel is reduced to the solid solution limit of carbon in ferrite the supply of carbon to the surface of the steel is reduced. Therefore there is less generation of carbon monoxide gas lowering the partial pressure of the carbon monoxide gas to below its critical level. This in turn has the effect of stopping the precipitation of any more graphite.

The carbon monoxide gas plays the role of the carrier of the carbon. The partial pressure of the carbon monoxide is increased by the decarburisation of the steel and is decreased by the precipitation of the graphite on the surface of the steel. If the system is a closed one the reactions will proceed without changing the CO/CO_2 ratio [3]. This means that the amount of graphite precipitated is dependent on whether the steel is in tight contact or not. If a single specimen is annealed by itself there will be little graphite formation. When two specimens are kept in tight contact the degree of graphitization is large. As the gap is increased the degree of graphitization will decrease until the gap reaches 0.5 mm and the amount of graphite has approached that of a single specimen [3]. This is shown schematically in Figure 2-1. The fact that very little graphite was formed when tight contact was not maintained was because the carbon monoxide carrier gas generated at the surface of the steel was rapidly dispersed into the atmosphere and hence the critical partial pressure of carbon monoxide was not maintained. Nakamura and Sato [4] found that the critical partial pressure of carbon monoxide which must be reached before graphitization occurs was 0.1% [4]. Clearly batch annealed steels are susceptible to surface graphitization because the tightly coiled sheet's maintain the carbon monoxide gas partial pressure.

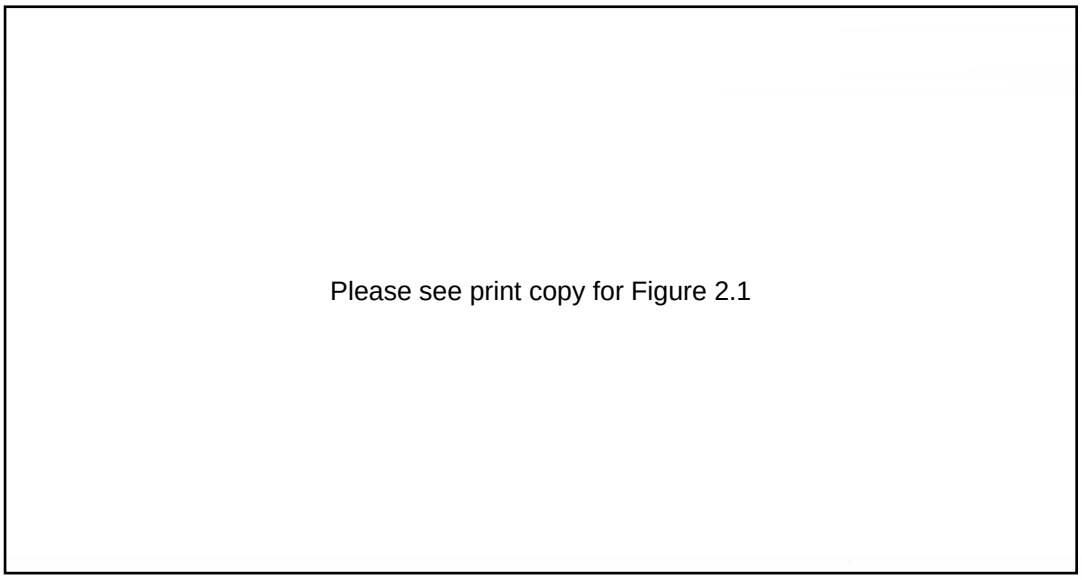

Figure 2-1: Variation in the reflection intensity of (002) plane of graphite with the relation of the clearance between 2 specimens in slow-cooling at the rate of 30 °C/hour after annealing in vacuo at 700 °C for 15 minutes [3].

Graphite may also form in steels that are annealed without tight contact. The amount of graphite in this case is much lower and can not be explained in terms of the previous mechanism. This form of graphite can be located internally but is usually on or near the surface. This graphite tends to precipitate in the vicinity of the cementite or at non-metallic inclusions such as FeO and MnO. In this case the mechanism for the formation of graphite is considered to be by the dissolution of cementite (reaction 2.g) [3, 6]. Okamoto [7] observed voids at the cementite ferrite interfaces or between the fractured segments of cementite particles in steels in the cold rolled state. These voids that were formed during the cold rolling process were not filled by iron atoms when annealed at 500 °C. These voids accommodate the volume expansion required for the formation of graphite [7]. Figure 2-2 shows schematically an example of fractured cementite particle with a 0.4 μm long void in cold rolled steel. The void is approximately 20% of the original cementite particle and is hence large enough to accommodate for the volume expansion accompanied with the graphitization of cementite which is approximately 14% as showed by equation 2.3, where V is the volume of cementite.

$$Fe_3C \leftrightarrow 3Fe + C_{gr} \qquad (2.g)$$

$$V = 0.911\ V + 0.227\ V = 1.138\ V \qquad (2.3)$$

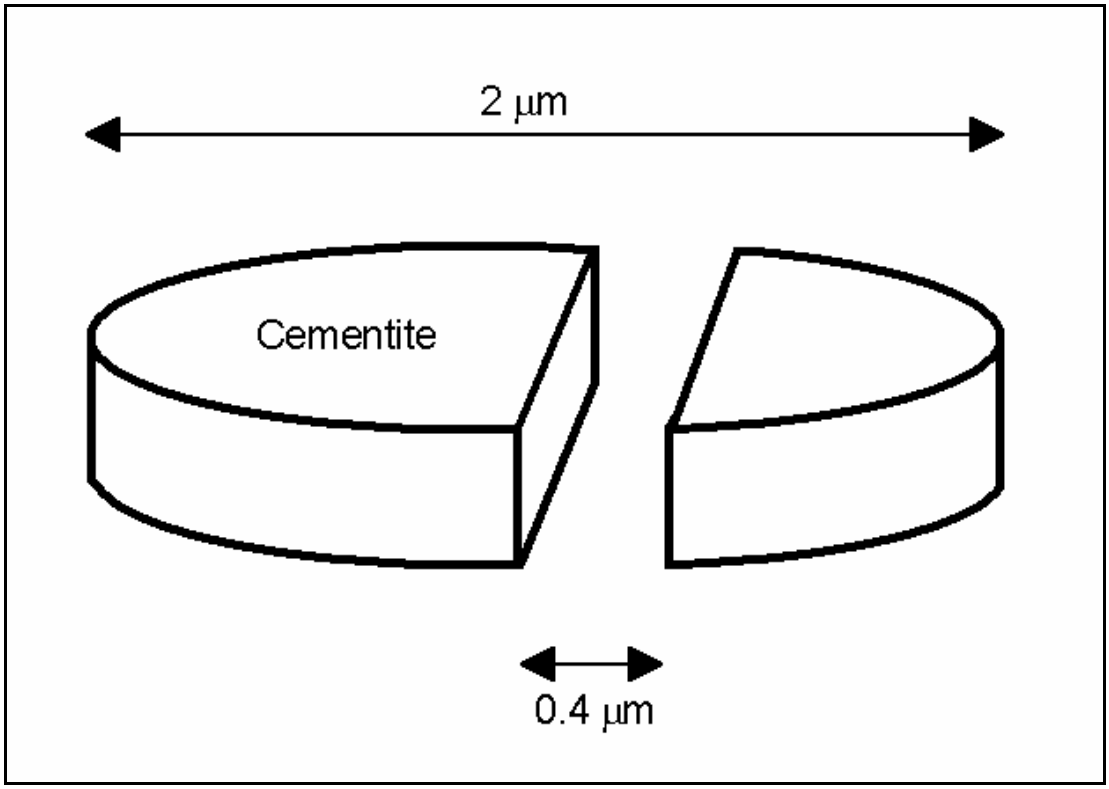

Figure 2-2: Schematic diagram of a fractured cementite particle.

The graphitization rate in ferrite by the dissolution of cementite is controlled by the diffusion of carbon and not by that of iron [8]. Therefore when graphitization takes place in steel many voids must be available to provide space for graphite. As this mechanism does not rely on atmosphere for the formation of graphite it is not surprising that graphite has been found to form in the interior of annealed high purity low carbon cold rolled steels [6, 7]. It should be noted that the amount of graphite formed from this mechanism is quite low compared to the atmosphere assisted surface graphite formation mechanism.

Surface graphite may be limited by adding small amounts of a third element into low carbon steel. There are three possible mechanisms suggested by Leroy et al. [9] in which surface graphitization can be reduced by the addition of a third element to the steel. The first was to stabilise the cementite at the annealing temperature, which tends to make reaction 2.f proceed to the right and reduce graphite formation. The second was to reduce the oxygen potential at the surface of the steel and decreases the amount of carbon oxides formed during the annealing treatment. This can occur

by the oxidation of some alloying elements due to the presence of carbon dioxide in the clearance by reaction 2.h.

$$(Fe,X) + CO_2 \leftrightarrow (Fe,X)O + CO \qquad (2.h)$$

This reaction takes oxygen from the atmosphere and places it on the surface of the steel. Consequently the decomposition of cementite in reaction 2.f is less effective and less graphite formation occurs. The last way surface graphite may be limited by the addition of a third element was by forming a superficial film i.e. a degreasing film which may act as a barrier for the carbon migration to the surface or may have an inhibiting action to carbon deposition.

The phenomenon of surface graphite formation is closely related to the decarburization of steel where the carbon in solid solution is selectively oxidised. Surface graphitization can also be explained in terms of decarburization of the steel followed by the decomposition of carbon monoxide precipitating graphite. Decarburization usually occurs when the steel is at a temperature above the A_3 or A_{cm} [10]. However, in the case of decarburization associated with surface graphitization it occurs at temperatures below A_1. Decarburisation transpires when a chemical concentration gradient occurs in the steel, which produces a flux of carbon out of the steel.

2.2.1 Morphology of Surface Graphite

The graphite appears as a black stain on the surface of the steel sheet prior to coating. When observed at higher magnifications it was noticed that the degree of blackening is different from grain to grain [3]. The graphite has been identified as having a hexagonal structure of a= 0.2464 nm, c=0.6736 nm and c/a=2.734 by x-ray diffraction [3]. The basal plane of graphite, $\{002\}_G$, is parallel to the steel surface [3]. The graphite precipitated preferentially on the surface of iron grains having the normal direction less than approximately 15 degrees in a cubic angle around the $<110>_\alpha$. If the surface iron grains have the normal direction $<110>_\alpha$ Figure 2-3 shows the coherency relationship between the graphite and the α-iron with $\{002\}_G$ // $\{1\ \bar{1}0\}_\alpha$ and $<100>_G$ // $<111>_\alpha$. The interatomic distance parallel to $<100>_G$ direction

on the $\{002\}_G$ plane is 0.246 nm. However the distances of the $\{100\}_\alpha$ and $\{111\}_\alpha$ planes are 0.287 nm and 0.249 nm, respectively. The deviation from the ideal geometric coherency relationship is about 10% [3]. This means that the areal deviation from the ideal geometric coherency relationship is larger than that generally accepted as a good condition for coherency [3].

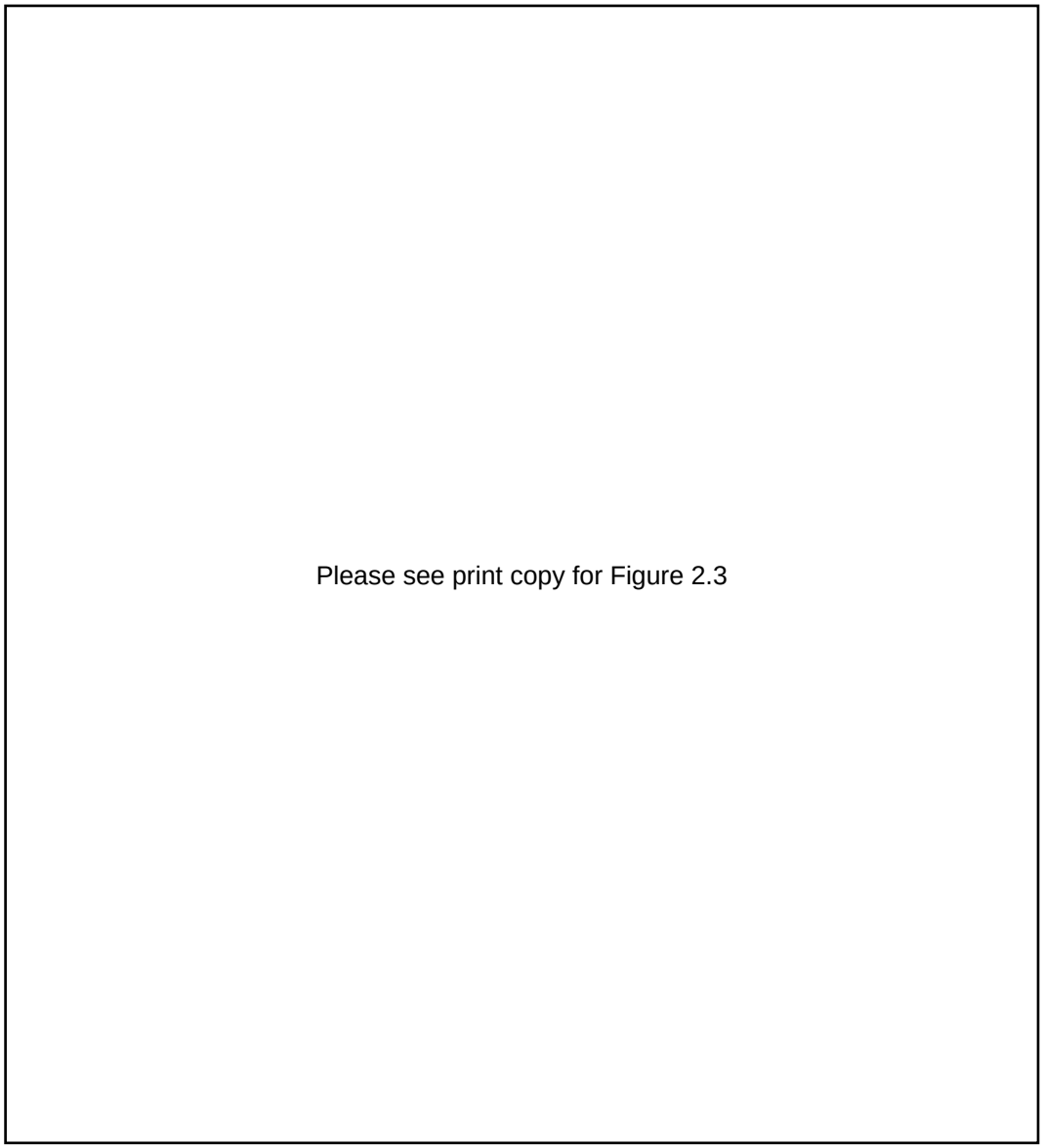

Figure 2-3: Arrangements of iron atoms on $\{002\}_G$ planes which are coherent with $\{011\}_\alpha$ planes of α–iron matrix [3].

The morphologies of the graphite formed under different annealing conditions are similar under high magnification examination [4]. This includes graphite formed in a carburizing gas atmosphere. This confirms the fact that surface graphite is formed by the precipitation of carbon from the CO carrier gas. The surface of the iron matrix

was observed to become roughened during the process of forming graphite and is believed to be caused by the repeated oxidation and reduction reactions occurring at the surface of the iron matrix [4].

2.2.2 Factors that Affect the Degree of Surface Graphitization

The degree of graphite formation during the annealing process is influenced by the clearance between the adjacent steel sheet's, the annealing atmosphere, the annealing temperature and the annealing time.

Annealing Temperature

The amount of graphite formed depends on the annealing temperature. Graphite formation peaks at a temperature of 675 °C and was not usually formed at temperatures below 600 °C [4]. Annealing above the A_1 transformation temperature dramatically reduces graphite because the solubility of carbon in γ-iron is about 40 times larger than that in α-iron. The carbon is retained in the steel and therefore does not diffuse to the surface. Graphite only forms on steels annealed above the A_1 transformation temperature that have been slowly cooled [3].

Annealing Time

The annealing time has an effect on the amount of graphite formed on the surface of cold rolled low carbon steels. Figure 2-4 shows that samples annealed for a longer period of time (6 hours) had more surface graphite than those annealed for short times (15 minutes). Graphite will continue to precipitate on the surface of the steel until the carbon concentration in the steel reaches that of the solid solubility limit of graphite in α-iron [3].

Annealing Atmosphere

The annealing atmosphere has a large effect on the degree of graphite formed on the surface of the steel sheet. Inokuti [3] showed that the degree of graphitization was much larger in steel specimens that were annealed under vacuum conditions. Specimens annealed in argon gas and nitrogen produced similar amounts of surface graphite. The comparative graphite formation is shown in Figure 2-4. Samples annealed in argon gas or in nitrogen gas only showed approximately one tenth of the

graphite that was formed on the surface of the specimens annealed under vacuum (Note different scales). A 7% H_2 + 93% N_2 atmosphere only produced approximately one ninetieth the amount of graphite on the surface of the steel specimens. Steels annealed in a hydrogen atmosphere show no surface graphite.

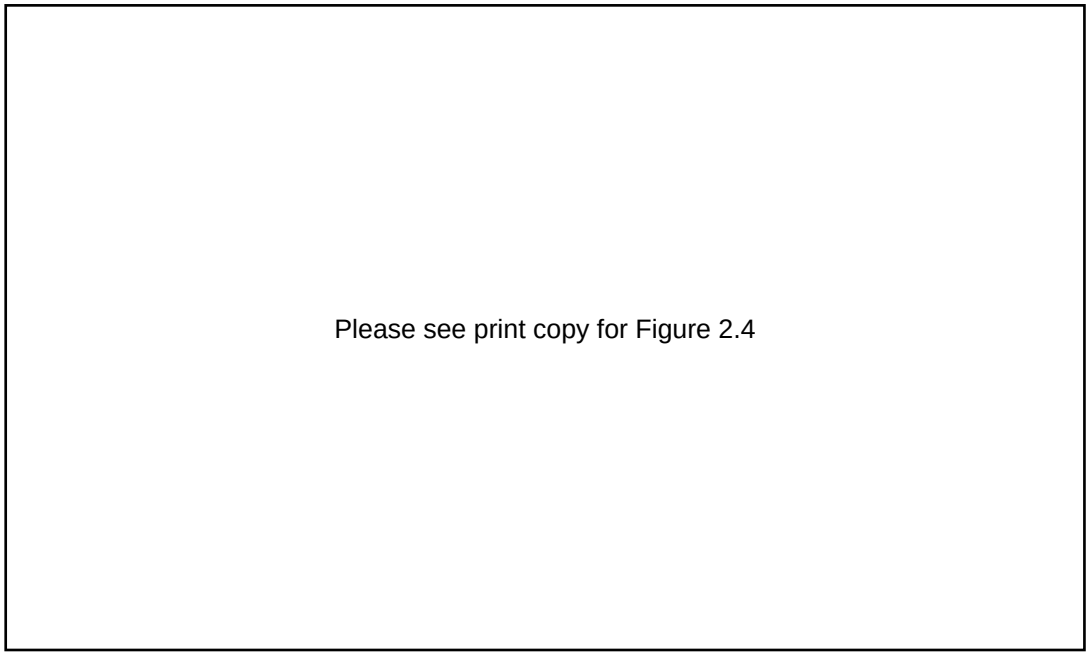

Figure 2-4: The variation in the reflection intensity of (002) plane of graphite for the specimens treated by slow-cooling at the rate of 30 °C/hour and by rapid-cooling after annealing in H_2, 7% H_2 + 93% N_2, N_2, Ar and vacuum at 700 °C for 15 minutes and 6 hours [3].

Nakamura and Sato [4] showed that the percentage of hydrogen in a mixed nitrogen and hydrogen gas environment had an effect on the degree of graphite formed. The greater the amount of hydrogen in the system the less graphite was formed on the surface of the steel. If the amount of hydrogen was increased to 40% no graphite was formed on the surface of the steel sheet.

No surface graphite was formed when a steel sheet was heated to the annealing temperature in a hydrogen atmosphere and then annealed in a 8% H_2 + 92% N_2 atmosphere [4]. Nakamura and Sato [4] proposed that the hydrogen in the atmosphere reacts with the oxygen on the surface of the steel to form H_2O. This oxygen was hence excluded from the graphite formation reactions, therefore CO was not produced and no graphite was precipitated. This indicates the importance of oxygen or the iron oxide layer on the surface graphite formation mechanism.

As mentioned earlier a critical partial pressure of carbon monoxide must build up between the steel sheet's for graphite to precipitate on the steel surface. If the partial pressure is increased above this critical value graphite starts to form and the higher the partial pressure above this critical value the more graphite formation. If the carbon monoxide partial pressure is increased to 2.5% Fe_3C will precipitate simultaneously with the graphite on the surface of the steel [4]. Clearly the annealing atmosphere is a vital factor of the surface graphitization mechanism.

2.2.3 Effect of Steel Composition on Surface Graphitization

The effect of the steel composition on the surface graphite formation can be broken into two major sections, the effect of carbon and the effect of third elements.

Effect of Carbon

The carbon concentration is an important factor for surface graphitization as the carbon in the steel is the supply of carbon for surface graphitization. Lowering the carbon concentration of the steel will reduce the amount of graphite precipitated on the surface of the steel sheet. If the carbon concentration is lower than the solubility limit of graphite in α-iron no graphite will form [3]. This is shown schematically in Figure 2-5. The surface graphite did not form, as there was no free carbon to react with the oxygen to produce the CO carrier gas. Increasing the amount of carbon above the solubility limit of graphite in α-iron increased the amount of surface graphite formed [3].

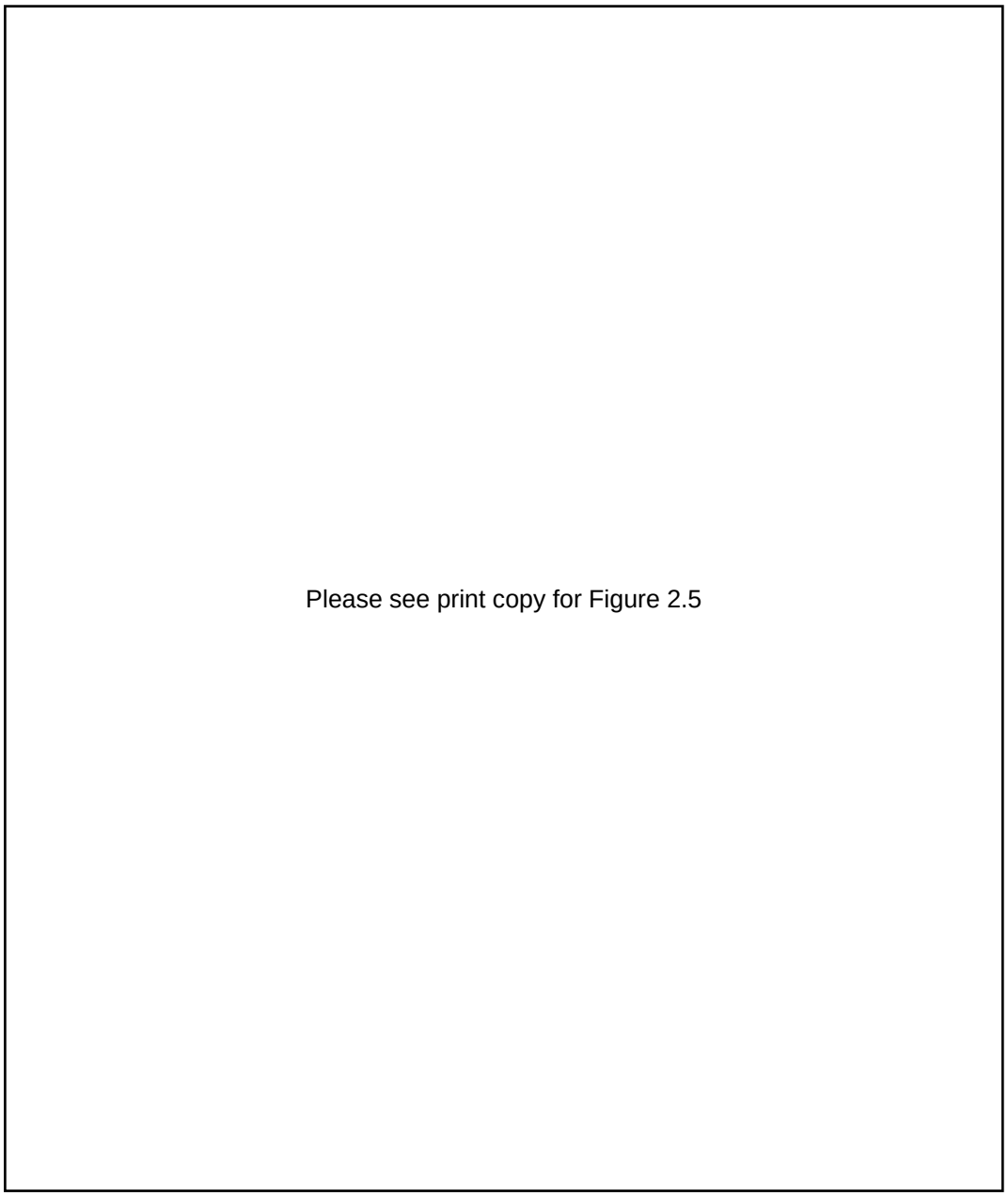

Figure 2-5: a) Relation between the reflection intensity of (002) plane of graphite and the carbon content in steel in rapid-cooling after annealing in vacuo at 700 °C for 6 hours, b) The variation of the surface coverage of graphite [3].

Effect of Third Elements

Third elements can affect the formation of surface graphite in steel. Inokuti [11] completed a comprehensive study on the effect of many elements on graphite formation in 1974. The effect of third elements can be effectively broken up into three categories: carbide formers which decrease surface graphite formation, the elements that promote slightly or have no effect on graphite formation and the

elements that have a low solubility in α-iron. Figure 2-6 and Figure 2-7 summarise his findings.

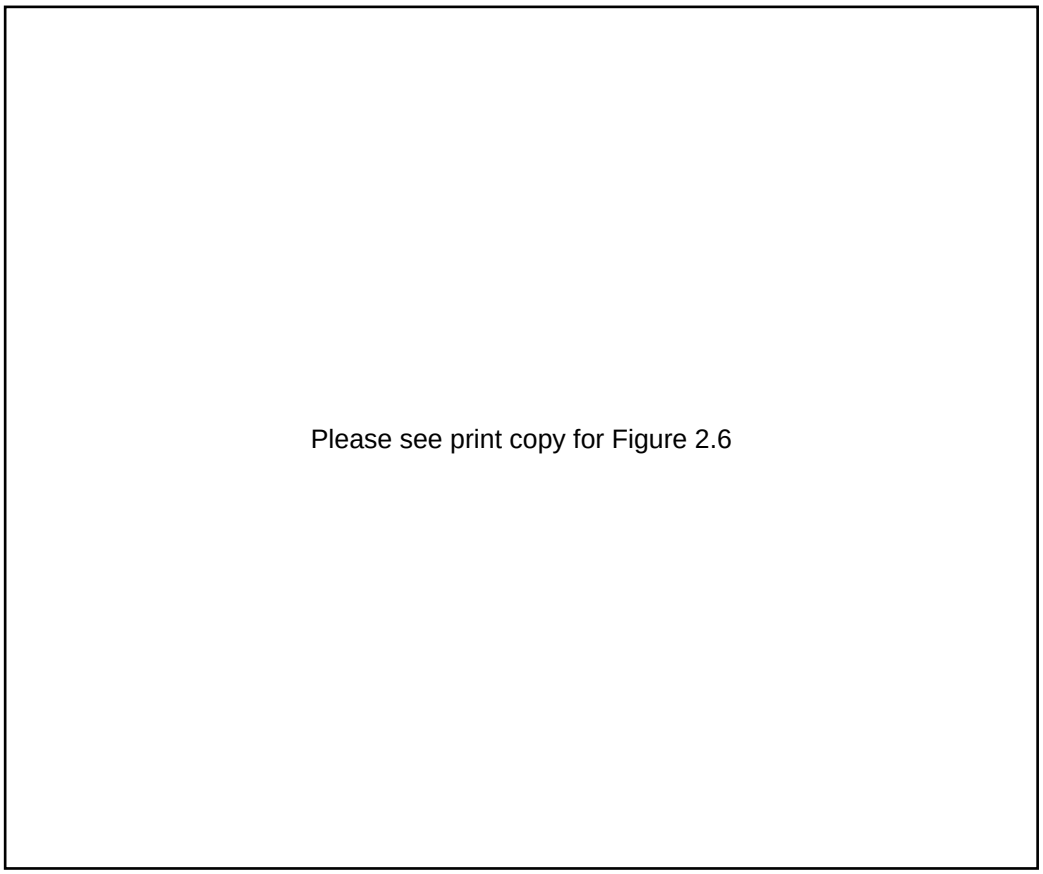

Figure 2-6: Relation between the reflection intensities of (002) plane of graphite and the concentrations of alloying elements, Ti, Zr, V, Nb, Ta, Cr, Mo, Co, Ni, Cu, Ag, Zn, B and Al after annealing in vacuo at 700 °C for 6 hours [11].

Effect of carbide formers

The elements that belong to this group include titanium, zirconium, vanadium, niobium, tantalum, chromium, molybdenum and boron. This group of elements decrease the amount of graphite formed on the surface of the steel sheet. The reasoned mechanism for this was by decreasing the solubility of the carbon and reducing and even prohibiting diffusion of carbon to the surface of the iron [11]. However, no evidence was given to support this mechanism. It is also possible for some of these elements to react with oxygen reducing the formation of carbon monoxide gas, which would suppress surface graphitization. Inokuti [11] noted a tendency for the lighter elements in this group to be better surface graphitization inhibitors.

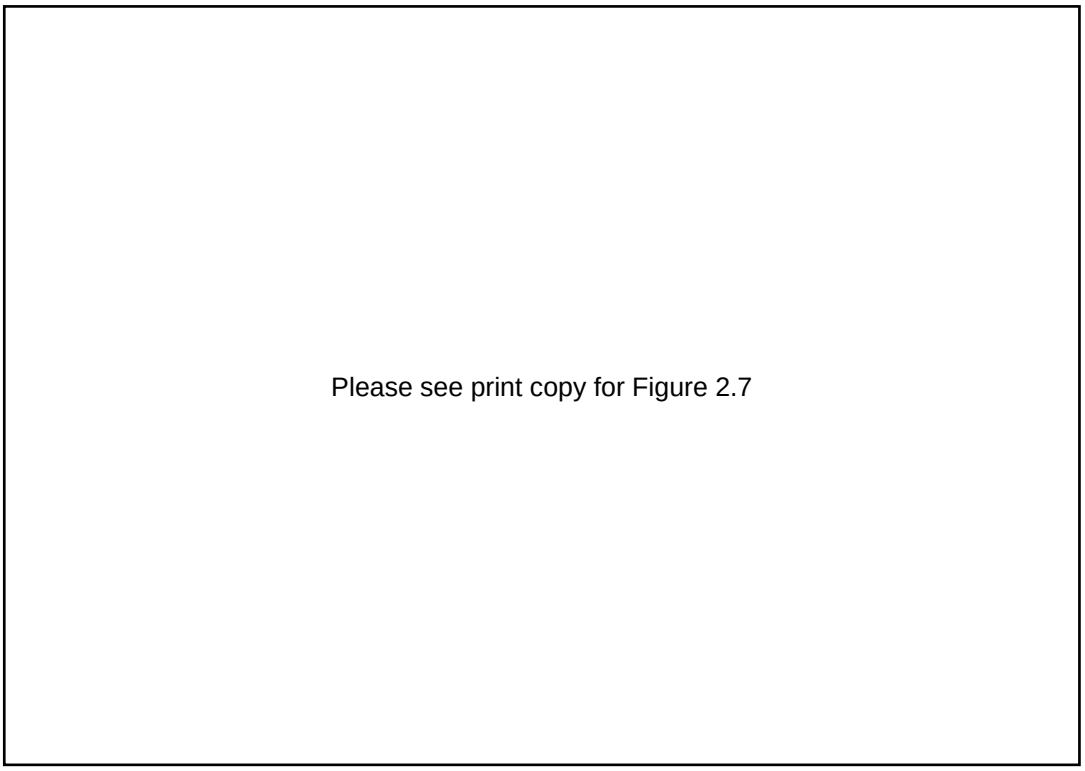

Figure 2-7: Relation between the surface coverage percents of graphite and the concentrations of alloying elements, Ti, Zr, V, Nb, Ta, Cr, Mo, Co, Ni, Cu, Ag, Zn, B and Al after annealing in vacuo at 700 °C for 6 hours [11].

Chromium

Chromium was found to strongly inhibit the formation of graphite in low carbon steel sheet by Inokuti [11] which was supported by the work of Nakamura and Sato [4]. This is not a surprising as chromium is known to reduce graphite formation in cast iron and high carbon steel [12]. Chromium is known to be a carbide forming element which decreases the solubility of carbon in the iron. Chromium is also believed to be an element that stabilises cementite. This prohibits the diffusion of the carbon to the surface of the steel inhibiting the formation of surface graphite.

Chromium also has a higher affinity for oxygen than carbon below 1200 °C. This suggests that chromium will take oxygen from the surface graphite formation mechanism and hence reduce the amount of CO formation. This is another possible mechanism that explains the surface graphite inhibition effect of chromium.

Elements that promote slightly or have no effect

The elements that belong to this group include manganese, cobalt, nickel, copper, zinc, aluminium, silicon, phosphorus and germanium. No mechanism has been proposed for the effect of these elements and why the graphite formation can be slightly promoted by the addition of these elements.

Manganese

The addition of manganese to low carbon steel has a peculiar effect on the graphite formation. Inokuti [11] found that adding manganese has the effect of greatly increasing the reflection intensity of the (002) plane of graphite hence meaning a much greater amount of graphite is present on the steel surface. However the surface coverage of the graphite only increases slightly from 70% to 78%. Figure 2-8 shows this effect of manganese on the graphite formation on the steel surface. This indicates that manganese has the effect of causing heavy graphite formation to take place locally on the surface of the steel. The addition of manganese to high carbon steel and white cast iron prevents graphitization but promotes the graphite formation on the surface of iron [13].

Elements that have a low solubility in α-iron

The elements that belong to this group include sulphur, selenium, tellurium, arsenic, antimony, bismuth, tin, lead and silver. These elements all very strongly inhibit the graphite formation on the surface of the steel specimens as well as have a very low solid solubility in α-iron. Hence, these elements tend to segregate to the grain boundaries or the iron surface [14]. The graphite formation may be inhibited by the occupation of the activated sites on the surface of iron by these elements during the annealing process. Most of these elements belong to groups 4B, 5B and 6B. There is a tendency for the heavier elements in each group to be better graphite inhibitors.

Interestingly copper is also an element that has a low solubility in α-iron however copper seems to increase the intensity of surface graphitization rather than decrease it. The reason for this is unclear however copper is known to promote graphitization in cast iron.

The pre-treatment of the steel in aqueous solutions of inorganic compounds containing the elements such as sulphur, selenium, tellurium, arsenic, antimony, bismuth, tin, lead and silver effectively inhibits the graphite formation on the surface of the steel. However, the effect was approximately only a tenth to a twentieth as great as if the elements were added into the steel. The amount of graphite formed in this case was in proportion to the amount of these elements absorbed onto the surface of the steel.

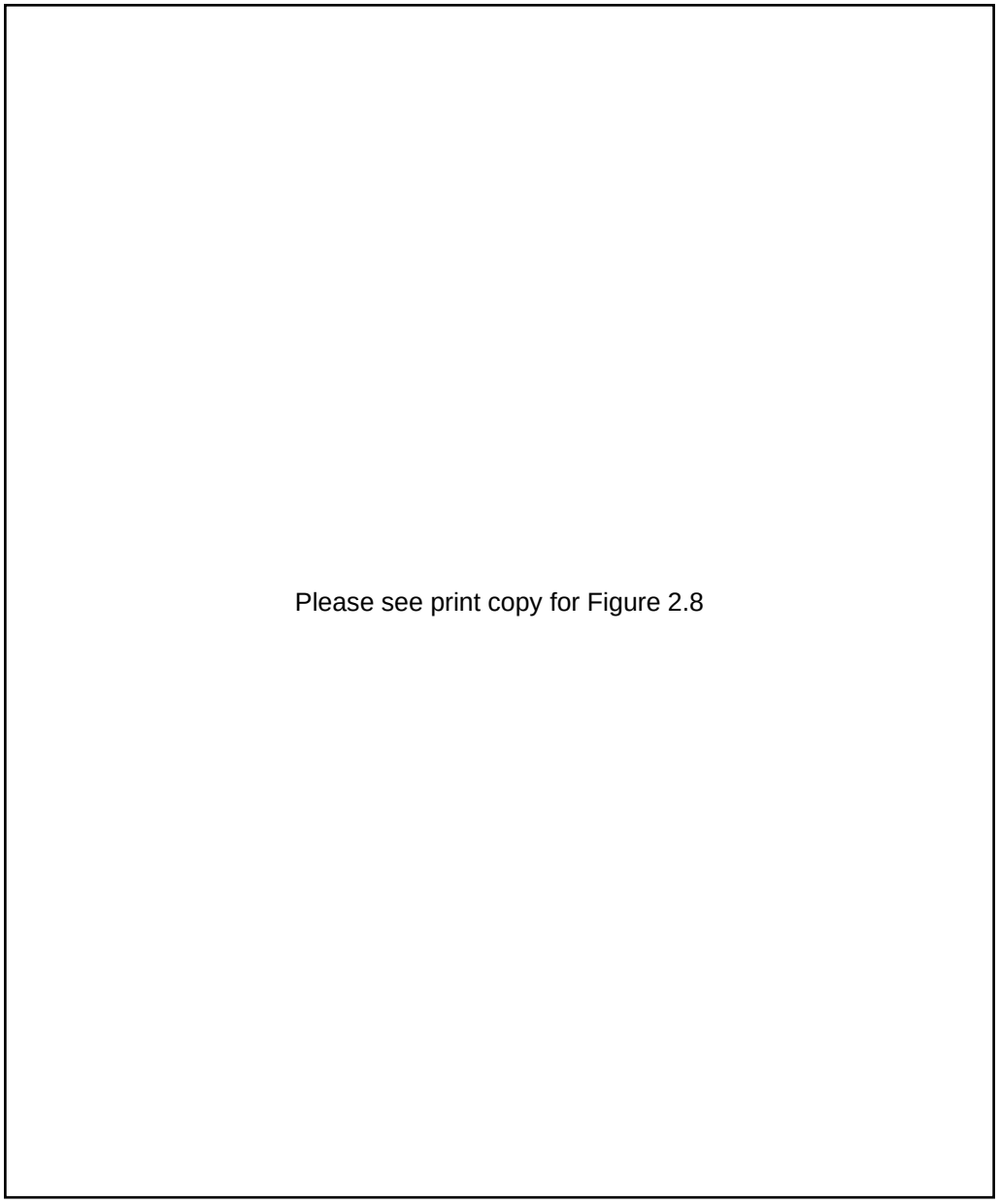

Figure 2-8: a) Relation between the reflection intensity of (002) plane of graphite and the concentration of manganese after annealing in vacuo at 700 °C for 6 hours, b) The relation between the surface coverage and the concentration of manganese [11].

2.3 Selective Oxidation

2.3.1 Oxidation

Oxidation occurs when metals or alloys are exposed to an oxidising environment. The first step in the metal-oxygen reaction occurs at the gas metal interface and involves the adsorption of gas on to the metal surface [15]. As the reaction proceeds, oxygen may dissolve into the metal, then an oxide is formed on the surface, as a film or as a separate oxide nuclei [16]. Reaction 2.i shows how a metal M will react with gaseous oxygen to form an oxide.

$$\left(\frac{2x}{y}\right)M + O_2 \longrightarrow \left(\frac{2}{y}\right)M_xO_y \qquad (2.i)$$

The overall driving force for metal oxidation is the reduction of free energy associated with oxide formation. An oxide may form if there is a reduction in the free energy change (ΔG^o). The free energy is defined by equation 2.4,

$$\Delta G^o = -RT\ln k \qquad (2.4)$$

where, k is the equilibrium constant for the reaction, R is the gas constant and T is the absolute temperature. Equation 2.4 can be re-written to give the equilibrium constant as shown in equation 2.5.

$$k = e^{\left(\frac{-\Delta G^o}{RT}\right)} \qquad (2.5)$$

Equation 2.6 shows the equilibrium constant for the reaction in terms of activity and the oxygen partial pressure,

$$k = \left(\frac{a_{M_xO_y}^{2/y}}{a_M^{2x/y}\ p(O_2)}\right) \qquad (2.6)$$

where, $a_{M_xO_y}^{2/y}$ is the activity of the bulk oxide raised to the power of 2/y, $a_M^{2x/y}$ is the activity of the metal raised to the power of 2x/y and $p(O_2)$ is the partial pressure of oxygen. Combining equations 2.5 and 2.6 results in equation 2.7

$$e^{\left(\frac{-\Delta G^o}{RT}\right)} = \left(\frac{a_{M_xO_y}^{2/y}}{a_M^{2x/y}\ p(O_2)}\right) \tag{2.7}$$

The activity of pure oxide is one and thus the value of $a_{M_xO_y}^{2/y}$ is replaced by one in the equation. By rearranging equation 2.7 the minimum oxygen partial pressure $p(O_2)^*$ required for reaction 2.i to proceed from left to right can be derived and is given by equation 2.8.

$$p(O_2)^* = \frac{1}{a_M^{2x/y}} e^{\left(\frac{\Delta G^o}{RT}\right)} \tag{2.8}$$

A diagram which shows the free energy change associated with the formation of oxides from selected elements per mole of oxygen in a given temperature range is known as the Ellingham diagram (Figure 2-9). For all metal oxides increasing the temperature decreases the reduction of the free energy and thus reduces the driving force for the oxidation of metals. The minimum partial pressure $p(O_2)^*$ to form an oxide at a given temperature may also be obtained from the Ellingham diagram. This can be done by drawing a line from zero degrees Kelvin to the oxide formation line at a given temperature and extending this line to intercept the oxygen partial pressure $p(O_2)$ axis. This intercept is the minimum partial pressure $p(O_2)^*$ required to form the oxide at this given temperature. For example to form Cr_2O_3 at 700 °C the minimum partial pressure $p(O_2)^*$ is 10^{-32} atmospheres as shown in Figure 2-10. The Ellingham diagram is therefore a very powerful tool in determining what oxides are thermodynamically stable at a given temperature and pressure.

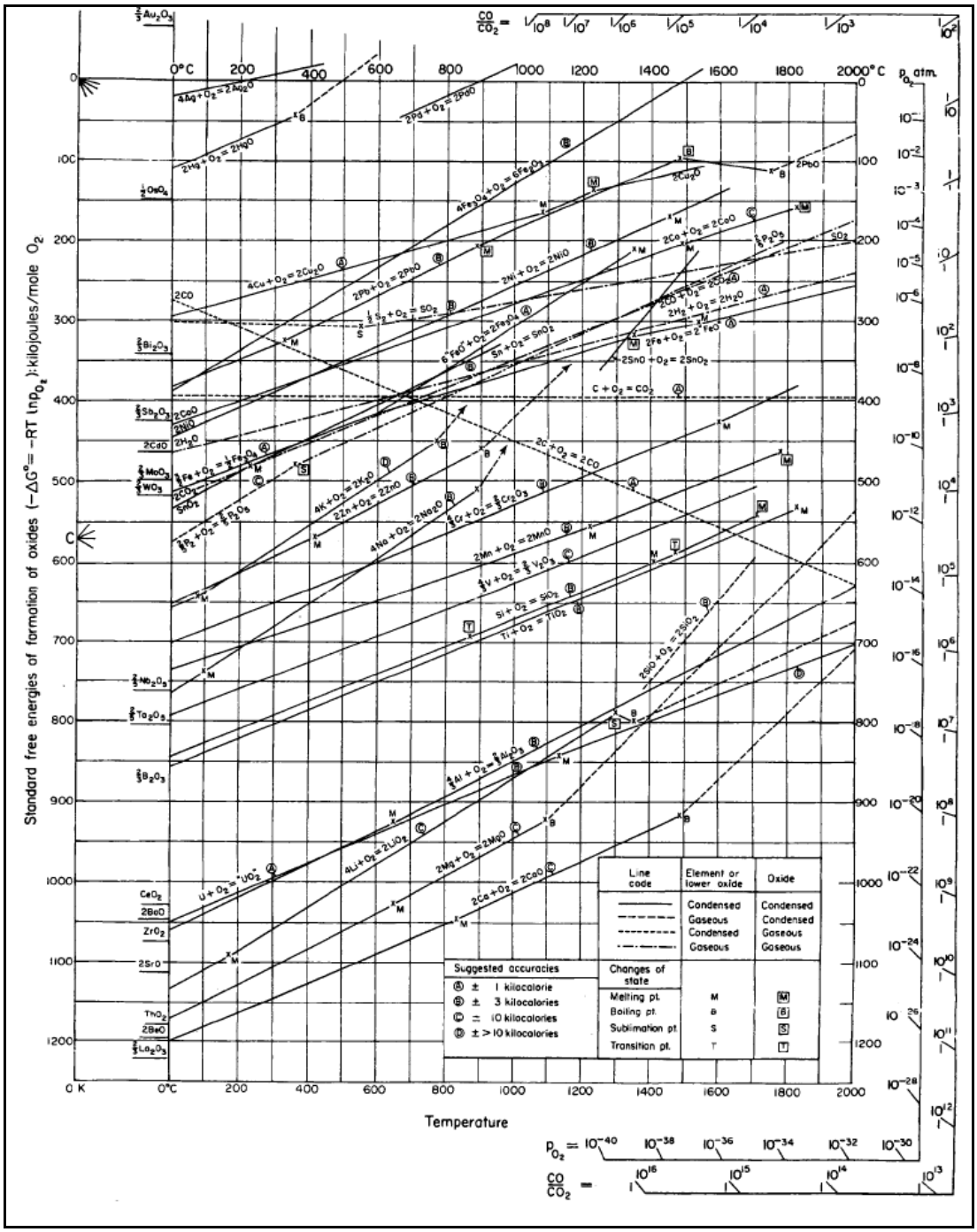

Figure 2-9: Ellingham diagram. The standard free energy of formation of selected oxides as a function of temperature.

As can be seen from the Ellingham diagram different oxides have different free energies of formation and hence the metal elements of these oxides will have different affinities for oxygen [17]. This difference in affinities can lead to a component element in alloys being preferentially oxidized. This preferential oxidation is known as selective oxidation. In ideal solid solutions the activity of an element in an alloy is equal to the fractional atomic concentration of the element [18]

thus the activity of each oxidisable component in an alloy is less than one and approximately equal to its atomic concentration in the alloy. The minimum partial pressure for oxidation $p(O_2)^*$ will increase with decreasing alloy concentration of M due to the reduction of the activity of M (a_M). Clearly the activity and the affinity for oxygen of an element in an alloy are two important factors that must be considered when an alloy is exposed to an oxidising environment.

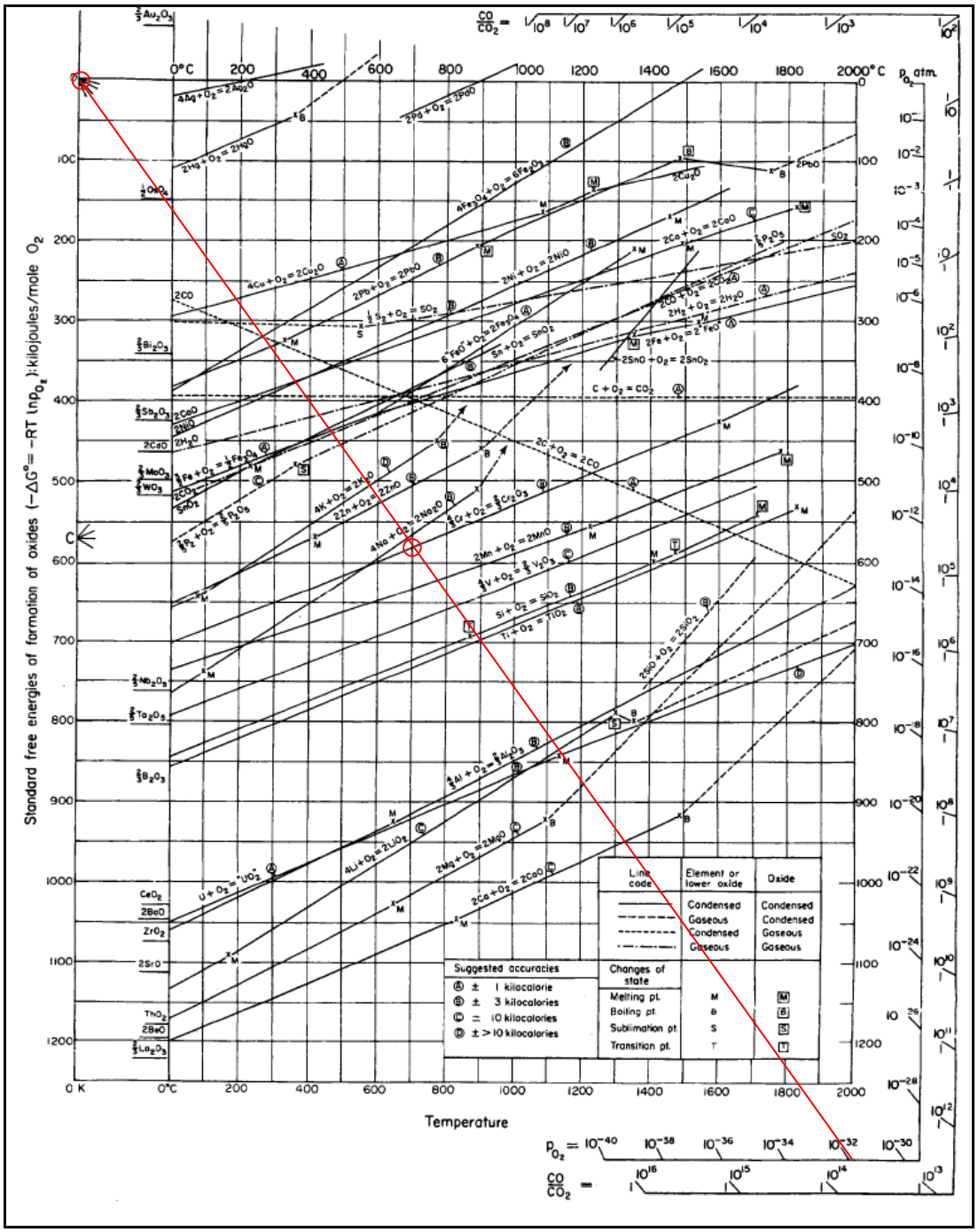

Figure 2-10: Ellingham diagram. The minimum partial pressure for chromium oxide formation at 700 °C is read from the diagram, $p(O_2) = 10^{-32}$ atm.

2.3.2 Selective Oxidation

Selective oxidation involves one or more components of an alloy being preferentially oxidised. This oxidation can be either internal or external oxidation depending on the location of the oxidation product. For external oxidation, elements react with oxygen to form an oxide on the alloy surface. Internal oxidation takes place when oxygen penetrates the alloy to react with an alloying element, the mobility of which is much lower than oxygen [16, 19] forming an oxide below the alloy surface.

Wagner [20] proposed a theory for selective oxidation of ideal single crystal binary alloys during isothermal annealing in an atmosphere of a constant partial pressure. There is a critical molar fraction $N^{o}_{X\,crit}$ of alloying element X in the binary alloy M-X below which the selective oxidation of X will be internal and above which the selective oxidation will be external. This critical value is given by equation 2.9.

$$N^{o}_{X\,crit} = \sqrt{\frac{\pi\, g^{*}\, V\, N^{S}_{O}\, D_{O}}{2\, n\, V_{XO_n}\, D_{X}}} \qquad (2.9)$$

where, g* is the critical volume fraction of precipitated oxides which leads to blocking of all oxygen inward diffusion paths. This has been estimated to be 0.3 by Rapp [21].

N^{S}_{O} is the molar fraction of dissolved oxygen at the surface,

V and V_{XO_n} are the molar volumes for the alloy and oxide XO_n respectively,

D_O and D_X are the bulk diffusion coefficients for oxygen and alloying element X respectively, and are given by the equation 2.10 and 2.11.

$$D_O = D'_O\, e^{\left(\frac{-Q}{RT}\right)} \qquad (2.10)$$

$$D_X = D'_X\, e^{\left(\frac{-Q}{RT}\right)} \qquad (2.11)$$

where, D' is a constant for the given diffusion system,

Q is the activation energy,

R is the gas constant,

T is the absolute temperature,

Wagner's model was based on an ideal single crystal and as such the presence of lattice defects such as grain boundaries were not taken into account. However when polycrystalline materials are selectively oxidised coarse oxides precipitate at lattice defects such as at the intersections between the grain boundaries at the free surface [22, 23, 24, 25]. This is due to the fact that grain and sub grain boundaries provide fast diffusion paths for the reactive elements [26].

Wagner's model can be modified to suit grain boundary oxidation of polycrystalline materials by replacing the bulk diffusion coefficients with grain boundary diffusion coefficients in equation 7 [22], giving equation 2.12.

$$N^{o}_{X\,crit.GB} = \sqrt{\frac{\pi g^{*} V N^{S}_{O} D_{O.GB}}{2 n V_{XO_n} D_{X.GB}}} \qquad (2.12)$$

Where $D_{O.GB}$ and $D_{X.GB}$ are the grain boundary diffusion coefficients for oxygen alloying element X respectively. Grain boundary diffusion is strongly dependant on the character of the grain boundaries and as such data is limited. However grain boundary diffusion coefficients can be produced by assuming that the grain boundary diffusion activation energies are half the values for bulk diffusion (Q_o and Q_x) in a single crystal lattice [27]. Mataigne et al. [22] applied this to Wagner's model and consequently equation 2.12 becomes:

$$N^{o}_{X\,crit.GB} = \sqrt{\frac{\pi g^{*} V N^{S}_{O} D'_{O} e^{\left(\frac{-Q_O}{2RT}\right)}}{2 n V_{XO_n} D'_{X} e^{\left(\frac{-Q_X}{2RT}\right)}}} \qquad (2.13)$$

By comparing equations 2.9 and 2.13 the following relationship between $N^{o}_{X\,crit.GB}$ and $N^{o}_{X\,crit}$ is obtained (equation 2.14).

$$N^{o}_{X\,crit.GB} = e^{\left(\frac{Q_o - Q_x}{4RT}\right)} . N^{o}_{X\,crit} \qquad (2.14)$$

The diffusion activation energy for alloy element X, Q_x is greater than the diffusion activation energy for oxygen Q_o thus the term $\left(\frac{Q_o - Q_x}{4RT}\right)$ is negative and $N^{o}_{X\,crit.GB}$ is less than $N^{o}_{X\,crit}$. If the composition of element X in a binary alloy is below $N^{o}_{X\,crit.GB}$ grain boundary internal oxidation will occur, if it is greater than $N^{o}_{X\,crit.GB}$ but less than $N^{o}_{X\,crit}$ gain boundary external oxidation will occur combined with bulk internal oxidation and if the composition of X is greater than $N^{o}_{X\,crit}$ bulk external oxidation will occur. Furthermore grain boundaries will generally have a higher concentration of alloying elements than the average of the alloy. Therefore external oxidation is usually first observed at grain boundaries before bulk external oxidation.

2.3.3 The Selective Oxidation of Steel

The selective oxidation of low carbon steels involves the impurity or alloying elements being oxidised during annealing. Steels are more complicated than binary alloys and their chemistry is more complex because many reactive elements can take part in the selective oxidation process. This can lead to oxidation products not being simple compounds. Wagner's model for selective oxidation was modified by comparing the oxygen inward flow to the collective outward flow of all the oxidisable elements in the steel in order to find the transition limit between external and internal oxidation modes for steels [22]. This is shown in equation 2.15

$$\sum_X N^{o}_X \sqrt{n\,D_X\,V_{XO_n}} \geq \sqrt{\frac{\pi\, g^*\, V}{2}}\ \sqrt{N^{S}_O\,D_O} \qquad (2.15)$$

where, N^{o}_X is the molar fraction of element X in the steel.

The left hand side (LHS) represents the linear superimposition of the individual contributions of the various oxidisable elements and the right hand side (RHS) depends on the oxygen inward flow through the free surface. External oxidation

should occur when the LHS is greater or equal to the RHS. In all other cases internal oxidation should occur. This model can be applied to grain boundary oxidation by changing the values of the bulk diffusion coefficients, D_x and D_o, to grain boundary diffusion coefficients, $D_{X.GB}$ and $D_{O.GB}$.

Although it seems to fit experimental observations made on the steels investigated by Mataigne et al. [22] this model does not take into account the possible interactions between distinct diffusing species and there are many physical constants in the model most of which are only approximately known. Also, the nature of the reaction product is not well defined because of the possibility of complex oxide formation. Metallurgical features that are not taken into account in this model, but can affect the diffusion kinetics, are the dislocation density related to degree of cold rolling, micro precipitation condition, grain boundary segregations and ferrite to austenite transformation if the temperature is above the A_1 transition temperature.

The annealing of low carbon steel is typically carried out in protective atmospheres that are reducing for iron. As such these atmospheres are regarded as having no free oxygen. However these atmospheres contain oxygen bearing gases and thus always have a slight oxygen partial pressure [28]. This slight oxygen partial pressure may not be reducing for the alloying elements present in the steel as the oxygen potential at the free surface can be high enough to promote oxygen adsorption, absorption and inward diffusion [25]. Elements with high affinities for oxygen in the steel diffuse to the free surface or grain boundaries and get oxidised either internally or externally depending on how far the oxygen atoms can travel before combining with the elements [29]. If the inward oxygen atom flow and outward oxidisable solute flow are well balanced internal oxidation will occur. However if the outward solute atom flow is predominant enough as to obstruct all oxygen diffusion paths external oxidation will occur [30]. External selective oxidation can cause the chemical composition of the steel surface to be inhomogeneous and thus adversely affect the adhesion of paints and the adhesion of metallic and inter-metallic compounds which are important coating treatments [31].

The general equation for selective oxidation of steels during annealing in a protective environment is given by reaction 2.j, where Me is a metal element. The oxidation occurs by the reduction of water vapour, as no free oxygen is present in the annealing gas. The formation of metal oxides in the annealing atmospheres is a function of the H_2/H_2O ratio and the metal's reduction potential [32] . A high H_2/H_2O ratio corresponds to a low dewpoint and a low H_2/H_2O ratio corresponds to a high dewpoint. Annealing steels in protective atmospheres with very low dewpoints can minimise or even prevent selective oxidation [32].

$$xMe + yH_2O \leftrightarrow Me_xO_y + yH_2 \qquad (2.j)$$

Elements such as manganese, chromium, silicon, vanadium, aluminium and titanium have a higher affinity for oxygen than iron and can be preferentially oxidised [30]. However the activity of these elements is usually very low in low carbon steels. Figure 2-11 shows how the oxidation of elements that are commonly found in steel changes with temperature and dewpoint of annealing gas. It shows that elements that are in low concentrations in the steel have a much lower affinity for oxygen when compared to the pure elements. This change is due to the activity being reduced significantly and was demonstrated by equation 2.8. Figure 2-11 also demonstrates that a low dewpoint is required to avoid oxidation of these alloying elements.

When selective oxidation occurs there is usually an alloy depleted layer associated with the diffusion of the alloying element into oxide [25, 33, 34]. This depleted layer is located deeper into the sample than the oxidised section and is caused by the diffusion of the oxidising element towards the oxygen.

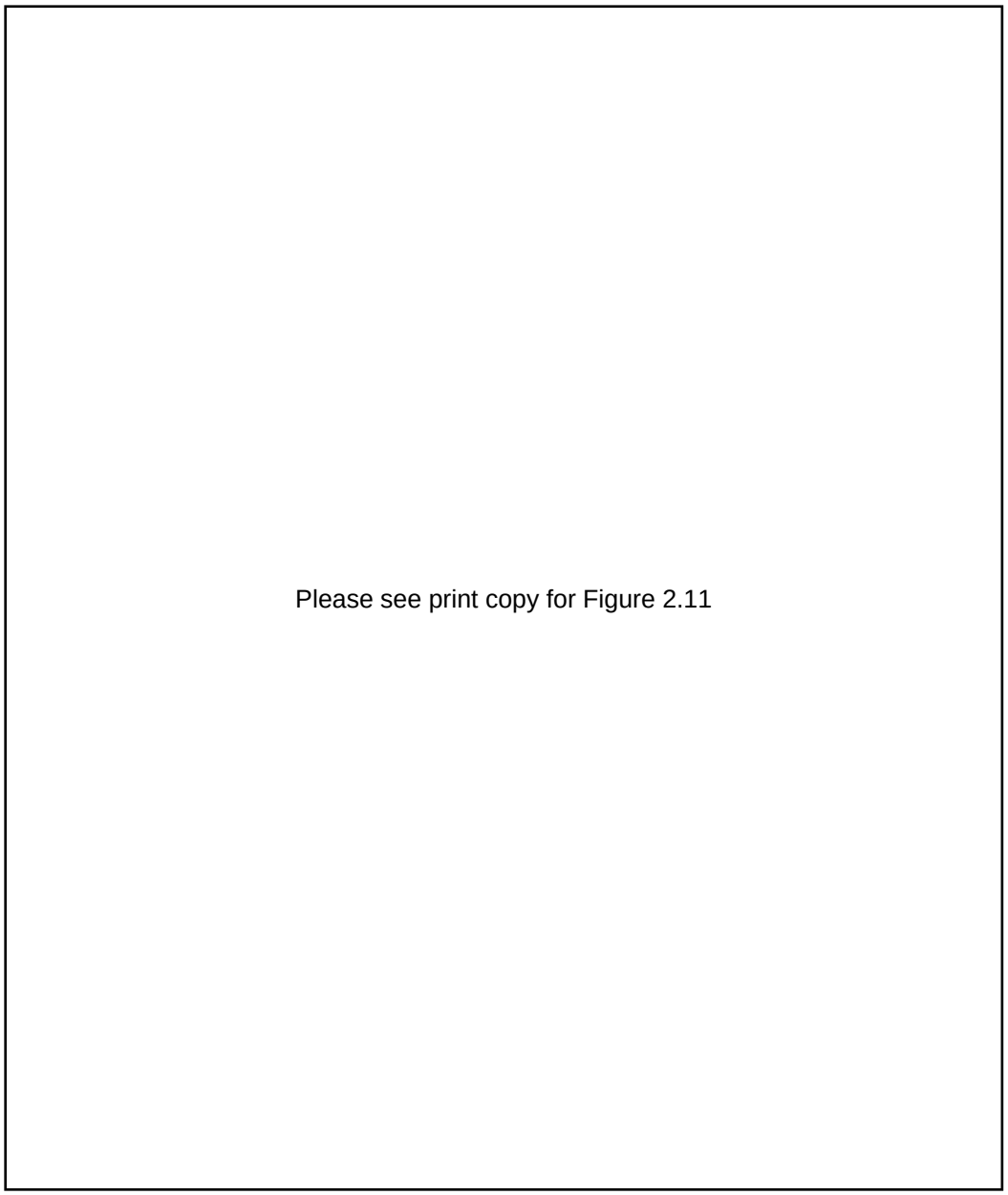

Figure 2-11: Influence of dewpoint and temperature on metal oxidation in a hydrogen atmosphere [32] .

Equilibrium surface segregation or Gibbs segregation is a phenomenon that leads to surface enrichments in a single layer of alloy atoms when steels are annealed. This surface segregation usually occurs in atmospheres when there is not enough oxygen present for selective oxidation to occur [29]. Equilibrium surface segregation involves atoms that were dissolved in steel segregating to the surface. The driving forces for this segregation is [30]:

- the saturation of the free bonds at the surface by the interaction with the atoms segregating,

- a reduction in the surface energy because the surface may be covered with a layer of atoms which has a lower surface energy than the initial iron surface,
- a reduction in the bulk elastic energy by the removal of atoms from the bulk solution. This is especially the case for interstitial atoms but also substitutional atoms larger than iron atoms,
- potential surface charge effects as most non-metal atoms become ionised upon segregation meaning that in a segregated state they are negatively charged and larger than in solution.

This segregation should lead to a decrease in the overall internal energy of the system. Equilibrium surface segregation may occur in steels that are being selectively oxidised. As such Gibbs segregation and selective oxidation can be thought of as competing mechanisms.

2.3.4 Effect of Temperature on Selective Oxidation of Steel

Increasing the annealing temperature will reduce the driving force for metals to be oxidised, as all metal oxidation reactions are exothermic. However increasing the temperature in most reported circumstance increases the amount of oxides formed on the steel surface. This can be explained by the rise in temperature increasing diffusion rates of alloying elements to the surface which results in a smaller fraction of uncovered surface [35]. Thus increasing temperature increases external selective oxidation. Figure 2-12 shows the effect of temperature on the selective oxidation of manganese. Increasing the temperature in this range greatly increased the amount of manganese observed on the steel surface.

The annealing temperature affects what elements will segregate to the surface of steels and the extent of their segregation [25]. Servais et al. [25] studied the elements that segregate to the surface of an LD rimming steel between room temperature and 1200 °C. They found nitrogen on the surface at temperatures between 250 °C and 550 °C with a maximum observed at 400 °C. Manganese was observed at the steel surface at temperatures around 500 °C. The oxygen content at the steel surface decreases as the temperature increases from 200 °C to 500 °C. This occurs with a decrease in carbon as it is presumably given off as carbon monoxide. However a

sharp increase in carbon content was observed at the surface above 600 °C. Phosphorus segregated to the surface of the steel over a narrow temperature range around 550 °C. Sulphur was detected on the surface of steel above 600 °C and was still observed up to 1200 °C. This phosphorus and sulphur segregation is likely to be related to Gibbs segregation. However it may have some impact on selective oxidation by blocking surface active sites present on the steel surface. Clearly, the annealing temperature has a profound effect on the oxidation products that will be observed on the steel surface.

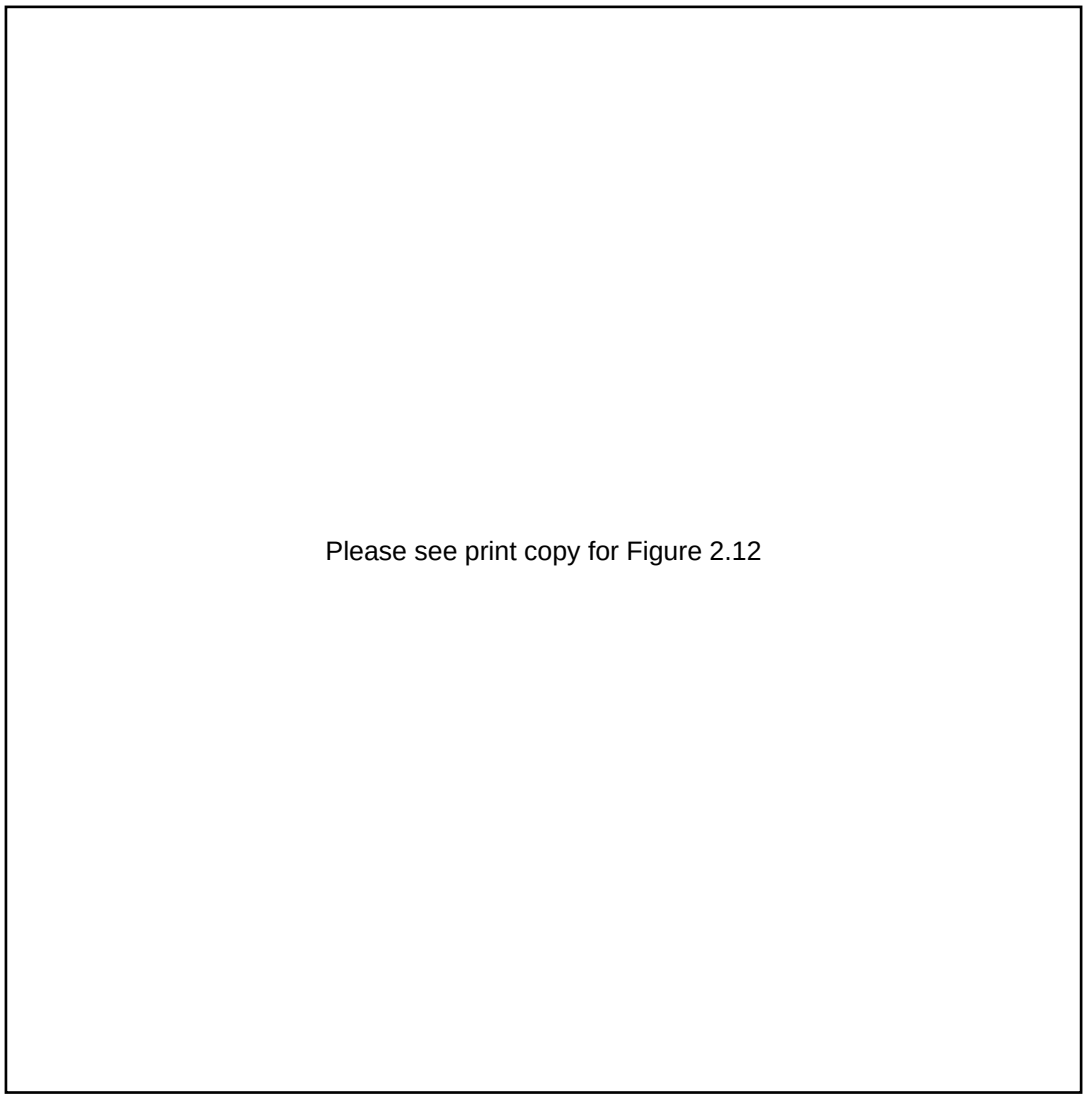

Figure 2-12: Rate of surface enrichment in manganese for 0.43 wt% Mn steel annealed in 6% H_2 + 94% N_2 containing 0.013% water vapour (dewpoint -40 °C) [36].

2.3.5 Effect of the Annealing Time on Selective Oxidation of Steel

In continuous annealing the steel is at high temperatures for short periods of time whereas in box or batch annealing the steel is at high temperature for very long periods of time. The amount of manganese on the surface of steels was observed to be much greater in steels that were box annealed compared to continuous annealed [36]. An extended annealing time generally results in a higher amount of oxide particles at the surface [36]. Surface manganese oxidation increases with time, while the rate of surface oxidation reduces with time (Figure 2-12). This may be because with increasing time the element being selectively oxidised at the surface will have further to diffuse to reach the surface.

2.3.6 Effect of Heating Rate on Selective Oxidation of Steel

What elements segregate to the surface and the amount of segregation is heating rate dependant [25] because different elements are more mobile at different temperatures in the steel. Therefore a slow heating rate should lead to a wider range of elements at the surface and as such a wider range of oxidation products would be expected.

2.3.7 Effect of Steel Composition on Selective Oxidation of Steel

The composition of the steel will affect which elements will segregate, and the extent of segregation [25]. In theory increasing the concentration of an alloying element in the steel will increase the activity of the element in the steel thus decrease the amount of oxygen required to form an oxide of this element (equation 2.8). Increasing the concentration of an alloying element in the steel will also have the effect of increasing the amount of this element at the surface and hence being able to join in the oxidation reactions. The coverage of manganese oxide on the surface after annealing increased with the increase of the bulk concentration of manganese in steel [23, 37, 38]. An increase in silicon in the steel has also been reported to increase the amount of silicon oxide observed on the steel surface [23]. In stainless steels it has been found that chromium segregation to the surface is increased by rising the chromium concentration of the steel [26].

The diffusion of alloying elements in steel has been shown to be an important factor in the selective oxidation of steel. The composition of the steel can profoundly affect the diffusion of both the inward oxygen flow and the outward solute flow. Elements that are known to segregate to grain boundaries are likely to diffuse through the steel quicker as grain boundaries act as fast diffusion paths. The addition of these elements to the steel can retard the diffusion of other elements to the steel surface by exhausting all the fast diffusion paths.

The alloying elements present in the steel will affect the morphology and the composition of the oxides formed. Angeli et al. [39] found that rod shaped particles were formed in some steels when annealed under certain conditions. These rod shaped particles were found to be manganese and boron particles unlike the typical manganese and phosphorus spherical oxide particles observed previously [39]. Clearly, the steel composition is extremely important factor in forming surface oxides and as such will dictate the type, morphology and size of the oxide particles formed.

2.3.8 Effect of Annealing Atmosphere on Selective Oxidation of Steel

The annealing atmosphere will have a dramatic effect on the selective oxidation of steels. This effect is due to the oxygen potential of the annealing atmosphere and is related to the available oxygen at the surface. The partial pressure of oxygen has possibly the most dramatic effect on the selective oxidation and segregation of elements in steel being annealed [25]. In some circumstances the oxygen potential determines if internal and /or external oxidation will occur [29].

The oxidation potential of the annealing gas is commonly measured by either the partial pressure of oxygen $p(O_2)$, the H_2/H_2O ratio or the dewpoint of the annealing gas. A high oxidation potential means a high partial pressure of oxygen $p(O_2)$ and a high dewpoint and a low H_2/H_2O ratio. The relationship between the dewpoint of the annealing gas and the saturation vapour pressure of water is given by equation 2.16 [40].

$$\log_{10} p(\text{sat } H_2O) = \left\{ \begin{array}{ll} 9.80\,DP/(273.8+DP) - 2.22 & \text{if } DP \le 0^oC \\ 7.58\,DP/(240+DP) - 2.22 & \text{if } DP > 0^oC \end{array} \right\} \quad (2.16)$$

Where, $p(\text{sat } H_2O)$ is the saturation vapour pressure of water in atmospheres (atm) and DP is the dewpoint of an annealing gas in degrees centigrade (°C).

The ratio of H_2O/H_2 can then be calculated if the partial pressure of hydrogen is known. For example, for the annealing atmosphere 5% H_2 + 95% N_2 the partial pressure of hydrogen $p(H_2)$ is 0.05 atm. The partial pressure of oxygen, $p(O_2)$ is related to the partial pressure ratio of $p(H_2O)$ to $p(H_2)$ by equation 2.17 [40].

$$\log_{10} p(O_2) = 2\left(3.00 - \frac{13088}{T} + \log_{10}\left(\frac{p(\text{sat } H_2O)}{p(H_2)} \right) \right) \quad (2.17)$$

The mass concentration of dissolved oxygen on the steel surface (C_O^{surf}) can be calculated from $p(O_2)$ using equation 2.18, which is based on the solubility of oxygen in α-iron.

$$\log_{10} C_O^{surf} = 1.00 + \frac{9398}{T} + \frac{1}{2}\log_{10} p(O_2) \quad (2.18)$$

The mass concentration of dissolved oxygen on the steel surface (C_O^{surf}) can be easily related to the molar fraction of dissolved oxygen at the surface (N_O^S) by converting from the mass concentration to molar fraction of dissolved oxygen on the steel surface.

Annealing at very low dewpoints often leads to a significant surface reconstitution and gives rise to a strongly facetted surface. The step edges of the facetted surface can act as preferential sites for nucleation of the oxides to minimise nucleation energy [39]. The chemistry of the oxides formed has been found to be dependant on the water vapour content of the atmosphere [41]. The total amount of oxides present after annealing, both internally and externally, increases with increasing dewpoint,

however the nature and distribution of the oxides is modified [42]. Clearly, the oxygen potential of the annealing gas is an important factor when annealing steels. Hudson et al. [36] reported that the surface manganese peaks at an optimum oxygen potential and reduces at both lower and higher oxygen potentials (Figure 2-13) [36]. At higher oxygen potentials inward diffusion of oxygen is fast and internal oxidation occurs with limited external oxidation and at lower oxygen potentials the supply of oxygen to the surface becomes a limiting factor for external selective oxidation and thus also a limited external oxidation is observed. External oxidation of manganese can be completely absent if the oxygen potential is low enough [38].

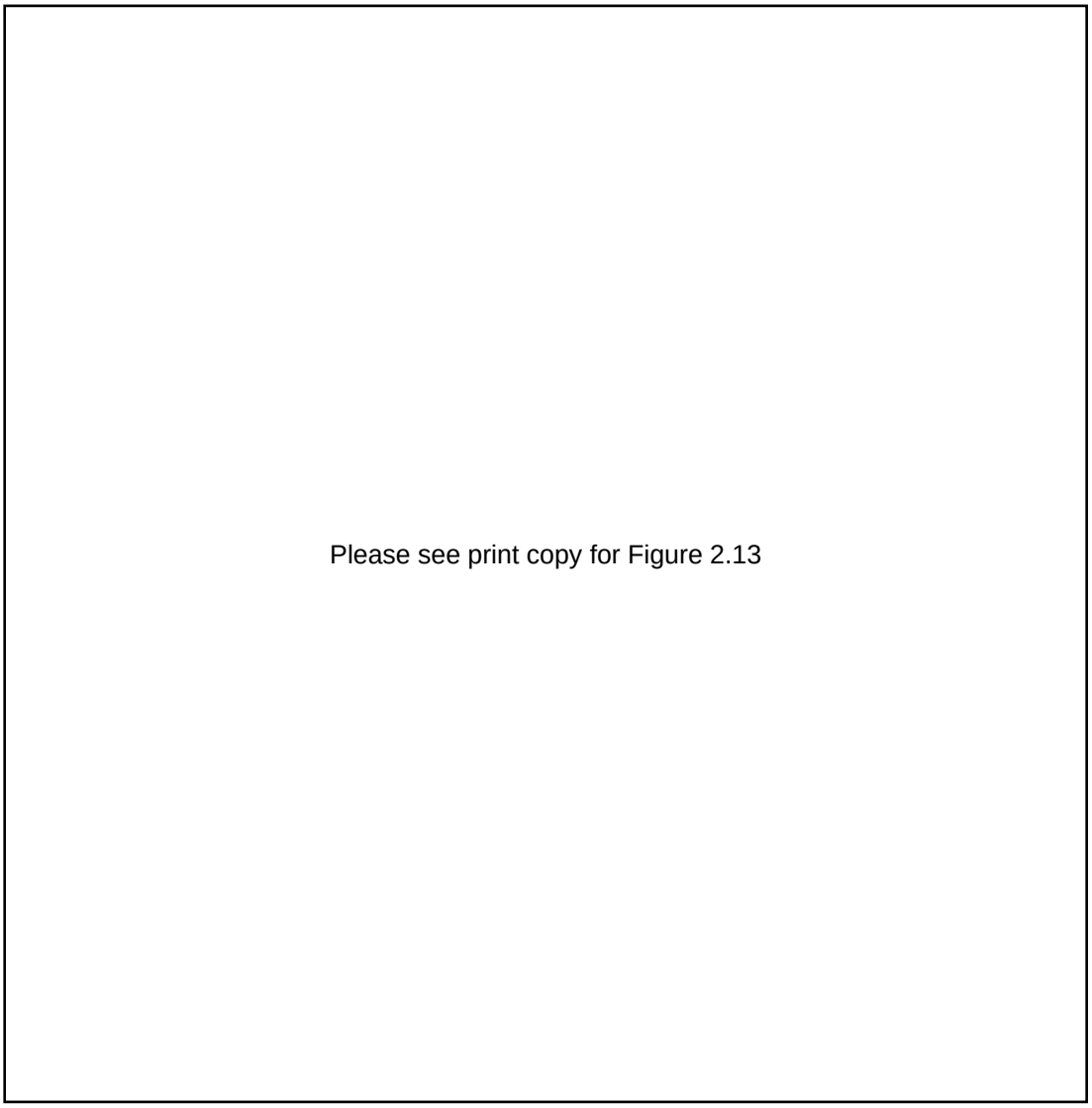

Figure 2-13: Manganese surface enrichment of a steel as influenced by oxygen potential of annealing atmosphere annealed for 7 hours at 732 °C in a 6% H_2 + 94% N_2 atmosphere [36].

In commercial steels it has been observed that the surface manganese segregation is much greater at the coil edge compared to the coil centre [23]. A reason for this is the greater exposure of the coil edges to the annealing atmosphere [38] leading to the coil edge being exposed to an atmosphere with an optimum oxygen potential for external selective oxidation. Therefore segregation of alloying elements on the steel surface is closely related to the external oxidation of the alloying elements and thus the oxidation potential of the annealing atmosphere.

2.3.9 Effect of Microstructure on Selective Oxidation of Steel

The microstructure of the steel is an important factor for selective oxidation. Surface steps, emerging dislocations and grain boundaries provide ideal heterogeneous nucleation sites for surface oxides. Grain boundaries also promote the diffusion of alloying elements to the steel surface for oxidation. For instance chromium segregation to the surface of steel was enhanced in steels with a fine microstructure [26]. The fine grain structure allows faster diffusion of chromium through the grain boundaries and sub grain boundaries because they act as fast diffusion paths. Cold working steel increases the density of vacancies and dislocations [43] and will increase the amount of fast diffusion paths in the steel [26]. Therefore cold rolled steels are more susceptible to surface selective oxidation.

The thickness of iron oxide layer prior to annealing can also affect the surface external oxidation as the initial iron oxide layer on the surface of the steel is reduced by the annealing atmosphere, which leads to the increase of the available oxygen in the annealing gas. Thus the thicker the iron oxide layer prior to annealing the higher the oxygen potential of the annealing atmosphere [24].

2.3.10 Oxides Commonly Found on the Surface of Steels after Annealing

Annealing of steel is usually carried out in atmospheres reducing to iron so the common iron oxides such as wustite (FeO), hematite (Fe_2O_3) and magnetite (Fe_3O_4), are generally not observed at the steel surface. However manganese, silicon, chromium, aluminium, vanadium and titanium oxides have been observed at the surface of steel during annealing [23]. These oxides may be complex and contain

more than one alloying element, if so they are termed mixed oxides and have rarely been fully characterised because they often have a complex nature.

Manganese Oxide

Manganese observed on the surface of low carbon steel after batch annealing is commonly in the form of oxide. The nature of these manganese oxides has been characterised by glow discharge optical emission spectroscopy (GDOES) [31] or by the combination of scanning electron microscopy (SEM) and energy dispersive x-ray spectroscopy (EDS) [38] and more commonly by x-ray photoelectron spectroscopy (XPS) [23, 37, 41]. The main manganese oxide found on the surface of low carbon steels was MnO identified by XPS although $MnFe_2O_4$ has also been suggested [38].

Manganese oxide formed on the surface of low alloyed steels (Fe-0.6 wt% Mn and Fe-1.5 wt% Mn) annealed at 800 °C in 5% H_2 + 95% N_2 gas atmosphere with a dewpoint of -30 °C was determined to be cubic MnO by using XPS and reflection high-energy electron diffraction (RHEED) [33]. MnO has the FCC NaCl crystal structure with a = 0.444 nm [44].

Mixed Manganese Oxides

Mixed manganese and iron oxide was observed on the steel surface after annealing. FeO/MnO solid solution was found to form on the surface of Fe-1.5 wt% Mn alloy annealed at 800 °C in 100% N_2 gas atmosphere with a dewpoint of -30 °C by XPS [41]. (Fe,Mn)O was characterised by electron probe micro-analysis on the surface of Fe-1 wt% Mn when annealed between 570-760 °C in high purity (99.99%) hydrogen [45]. (Fe,Mn)O has also been identified by XPS on the surface of LD rimming steel strip which has been batch annealed [25]. The formation of these iron manganese mixed oxides is not surprising due to the fact that MnO and FeO have the same FCC NaCl type crystal structure with lattice parameters of 0.444 nm and 0.429 nm respectively [44]. Mixed manganese, iron and chromium oxides are also reported on the surface of annealed steel sheet's [25]. These complex oxides are discussed in the mixed chromium oxide section in more detail.

Chromium Oxide

Chromium is deliberately added to stainless steels to preferentially oxidise and form a protective Cr_2O_3 protective layer. In low carbon steels it is expected that chromium would be selectively oxidised during batch annealing in a protective atmosphere. However, no evidence of Cr_2O_3 precipitates in low carbon steels has been found in the literature.

Mixed Chromium Oxides

The mixed spinel oxide $(Fe,Mn)Cr_2O_4$ was identified by XPS to form on the surface of a batch annealed LD rimming steel [25]. $MnCr_2O_4$ spinel type oxide has often been observed in the Cr_2O_3 oxide scale of manganese containing stainless steels. This $MnCr_2O_4$ spinel layer has been reported to form at the gas and Cr_2O_3 scale interface of 430 stainless steel in an oxidising atmosphere at 1000 °C [46] and in the top layer of the Cr_2O_3 scale when iron, chromium and manganese ternary alloys were annealed at 900 °C [47]. A spinel oxide layer (either $MnCr_2O_4$ or $(MnFe)Cr_2O_4$) was also reported to form on a $(Cr,Fe)_2O_3$ scale when type 304 stainless steel was annealed in an oxidising atmosphere at 600 °C to 1000 °C [48]. A $Mn_{1.5}Cr_{1.5}O_4$ spinel oxide was observed in the outer layer of Cr_2O_3 scale layer of a F17Ti stainless steel annealed at 1000 °C in air [49]. It is clear that chromium oxide in the presence of manganese oxide tends to form a spinel oxide.

Clearly $MnCr_2O_4$ has been observed as the outermost layer of oxidation scales when stainless steels were exposed to oxidising environments at high temperatures. However, the formation of this layer is not well understood. Marasco and Young [47] reported the $MnCr_2O_4$ layer thickened with manganese diffusion through the chromium oxide scale. Stott et al. [50] explained it in terms of fast diffusion of manganese and they believed that $MnCr_2O_4$ formed transiently on the metal surface and then diffused through the Cr_2O_3 scale, forming the outermost $MnCr_2O_4$ layer. Saeki et al. [46] however suggested that the formation of the outermost layer of $MnCr_2O_4$ may involve the decomposition of Mn_2O_3, followed by the solid state reaction, ($MnO + Cr_2O_3 \rightarrow MnCr_2O_4$), at the gas/$Cr_2O_3$ interface, as they did not observe any inner layer of $MnCr_2O_4$.

Spinel Oxides

In the case of steels, spinel phases often appear in greatest abundance upon oxidation [15]. The $MnCr_2O_4$ spinel is referred to as chromium galaxite, and sometimes written as the double oxide $MnO.Cr_2O_3$ [51]. Often double oxides can be more stable than the component oxides [15]. Spinel oxides have the general formula of AB_2O_4 and have a face centred cubic structure [52]. The unit cell (Figure 2-14) contains 32 anions and forms 64 tetrahedral interstices of which 8 are occupied by cations and 32 octahedral interstices of which 16 are occupied by cations. The cubic close packing of oxygen would be perfect if the oxygen parameter, u = 0.375. The oxygen parameter, u is the fraction of the cubic unit cell edge defining the position of the oxygen ion at fractional co-ordinates u, u, u [53]. In most spinels u >0.375, and the close packing is not ideal [54]. A large u-parameter (0.38 to 0.39) leads to unusually large tetrahedral interstices [54]. This means the spinel structure can accommodate relatively large cations in the tetrahedral site (eg. Mn^{2+}). In spinels the octahedral and tetrahedral interstices tend to be of similar size. This can make it difficult to decide which cations are present in which site. The site preference energies (P-values) are tabulated, based on approximate energy calculations [54], and shown in Table 2-1 which demonstrates the preference of various cations to locate in the octahedral site in spinels.

Table 2-1: The octahedral site preference energies for various cations in spinels. The values for P are in K.Cal/g-atomic weight. The larger (and the more positive) the values of P, the greater is the preference of the ion for the octahedral site in spinels [55].

Please see print copy for Table 2.1

In the $MnCr_2O_4$ spinel it is therefore expected that the chromium ions are located in the octahedral sites and the manganese ions are located in the tetrahedral sites. Two types of spinel exist. The first is the normal spinel in which the A^{2+} ions are on the tetrahedral sites and the B^{3+} ions are on the octahedral sites. In the inverse spinel the

A^{2+} ions and half the B^{3+} ions are on the octahedral sites and the other half of the B^{3+} ions are on the tetrahedral sites. The $MnCr_2O_4$ spinel is therefore a normal spinel.

Figure 2-14 shows the expected location of the ions in the $MnCr_2O_4$ spinel and demonstrates that the {002} plane is the same as the {004} plane.

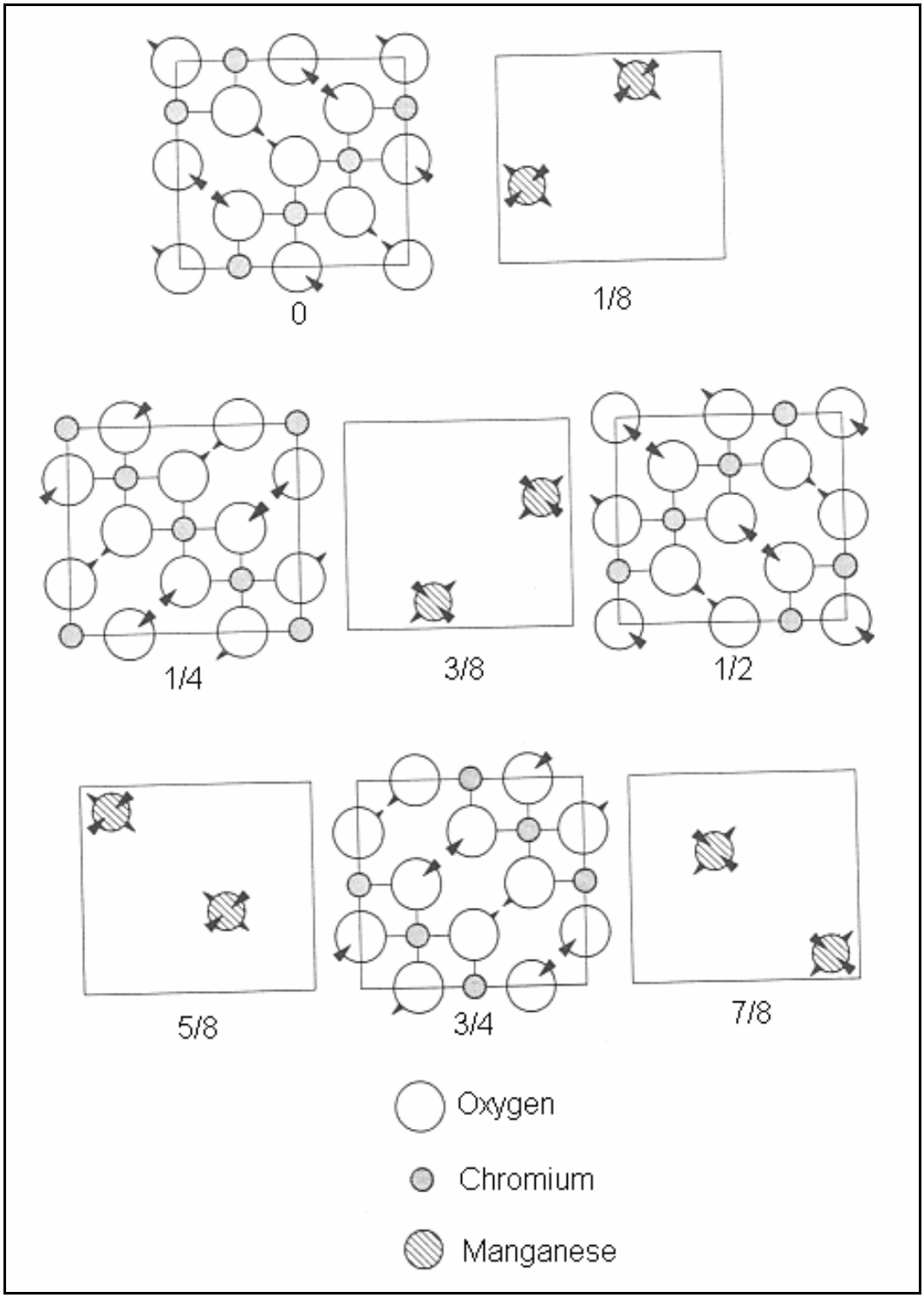

Figure 2-14: Expected location of ions in the $MnCr_2O_4$ spinel unit cell.

2.4 Nitrogen Pick-up

Nitrogen enters the steel in two main processes: steel making and heat treatment. This chapter will concentrate on nitrogen pick up during batch annealing. Many steel makers batch anneal their cold rolled strip in nitrogen hydrogen mixed gases and nitrogen pick-up in this process can have a negative effect on the mechanical properties of the steel.

Nitrogen pick up occurs when nitrogen gas (N_2) is adsorbed onto the steel surface. The adsorbed nitrogen diffuses into the steel from the surface and is dissolved in the bulk iron. The dissolved nitrogen atoms combine with free aluminium atoms in the steel to form aluminium nitride (AlN) by reaction 2.k where $\underline{Al}$ and $\underline{N}$ denote aluminium and nitrogen in solid solution in the steel respectively.

$$\underline{Al} + \underline{N} \rightarrow AlN \qquad (2.k)$$

The precipitation of aluminium nitride provides a driving force for nitrogen diffusion into the steel during annealing as it removes the nitrogen from solid solution in the steel producing a concentration gradient. The aluminium nitride usually forms a distinct layer below the surface of the steel. The thickness of this layer is proportional to the amount of nitrogen picked-up by the steel. Aluminium killed steels show the greatest amount of nitrogen pick up because of the higher amount of available dissolved aluminium present in the steel.

Lowry et al. [56] suggested that nitrogen pick-up is a diffusion controlled mechanism operating within the steel and that the nitrogen pick up was not controlled by the nitrogen supply to the steel. However, Perrin et al. [57] showed that if the annealing environment contained oxygen this was not the case and the diffusion of nitrogen was not the rate determining factor for nitrogen pick-up. In this case the rate controlling step for nitrogen pick-up was found to be the surface reaction [58] (nitrogen gas being adsorbed and dissolving into the iron). Therefore the rate of nitrogen pick-up depends on the number of surface active sites on the steel surface and the probability that nitrogen atoms will jump into an activated state.

Nitrogen adsorption can be reduced during annealing by adding surface active elements into the annealing gas, by decreasing the nitrogen partial pressure and by increasing the dewpoint of the gas [57]. The exposure of gases such as oxygen and carbon dioxide will inhibit nitrogen pick-up as the probability that nitrogen atoms will jump into an activated state is decreased. Nitrogen pick-up will also be inhibited if the surface of the steel contains active surface elements such as sulphur, which can block possible sites for nitrogen adsorption [57].

Nishikida et al. [59] demonstrated the effect of annealing temperature and the dewpoint of the annealing atmosphere has on the nitrogen level in steels as shown in Figure 2-15. Increasing the dewpoint reduces the nitrogen pick-up because of the competition between nitrogen and oxygen for the surface active sites on the steel.

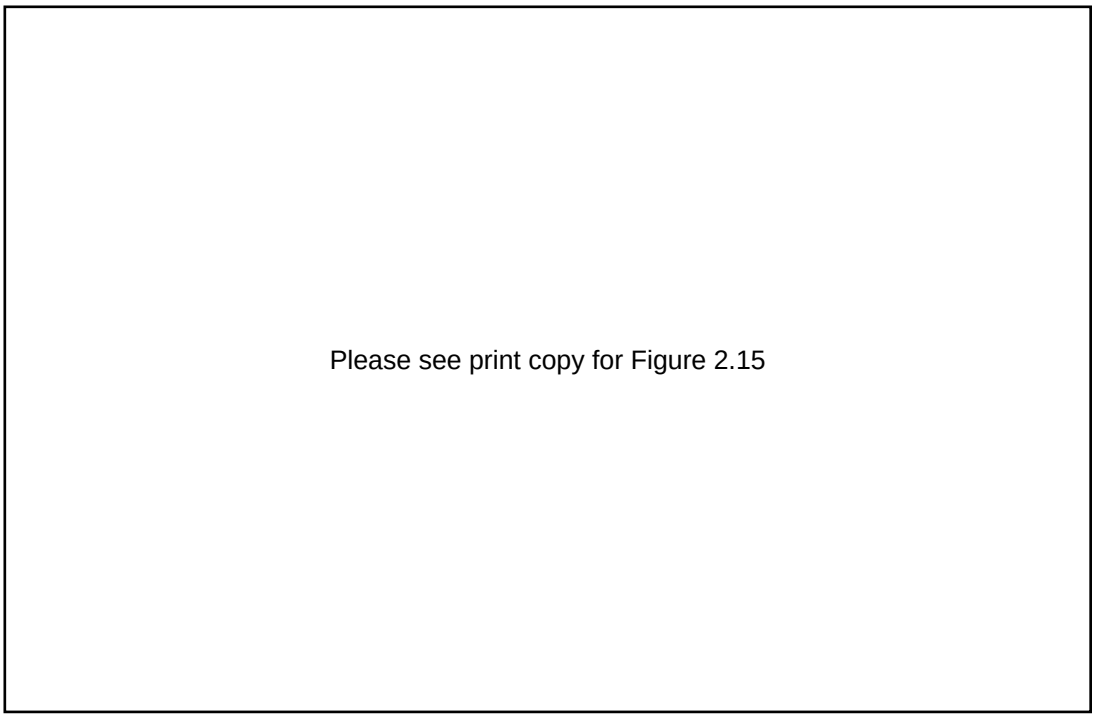

Figure 2-15: Effect of annealing temperature and dewpoint on nitrogen pick-up in cold rolled steel sheet's [59].

During annealing gases given off from the steel are largely reducing in nature and have a different composition from that of the annealing gas. Consequently the gas in between the coil wraps is different to the gas composition that surrounds the coils [60]. Nitrogen pick-up tends to occur more in tight coil annealing than open coil annealing due to the difference in gas compositions.

Nitrogen pick-up generally increases with an increasing annealing temperature [59, 60]. This trend has been observed up to 800 °C. The longer the time the steel is held at the annealing temperature the more nitrogen pick-up observed [60].

2.5 Surface Characterisation Techniques

Many techniques may be used to characterise the surface of selectively oxidised steels. Some important methods used for surface characterisation are briefly discussed in this section including scanning electron microscopy (SEM), transmission electron microscopy (TEM), auger electron spectroscopy (AES), x-ray (excited)-photoelectron spectrometry (XPS), secondary ion mass spectrometry (SIMS) and secondary neutrals mass spectrometry (SNMS).

2.5.1 Scanning Electron Microscopy (SEM)

SEM is a widely used technique to characterise surfaces. Figure 2-16 illustrates the scanning electron microscope. A primary high energy (up to 30 keV) electron beam strikes the sample and the electrons are elastically and inelastically scattered by atoms in the sample. Through these scattering events, the primary electron beam effectively spreads and fills a teardrop-shaped volume, known as the interaction volume, extending to a depth of about, less than 100 nm to 5 µm into the surface. Figure 2-17 shows the interaction volume of a sample. Interactions in this region lead to the subsequent emission of electrons, which are then detected to produce an image.

Many signals are generated inside a scanning electron microscope when an electron beam interacts with a specimen [61]**.** The signals given off from a specimen include secondary electrons, backscatter electrons, elastically scattered electrons, Low-loss electrons, characteristic x-rays, auger electrons and light (Cathodoluminescence).The most commonly used signal for imaging is secondary electrons. Due to their low energy (<50 eV) secondary electrons can only escape from the specimen within a few nanometres from the surface. The electrons are detected and the resulting signal is rendered into a two-dimensional intensity distribution that can be viewed as an image. The brightness of the signal depends on the number of secondary electrons reaching the detector. If the beam enters the sample at a perpendicular angle the activated region is uniform about the axis of the beam and a certain number of electrons "escape" from within the sample. The higher the angle of incidence of the beam with the sample one side of the axis of the beam will have a much smaller

"escape" distance and more secondary electrons will be emitted. Thus steep surfaces and edges tend to be brighter than flat surfaces resulting in images with good three-dimensional appearance. This mode of imaging can be very effective in observing surface precipitates.

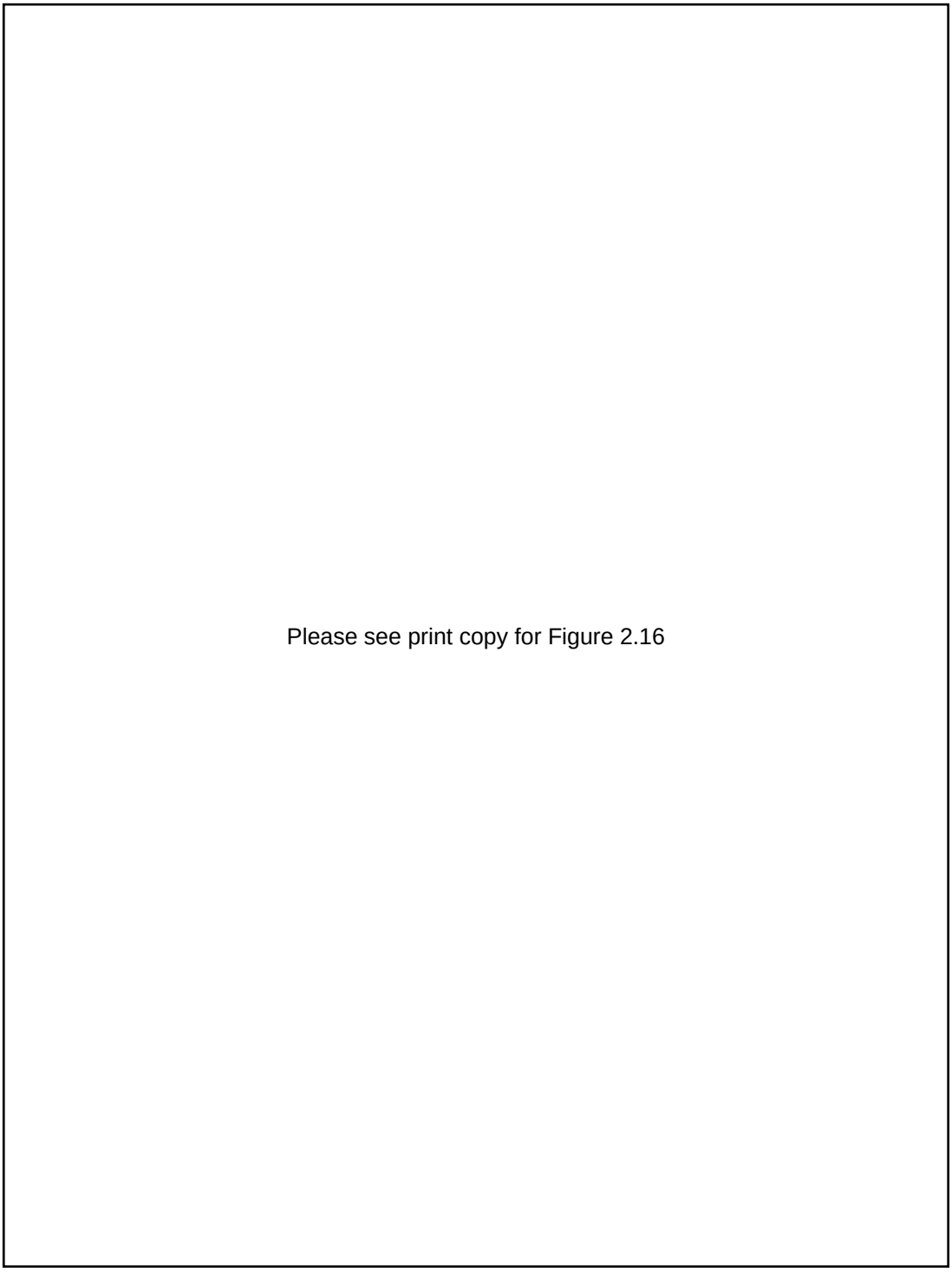

Figure 2-16: Schematic drawing of the scanning electron microscope were, BSE = backscattered electrons, SE = secondary electrons, SC = specimen current, EBIC = electron-beam-induced current, X = x-rays and CRT = cathode-ray tube [62].

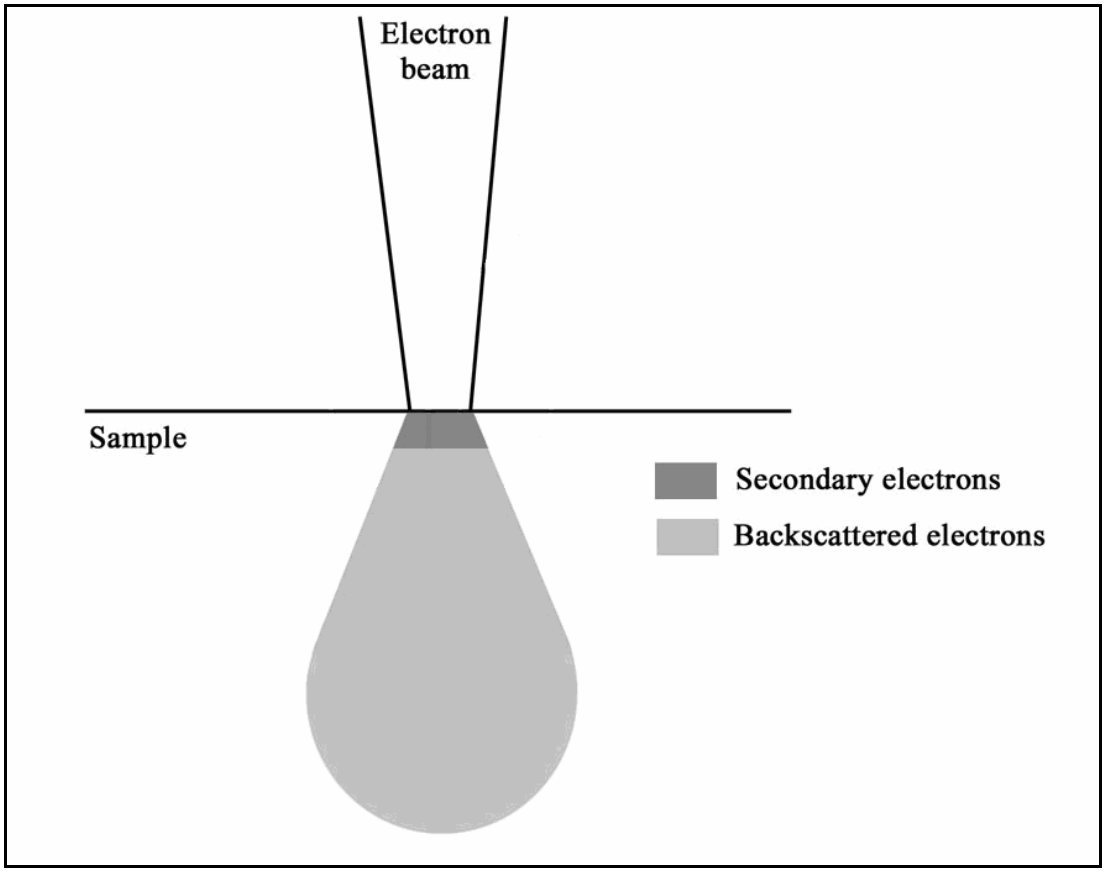

Figure 2-17: Interaction volume between the electron beam and the specimen in SEM.

In addition to the secondary electrons, backscattered electrons may also be detected. Backscattered electrons leave the specimen with an appreciable fraction of the primary beam energy. For the electrons to be backscattered from a sample a primary electron must experience one or more close encounters with the nuclei of the target atoms. Backscattered electrons are dependant on the mean atomic number, so phases with different mean atomic numbers can be recognised. In particularly oxides on the surface of steel are easily imaged due to the difference in atomic numbers between the steel and the oxide. Backscattered electrons are able to escape from far deeper in the sample (Figure 2-17) and as such changes in composition just below the surface may be observed. As the interaction volume is greater for backscattered electrons the spatial resolution is not as good secondary electron imaging.

Scanning electron microscopes are generally equipped with an energy dispersive x-ray spectrometer (EDS) which collects characteristic x-rays that are emitted from the

sample. Due to the large interaction volume associated with SEM, EDS is not limited to the surface. In the case of fine precipitates the matrix is often detected.
SEM has commonly been used in conjunction with other techniques such as XPS [23], AES [22] and SIMS [22] to study surface oxidation of steels.

Advantages

- The ability to image a comparatively large area of the specimen.
- The ability to image bulk materials with very little sample preparation.
- The variety of analytical modes available for measuring the composition and nature of the specimen.
- Good depth of field.

Limitations

- The resolution in SEM is limited by the size of the electron spot and the interaction volume. The spot size and the interaction volume are both large compared to the distances between atoms, so the resolution of the SEM is not high enough to image down to the atomic scale.

2.5.2 Transmission Electron Microscopy (TEM)

In conventional transmission electron microscopy a thin specimen is irradiated with an electron beam with a uniform current density. Electrons interact with the sample and are either elastically or inelastically scattered. The electron intensity distribution below the sample is imaged with a three or four stage lens system onto a fluorescent screen [63]. TEM is a technique with a higher spatial resolution than SEM. TEM allows the direct observation of crystal structure by diffraction and therefore has an advantage over other methods. Figure 2-18 shows the two main operation modes of TEM, diffraction and imaging. Transmission electron microscopes are often equipped with specimen holders that allow the user to tilt the specimen to a range of angles in order to obtain specific diffraction conditions, and apertures placed below the specimen allow the user to select electrons diffracted in a particular direction.

TEM is often equipped with EDS and electron energy loss spectrometer (EELS) and thus micro even nano-analysis can be easily carried out in TEM. The interaction

volume is much smaller in the TEM compared to SEM allowing high spatial resolution EDS.

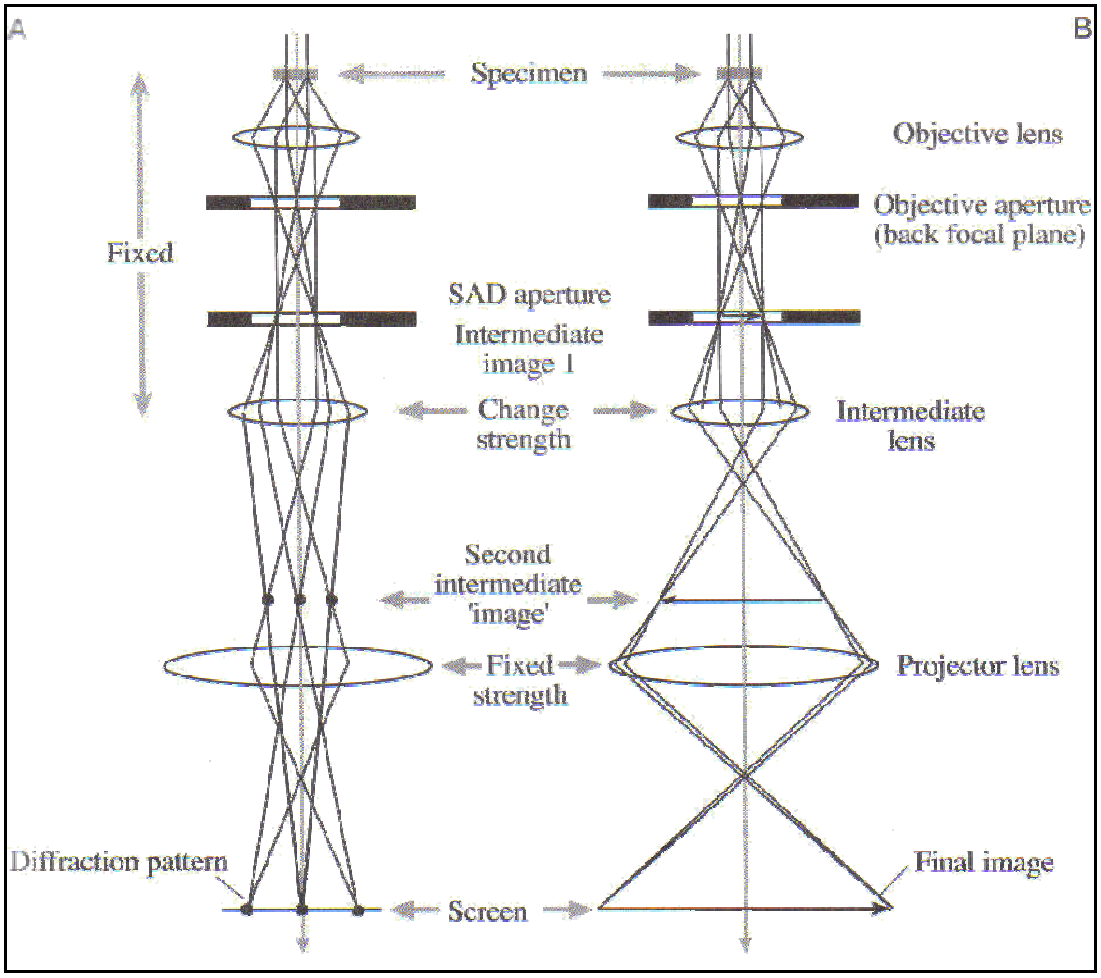

Figure 2-18: The two basic operations of the TEM imaging system involve A) projecting the diffraction pattern on the viewing screen and B) projecting the image onto the screen.

The specimens for TEM must be very thin and able to withstand the high vacuum present inside the instrument. Therefore the materials require extensive sample preparation to produce a sample thin enough to be electron transparent, which makes TEM analysis a relatively time consuming process with a low throughput of samples. Care must be taken to ensure the structure of the sample is not changed during the preparation process.

Advantages

- High spatial resolution.
- Direct determination of crystal structure.

Limitations

- Sample preparation can be difficult and may be very time consuming.
- The field of view is relatively small in TEM, raising the possibility that the region analysed may not be characteristic of the whole sample.
- The sample may be damaged by the electron beam due to the fragility of very thin samples.

2.5.3 Auger Electron Spectroscopy (AES)

Auger electron spectroscopy is another frequently applied technique to analyse the elemental composition of solid surfaces. Like SEM a primary electron beam excites atoms present at the surface. As the elements at the surface relax element specific auger electrons are emitted. Figure 2-19 show how auger electrons are produced by an electron beam. An energy analysis of the emitted auger electrons is performed and the auger electron intensities are recorded in dependence on the kinetic energy to give the Auger spectrum. This technique has been used to study surface segregation in steels [43].

Advantages

- AES has a high lateral resolution (<50nm), which is one of its main advantages.
- Electrons of the energy range required for auger electron spectroscopy (20 eV - 2.5 keV) can only travel short distances in a solid. Therefore the information depth is limited to only a few atomic layers at the surface of a solid.
- This technique can be combined with controlled ion sputtering to produce a depth profile.
- All elements except hydrogen and helium can be detected.

Limitations

- Generally an Auger spectrum only demonstrates the elements present and not their chemical states. As such a metal cannot be distinguished from its oxide. However, high resolution Auger spectroscopy can provide chemical information of elements present at the surface as changes in the oxidation

state result in shifts in the kinetic energy of Auger lines. High resolution AES can be very time consuming.

- The peaks in the Auger spectrum are generally rather broad which means that peak overlapping can be a problem.
- In some circumstances electron beam damage can alter the surface composition.

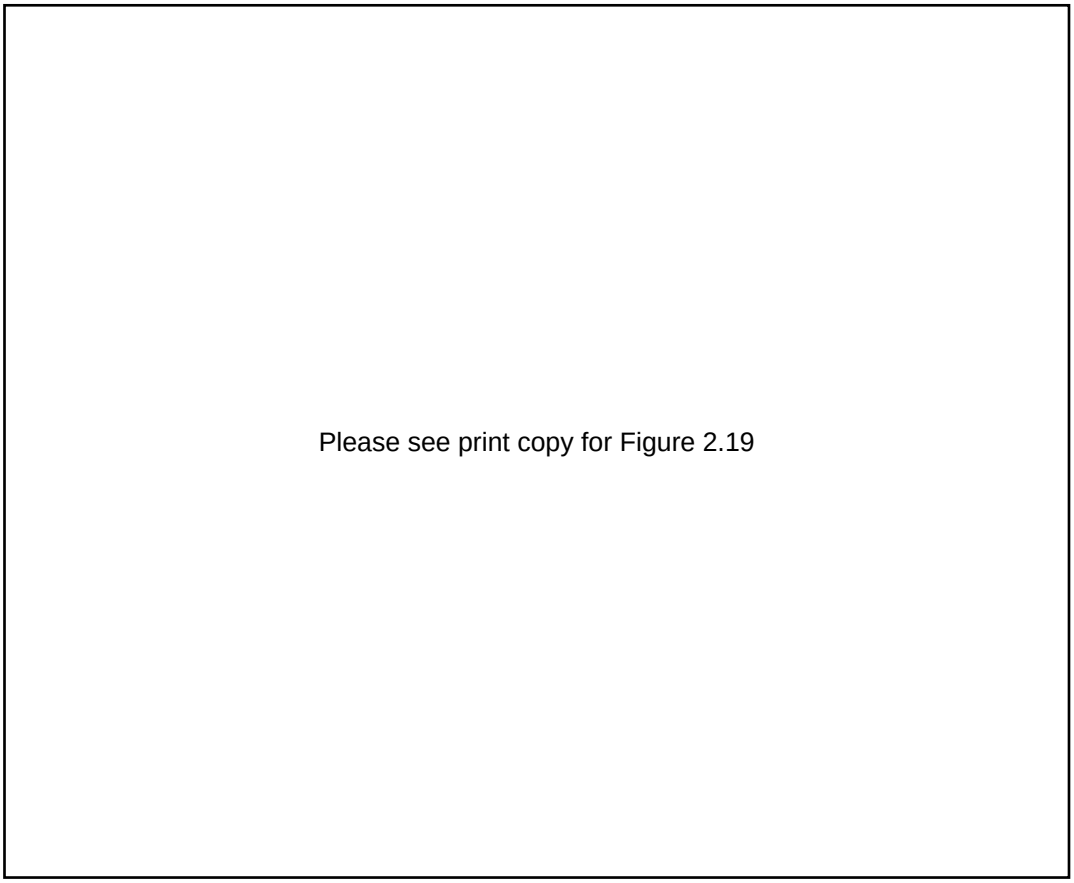

Figure 2-19: Schematic diagram showing the competitive processes of x-ray and auger electron emission [64].

2.5.4 X-Ray (excited)-Photoelectron Spectrometry (XPS)

This technique is also known as Electron Spectroscopy for Chemical Analysis (ESCA). In XPS elemental analysis of the surface is possible but also additional chemical information may be derived on binding states for surface atoms. X-rays excite the electronic core levels of the surface atoms so they emit photoelectrons with element specific kinetic energies. The energies of the emitted photoelectrons are characteristic to the elements so chemical analysis is possible by measuring the energies and the intensities of the photoelectrons. The energy of the photoelectrons

emitted from the solid is not only dependent on the element of the atom but also on the chemical environment of this atom. This dependence on the chemical environment causes small energy shifts. Determining the magnitude and direction of these energy shifts gives information on the chemical bonding state of the analysed atoms. This technique has been widely used to investigate selective oxidation of steels [23, 29, 33, 34, 37]

Advantages

- The presence of oxides can be distinguished from metals due to the change in binding energies.
- Quantitative analysis is possible using handbook sensitivity factors or calibration standards.
- The information depth is limited to only a few atomic layers at the surface of a solid.
- The x-ray source used in XPS causes less damage to the sample than electron beams or ion beams.
- By combining with ion sputtering techniques it is possible for depth profiling.
- All elements except hydrogen and helium can be detected.

Limitations

- The main disadvantage associated with this technique is that the lateral resolution is rather poor (typically the analysed area is a few mm^2).

2.5.5 Secondary Ion Mass Spectrometry (SIMS)

In secondary ion mass spectrometry the surface is bombarded with energetic primary ions. A series of atomic collision cascades occurs in the surface layers and secondary ions are ejected (emitted). The secondary ions contain information on the composition of the material being bombarded and are individually detected and tabulated as a function of their mass-to-charge ratio. Two different types of SIMS are possible, “static” and “dynamic”. Static SIMS involves low incident ion beam current densities and a very surface sensitive method is achieved as only a small fraction of the surface monolayer is removed. In dynamic SIMS a bulk analysis is possible due to high incident ion beam current densities meaning a high rate of

material removal. This technique has been used to investigate selective oxidation in steel [34].

Advantages

- This technique is well suited to depth profiling as the profiling beam provides the depth signal and the emitted species reflect the true chemical composition of the bulk solid. Ion beams can be readily focussed and deflected on a sample so that chemical composition imaging is possible.
- Has an advantage over other forms of surface spectroscopy in terms of detection sensitivity [65].
- All elements may be detected including the separation of isotopes.

Limitations

- A wide variation in secondary-ionization probabilities.
- Secondary ionization probabilities are also strongly dependent on the local chemical environment from which the species of interest emerges, the so-called matrix effect.
- The complexity of the SIMS mass spectrum.

2.5.6 Secondary Neutrals Mass Spectrometry (SNMS)

During ion bombardment of a solid surface not only are ions emitted but also neutrals are removed. These neutrals can be post ionised by laser or electron beams and detected by mass spectrometry.

Advantages

- An advantage of this technique over SIMS is the much higher number of sputtered neutrals compared to ions.
- The so called matrix effects which make the quantification of SIMS results difficult are avoided with SNMS.
- All elements may be detected including the separation of isotopes.

Limitations

- Low lateral resolution.

2.5.7 Ion Sputtering

Controlled ion sputtering is removal of surface layers by energetic noble gas ions. This is often used in combination with other techniques for depth profiling. However, ion bombardment for depth profiling has been found in some circumstances to cause chemical alterations to oxides.

2.6 Summary

Surface graphitization is a problem that often affects batch annealed low carbon steels. Although adding chromium to low carbon batch annealed steel is effective at minimising surface graphitization it has been found to cause another defect. Tinplated, chromium containing low carbon batch annealed steel often has the 'edge defect'. Chromium is known to have a higher affinity for oxygen than iron meaning it can selectively oxidise during batch annealing.

This investigation aims to identify the cause of the 'edge defect' and the effect of the annealing temperature, steel composition and annealing environment has on its formation. SEM and TEM will be used to characterise the steel surface of batch annealed and laboratory annealed chromium containing low carbon steels to satisfy these aims.

Chapter 3 : Experimental

3.1 Materials

The steels used in this investigation were divided into two distinct sections. Laboratory annealed steels and industrial batch annealed steels. The compositions of these steels were measured by atomic emission spectroscopy and are given in Table 3-1. Letters L and B in Table 3-1 are assigned for laboratory and industrial batch annealed steels respectively. The steels were received either as cold rolled strip or blackplate, i.e. batch annealed cold rolled strip. The strips were approximately 0.3 mm thick and 940 mm wide.

Tinplated steels were de-tinned using 10% hydrobromic acid + 90% ethanol solution. Etched samples were etched in an 8% sulphuric acid solution for two seconds to simulate the industry pickling process.

Table 3-1: Composition of steels used in this investigation in wt%, balance iron.

	C	Cr	Mn	P	S	Ni	Al	Si	Mo	Cu	Sn	Nb	Ti	V	N
L1	0.046	0.012	0.18	0.012	0.015	0.029	0.023	<0.005	0.002	0.010	<0.002	<0.001	<0.003	<0.003	0.0025
L2	0.065	0.059	0.24	0.014	0.013	0.028	0.033	0.005	<0.002	0.009	<0.002	<0.001	<0.003	<0.003	0.0015
L3	0.011	0.061	0.23	0.012	0.014	0.030	0.052	<0.005	<0.002	0.014	<0.002	<0.001	<0.003	<0.003	0.0017
L4	0.039	0.020	0.18	0.011	0.007	0.020	0.036	<0.005	<0.002	0.029	<0.002	<0.001	<0.003	<0.003	0.0018
L5	0.055	0.062	0.21	0.012	0.011	0.019	0.038	<0.005	<0.002	0.013	<0.002	<0.001	<0.003	<0.003	0.0021
L6	0.060	0.070	0.21	0.013	0.011	0.019	0.038	<0.005	<0.002	0.018	<0.002	<0.001	<0.003	<0.003	0.0023
L7	0.060	0.052	0.18	0.012	0.005	0.018	0.036	<0.005	<0.002	0.018	<0.002	<0.001	<0.003	<0.003	0.0019
L8	0.043	0.039	0.33	0.015	0.011	0.020	0.060	<0.005	<0.002	0.018	<0.002	<0.001	<0.003	<0.003	0.0025
L9	0.070	0.015	0.28	0.015	0.017	0.029	0.021	<0.005	0.003	0.012	<0.002	<0.001	<0.003	<0.003	0.0100
B1	0.015	0.050	0.23	0.011	0.011	0.024	0.041	<0.005	0.002	0.017	0.002	0.001	<0.003	<0.003	0.0025
B2	0.037	0.058	0.25	0.017	0.015	0.021	0.053	<0.005	0.002	0.008	0.002	0.001	<0.003	<0.003	0.0030
B3	0.037	0.058	0.25	0.017	0.015	0.021	0.053	<0.005	0.002	0.008	0.002	0.001	<0.003	<0.003	0.0030

3.2 Annealing

3.2.1 Laboratory Annealing

Specimens with the size of 10 mm x 20 mm were cut from the cold rolled strip and were ultrasonically cleaned in acetone for 5 minutes to remove any excess rolling oil. The laboratory steels were annealed under two different conditions. The first condition was a 5% H_2 + 95% N_2 environment and other in an evacuated vacuum environment.

5% H_2 + 95% N_2 Gas Environment

The cold rolled samples were annealed in a three zoned stainless steel tube furnace (Figure 3-1). The tube had a diameter of 15 cm and a length of 150 cm. The annealing temperatures were between 650 °C and 750 °C. The furnace was heated at a rate of 4 degrees per minute till the pre-determined annealing temperature was reached. The samples were held at temperature for 20 hours and then slow cooled. Figure 3-2 illustrates the annealing cycles. The furnace was purged with N_2 gas and then 5% H_2 + 95% N_2 gas before annealing to remove any residual oxygen from the furnace. The annealing environment was a 5% H_2 + 95% N_2 environment with a dewpoint of -44 °C at room temperature. The flow rate of the annealing gas was 225 cm^3/min. The dewpoint of the outgas during the annealing cycle was measured for the 700 °C annealing cycle and is shown in Figure 3-3. The samples were directly exposed to the annealing atmosphere during the annealing treatment.

Please see print copy for Figure 3.1

Figure 3-1: Three zoned stainless steel tube furnace.

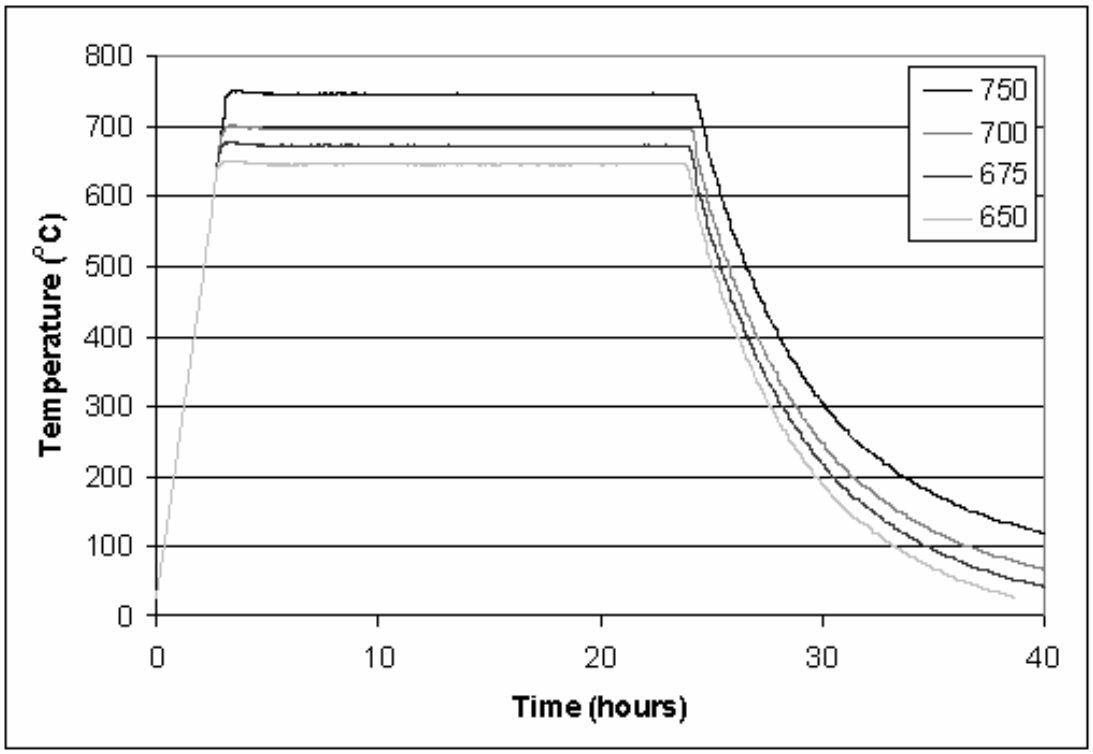

Figure 3-2: Annealing cycle for laboratory annealed steels in 5% H_2 + 95% N_2 gas atmosphere.

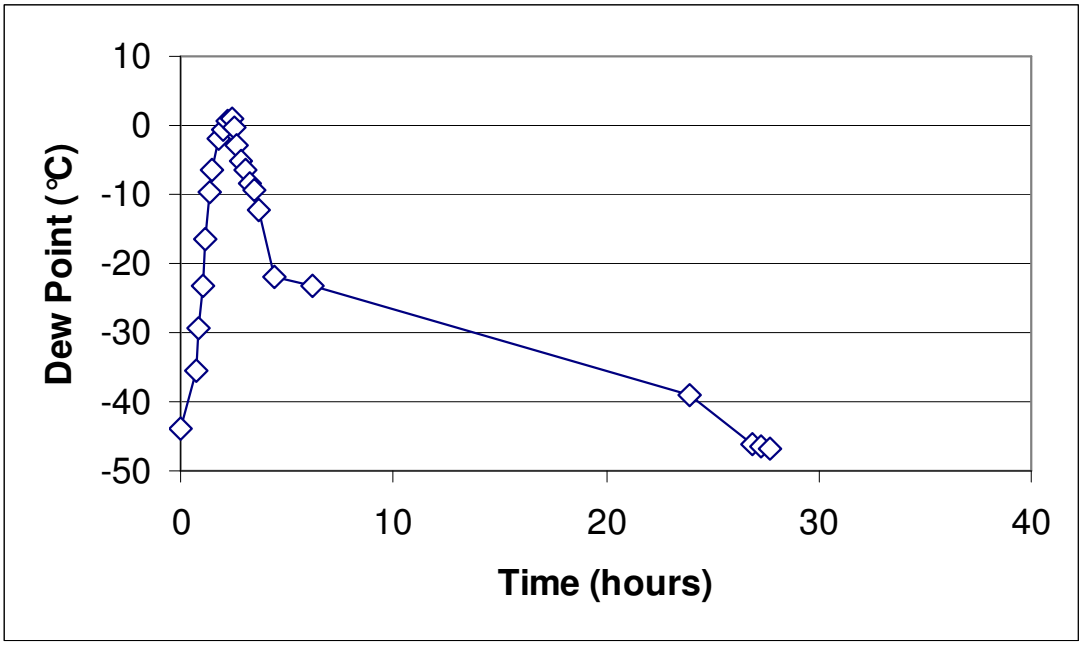

Figure 3-3: The change in dewpoint of the outgas with annealing time for the 700 °C annealing cycle in 5% H_2 + 95% N_2 gas atmosphere.

Evacuated (Vacuum) Environment

The cold rolled samples were placed in a 20 mm diameter quartz tube with a length of 100 cm. The tube was evacuated using a vacuum system to a recorded pressure at room temperature. The pressures were between 10^{-1} and 10^{-5} torr at room temperature. The evacuated tube was closed and heated in a three zone furnace to the annealing temperature over a period of 20 minutes. The tube was held at the annealing temperature in the furnace for the annealing time, (6 hours to 72 hours), then removed from the furnace to cool. Once cooled to room temperature samples were removed from the quartz tube.

3.2.2 Industrial Batch Annealing

In the batch annealing process, coils were stacked and annealed in large furnaces in a 4% H_2 + 96% N_2 gas atmosphere. The dewpoint of the annealing gas was reported as being approximately -40 °C from the gas suppliers. Figure 3-4 and Figure 3-5 demonstrate the batch annealing process. The furnace holds 4 stacks of coils each stack containing 4 to 5 coils. The coils weigh between 10-20 tones with a width of 700-1020 mm and length of approximately 11 000 m. A steel cover was placed over the coils and a refractory (kaowool) seal was used to seal the bottom. A positive gas

pressure was used. The annealing cycle for the coils was approximately 168 hours long with 60 hours taken to heat to the annealing temperature of approximately 700 °C. Coils were held at this temperature for 10 hours then cooled to room temperature over a period of 98 hours.

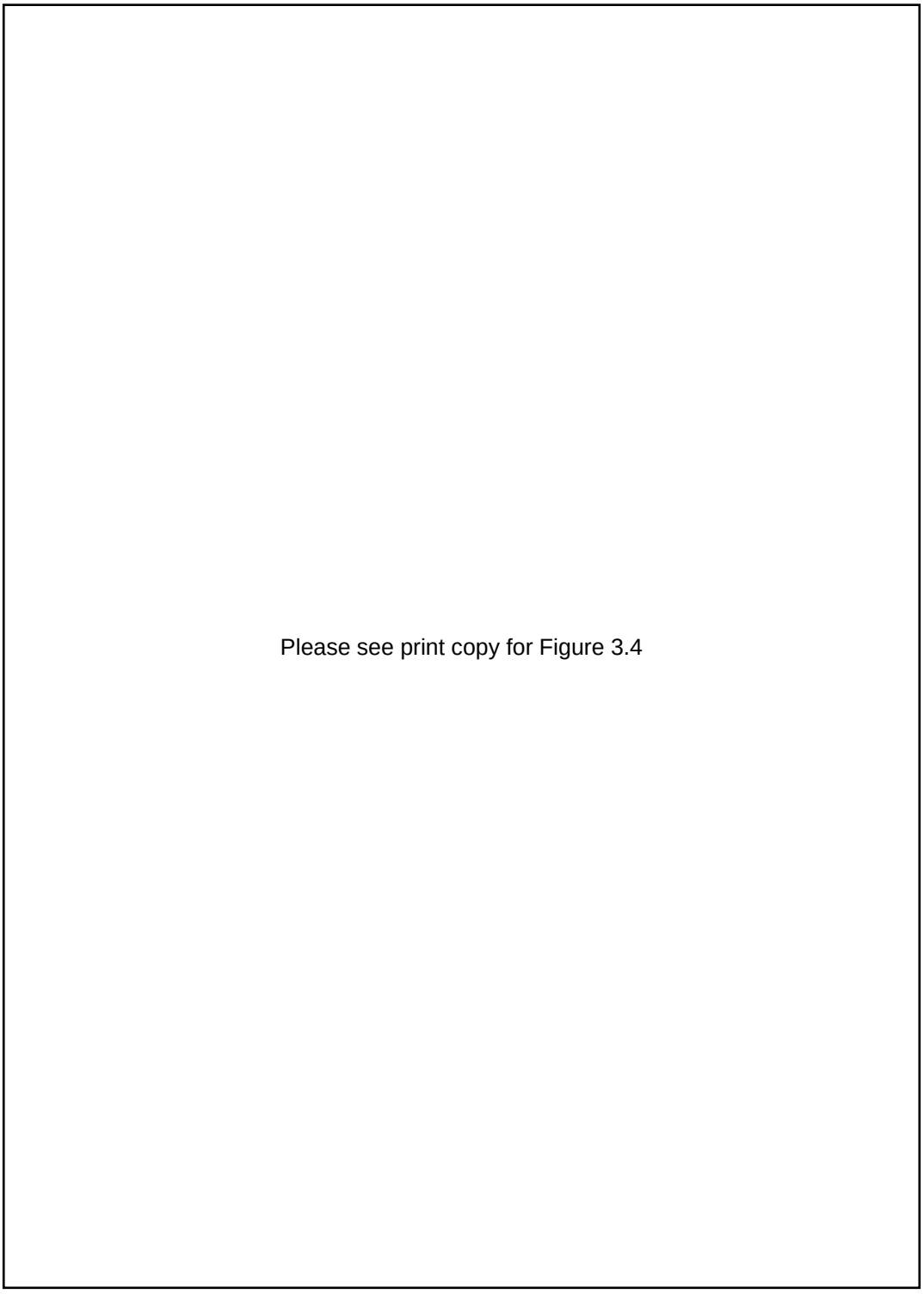

Figure 3-4: The batch annealing process with: a) coils being stacked and b) being covered.

Please see print copy for Figure 3.5

Figure 3-5: The batch annealing process with: a) the furnace being placed on and b) being cooled.

3.3 Characterisation

3.3.1 Scanning Electron Microscopy (SEM)

After annealing the steel surfaces were characterised by SEM. Steel samples were mounted on a stub using double sided carbon tape for characterisation in a Leica Stereoscan 440 scanning electron microscope equipped with windowless energy dispersive spectrometer (EDS) (Figure 3-6). The steel surfaces were imaged with secondary as well as backscattered electrons. The accelerating voltage was 20 keV and the working distance for secondary electron imaging was about 25 mm and about 15 mm for backscattered electron imaging. Both tungsten and LaB_6 filaments were used in this investigation with a probe current of 600 pA and 300 pA respectively. EDS occurred at a working distance of 25 mm and the probe current was adjusted to give 25% dead time. The acquisition time was for a 120 seconds live time.

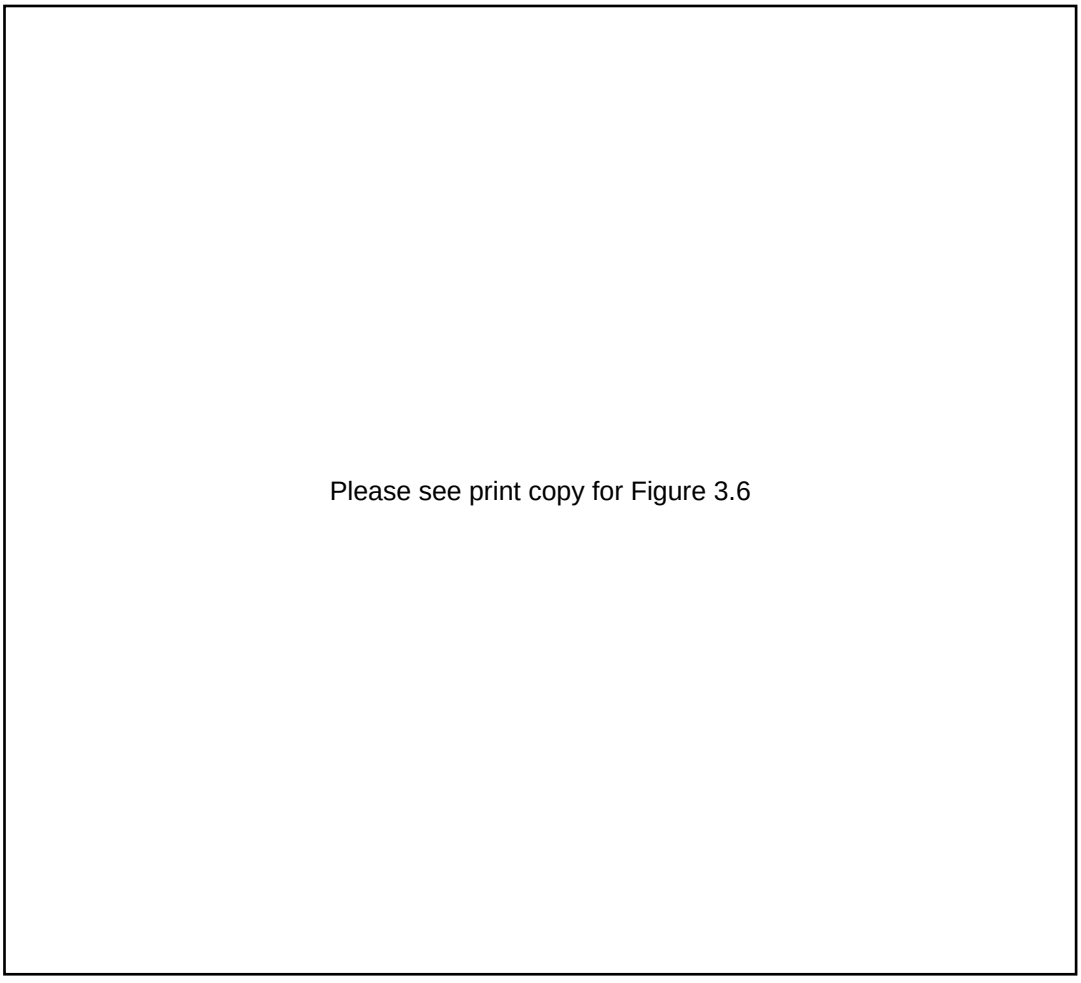

Figure 3-6: Leica Stereoscan 440 scanning electron microscope

3.3.2 Transmission Electron Microscopy (TEM)

TEM characterisation was carried out using a JEOL JEM 2011 transmission electron microscope equipped with windowless energy dispersive spectrometer (EDS) capable of detecting light elements down to boron (Figure 3-7). Carbon extraction replicas as well as a thin foil of cross section sample were prepared for TEM characterisation. The operating voltage used was 200 keV. EDS acquisition was for a live time of 60 seconds and the beam conditions were changed to give optimum count rate and beam size. Calibration prior to diffraction experiments was carried out using a polycrystalline gold sample or an aluminium thin foil sample.

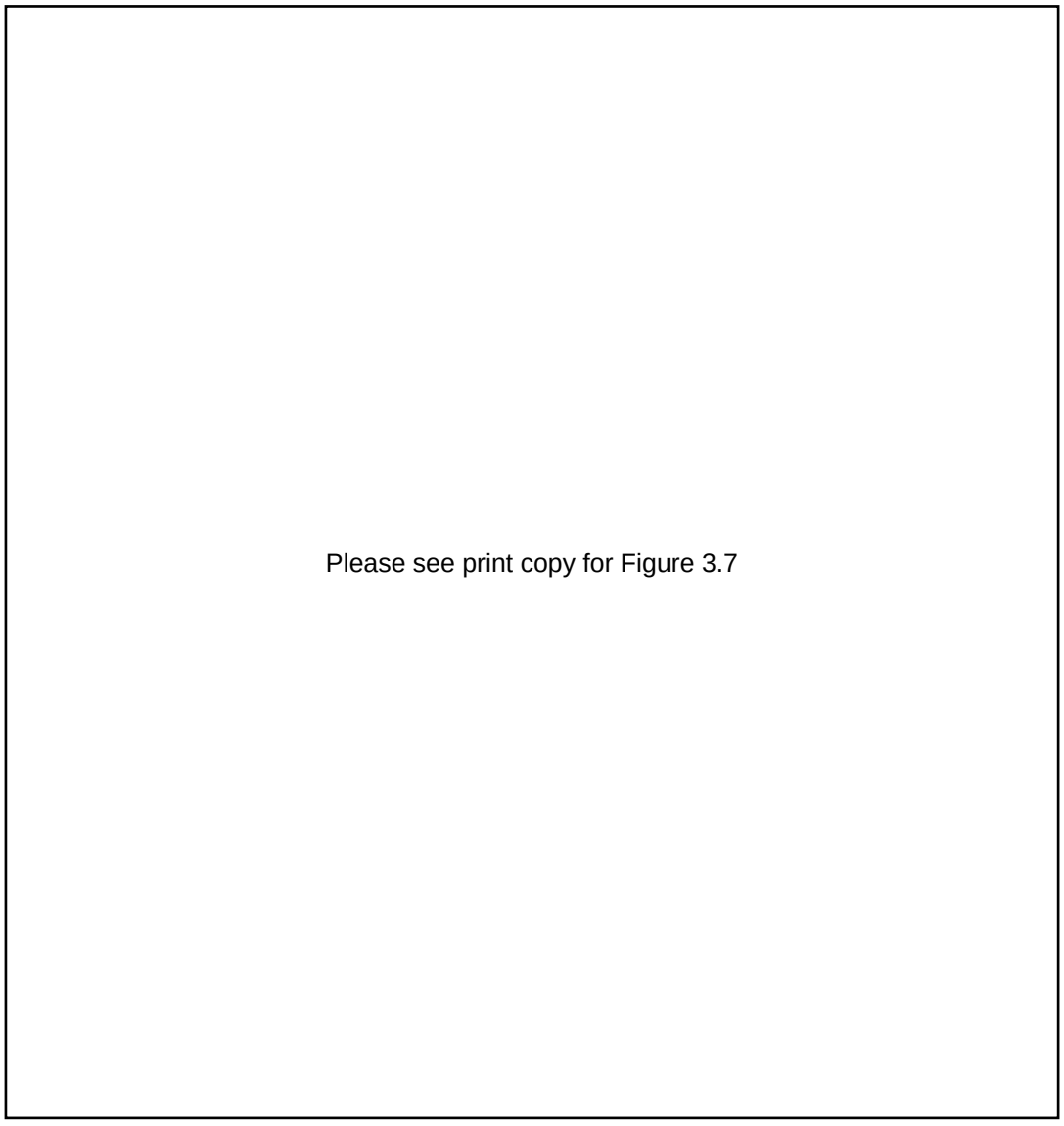

Figure 3-7: JEOL JEM 2011 transmission electron microscope.

Carbon Extraction Replica Preparation

For surface characterisation carbon extraction replicas were made of the steel surface. This process involved applying a coating of carbon to the steel surface. The carbon was then lightly scored with a scalpel so squares approximately 2 x 2 mm were produced. The steel with the carbon coating was then placed in 8% nital until the carbon squares floated away from the steel surface. These carbon squares were collected on a 3 mm in diameter, 200 mesh copper grid. The replicas were then cleaned in a five step process of: pure ethanol, 75% ethanol + 25% distilled water, 50% ethanol + 50% distilled water, 25% ethanol + 75% distilled water and finally distilled water. The carbon replicas were then dried on filter paper.

Cross Section of Thin Foil Sample

A cross section foil samples for TEM examination was prepared using a xT Nova NanoLab 200 Dualbeam focussed ion beam (FIB) miller (Figure 3-8).

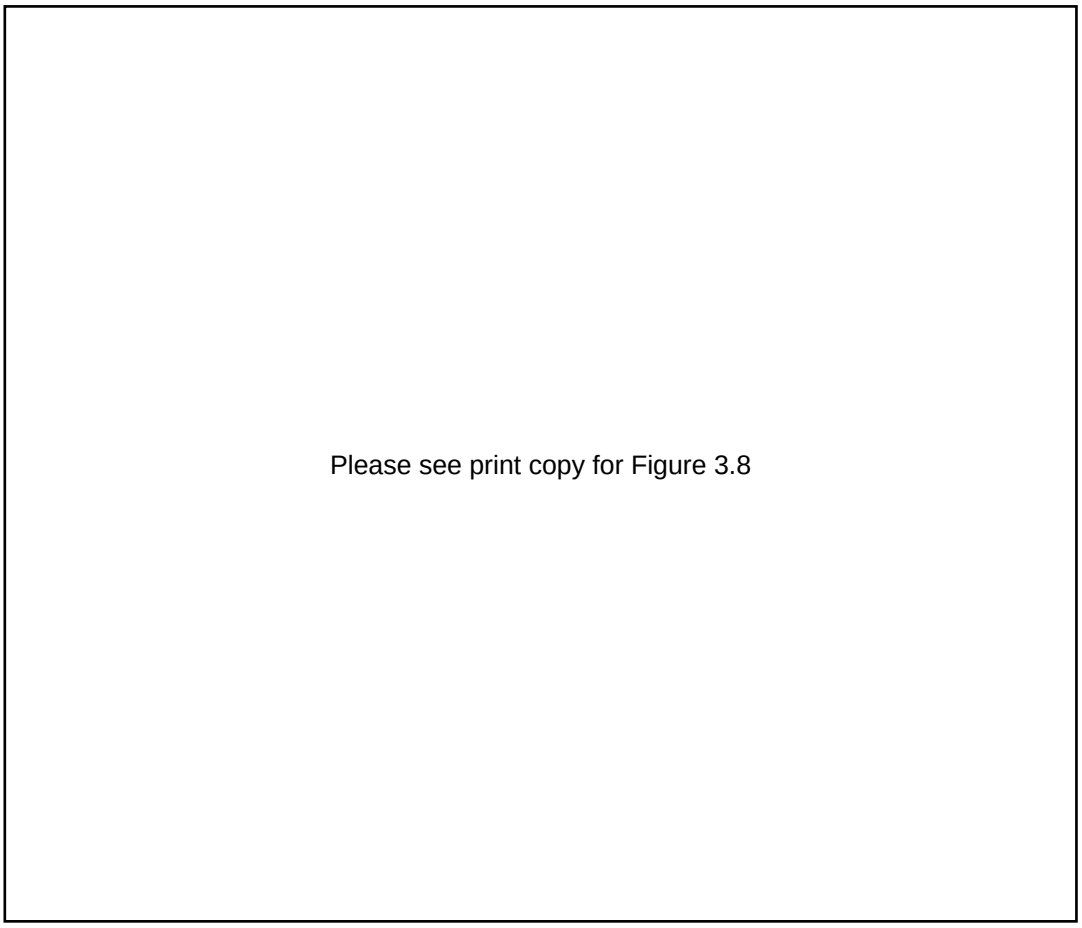

Figure 3-8: xT Nova NanoLab 200 Dualbeam (FIB).

A focused gallium ion beam was used to cut a thin cross section suitable for TEM examination. In this process the region of interest was coated with platinum for protection. Figure 3-9 shows the start of the milling process with the area between the two X marks the region from which the cross section TEM sample was produced. This area was coated with platinum before milling. The dark groove in front of the platinum coating shows the start of the milling. Both sides of the platinum coated region were milled to produce a trench on either side.

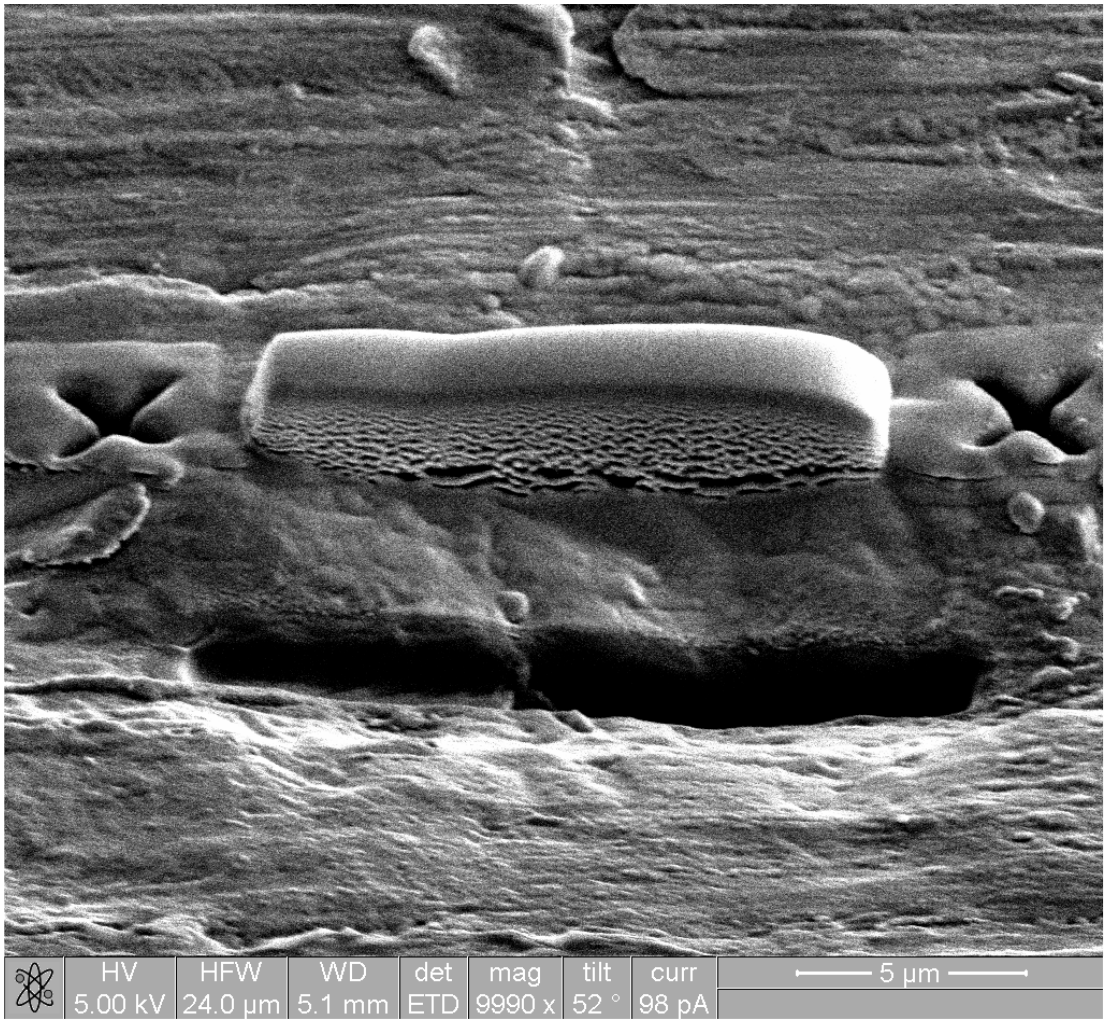

Figure 3-9: Secondary electron image of steel surface showing the position (between the two X marks) from which the sample was cut. The sampling region was plated with platinum, and the groove in front of this region demonstrates where milling was started.

After this a 'U' shaped cut was made so the sample was no longer attached at the bottom (Figure 3-10). Fine milling was then used to further thin the sample until it was transparent to electrons, judging by the contrast between the platinum coating and the steel. Finally sides of the sample were cut (indicated by dashed white lines in

Figure 3-10) to allow the specimen to be removed from the steel. Once cut a manipulator (fine glass needle) was used to transfer the sample to a carbon coated copper grid.

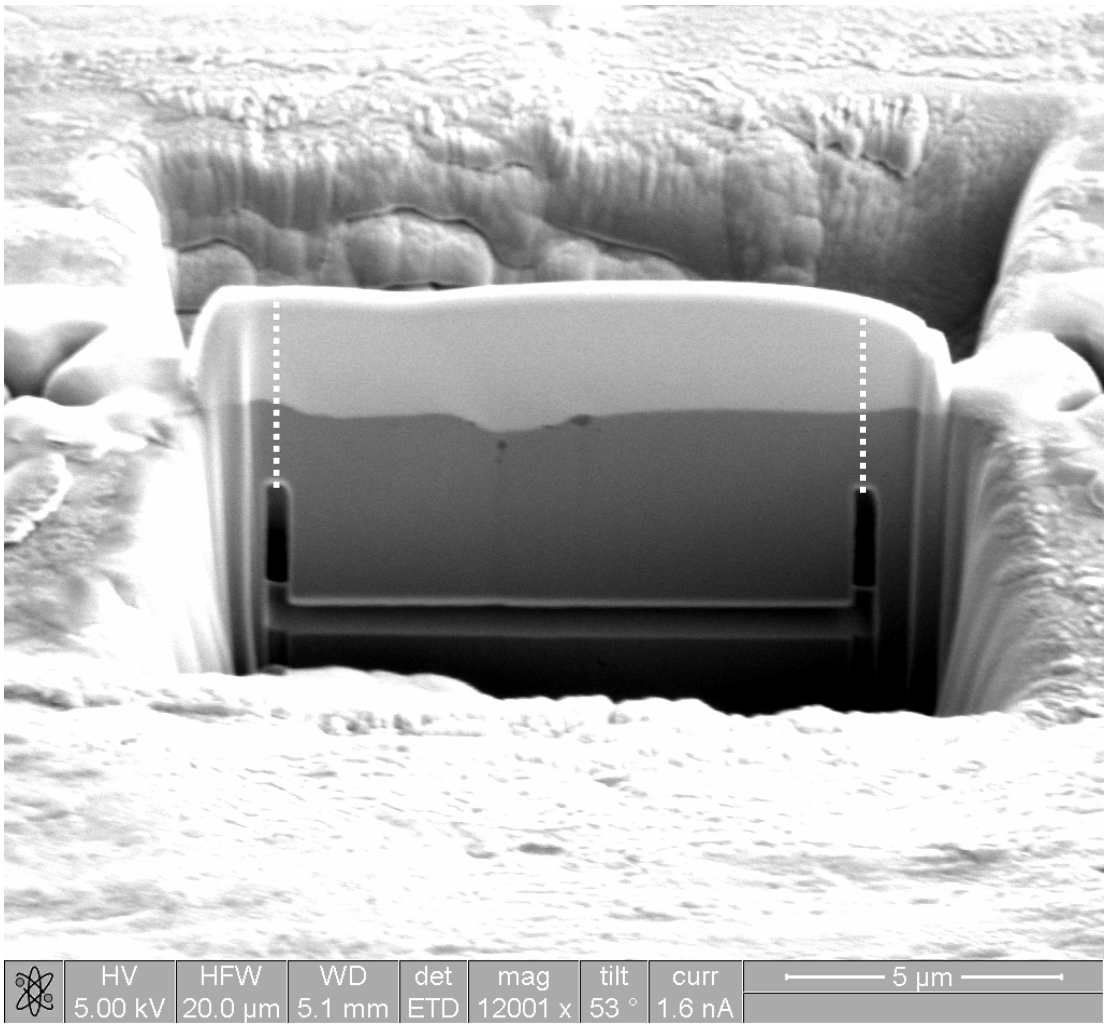

Figure 3-10: Secondary electron image of TEM cross-section sample in the process of preparation by focussed ion beam milling. The brighter surface layer is platinum and the darker under layer is part of the steel sheet. A surface and an internal precipitate are still visible in the cross-section of the steel sheet. Dashed white lines indicate where the final cuts were made to allow the specimen to be removed from the base steel.

3.3.3 X-Ray Diffraction (XRD)

Steel samples and powders were mounted onto a specimen holder and inserted into a Phillips 1370 XRD and analysed (Figure 3-11). Steel samples were glued to a glass slide and inserted into XRD machine. Powder samples were mixed with ethanol and made into paste. The paste was then put on a glass slide and allowed to try before placing in XRD machine. The anode was copper, producing Cu Kα radiation with a

wavelength of 0.154 nm. The scans were run from 10° to 100° with a step size of 0.05° and a speed of 2 °/min.

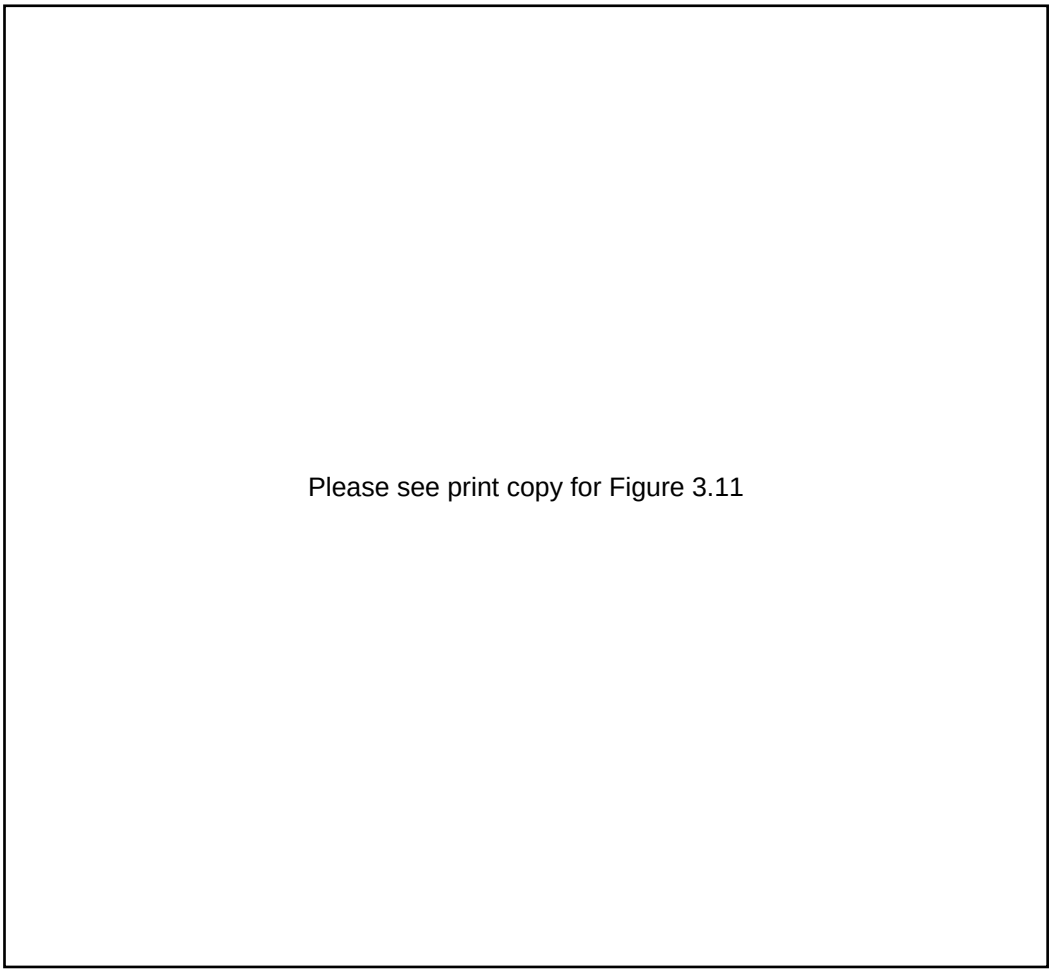

Figure 3-11: Phillips 1370 XRD.

3.3.4 Nitrogen Level Analysis

The nitrogen content was measured at various locations across the width of the strip using a standard inert gas fusion technique by Bluescope Steel. This technique involves fusing the sample, which releases the nitrogen and oxygen from the steel. The inert gas stream with the nitrogen and oxygen is then sent to an appropriate infrared detector for measurement. Instrument calibrations are performed using known reference standards.

3.4 Image Analysis

Images taken were analysed using analySIS® image analysis software. For SEM investigation backscatter electron images with a magnification of 5 kX were analysed. Due to the large variation in particle size observed in the TEM investigation different magnification were analysed. Individual precipitates were manually traced (as shown in Figure 3-12) and the area of each precipitate recorded. Assuming the precipitates are circular, the areas of the precipitates were converted to a diameter. Over 100 precipitates were traced per sample unless otherwise stated.

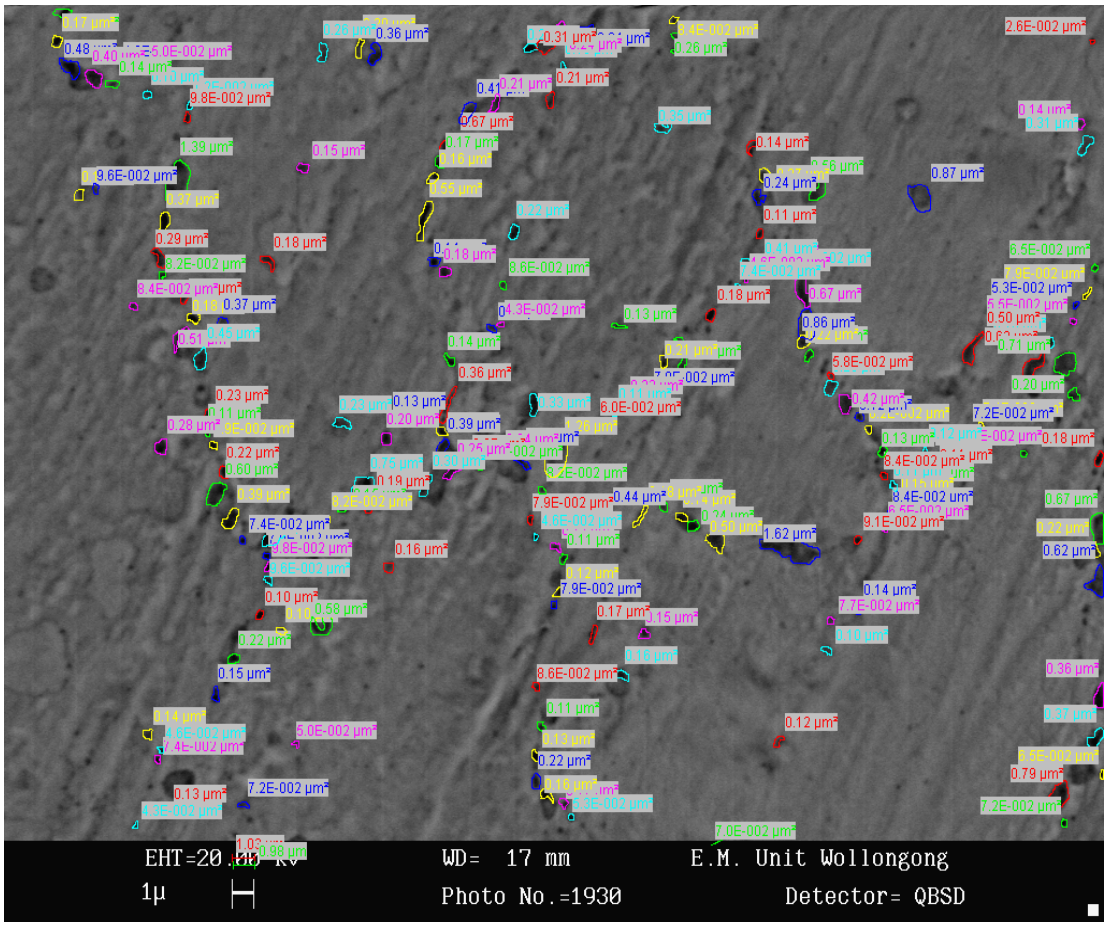

Figure 3-12: Example of an image being analysed were individual precipitates were manually traced.

3.5 Solid State Reaction between MnO and Cr_2O_3

Powders were sourced from Sigma-Alderich. Manganese (II) Oxide (MnO) was 99% pure and had a mesh size of -60. Chromium (III) Oxide (Cr_2O_3) was 98+% pure and had a particle size of 1 micron. The desired mass ratio of powders was measured using scales. Typically both a 50/50 mass ratio and calculated stichometric ratio were used. The powders were then mixed and ground in a mota and pestle. The powders were then pressed into a pellet. PVA wood glue was used as a binder. The pellets were annealed in the same environment as the steels. Powders were characterised using XRD.

Images in this chapter were too large to include.

Please see the print copy.

Chapter 4 : Results

4.1 Characterisation of the Edge Defect

The 'edge defect' characteristically showed as a band of low reflectivity near the edge of the tinplated coil. This band was usually 20 – 50 mm in width and located 20 – 100 mm from the coil edge. Figure 4-1 shows an image of a typical band of low reflectivity. A SEM image of the affected area (Figure 4-2) reveals that the cause of the region of low reflectivity was an uneven tin coating. Figure 4-3 shows a SEM EDS spectrum of a typical dark area shown in Figure 4-2. The Fe Kα peak was from the matrix and the Sn Lα peak was from the tin coating leaving small Cr Kα and Mn Kα peaks. Therefore it was expected that the uneven tin plating was caused by particles containing chromium and manganese. A small oxygen peak was observed on the shoulder of the Fe Lα peak and a small carbon peak was also observed.

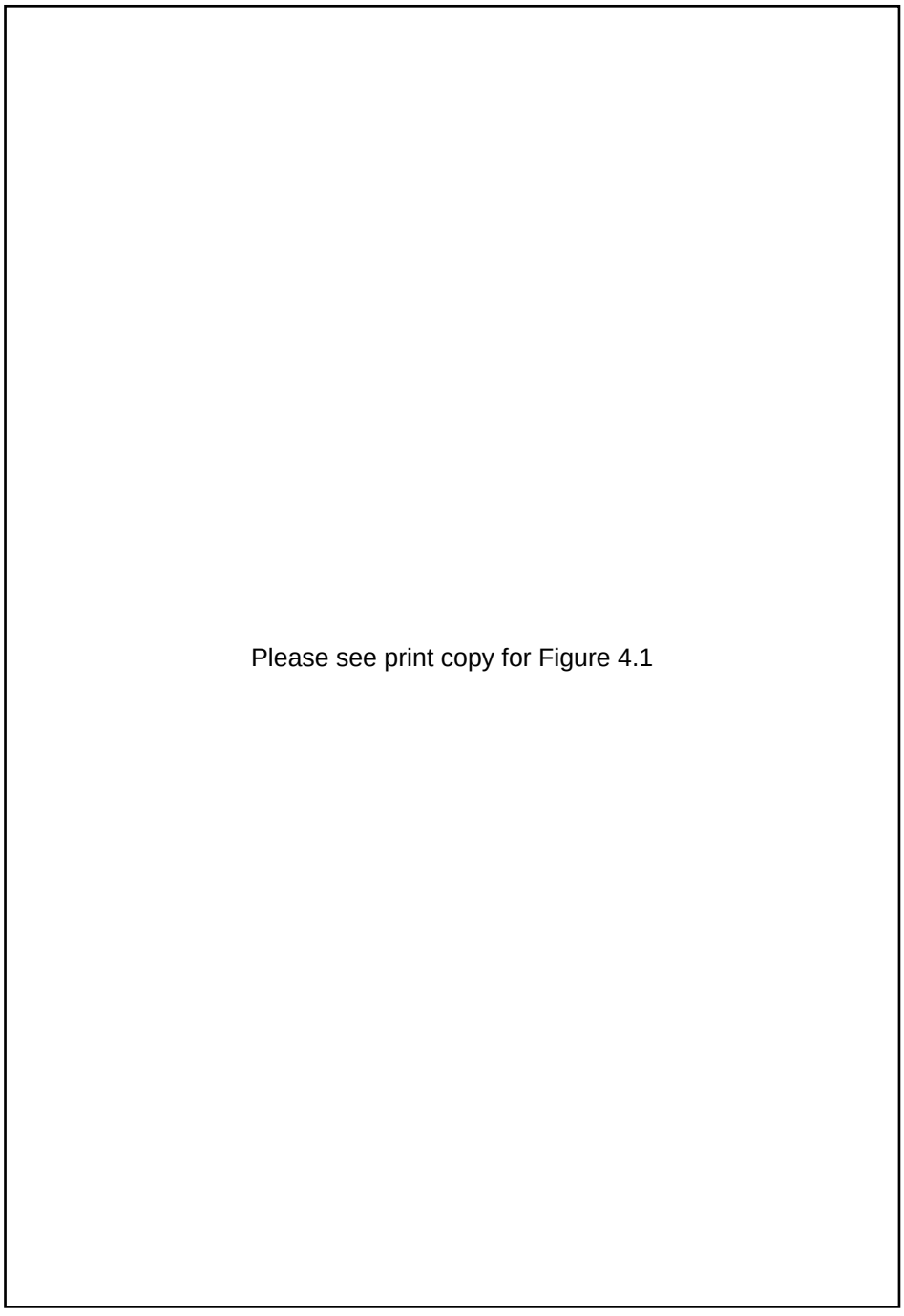

Figure 4-1: Band of low reflectivity located near the coil edge of a tinplated sample.

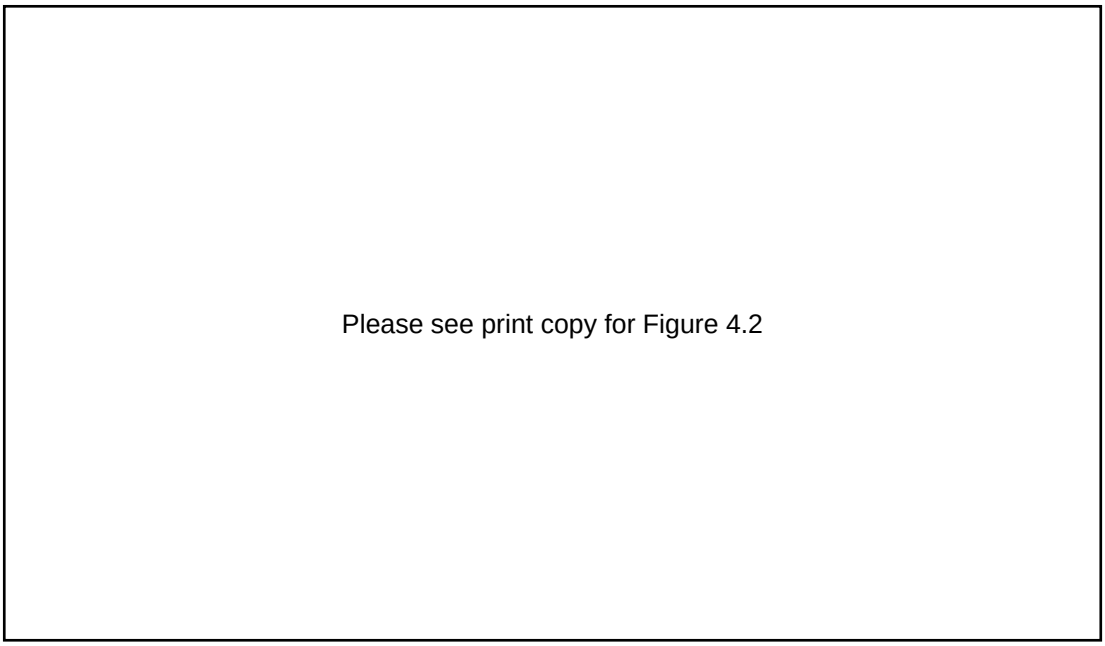

Figure 4-2: SEM image of region of low reflectivity showing uneven tin coating caused by surface grain boundary precipitates. Arrow indicates location of Figure 4.3 EDS spectrum.

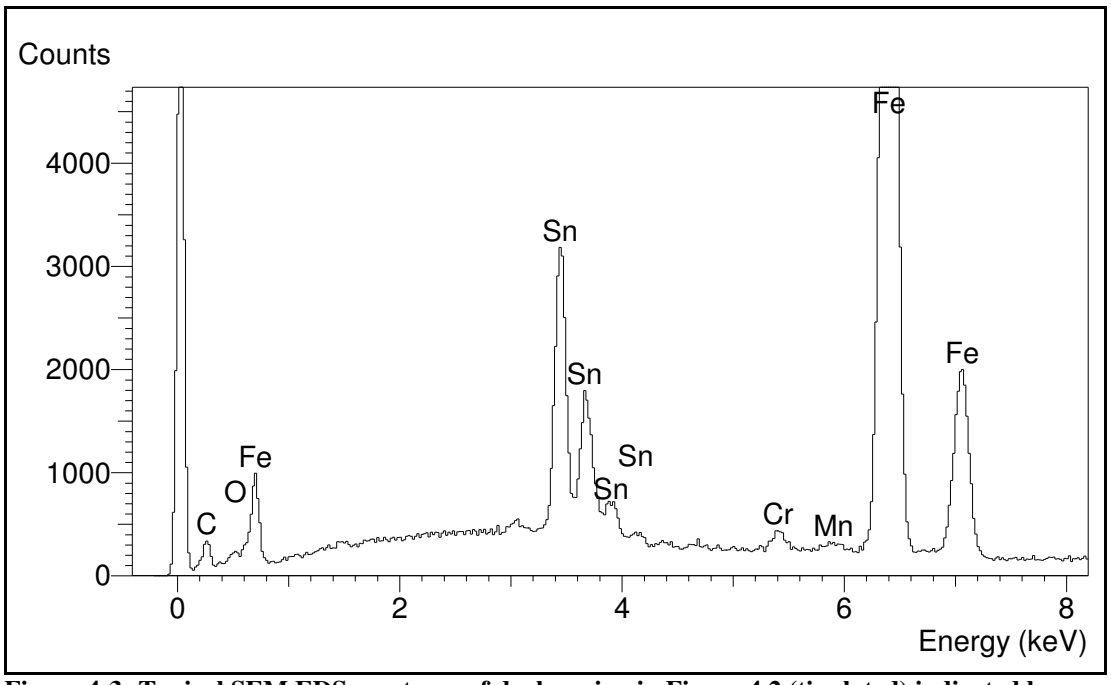

Figure 4-3: Typical SEM EDS spectrum of dark region in Figure 4.2 (tinplated) indicated by arrow in Figure 4.2.

A sample from the region of low reflectivity was mounted at an angle of 20 degrees, polished, etched and observed by SEM (Figure 4-4). This showed that the precipitates were limited to the steel surface.

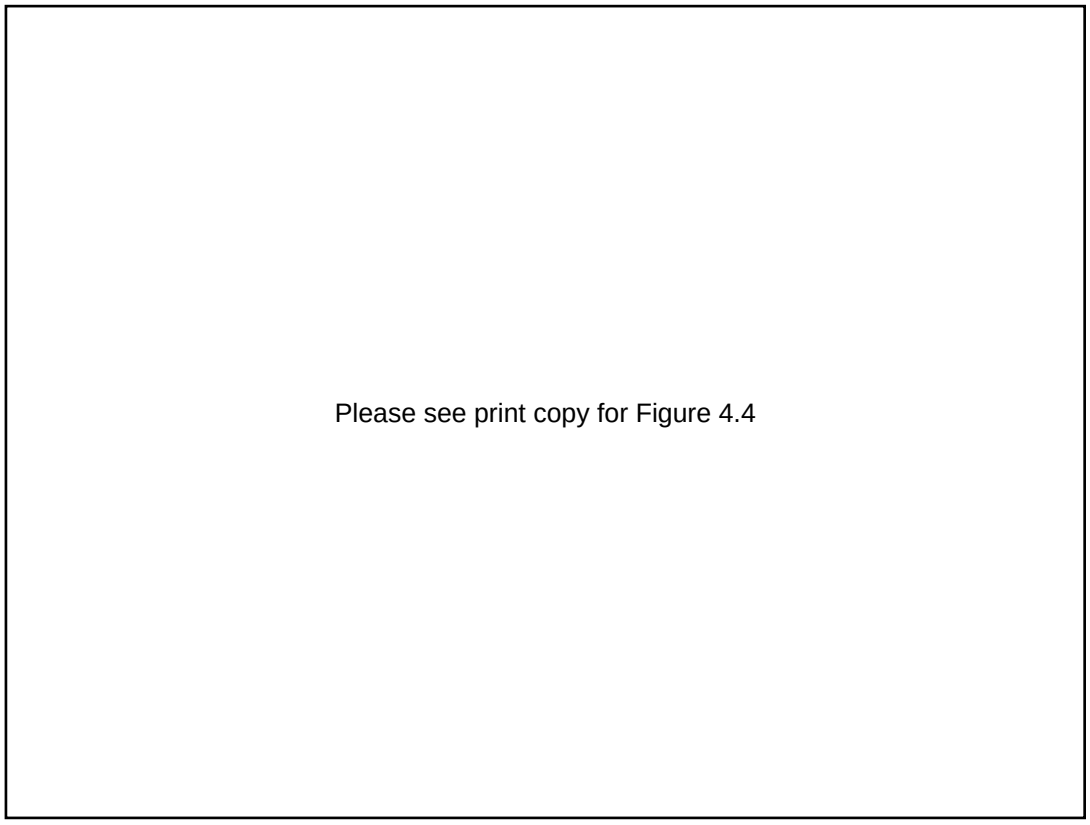

Figure 4-4: SEM image of 'edge defect' mounted at an angle of 20 degrees from the parallel, polished and etched in nital.

The tinplating was removed from the region of low reflectivity and carbon extraction replicas were made of the steel surface and observed by TEM (Figure 4-5). The precipitates were predominantly located at grain boundaries. A typical TEM EDS spectrum from the grain boundary precipitates is given in Figure 4-6, which shows grain boundary precipitates were chromium, manganese and oxygen rich. The C Kα peak was from the carbon replica and the Cu Kα peak was from the copper grid. The precipitates were clearly chromium and manganese based oxides with a Cr/Mn ratio of about 2. Therefore, the precipitates are likely to be $MnCr_2O_X$. Electron diffraction was carried out on these particles in order to determine the crystal structure.

Please see print copy for Figure 4.5

Figure 4-5: TEM image of carbon replica sample showing precipitates extracted from steel surface.

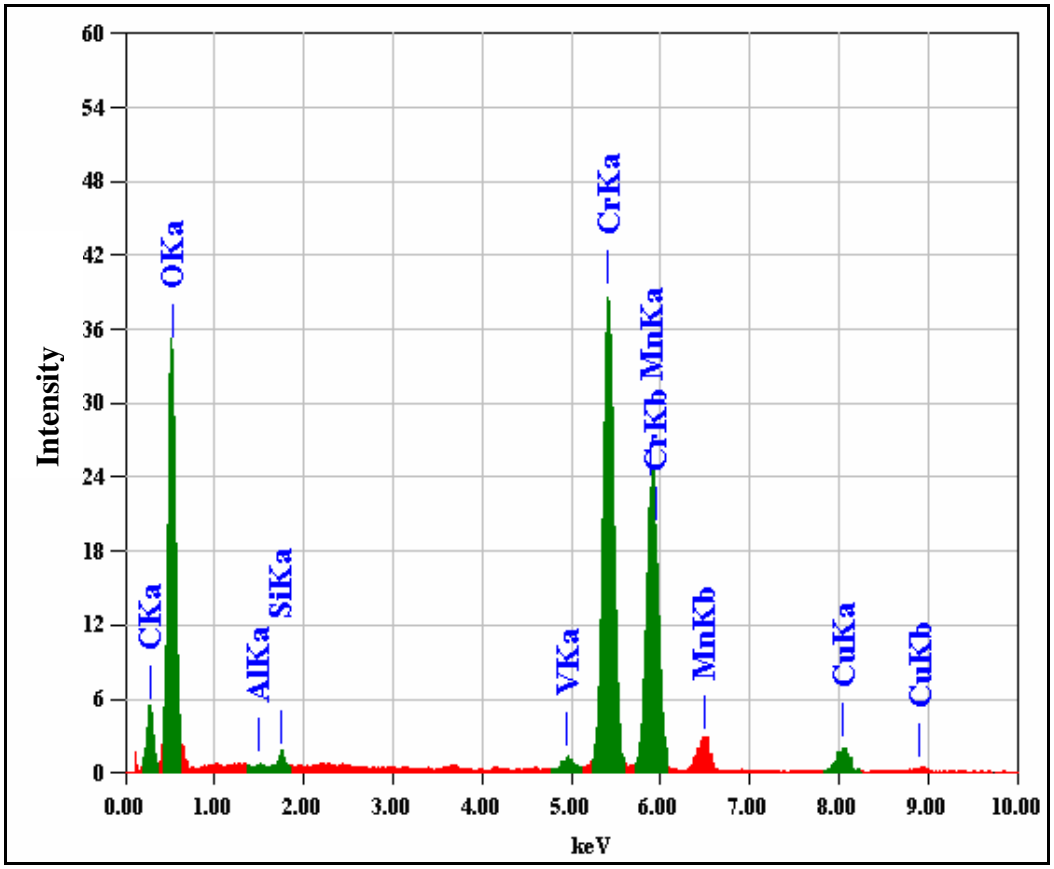

Figure 4-6: A typical TEM EDS spectrum of the grain boundary precipitates showing that the main constitutes are chromium, manganese and oxygen.

A part of the Kikuchi map of the precipitates was established experimentally and is given in Figure 4-7. Figure 4-8 shows the standard Kikuchi map for an FCC crystal structure. By comparing these two Kikuchi maps it was concluded that the precipitates have a FCC Bravais lattice.

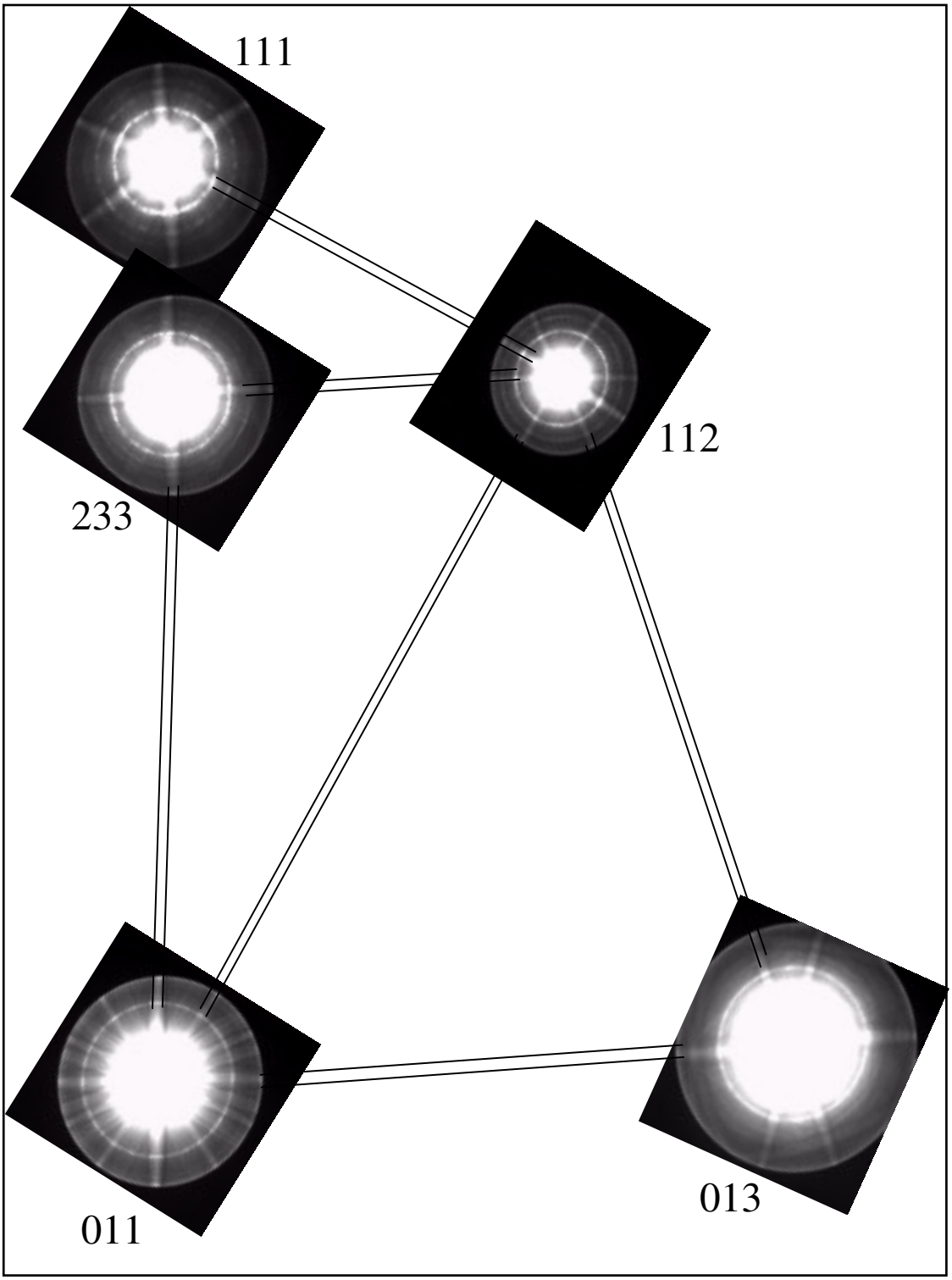

Figure 4-7: Kikuchi map produced from a surface grain boundary precipitate.

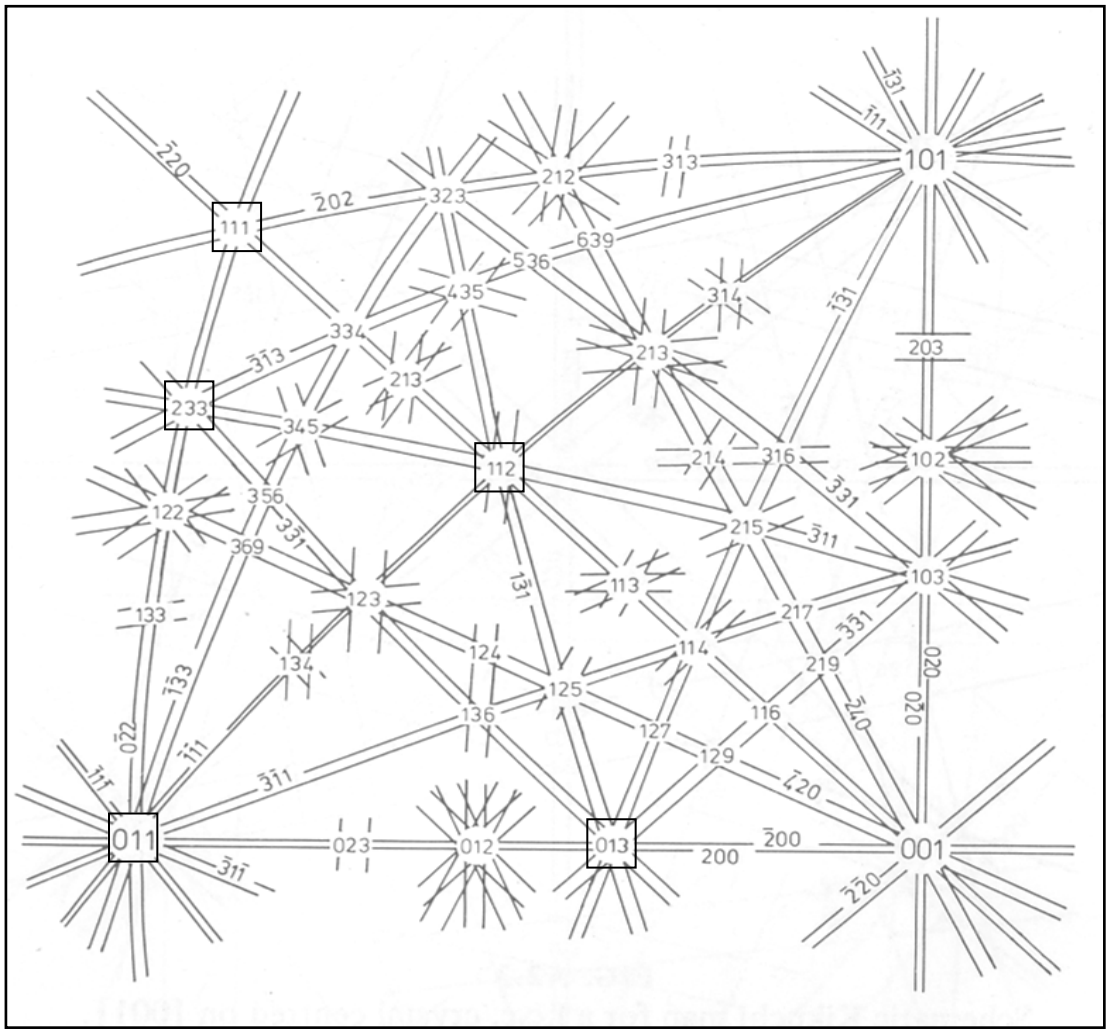

Figure 4-8: Schematic Kikuchi map for a FCC crystal extending over two standard triangles, □ depicting zone axes shown in Figure 4-7.

Convergent beam and nano-electron diffraction patterns for [011], [$\bar{1}$11] and [013] zone axes of the oxide were taken and are shown in Figure 4-9 to Figure 4-11 respectively. The left sides of these images are the convergent beam electron diffraction (CBED) patterns and the right sides are either nano-diffraction patterns or selective area diffraction patterns. For the [$\bar{1}$11] zone axis (Figure 4-10) the zero order Laue zone shows symmetry of 6mm and the whole pattern (zero and high order Laue zones) shows symmetry of 3m. This again confirms that the precipitate has a cubic crystal structure. The diffraction patterns were consistently indexed according to the crystal structure of $MnCr_2O_4$, which has a FCC crystal structure.

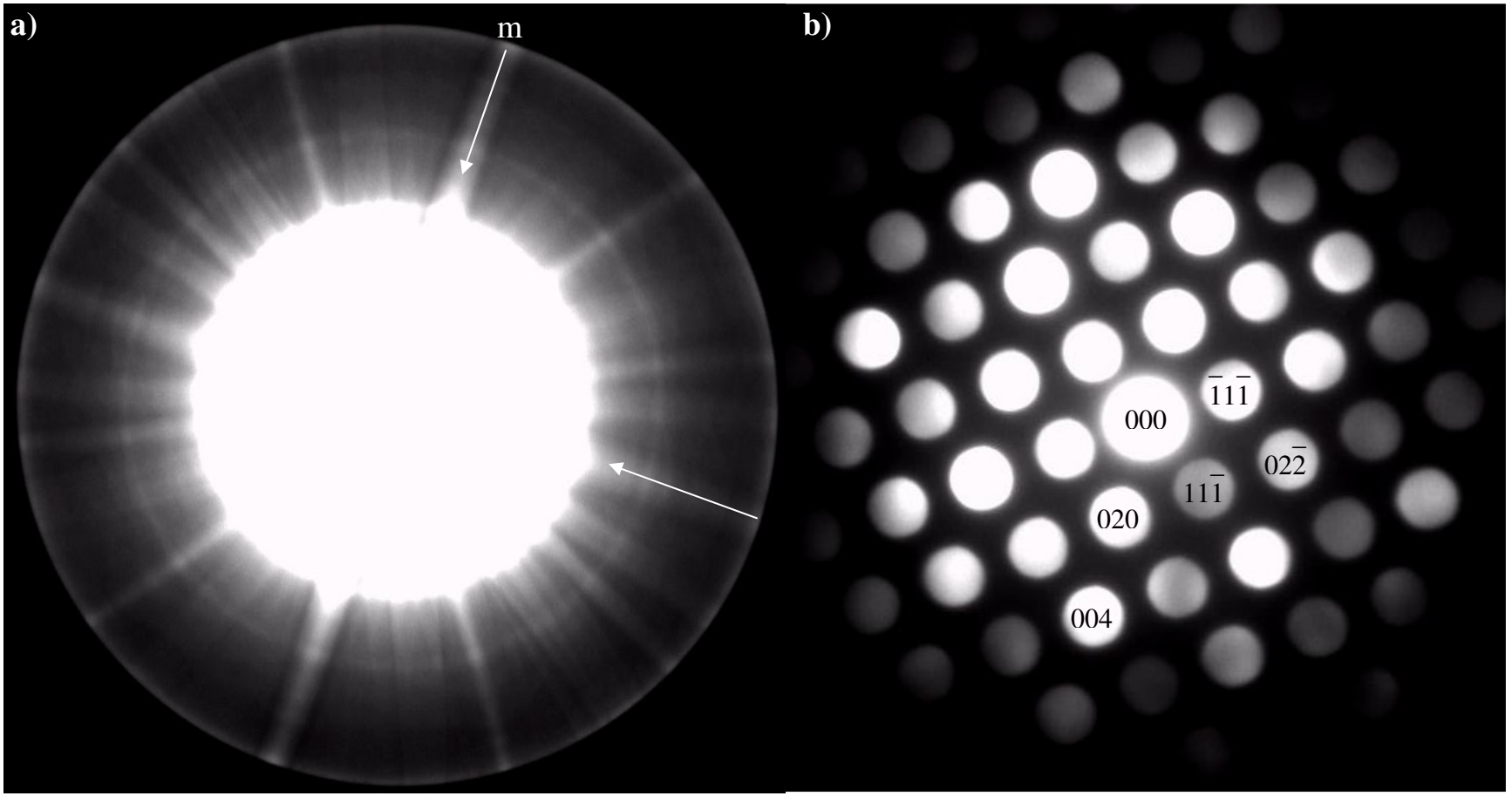

Figure 4-9: a) Convergent beam diffraction pattern of the [011] zone axis with a whole pattern symmetry of 2mm, (b) Indexed nano-diffraction pattern of the [011] zone axis.

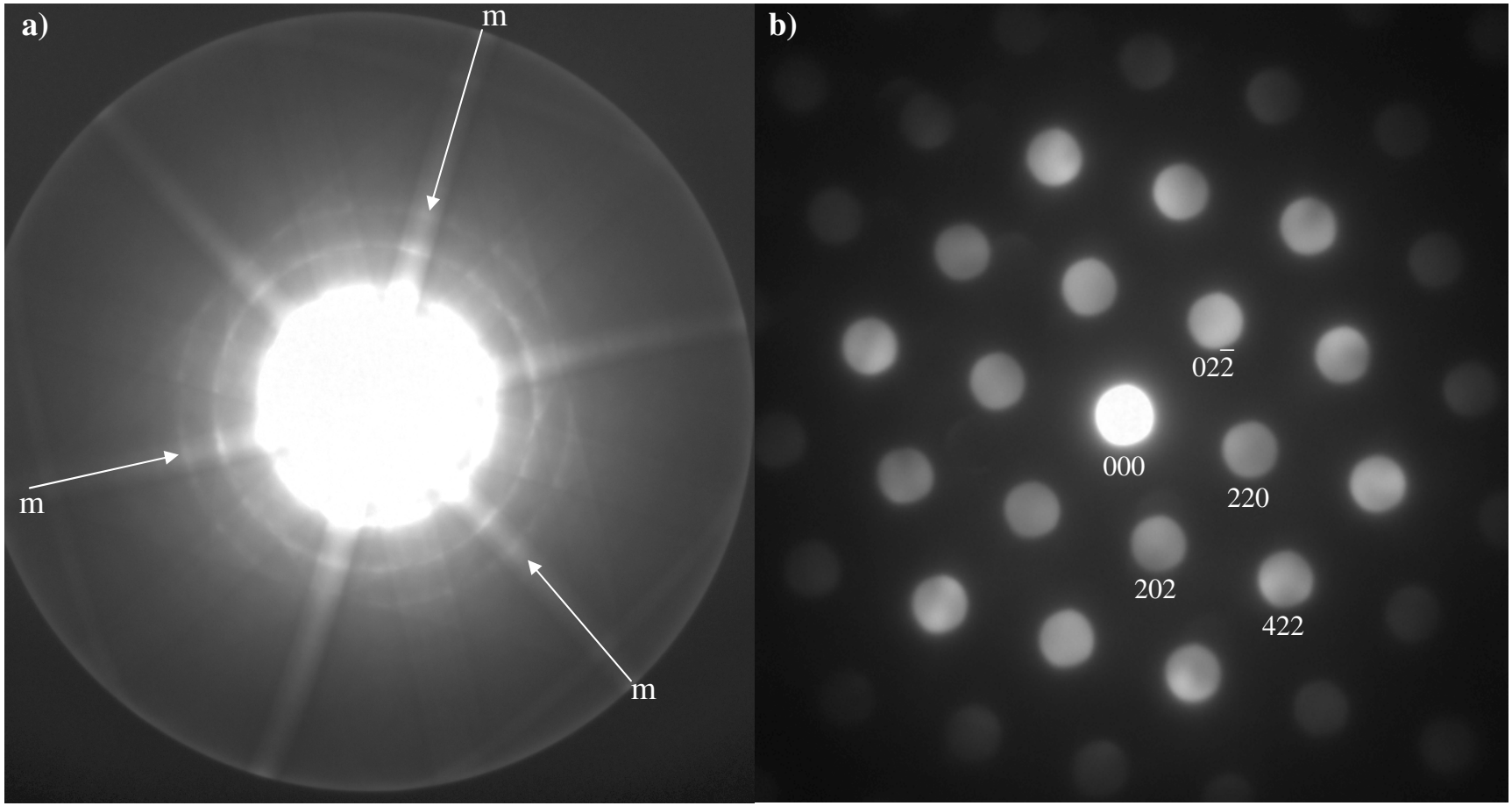

Figure 4-10: a) Convergent beam diffraction pattern of the [$\bar{1}$11] zone axis with a whole pattern symmetry of 3m, (b) Indexed nano-diffraction pattern of the [$\bar{1}$11] zone axis.

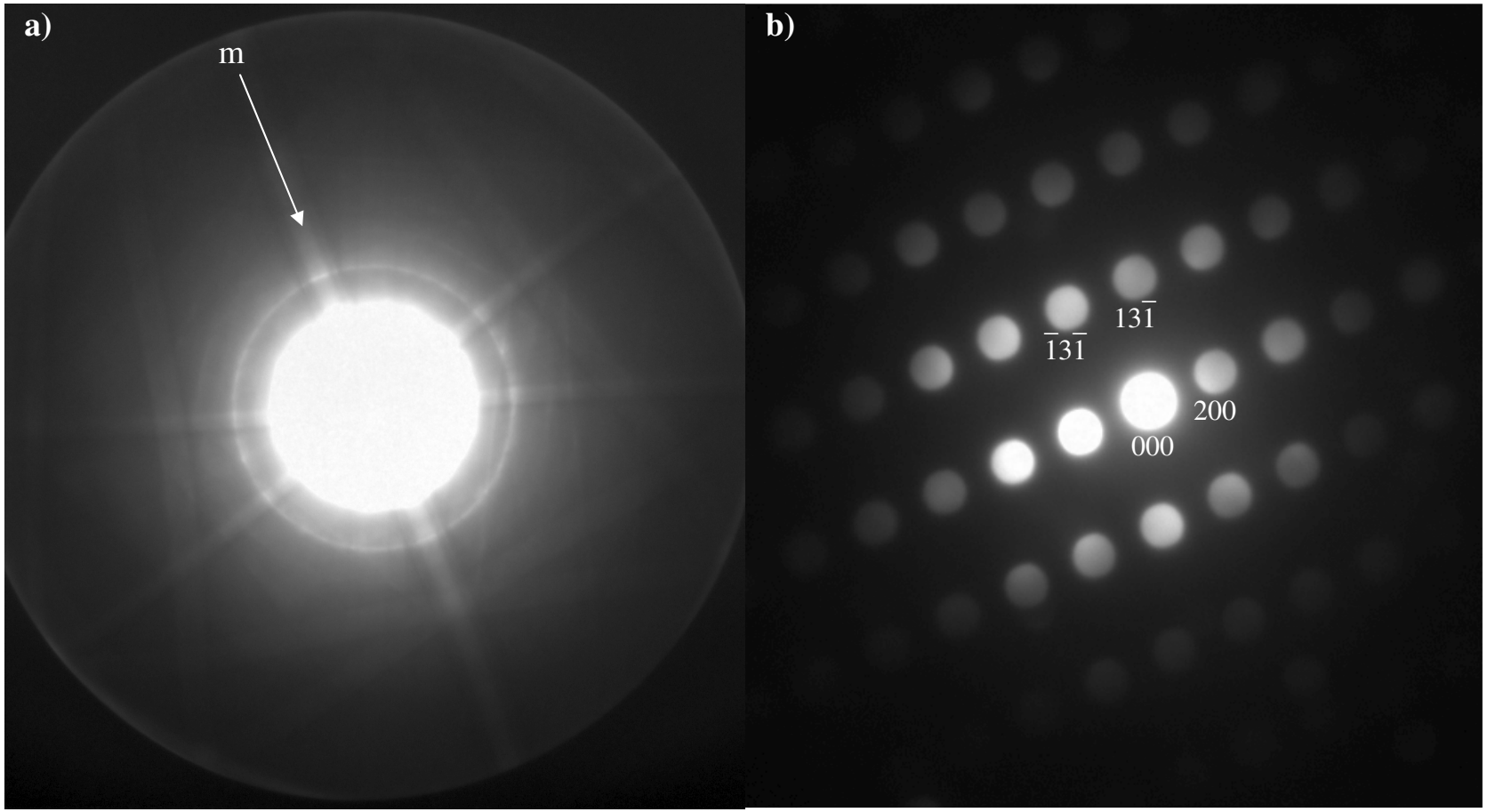

Figure 4-11: a) Convergent beam diffraction pattern of the [013] zone axis with a whole pattern symmetry of m, (b) Indexed nano-diffraction pattern of the [013] zone axis.

Figure 4-12 shows the indexed nano-electron diffraction pattern of the [001] zone axis of the oxide. The (002) diffraction is not present in the [001] zone axis but is present in the [011] and other zone axes due to double diffraction.

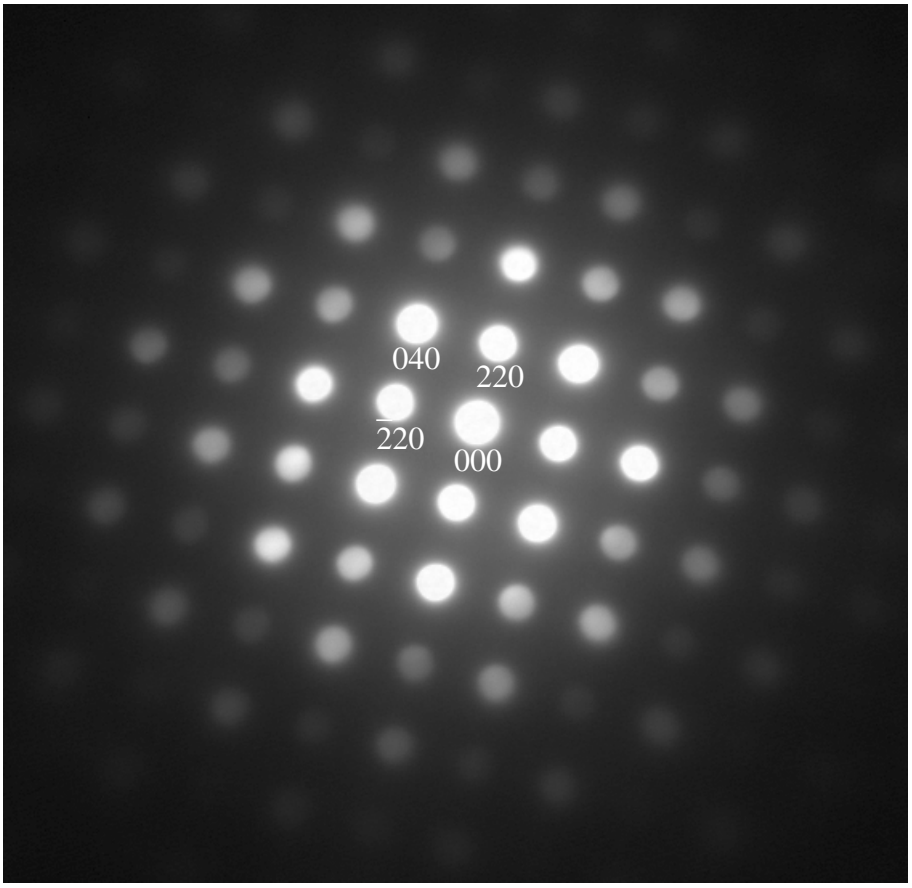

Figure 4-12: Indexed nano-diffraction pattern of the [001] zone axis.

Table 4-1 shows that the measured and calculated angles between planes and the ratios of d-spacings agree very well for the zones measured in this investigation. Note the [$\bar{1}$14], [$\bar{1}$12] and [$\bar{2}$33] zone axes are not shown. The lattice parameter was measured to be 0.83 nm, which is close to 0.845 nm reported in the literature for the $MnCr_2O_4$ spinel [46].

Table 4-1: Measured and calculated angles and ratios between diffractions for the zone axes in this investigation.

Zone Axis	g_{hkl}		Angle Between g_A & g_B (°)		g_A / g_B	
	g_A	g_B	Measured	Calculated	Measured	Calculated
[001]	(400)	(220)	44.2	45.0	1.45	1.41
[001]	(220)	$(\bar{2}20)$	89.2	90.0	1.03	1.00
[011]	(200)	$(11\bar{1})$	55.4	54.7	1.15	1.15
[011]	$(02\bar{2})$	(200)	90.4	90.0	1.43	1.41
[011]	$(\bar{1}1\bar{1})$	$(11\bar{1})$	70.5	70.5	1.00	1.00
$[\bar{1}11]$	(220)	(202)	59.9	60.0	1.01	1.00
$[\bar{1}12]$	(220)	$(1\bar{1}1)$	90.4	90.0	1.61	1.63
$[\bar{2}33]$	(311)	$(02\bar{2})$	89.5	90.0	1.17	1.17
[013]	$(13\bar{1})$	(200)	72.8	72.5	1.70	1.66
$[\bar{1}14]$	$(\bar{1}21)$	(220)	64.1	64.8	1.18	1.17

The symmetries of convergent beam diffraction patterns were used to determine the point group of the precipitates. The symmetries of the whole patterns (zero and high order Laue zones) of the [001], [011], [$\bar{1}$11] and [013] are 4mm, 2mm, 3m and m respectively. The possible diffraction groups and point groups for these 4 zone axes are listed in Table 4-2. It shows that the only possible point group that matches all 4 zones is the m3m. Therefore the point group of the precipitate is m3m, which is consistent with the space group of Fd3m of the $MnCr_2O_4$ spinel.

Table 4-2: Possible diffraction groups and point groups for the [001], [011], [$\bar{1}$11] and [013] zone axes.

Zone Axis	Whole Pattern Symetry	Possible Diffraction Groups	Possible Point Groups
001	4mm	4mm	4mm
		$4mm1_R$	4/mmm m3m
011	2mm	2mm	mm2 6m2
		$2mm1_R$	mmm 4/mmm 6/mmm m3 m3m
		4_Rmm_R	$\bar{4}$2m $\bar{4}$3m
$\bar{1}$11	3m	3m	3m $\bar{4}$3m
		$3m1_R$	6m2
		6_Rmm_R	$\bar{3}$m m3m
013	m	m	m mm2 4mm $\bar{4}$2m 3m $\bar{6}$ 6mm 6m2 $\bar{4}$3m
		$m1_R$	mm2 4mm $\bar{4}$2m 6mm 6m2 $\bar{4}$3m
		2_Rmm_R	2/m mmm 4/m 4/mmm $\bar{3}$m 6/m 6/mmm m3 m3m

4.2 Steels Laboratory Annealed in Evacuated (Vacuum) Environment

Steel L2 was annealed in evacuated quartz tube at different air pressures in an attempt to simulate the formation of the surface $MnCr_2O_4$ spinel oxide precipitates. Steel L2 was chosen because of its relatively high manganese and chromium levels and its similarity to the typical batch annealed steel. The samples were annealed at 700 °C for 6 hours at pressures varying from $1x10^{-1}$ to $1x10^{-5}$ Torr and characterised by SEM.

4.2.1 SEM Characterisation

Figure 4-13, Figure 4-14 and Figure 4-15 show the surface of steel L2 after annealing at $1x10^{-1}$, $3x10^{-2}$ and $8x10^{-4}$ Torr respectively. The sample annealed at $1.7x10^{-5}$ Torr (Figure 4-16) showed no surface precipitates. The mean particle area of oxides observed on the surface for each pressure was measured and converted to the mean particle diameter and is shown on Figure 4-17. The surface precipitates size changes dramatically with the annealing pressure. The maximum particle size observed when the pressure at room temperature was approximately $1x10^{-3}$ Torr.

SEM EDS of a typical precipitate on the steel surface after annealing is shown in Figure 4-18. This demonstrates that these precipitates have a much larger Mn Kα peak than Cr Kα peak suggesting that these precipitates are not $MnCr_2O_4$. Rather SEM EDS suggest these precipitates are (MnFe)O.

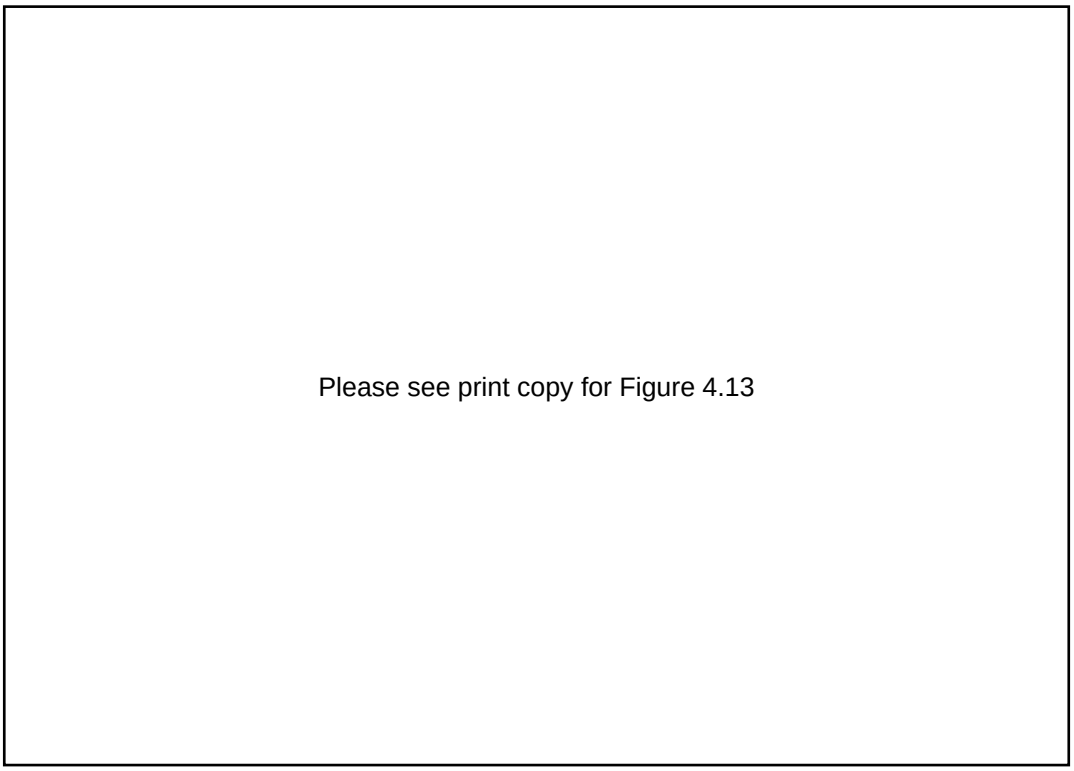

Figure 4-13: Secondary electron image of the surface of steel L2 annealed at 700 °C in an air pressure of $1x10^{-1}$ for 6 hours.

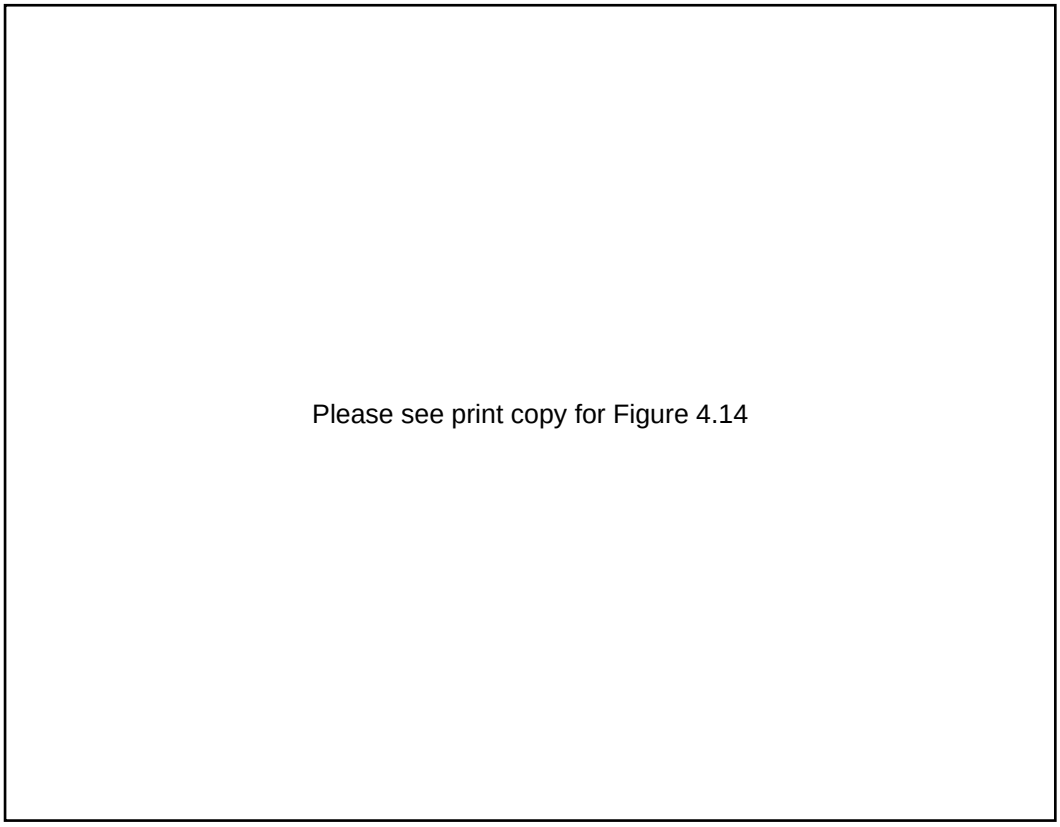

Figure 4-14: Secondary electron image of the surface of steel L2 annealed at 700 °C in an air pressure of $3x10^{-2}$ for 6 hours.

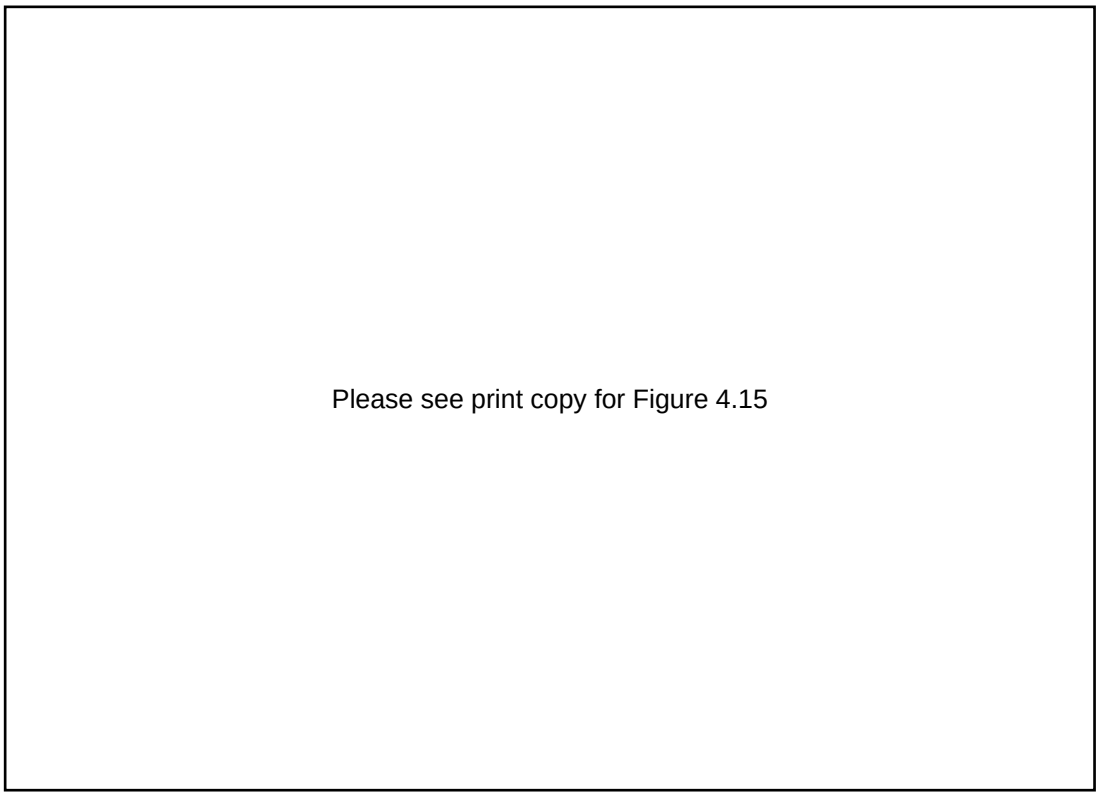

Figure 4-15: Secondary electron image of the surface of steel L2 annealed at 700 °C in an air pressure of $8x10^{-4}$ for 6 hours.

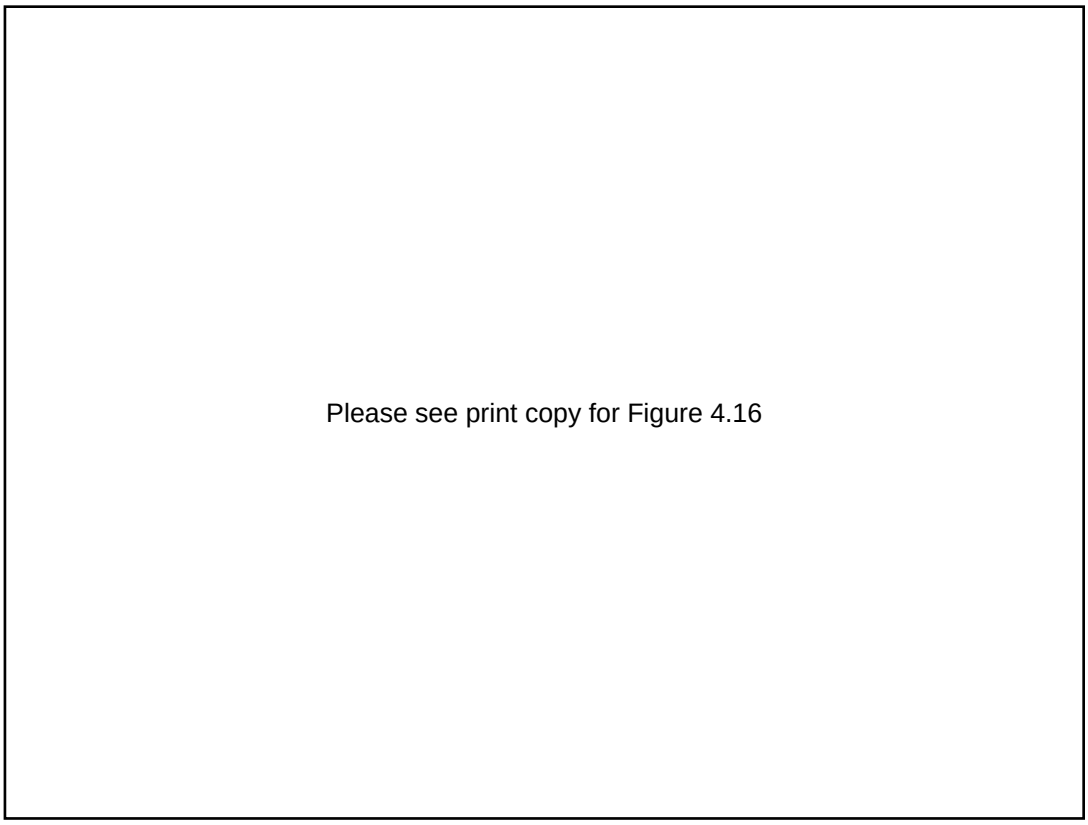

Figure 4-16: Secondary electron image of the surface of steel L2 annealed at 700 °C in an air pressure of $1.7x10^{-5}$ for 6 hours.

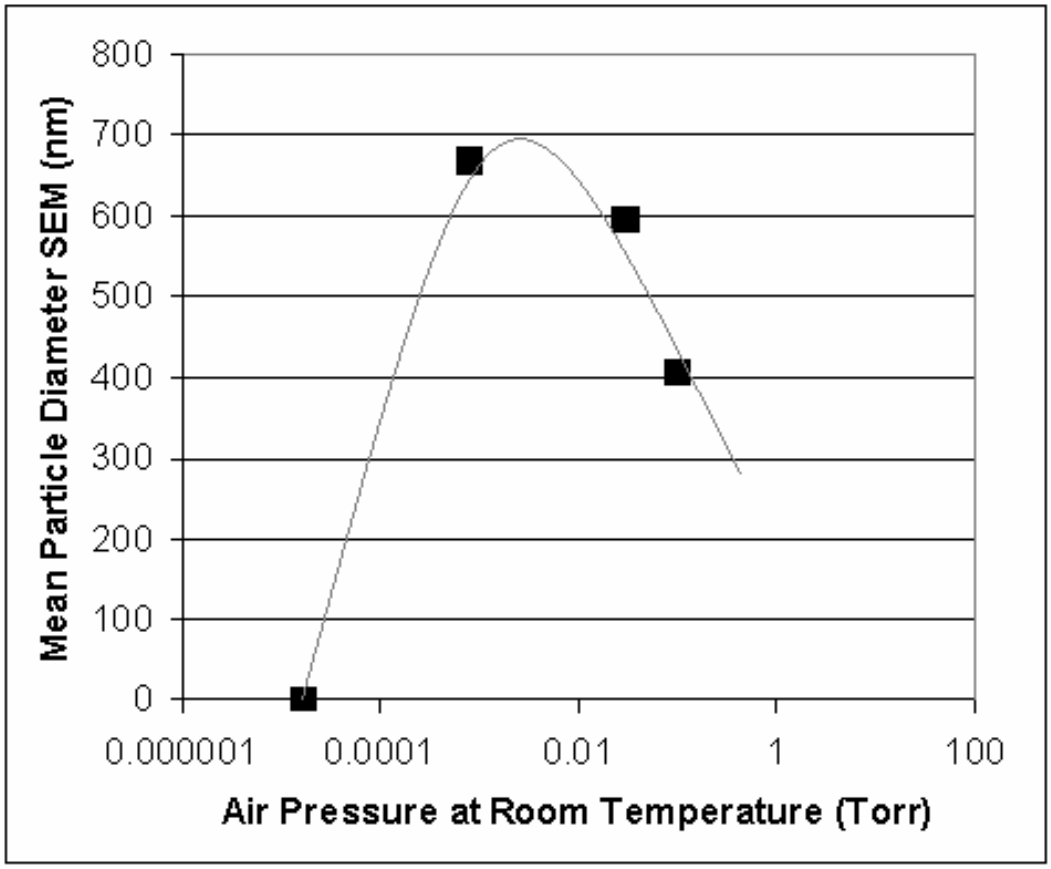

Figure 4-17: The change in mean particle diameter of precipitates measured by SEM with annealing air pressure when annealed at 700 °C for 6 hours.

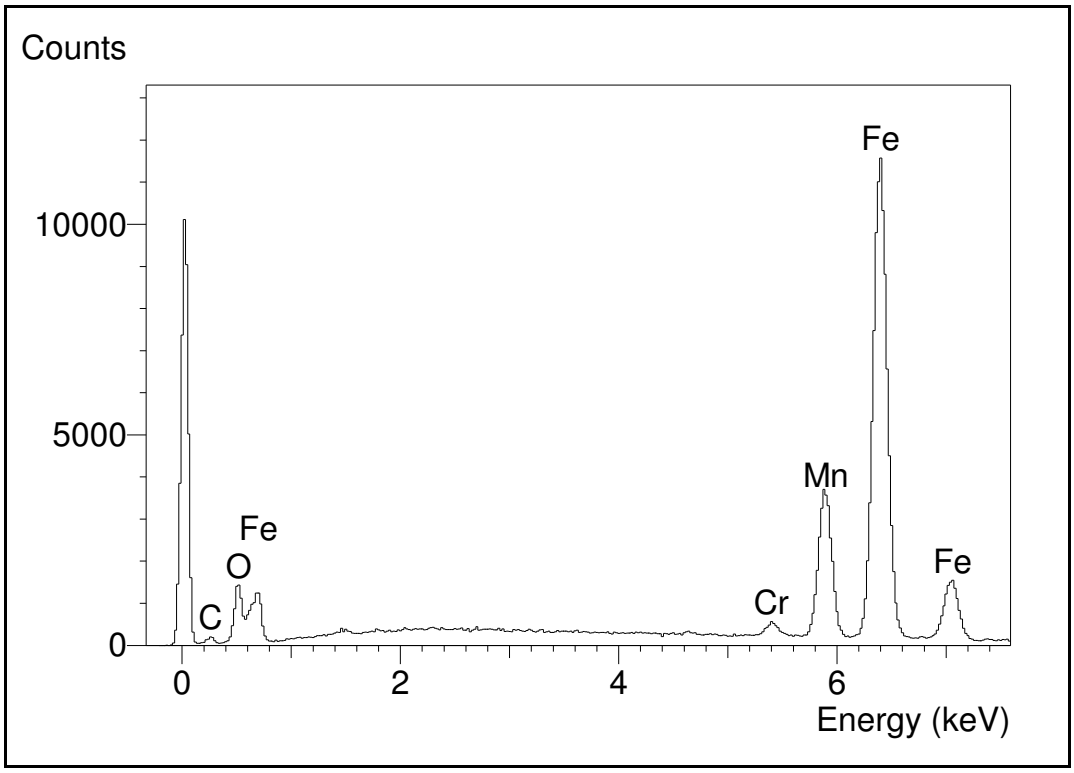

Figure 4-18: Typical SEM EDS of precipitates on steel surface.

4.3 Characterization of (MnFe)O

4.3.1 XRD Characterisation

To characterize the (MnFe)O oxides found on the steel surface after annealing in an evacuated (vacuum) environment steel L2 was annealed for 72 hours for XRD characterization. Figure 4-19 shows a secondary electron image of the steel surface, which was annealed for 72 hours at 700 °C and a pressure of 10^{-2} Torr. The surface precipitates were not only much coarser but also were present within the grains (bright contrast), as well as at grain boundaries (dark contrast). The different contrasts were caused by the different heights of these particles relative to the specimen surface. The fully grown surface precipitates have a cuboid morphology. Again SEM EDS of these large precipitates indicate they were (MnFe)O. Substantial iron was observed in the cuboid particles, which is probably due to the poorer vacuum during the longer heat treatment.

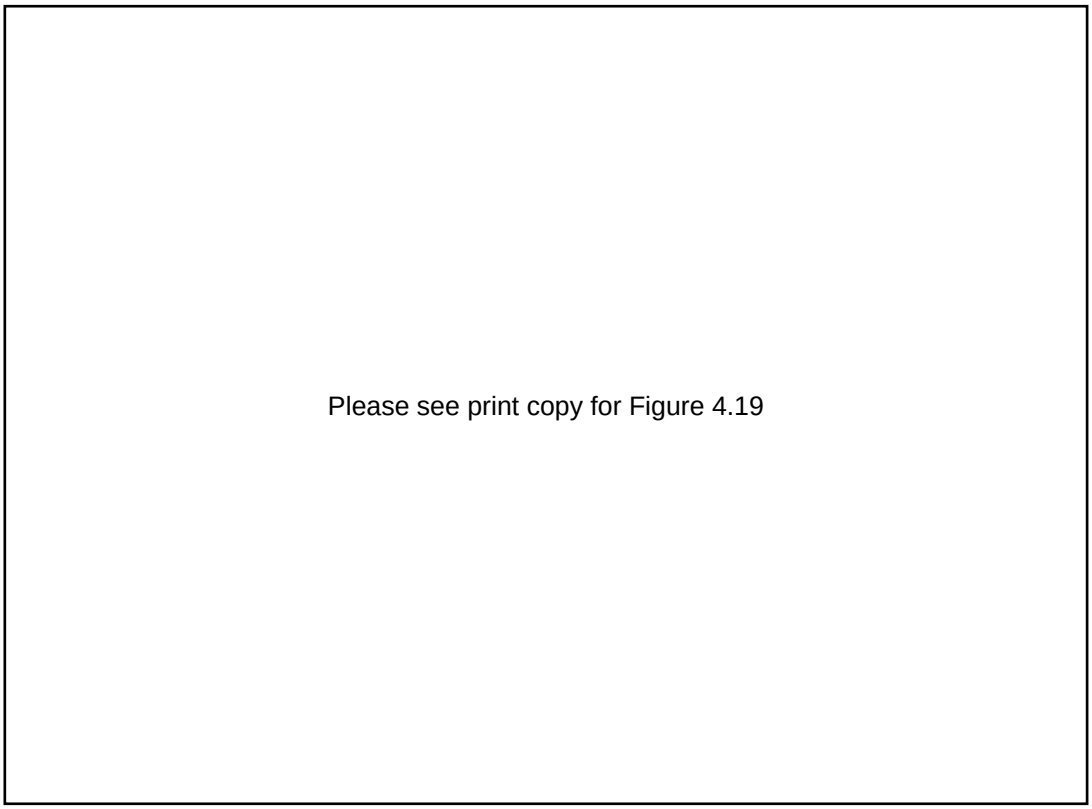

Figure 4-19: Secondary electron image of the surface of steel L2 annealed at 700 °C in an air pressure of $1x10^{-2}$ for 72 hours.

An XRD spectrum from the sample annealed for 72 hours is shown in Figure 4-20. In addition to the peaks generated by the iron matrix, the remaining peaks were indexed as the {111}, {200} and {220} of FCC with a lattice parameter a = 0.43 nm which is between the lattice parameters a = 0.429 nm of FeO and a = 0.444 nm of MnO. This confirms that these precipitates are (MnFe)O.

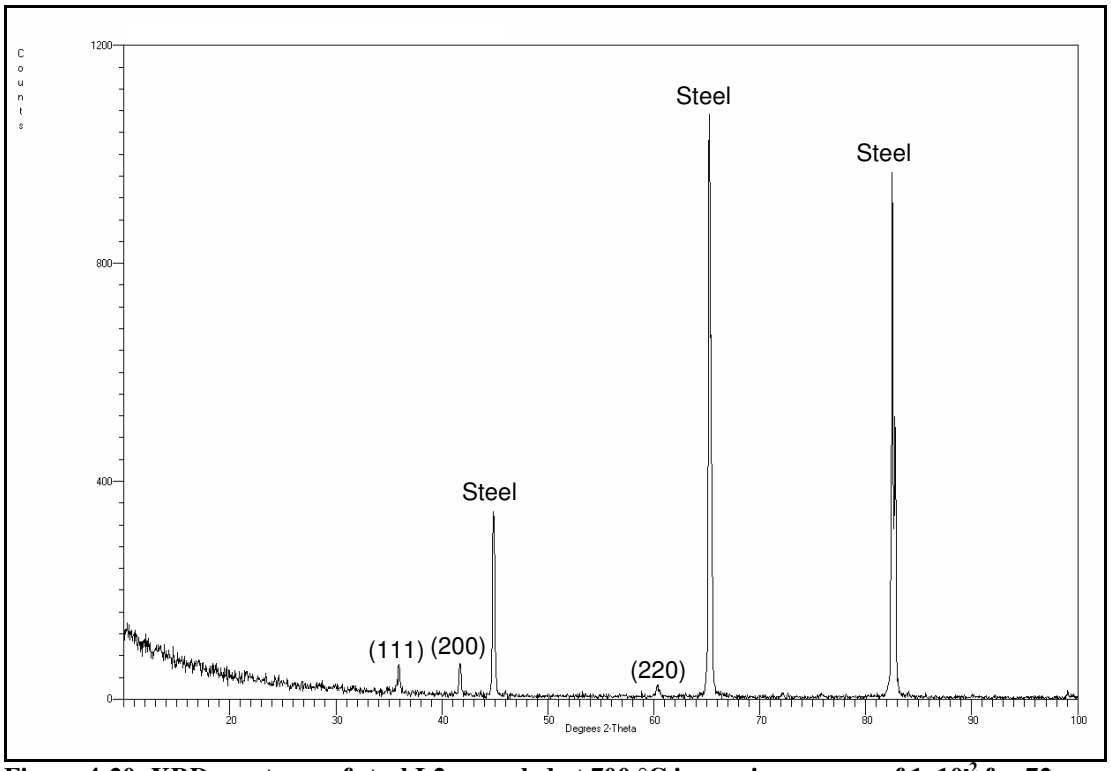

Figure 4-20: XRD spectrum of steel L2 annealed at 700 °C in an air pressure of $1x10^{-2}$ for 72 hours showing the (111), (200) and (200) peaks of FCC crystal structure with a=0.43 nm.

4.3.2 TEM Characterisation

The (MnFe)O type oxide was not observed on the tinplated steel surface. However industrial annealed steels that have not been pickled (blackplate) have these (MnFe)O precipitates. Figure 4-21 shows an SEM image of surface of steel B1 and Figure 4-22 shows that these precipitates have a SEM EDS spectrum suggesting that they are (MnFe)O.

Please see print copy for Figure 4.21

Figure 4-21: Secondary electron image of the surface of steel B1, 40 mm from coil edge.

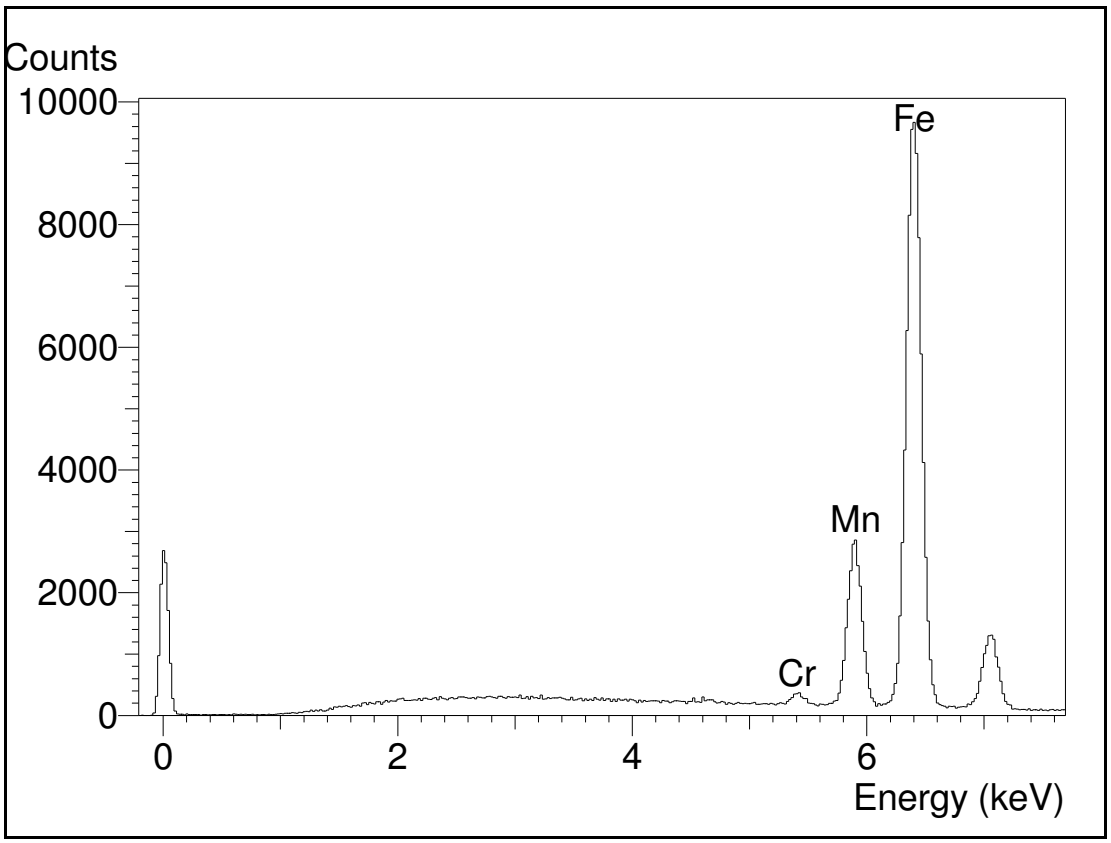

Figure 4-22: SEM EDS of precipitate on surface steel B1, 40 mm from coil edge.

A sample taken in the area about 15 mm from the edge of coil B1 was used to prepare a TEM cross-section specimen. Figure 4-100 shows a relatively coarse grain boundary precipitate about 300 nm in diameter. Within the coarse precipitate a small core region is evident (B). EDS spectra from the small core area (B) and the area marked (A) are given in Figure 4-24 and Figure 4-25 respectively. Figure 4-24 shows that the core precipitate is enriched in chromium compared to the surrounding region. Figure 4-25 demonstrates the surrounding region is (MnFe)O. The Cu Kα and C Kα peaks were from the copper grid and carbon replica. The small Cr Kα peak was due to the precipitate core. The core precipitate is likely the $MnCr_2O_4$ spinel.

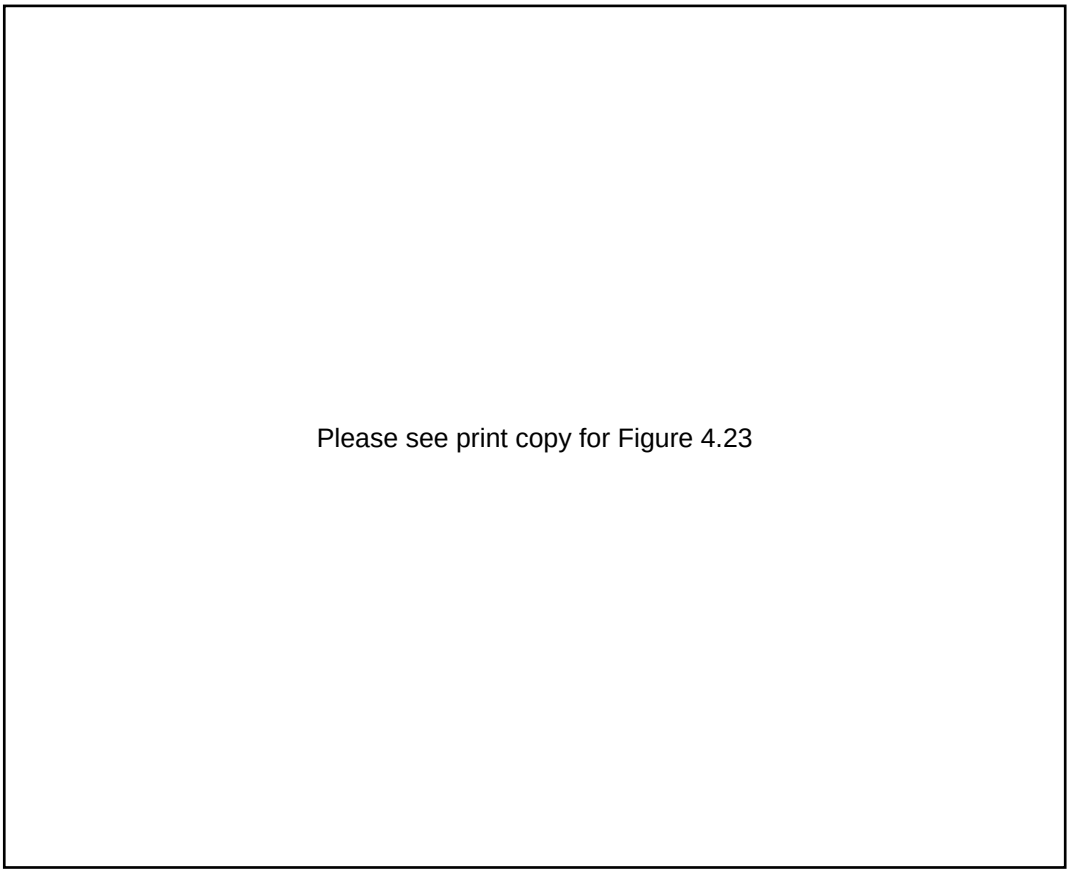

Figure 4-23: TEM images showing grain boundary precipitates below the steel surface. Pt: platinum coating, A, B, C, D: areas analysed by EDS.

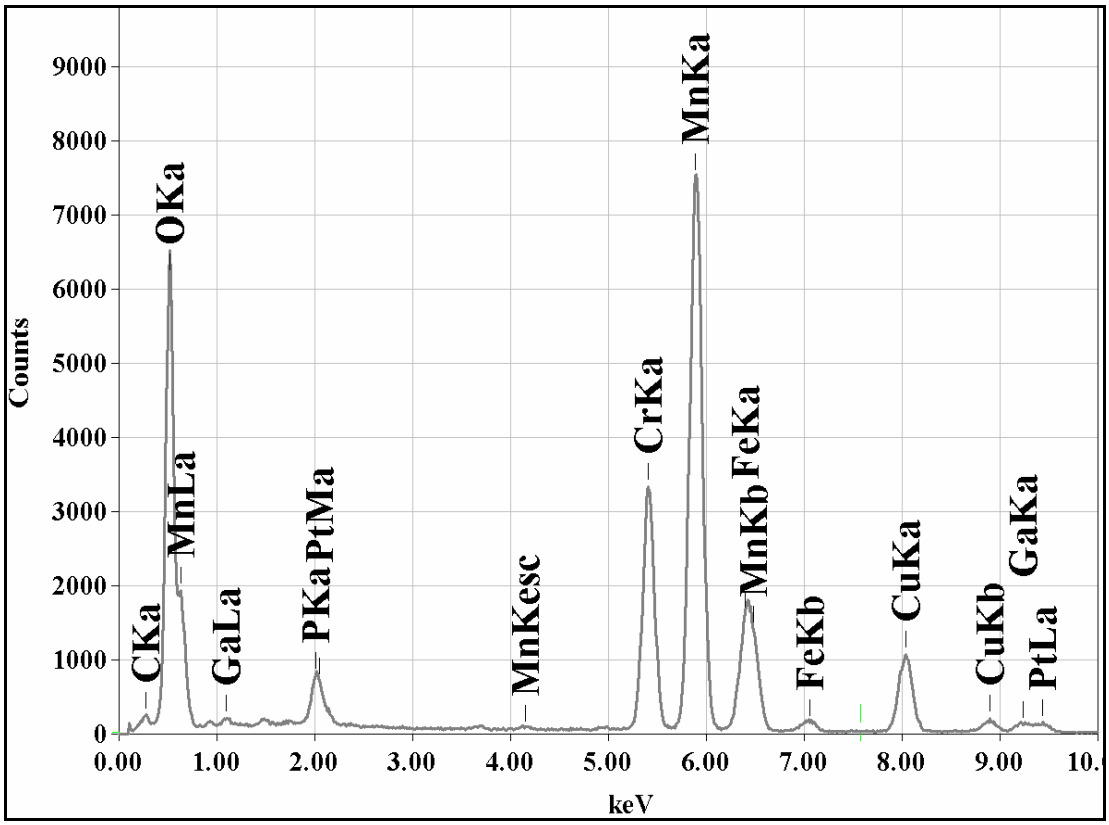

Figure 4-24: EDS spectrum of area B in Figure 4-23.

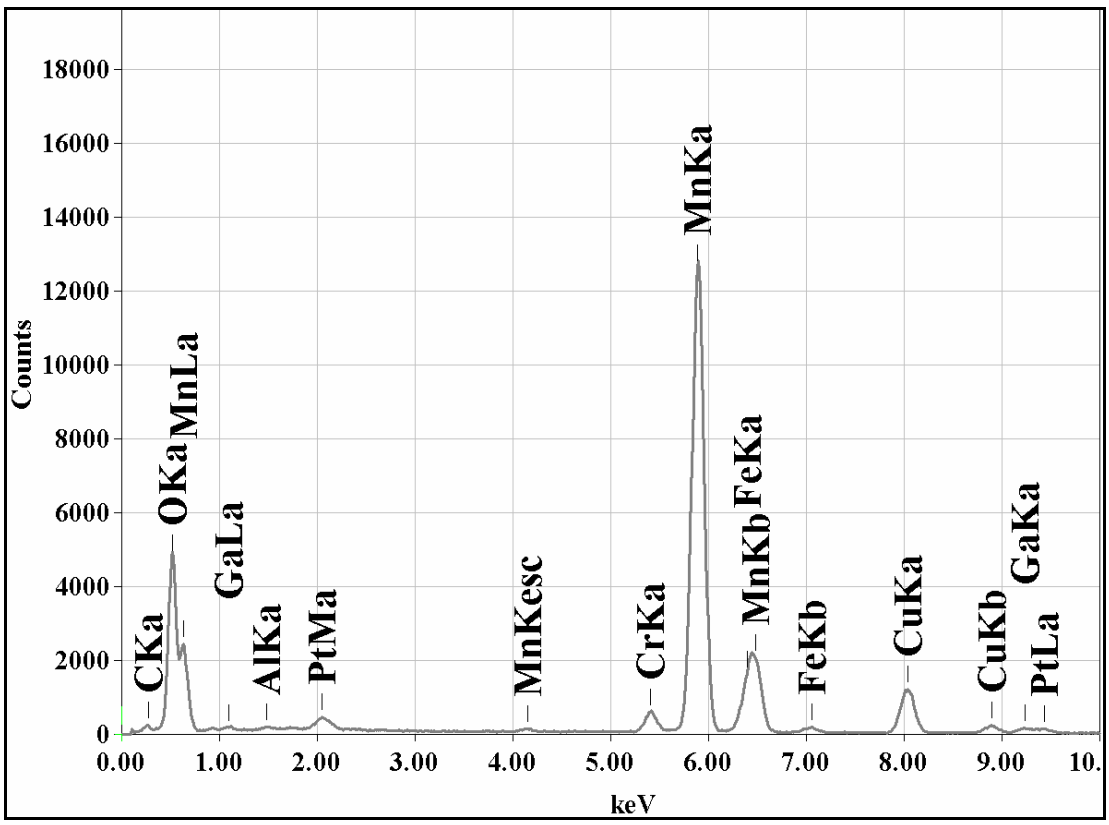

Figure 4-25: EDS spectrum of area A in Figure 4-23.

An indexed selected area diffraction pattern of the coarse internal precipitate is shown in Figure 4-26. As expected the particle has a FCC crystal structure with a lattice parameter of approximately 0.44 nm, which matches that of MnO. This confirms that the coarse surface precipitates observed in this investigation were (MnFe)O. However, only a small amount of iron is present in the oxide.

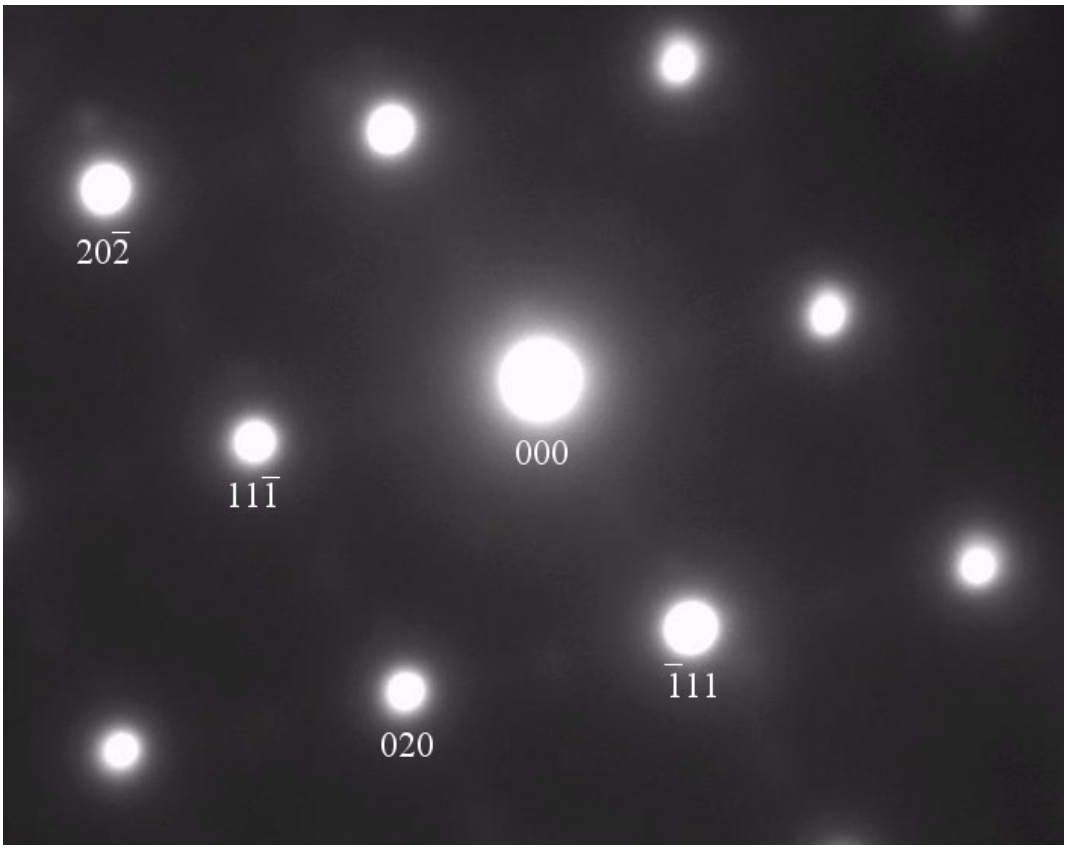

Figure 4-26: Indexed selective area diffraction pattern of manganese and oxygen rich precipitate. The zone axis is $[101]_{FCC}$.

4.4 Solubility of Oxides in Cleaning and Pickling Solutions

Clearly two different oxides were present on the steel surface after annealing, a coarser manganese oxide and a finer chromium and manganese rich spinel. As the coarser manganese oxides were not observed on the surface of the tinplated steel or on the carbon extraction replicas it was likely that the manganese oxides were lost in the cleaning and pickling processes prior to the tinning operations and in the preparation of the carbon extraction replicas. The cleaning operation was simulated in the laboratory by exposing the steel surface to NOVAMAX 187W cleaning solution for 5 seconds. The NOVAMAX 187W cleaning solution was 27% sodium hydroxide, 4% potassium hydroxide, 5% alkaline salts, <10% surfactants and water. This treatment did not remove any surface oxides from the steel surface.

The industry pickling treatment was simulated in the laboratory by exposing the steel surface to 8% sulfuric acid for 2 seconds. Figure 4-27 shows the steel surface after pickling. Figure 4-28 shows SEM EDS of the pickled steel surface. The size of the Mn Kα peak was significantly reduced indicating the (MnFe)O was removed from the surface. This is not surprising as the aim of pickling is to remove oxides from the steel surface. Small Cr Kα and Mn Kα peaks remain signifying that the $MnCr_2O_4$ spinel oxide is not removed from the steel surface by the pickling operation.

Clearly after annealing two different grain boundary oxide precipitates were present on the steel surface. The first was (MnFe)O the coarser of the two which was easily removed from the steel surface by pickling. The second was the finer $MnCr_2O_4$ spinel, which was not removed from the steel and is responsible for the ‘edge defect’.

Please see print copy for Figure 4.27

Figure 4-27: SEM image of steel surface after pickling in 8% sulfuric acid for 2 seconds.

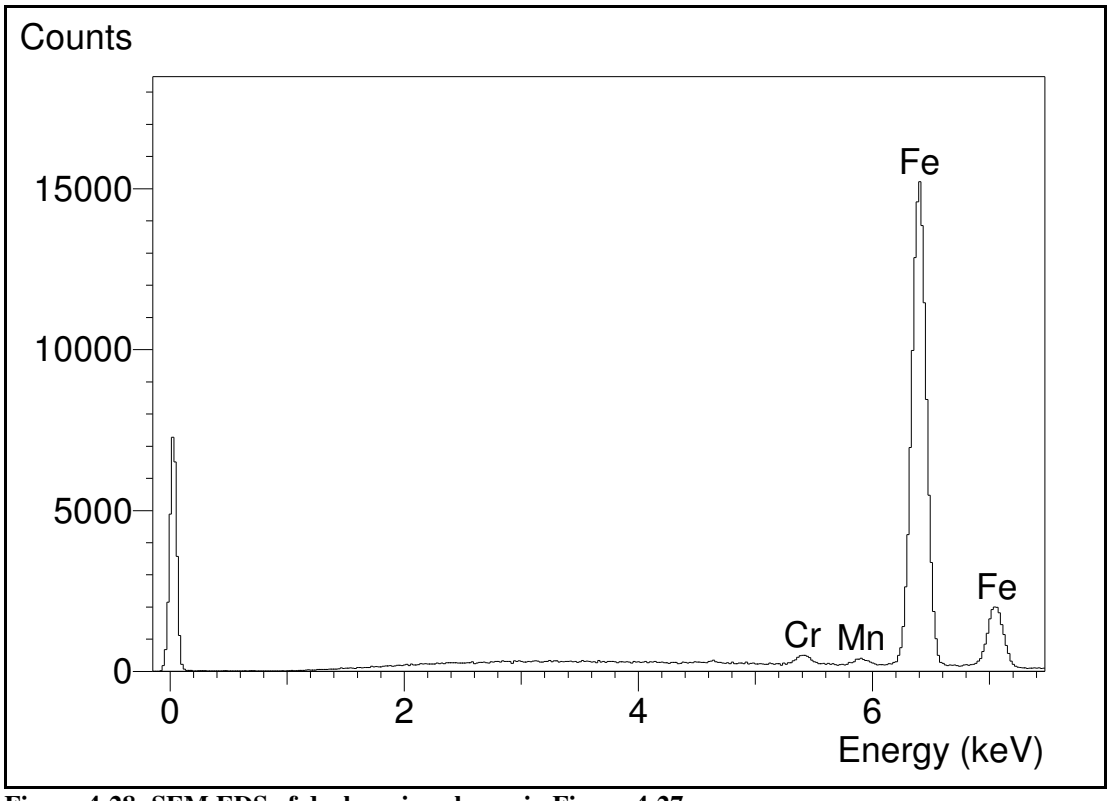

Figure 4-28: SEM EDS of dark region shown in Figure 4-27.

4.5 Steels Laboratory Annealed in 5% H_2 + 95% N_2

Steels L1 to L9 were annealed for 20 hours in a 5% H_2 + 95% N_2 environment at temperatures between 650 °C and 750 °C.

4.5.1 SEM Characterisation

SEM investigation including secondary electron and backscattered electron imaging of steels annealed at 650 °C did not show any grain boundary oxides as shown by Figure 4-29. Backscatter electron images of surface of steels annealed at 675 °C, 700 °C and 750 °C are shown in Figure 4-30 to Figure 4-55. The (MnFe)O surface precipitates were predominantly located at grain boundaries and were coarser than the spinel $MnCr_2O_4$ precipitates.

Please see print copy for Figure 4.29

Figure 4-29: Secondary electron image of the surface of steel L8 annealed at 650 °C in 5% H_2 + 95% N_2 for 20 hours.

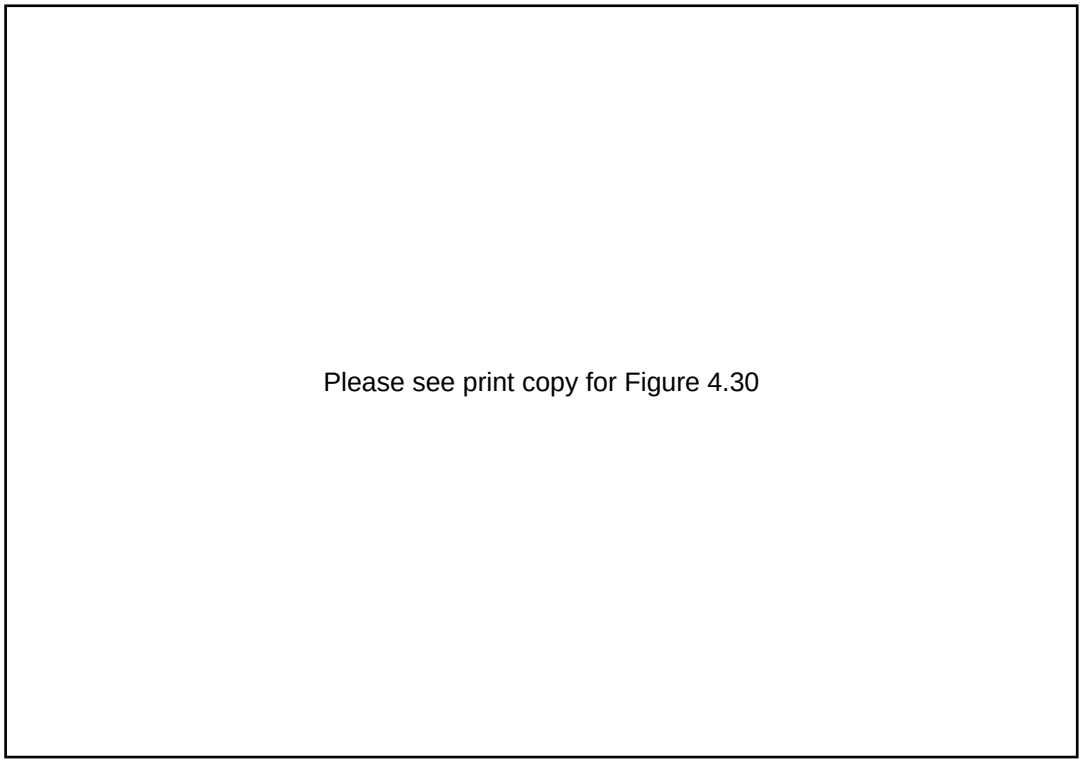

Figure 4-30: Backscatter electron image of the surface of steel L1 after annealing at 675 °C in 5% H_2 + 95% N_2 for 20 hours.

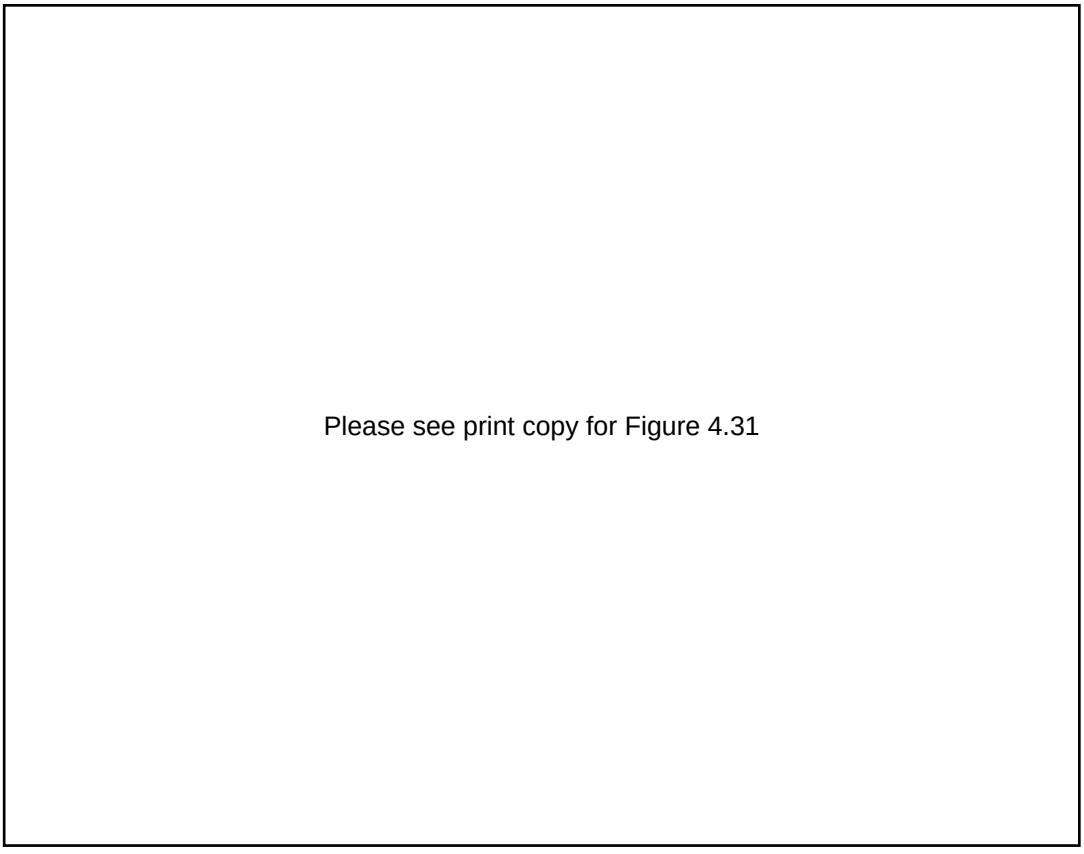

Figure 4-31: Backscatter electron image of the surface of steel L2 after annealing at 675 °C in 5% H_2 + 95% N_2 for 20 hours.

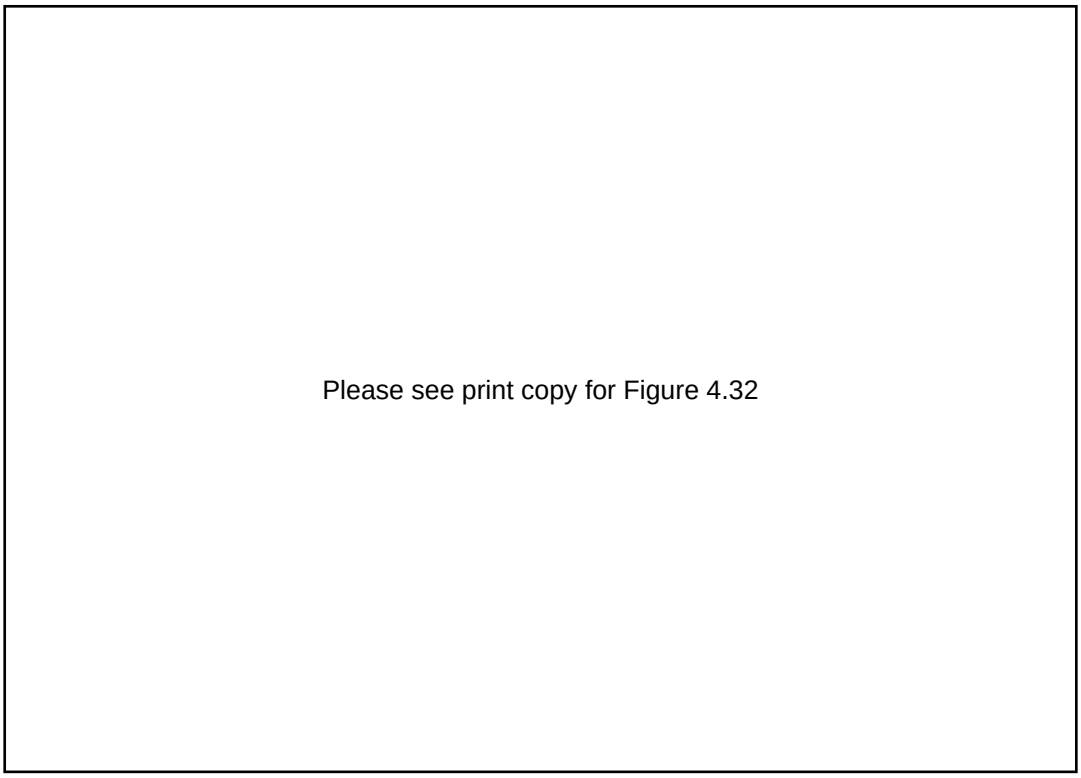

Figure 4-32: Backscatter electron image of the surface of steel L3 after annealing at 675 °C in 5% H_2 + 95% N_2 for 20 hours.

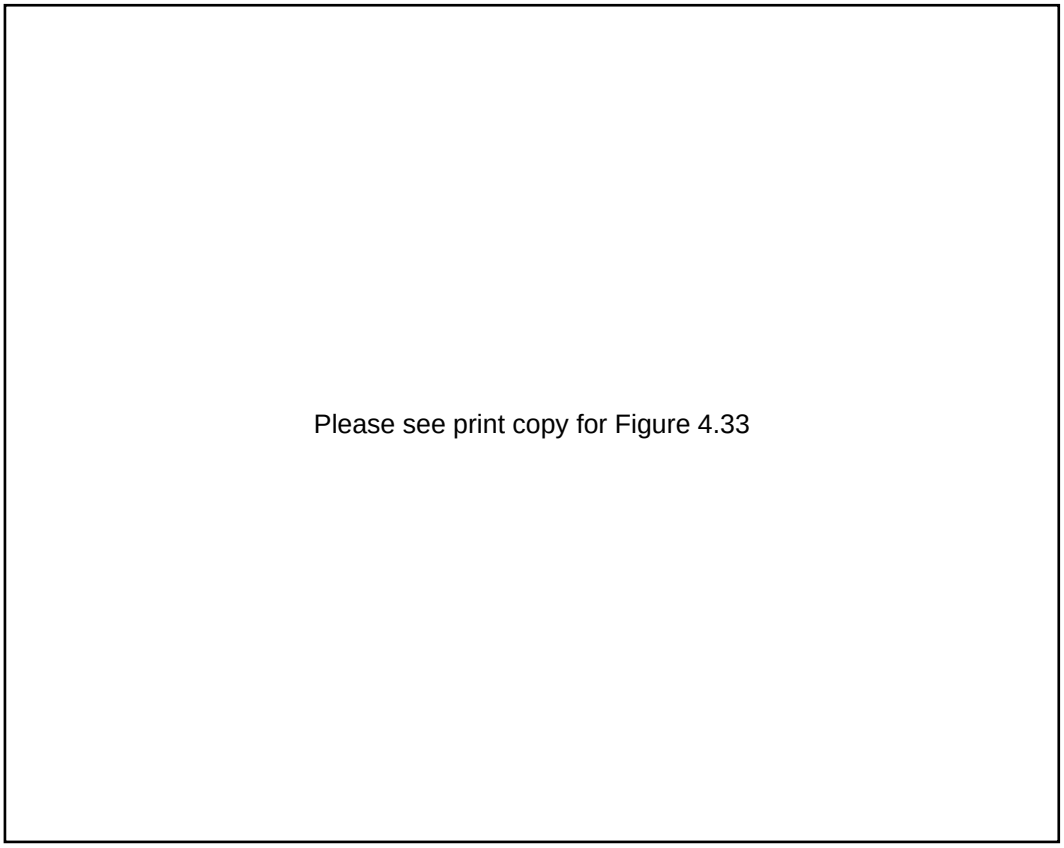

Figure 4-33: Backscatter electron image of the surface of steel L4 after annealing at 675 °C in 5% H_2 + 95% N_2 for 20 hours.

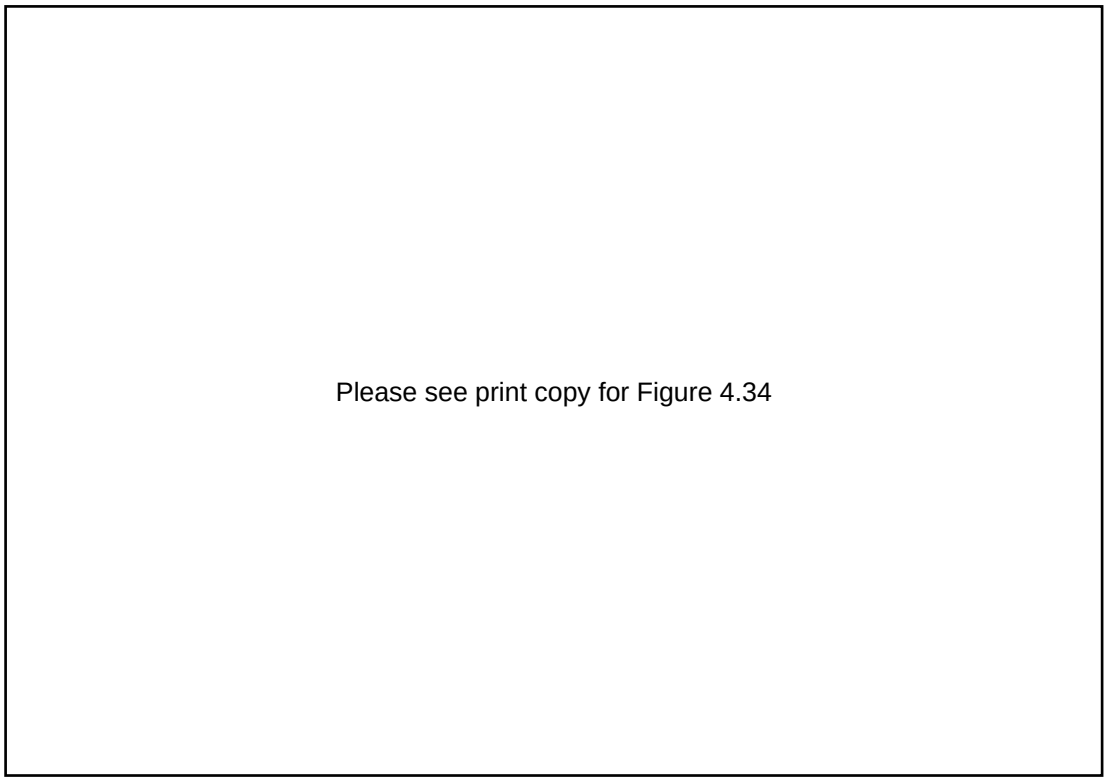

Figure 4-34: Backscatter electron image of the surface of steel L5 after annealing at 675 °C in 5% H_2 + 95% N_2 for 20 hours.

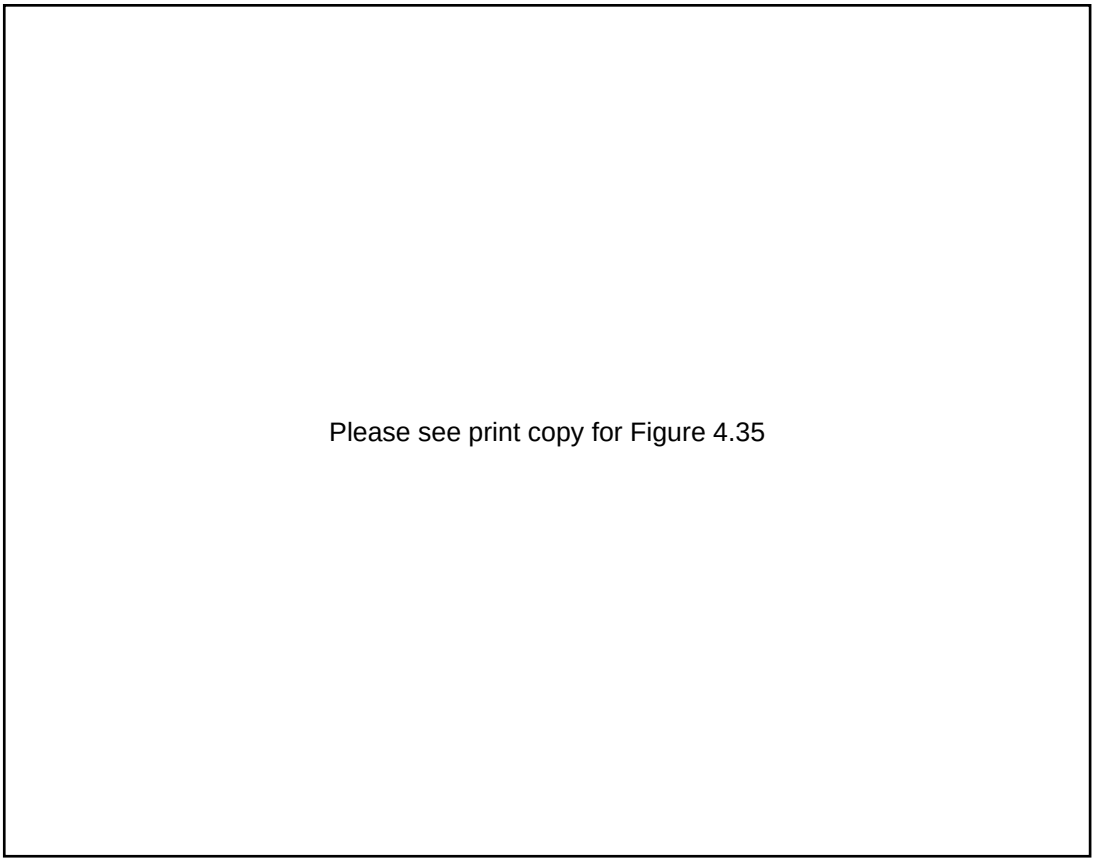

Figure 4-35: Backscatter electron image of the surface of steel L6 after annealing at 675 °C in 5% H_2 + 95% N_2 for 20 hours.

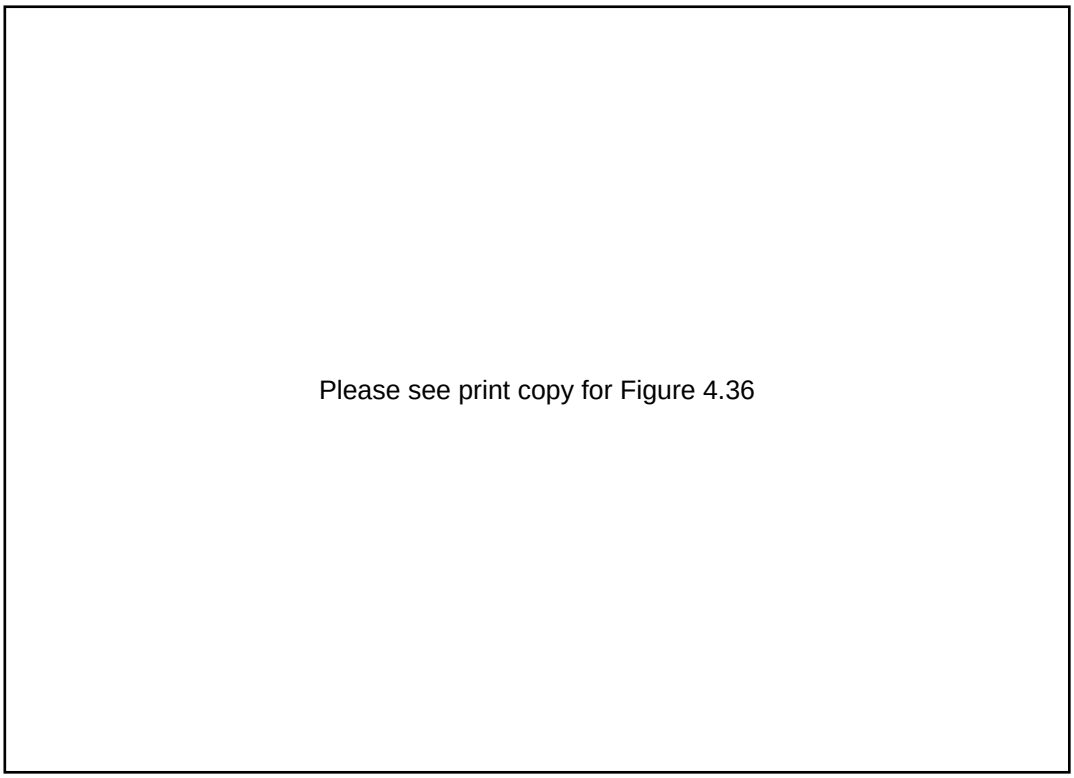

Figure 4-36: Backscatter electron image of the surface of steel L7 after annealing at 675 °C in 5% H_2 + 95% N_2 for 20 hours.

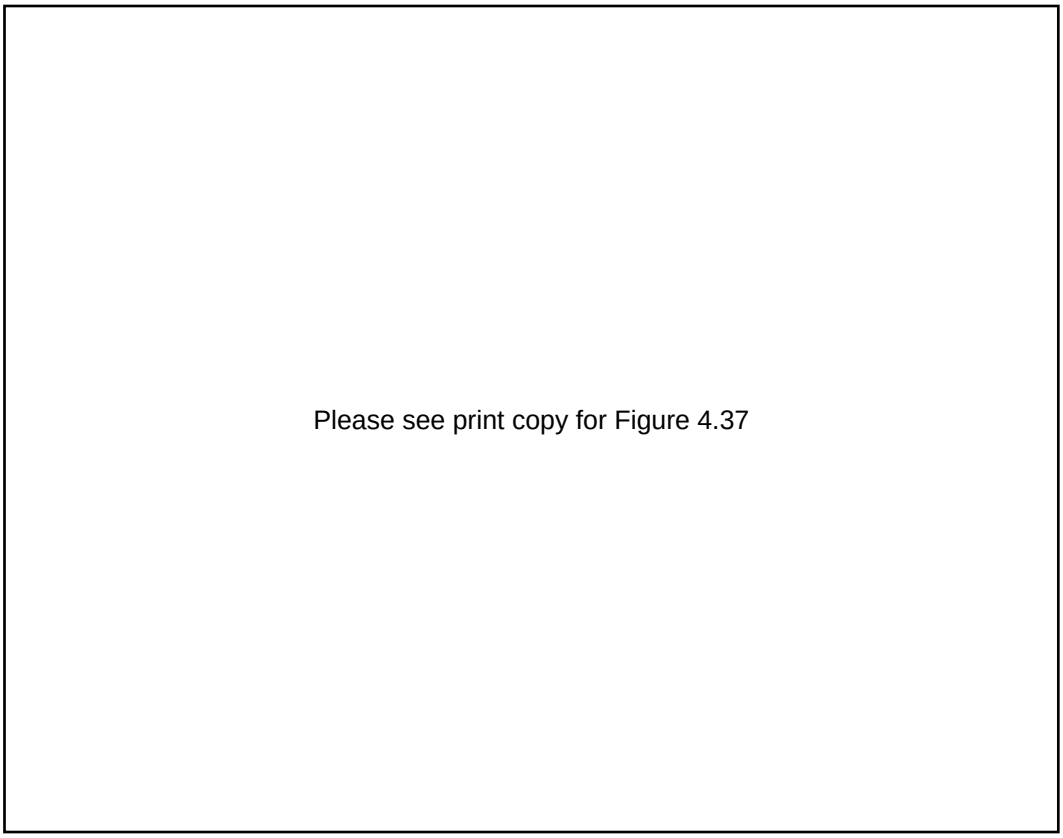

Figure 4-37: Backscatter electron image of the surface of steel L8 after annealing at 675 °C in 5% H_2 + 95% N_2 for 20 hours.

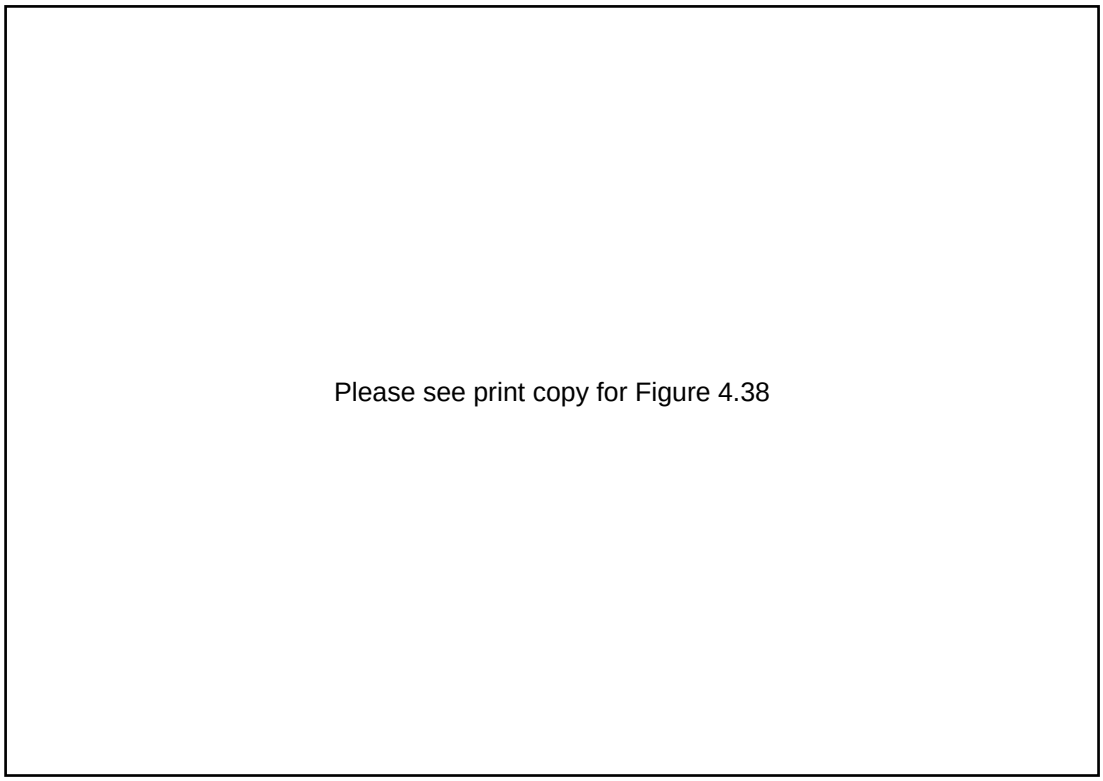

Figure 4-38: Backscatter electron image of the surface of steel L9 after annealing at 675 °C in 5% H_2 + 95% N_2 for 20 hours.

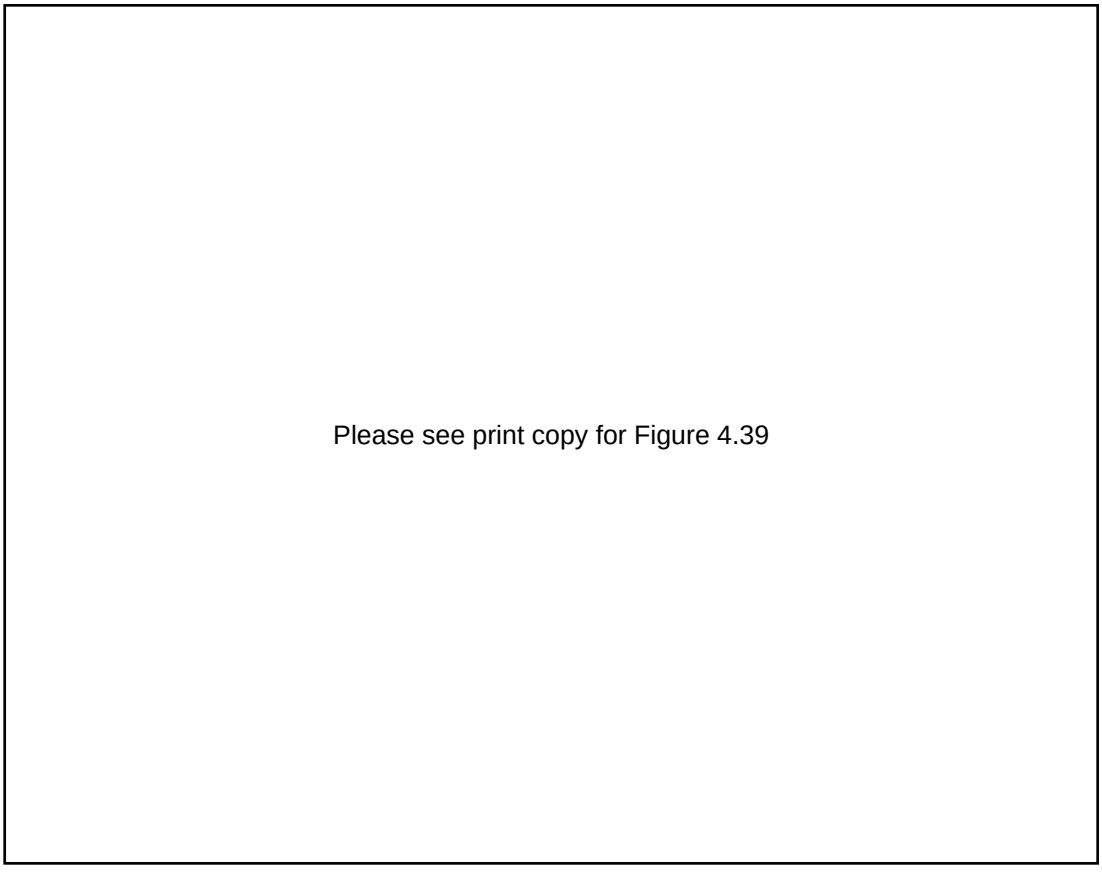

Figure 4-39: Backscatter electron image of the surface of steel L1 after annealing at 700 °C in 5% H_2 + 95% N_2 for 20 hours.

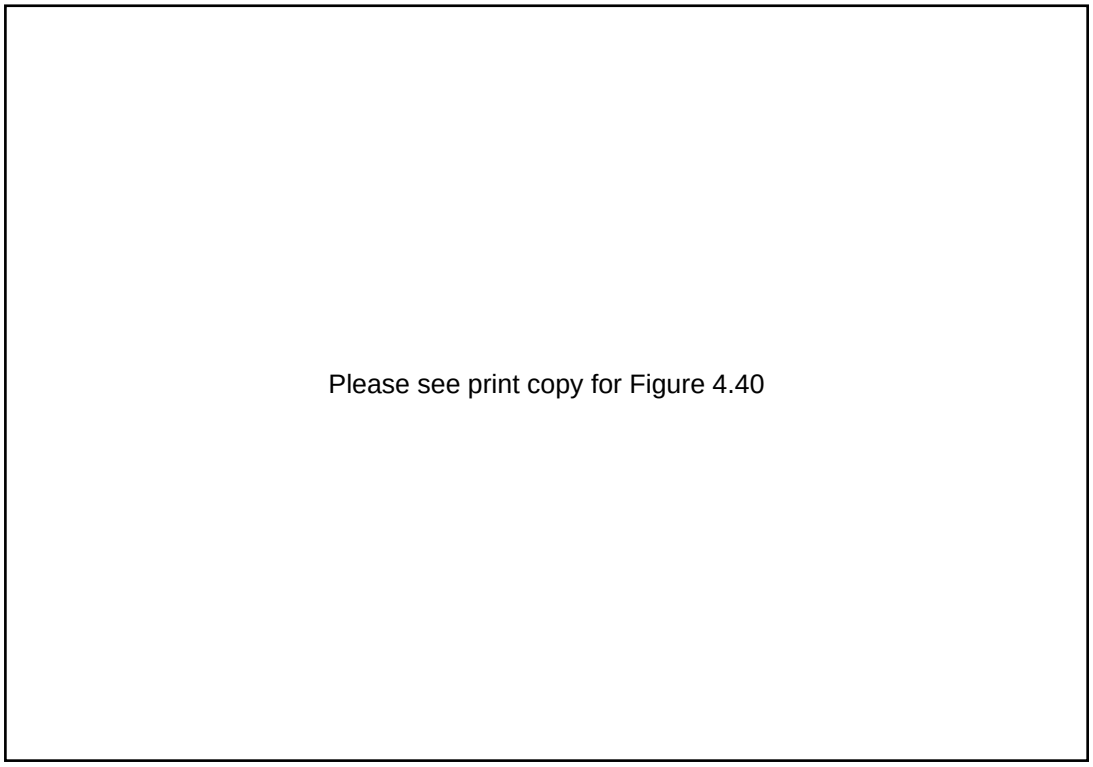

Figure 4-40: Backscatter electron image of the surface of steel L2 after annealing at 700 °C in 5% H_2 + 95% N_2 for 20 hours.

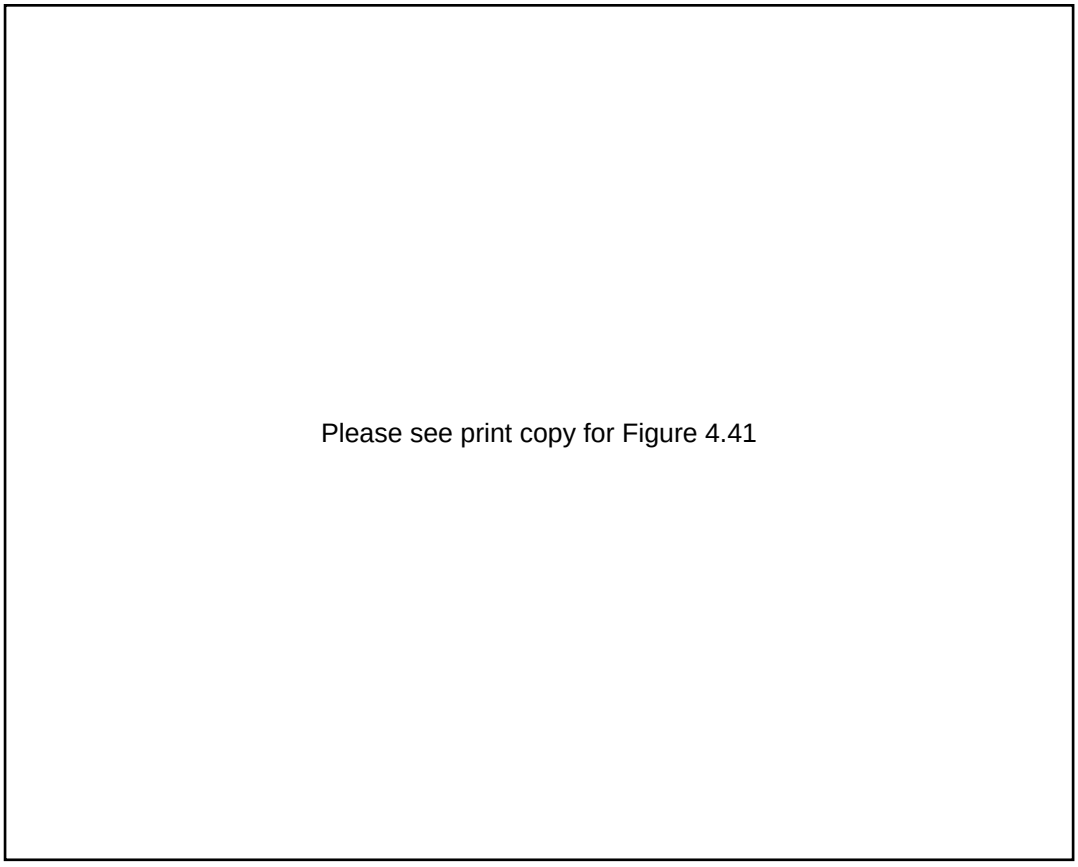

Figure 4-41: Backscatter electron image of the surface of steel L3 after annealing at 700 °C in 5% H_2 + 95% N_2 for 20 hours.

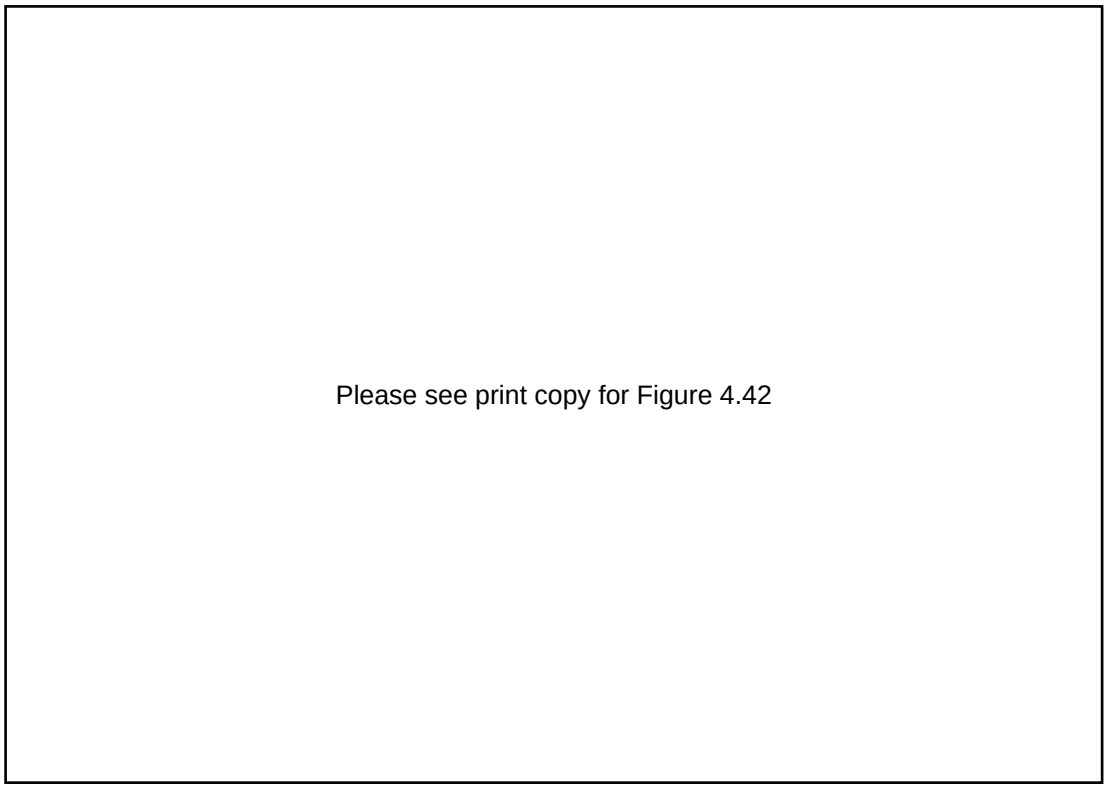

Figure 4-42: Backscatter electron image of the surface of steel L4 after annealing at 700 °C in 5% H_2 + 95% N_2 for 20 hours.

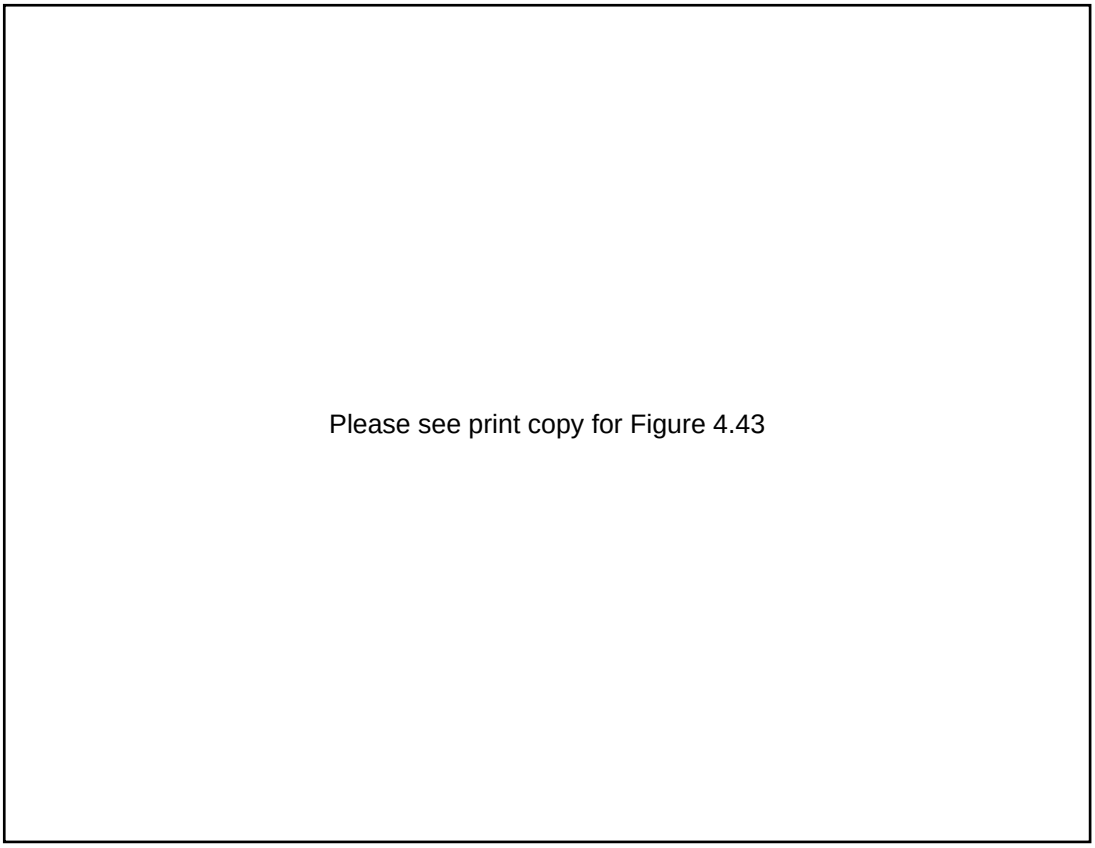

Figure 4-43: Backscatter electron image of the surface of steel L5 after annealing at 700 °C in 5% H_2 + 95% N_2 for 20 hours.

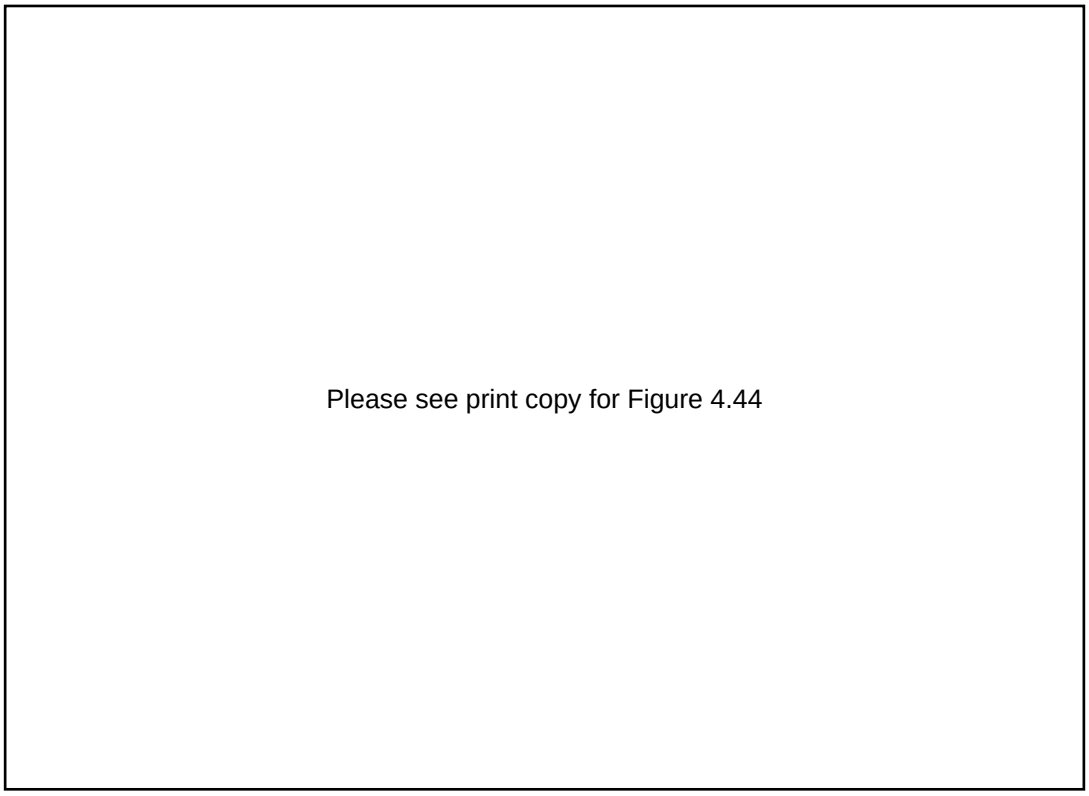

Figure 4-44: Backscatter electron image of the surface of steel L6 after annealing at 700 °C in 5% H_2 + 95% N_2 for 20 hours.

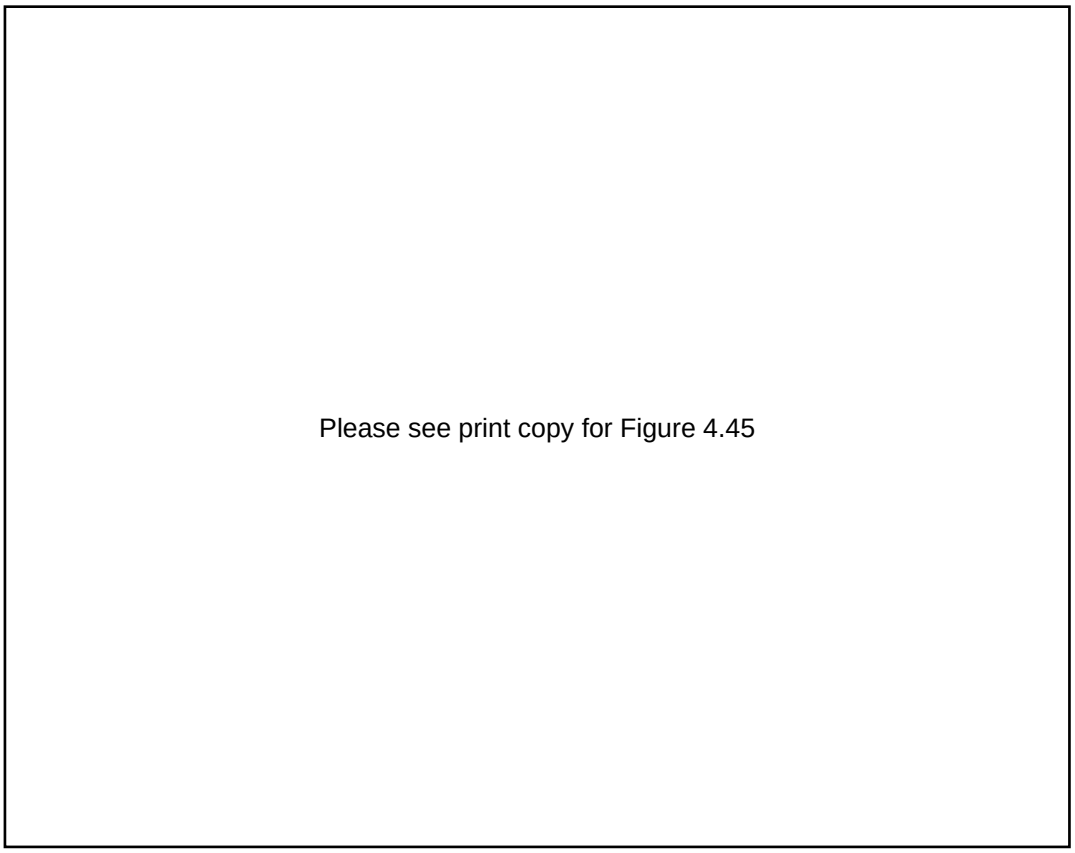

Figure 4-45: Backscatter electron image of the surface of steel L8 after annealing at 700 °C in 5% H_2 + 95% N_2 for 20 hours.

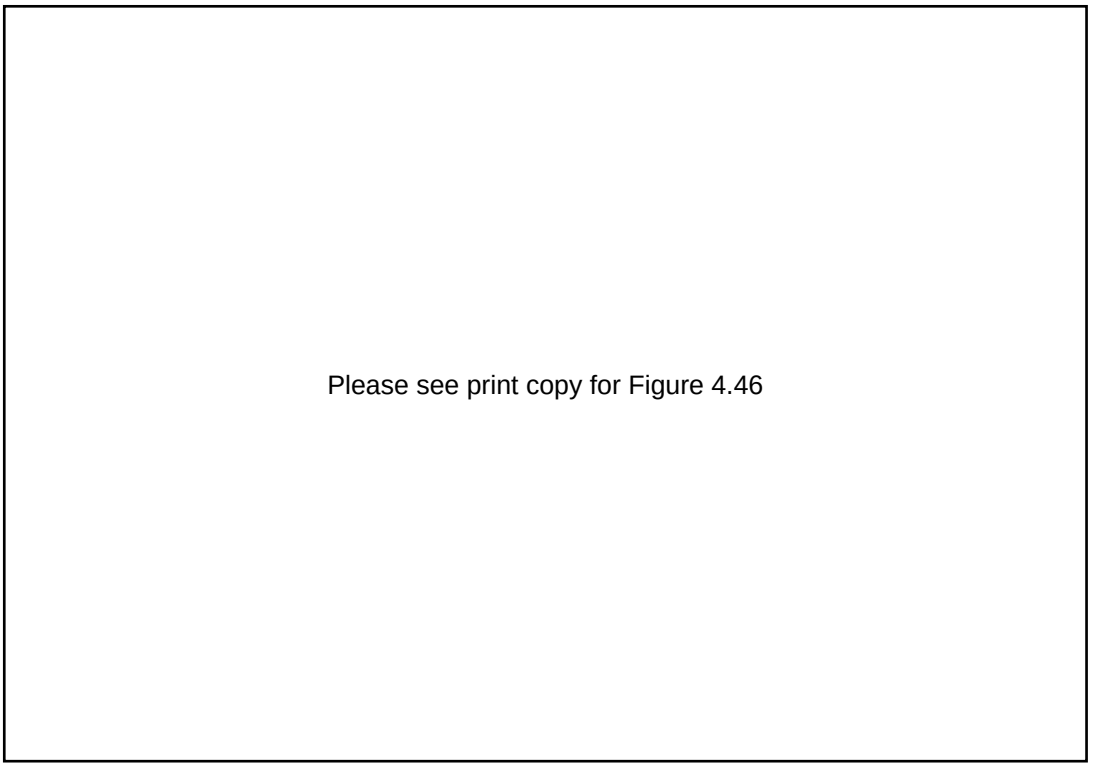

Figure 4-46: Backscatter electron image of the surface of steel L9 after annealing at 700 °C in 5% H_2 + 95% N_2 for 20 hours.

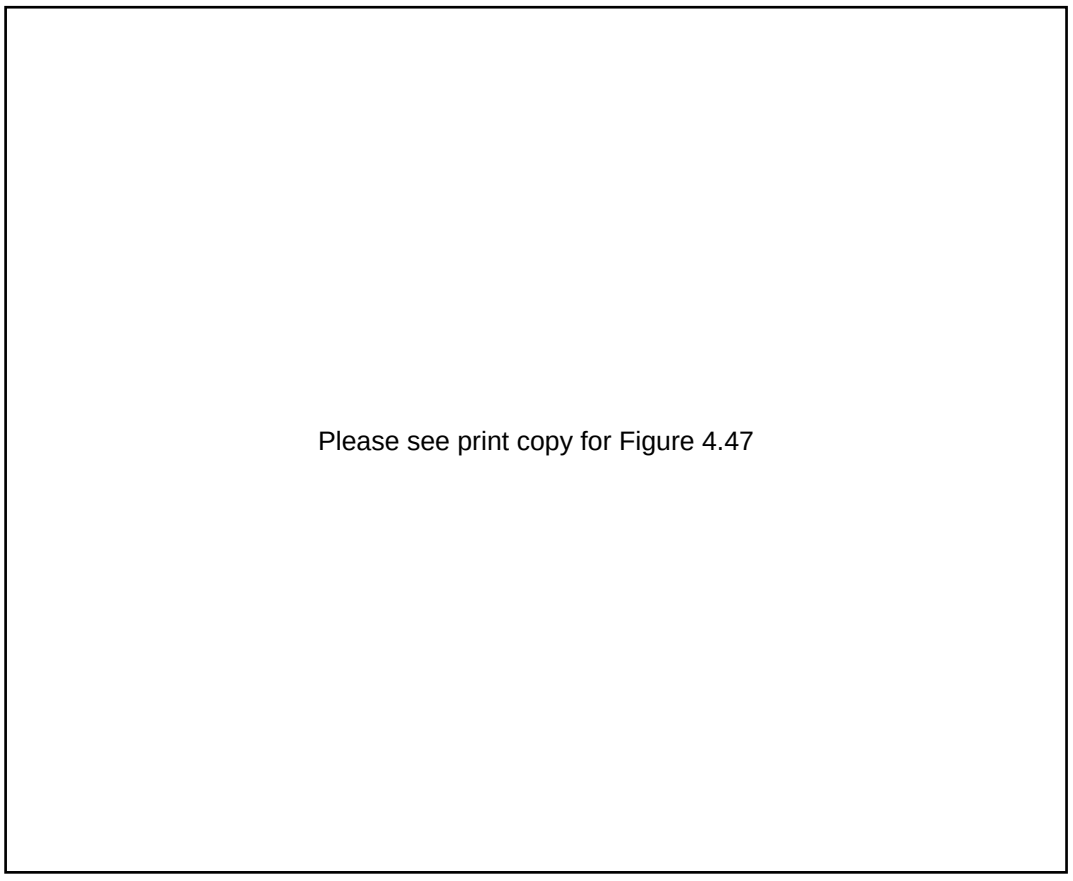

Figure 4-47: Backscatter electron image of the surface of steel L1 after annealing at 750 °C in 5% H_2 + 95% N_2 for 20 hours.

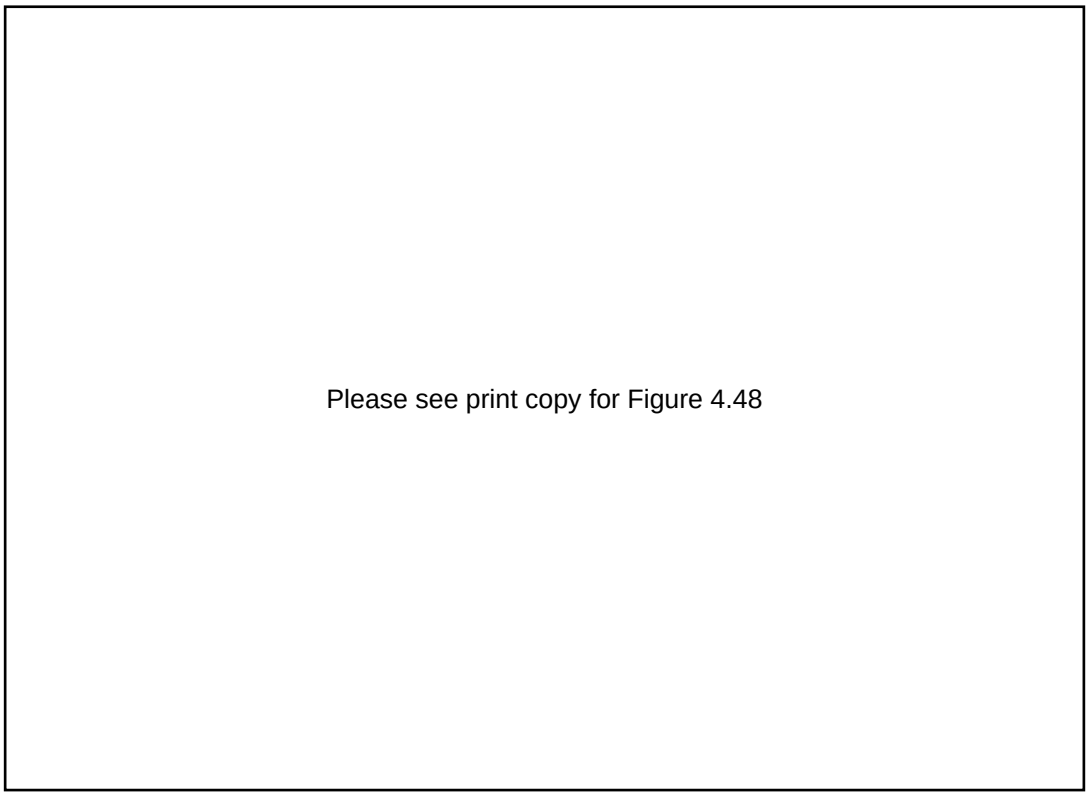

Figure 4-48: Backscatter electron image of the surface of steel L2 after annealing at 750 °C in 5% H_2 + 95% N_2 for 20 hours.

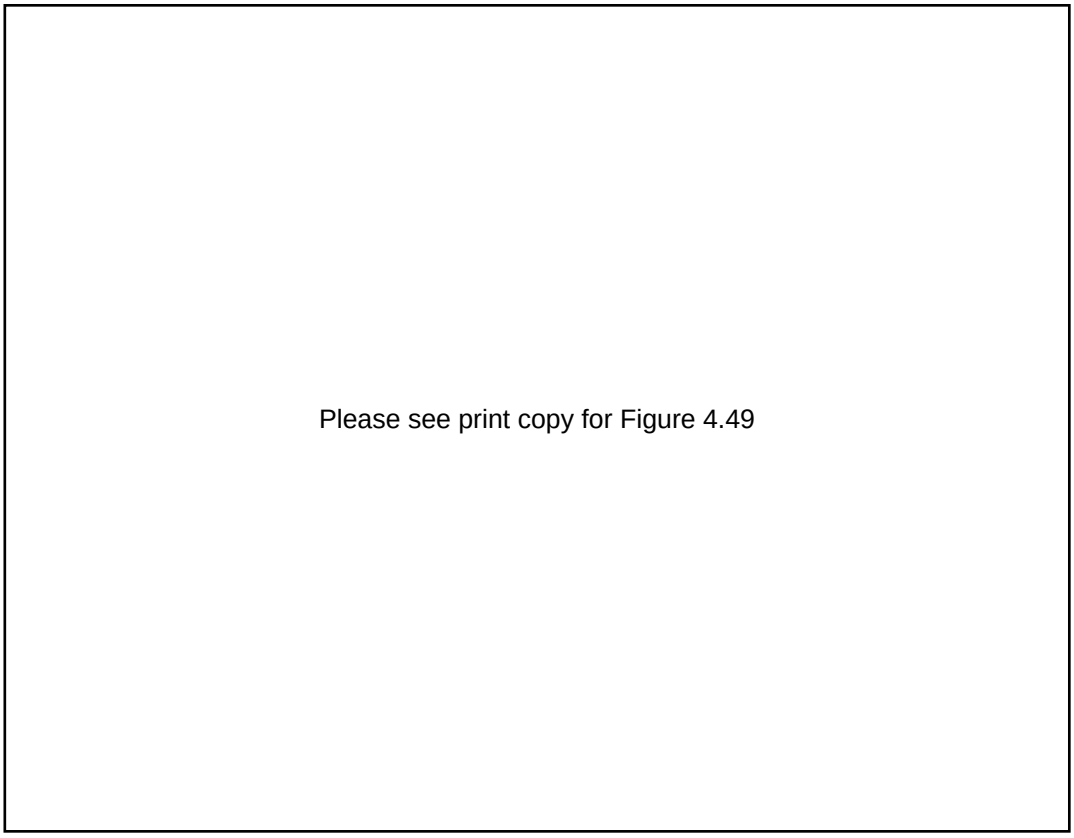

Figure 4-49: Backscatter electron image of the surface of steel L3 after annealing at 750 °C in 5% H_2 + 95% N_2 for 20 hours.

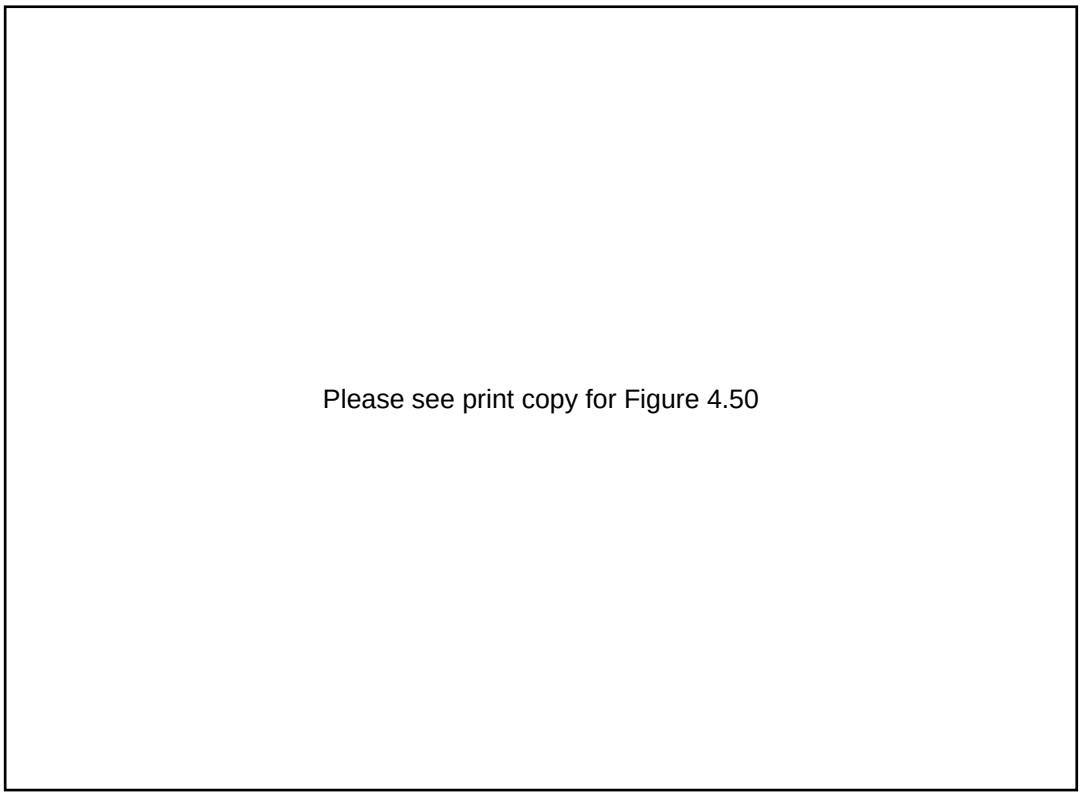

Figure 4-50: Backscatter electron image of the surface of steel L4 after annealing at 750 °C in 5% H_2 + 95% N_2 for 20 hours.

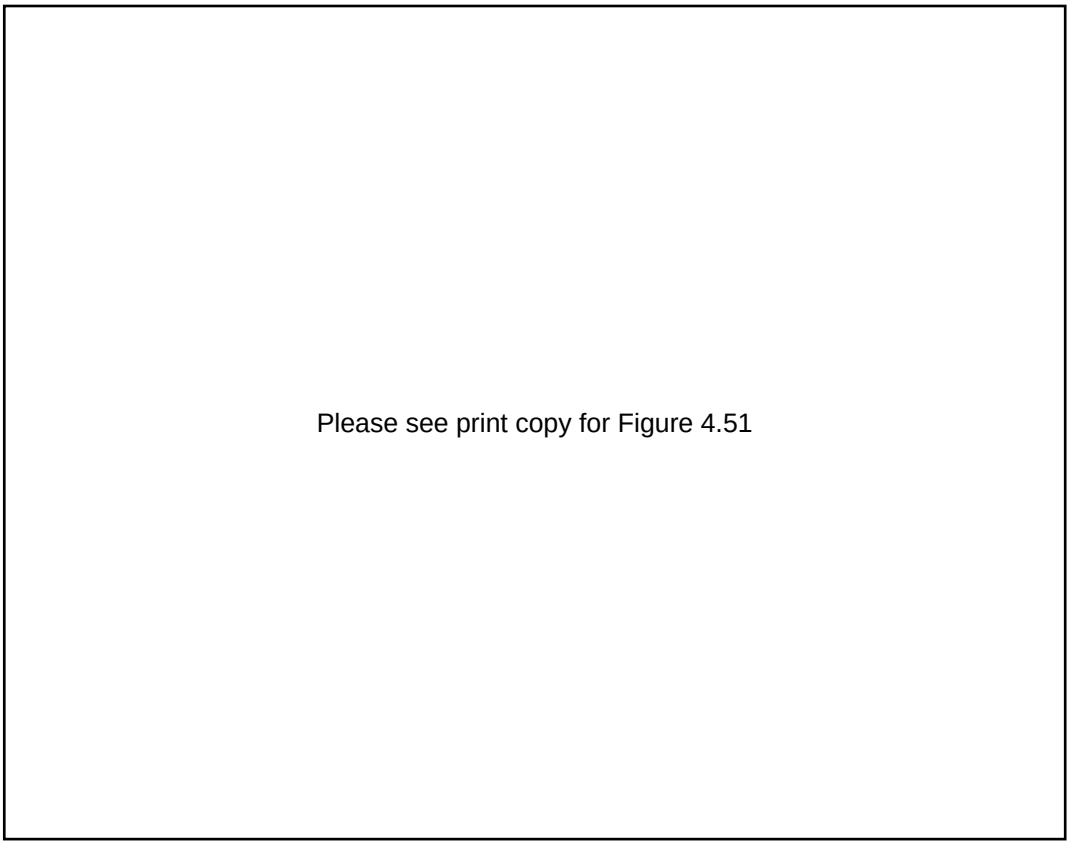

Figure 4-51: Backscatter electron image of the surface of steel L5 after annealing at 750 °C in 5% H_2 + 95% N_2 for 20 hours.

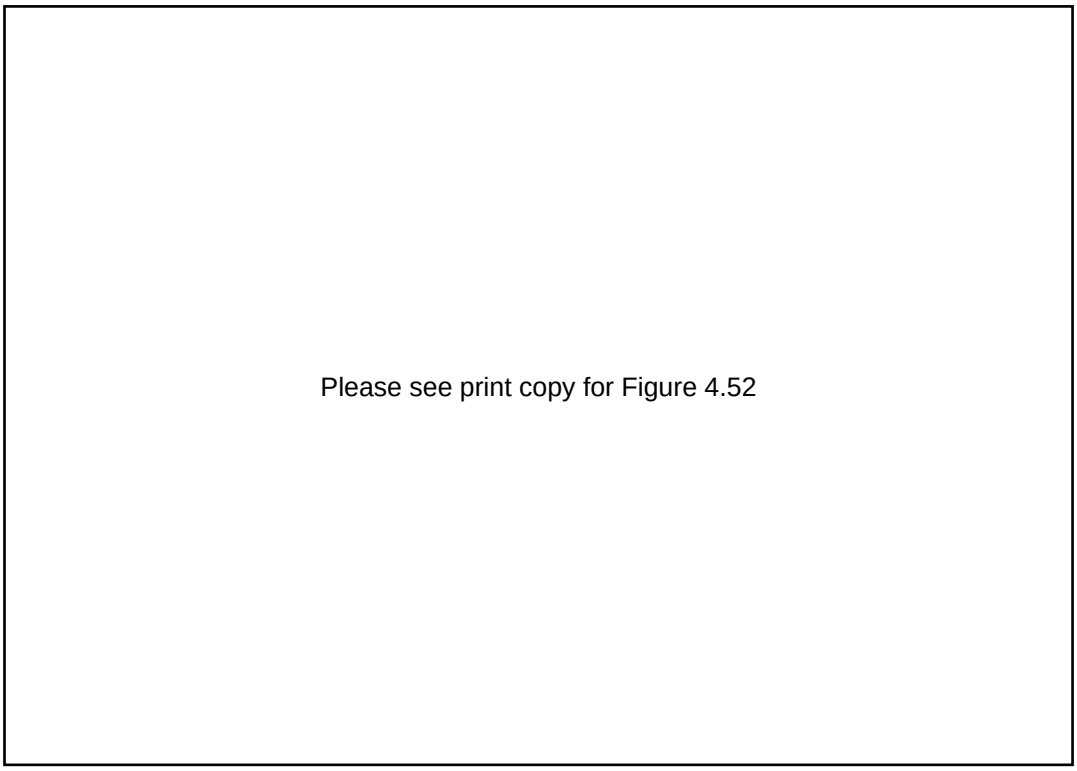

Figure 4-52: Backscatter electron image of the surface of steel L6 after annealing at 750 °C in 5% H_2 + 95% N_2 for 20 hours.

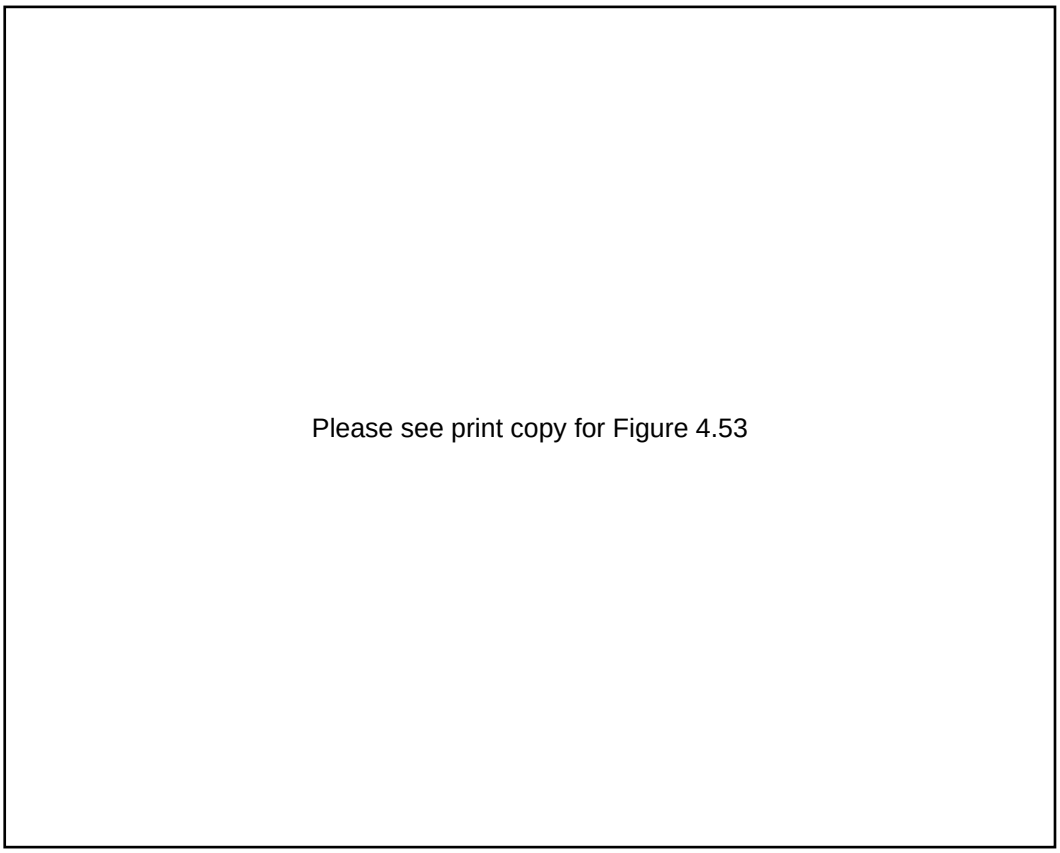

Figure 4-53: Backscatter electron image of the surface of steel L7 after annealing at 750 °C in 5% H_2 + 95% N_2 for 20 hours.

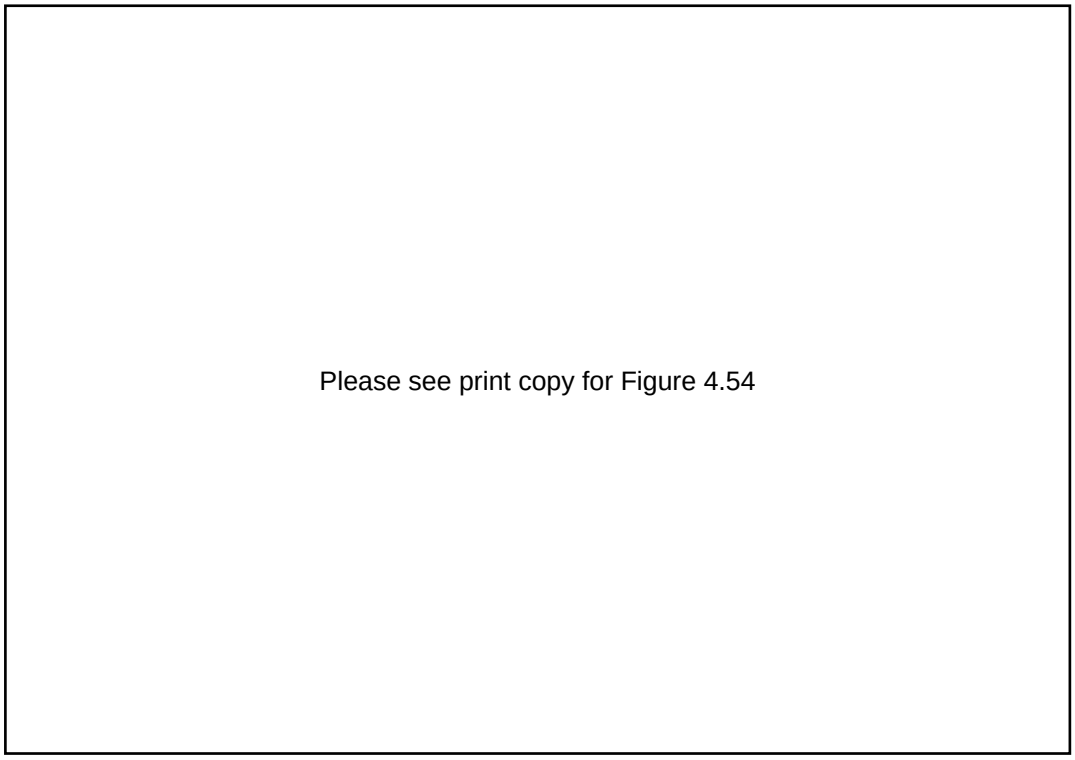

Figure 4-54: Backscatter electron image of the surface of steel L8 after annealing at 750 °C in 5% H_2 + 95% N_2 for 20 hours.

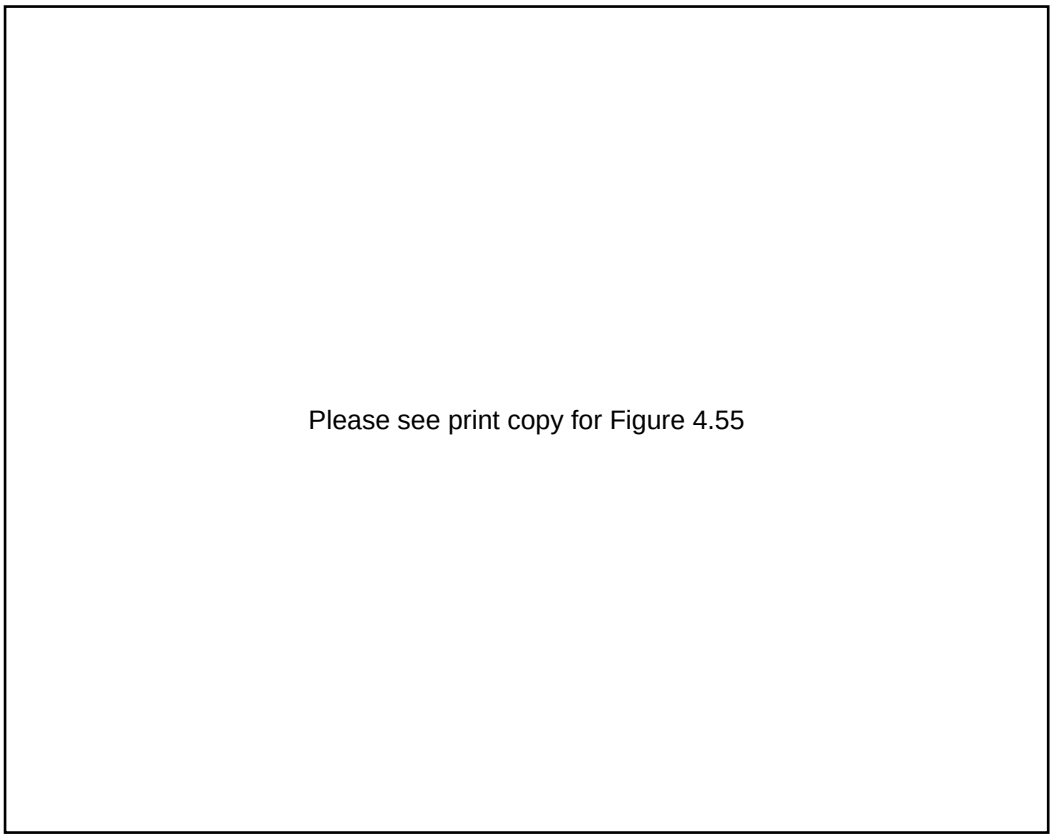

Figure 4-55: Backscatter electron image of the surface of steel L9 after annealing at 750 °C in 5% H_2 + 95% N_2 for 20 hours.

The SEM EDS specta from the grain boundary precipitates were consistent for the different annealing temperatures. A typical SEM EDS spectrum of these precipitates is given in Figure 4-56. Clearly the surface precipitates are (MnFe)O with fine $MnCr_2O_4$. The very high Fe Kα peak was predominantly due to the iron matrix.

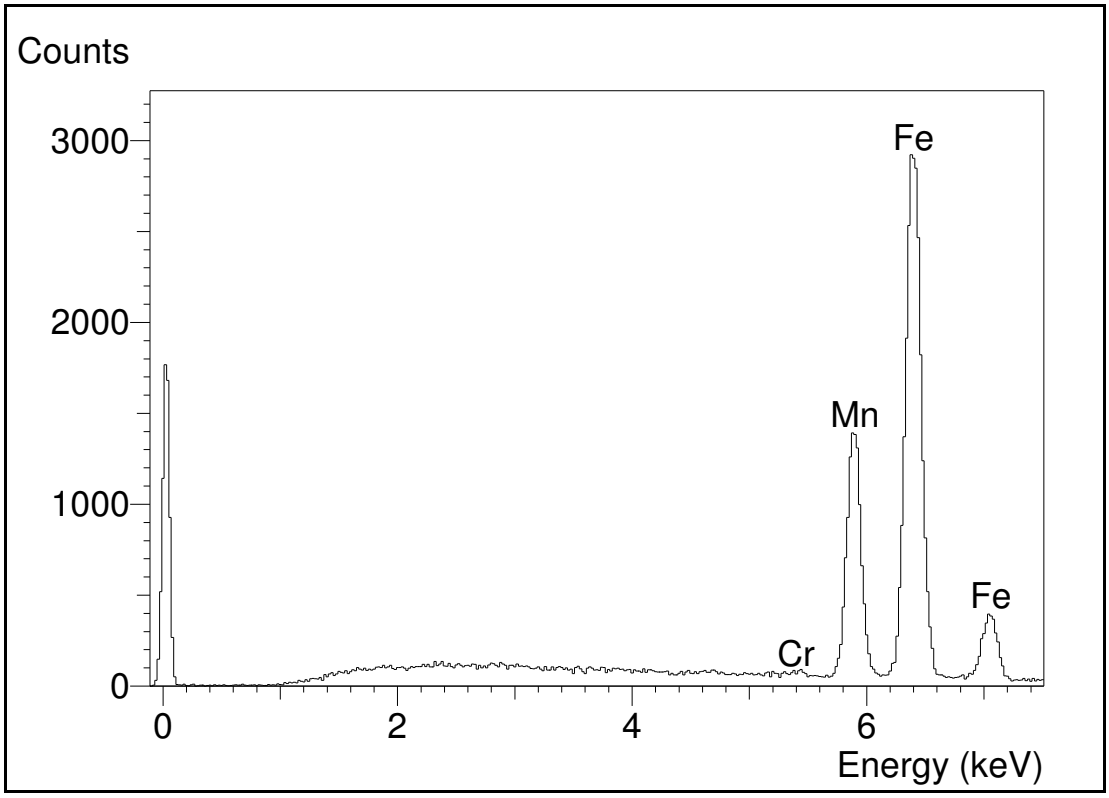

Figure 4-56: EDS of typical grain boundary precipitates observed by SEM.

The sizes of the precipitates observed by SEM were measured from the backscattered electron images using an image analyser. Table 4-3 shows the measured mean particle diameter and the percentage of the steel surface covered by the precipitates. The effect of annealing temperature and manganese level in the steel on the mean particle diameter of surface particles and the percentage of the surface covered by particles is shown graphically in Figure 4-57 and Figure 4-58 respectively.

At 675 °C all the steels had a similar mean oxide diameter except the steel with the highest manganese level (L8), which was greater than 200 nm larger. These steels also had the lowest percentage of the surface covered by oxides increasing from 0.8% for the lowest manganese level to 2.8% for the steel with the highest manganese level.

The steels annealed at 700 °C unexpectedly had a lower mean oxide diameter than the steels annealed at 675 °C. However the surface area covered by these precipitates was higher ranging from 1.5% for the lowest manganese level to 5.3% for the steel with the highest manganese level.

The steels annealed 750 °C showed similar mean oxide particle diameter's to that of the steels annealed at 675 °C. Again the surface area covered by these oxides is larger with the increasing temperature. The surface area covered ranges from 3.4% for the lowest manganese level to 7.9% for the steel with the highest manganese level.

The clear trend in these results is that increasing the annealing temperature or the manganese level in the steel will increase in the percentage of the surface covered by oxides.

Table 4-3: The mean particle diameter and percentage of the steel surface covered by particles for steels annealed in 5% H_2 + 95% N_2 atmosphere as observed by SEM.

Temperature (°C)	Steel	Mean Particle Diameter (nm)	Surface Area (%)
675	L1	799	0.8
	L2	909	1.6
	L3	983	0.9
	L4	957	1.3
	L5	945	1.7
	L6	1010	1.6
	L7	935	1.4
	L8	1270	2.8
	L9	910	1.3
700	L1	640	1.5
	L2	653	4.5
	L3	690	2.4
	L4	750	3.3
	L5	587	3.0
	L6	572	2.6
	L8	990	5.3
	L9	935	4.1
750	L1	998	3.8
	L2	893	3.9
	L3	1250	4.7
	L4	890	3.4
	L5	927	4.0
	L6	908	3.5
	L7	921	3.6
	L8	1114	7.9
	L9	1000	4.6

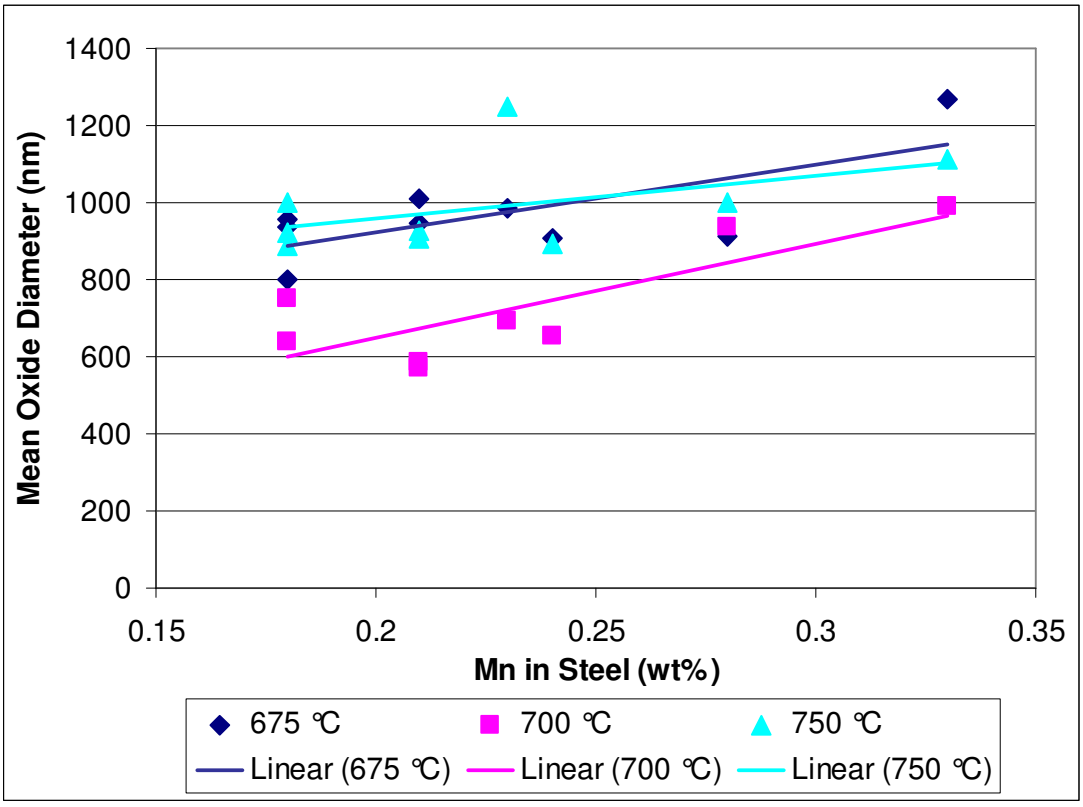

Figure 4-57: The effect of annealing temperature and manganese level in the steel on the mean particle diameter of surface particles formed during annealing in 5% H_2 + 95% N_2 atmosphere as observed by SEM.

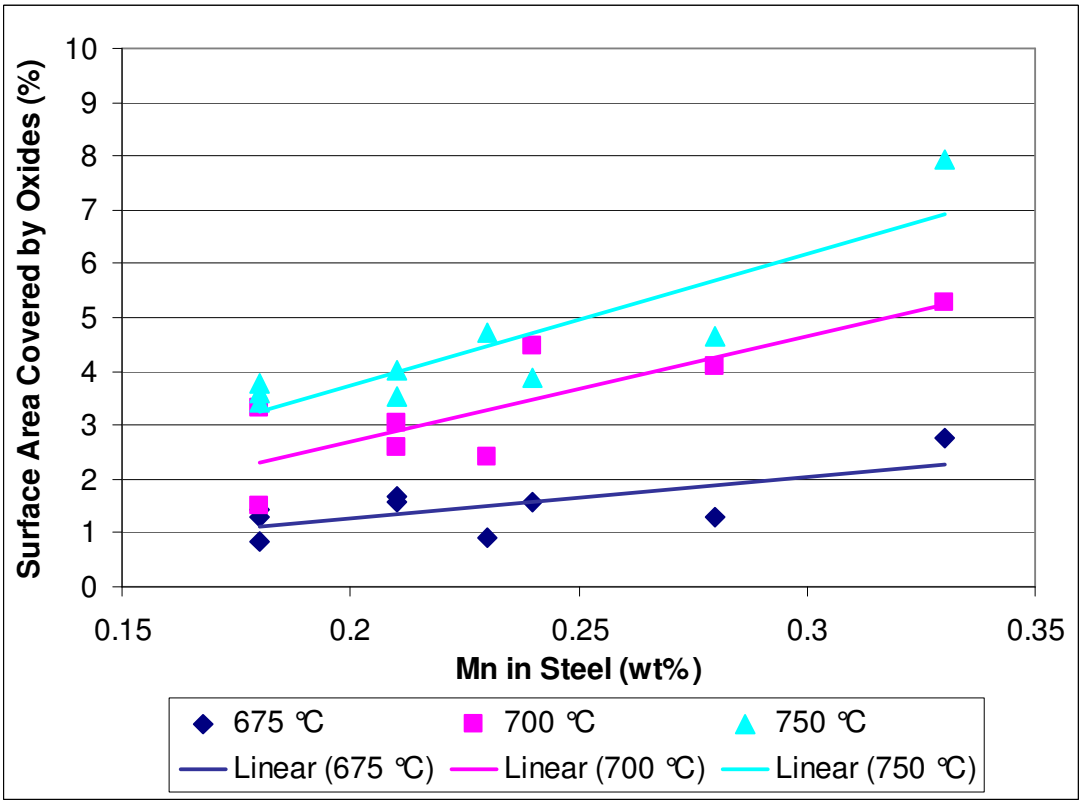

Figure 4-58: The effect of annealing temperature and manganese level in the steel on the percentage of the surface covered by surface particles formed during annealing in 5% H_2 + 95% N_2 atmosphere as observed by SEM.

4.5.2 TEM Characterisation

Carbon extraction replicas of the samples annealed at 650 °C in 5% H_2 + 95% N_2 atmosphere did not show any grain boundary oxide precipitates. Carbon extraction replicas of the samples annealed at 675 °C in 5% H_2 + 95% N_2 atmosphere showed grain boundary precipitates (Figure 4-59 to Figure 4-67).

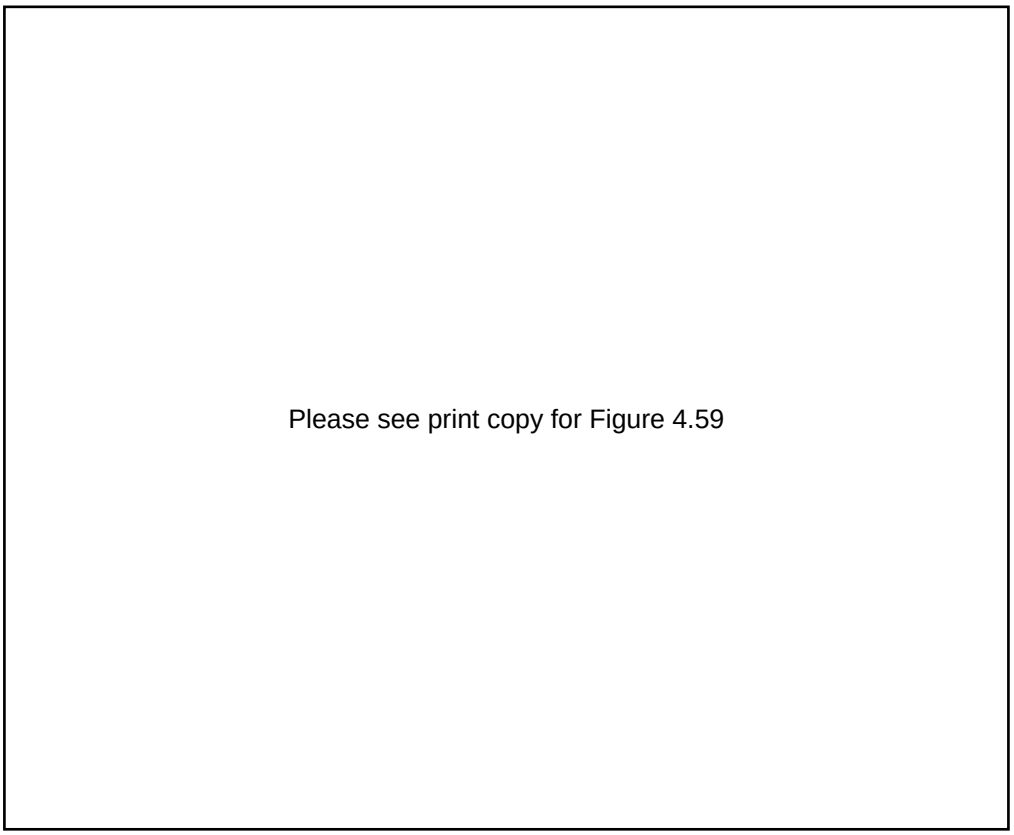

Figure 4-59: TEM image of carbon extraction replica made from steel L1 after annealing at 675 °C in 5% H_2 + 95% N_2 atmosphere for 20 hours and slight etching.

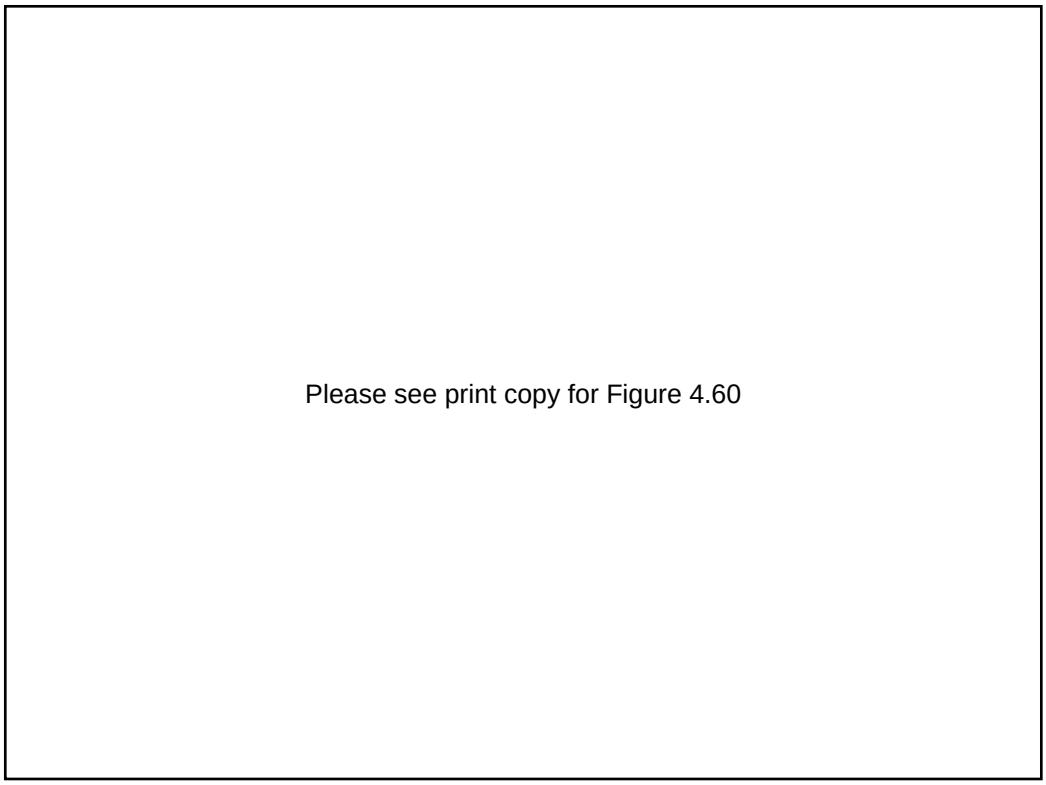

Figure 4-60: TEM image of carbon extraction replica made from steel L2 after annealing at 675 °C in 5% H_2 + 95% N_2 atmosphere for 20 hours and slight etching.

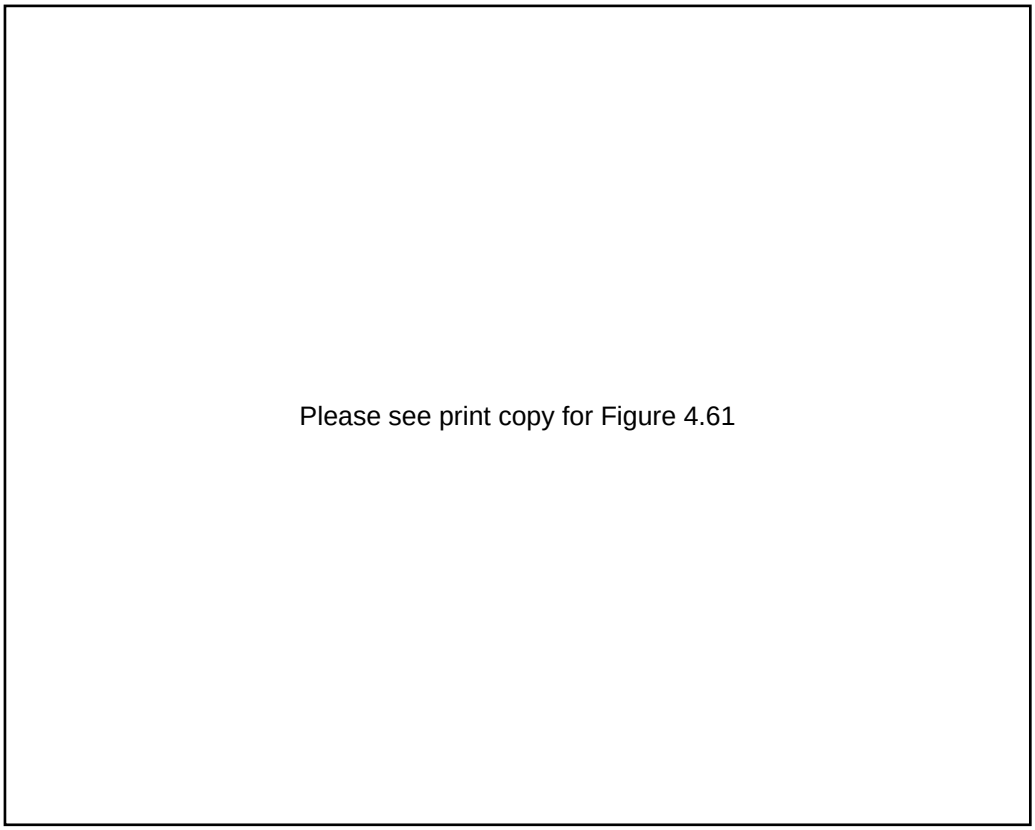

Figure 4-61: TEM image of carbon extraction replica made from steel L3 after annealing at 675 °C in 5% H_2 + 95% N_2 atmosphere for 20 hours and slight etching.

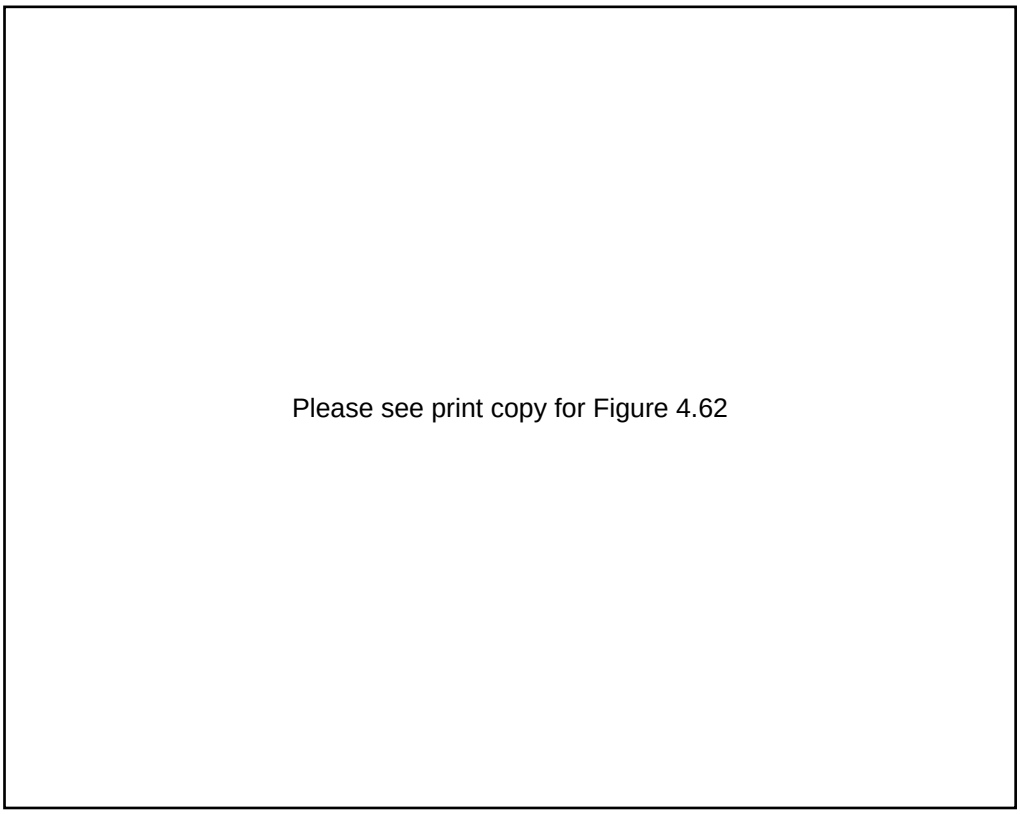

Figure 4-62: TEM image of carbon extraction replica made from steel L4 after annealing at 675 °C in 5% H_2 + 95% N_2 atmosphere for 20 hours and slight etching.

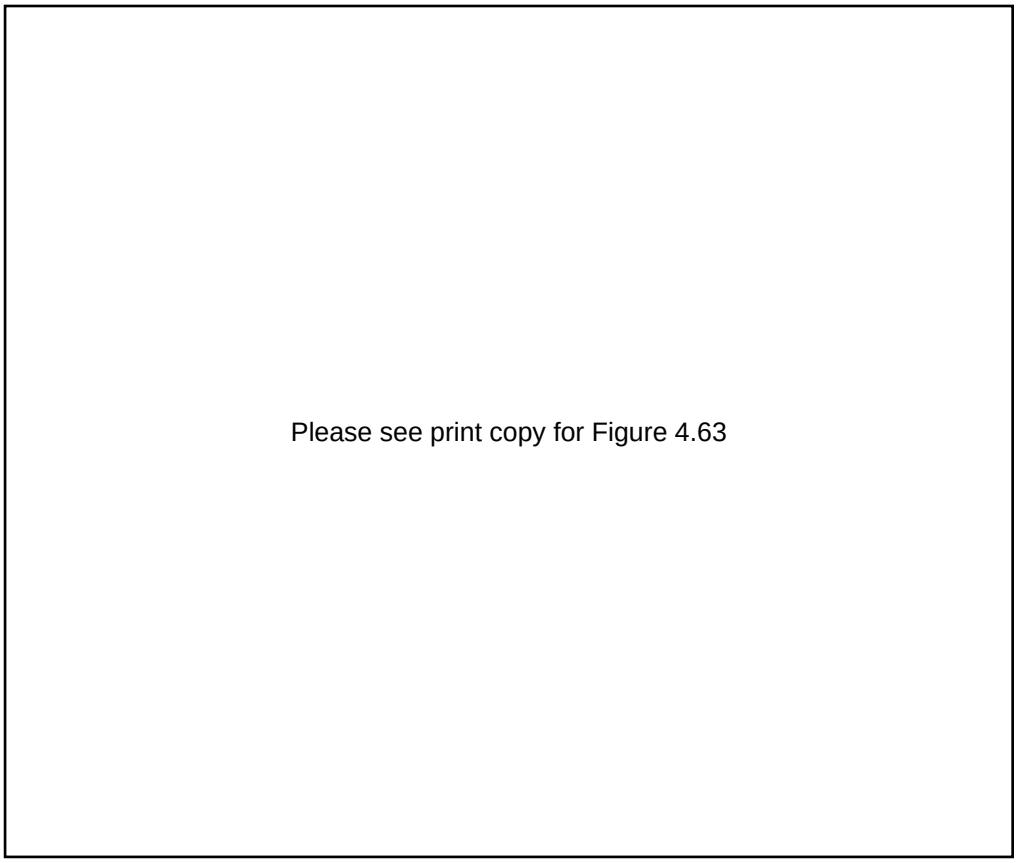

Figure 4-63: TEM image of carbon extraction replica made from steel L5 after annealing at 675 °C in 5% H_2 + 95% N_2 atmosphere for 20 hours and slight etching.

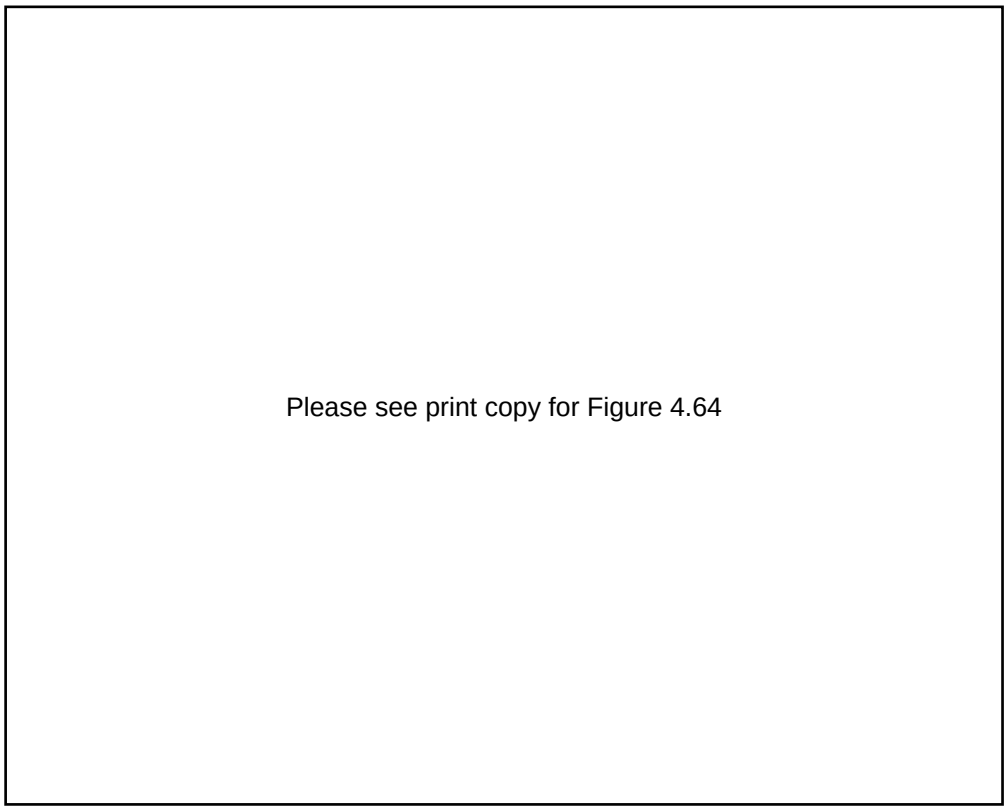

Figure 4-64: TEM image of carbon extraction replica made from steel L6 after annealing at 675 °C in 5% H_2 + 95% N_2 atmosphere for 20 hours and slight etching.

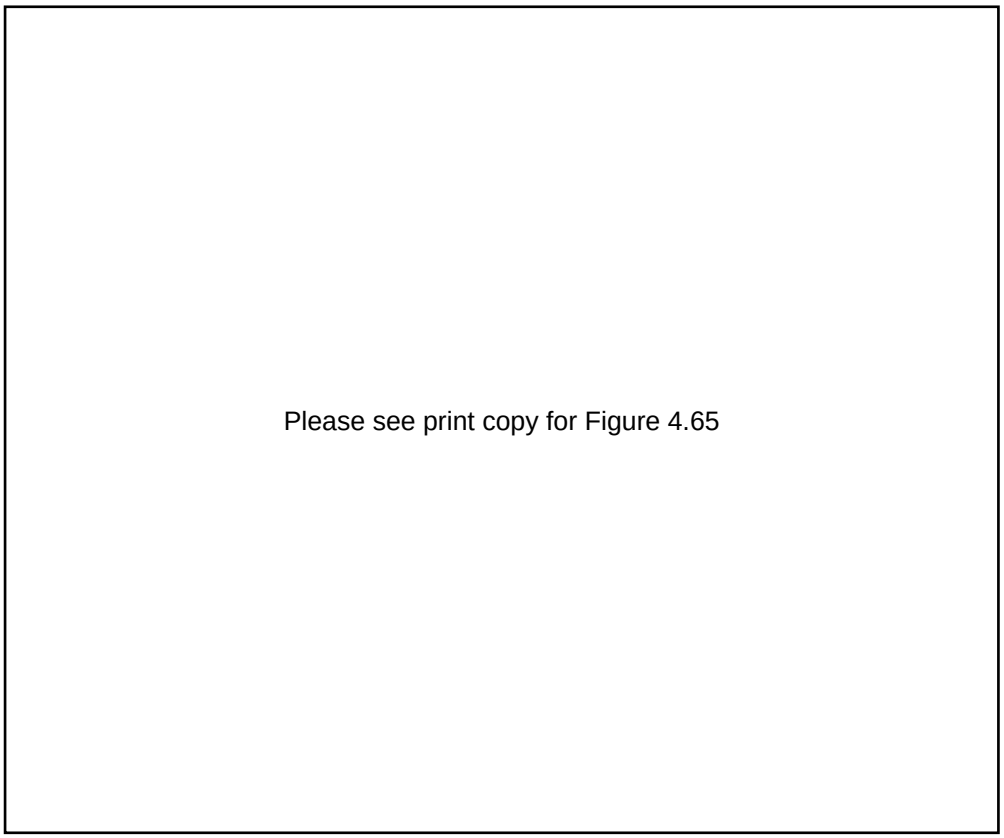

Figure 4-65: TEM image of carbon extraction replica made from steel L7 after annealing at 675 °C in 5% H_2 + 95% N_2 atmosphere for 20 hours and slight etching.

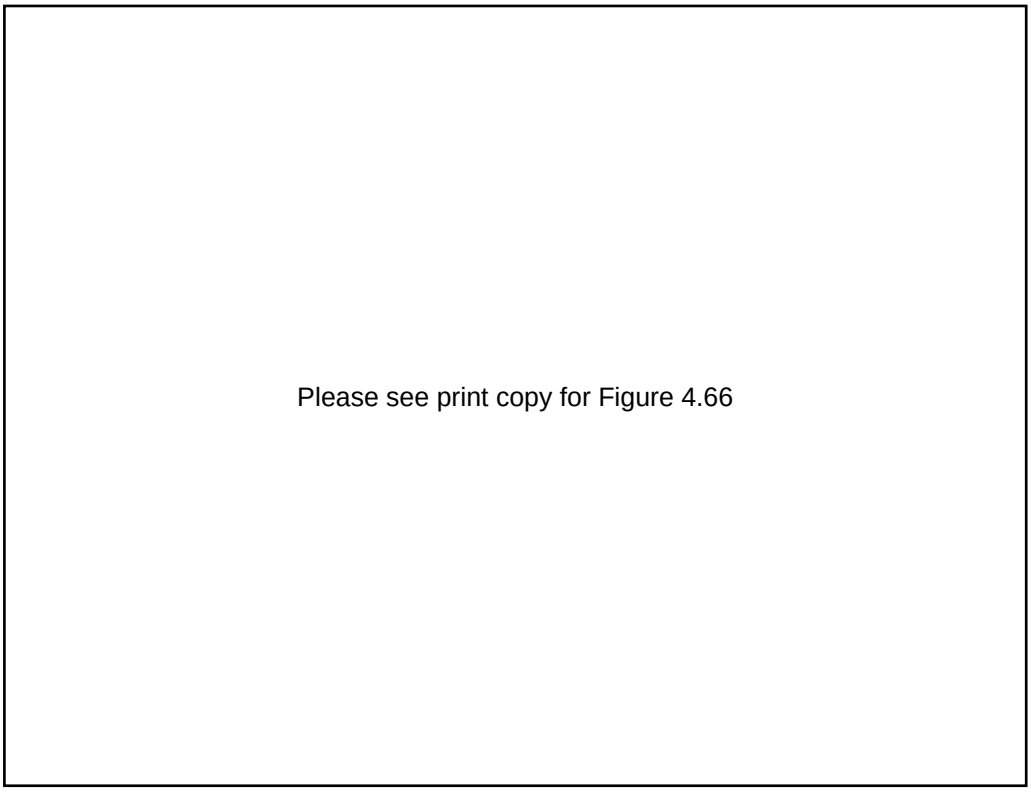

Figure 4-66: TEM image of carbon extraction replica made from steel L8 after annealing at 675 °C in 5% H_2 + 95% N_2 atmosphere for 20 hours and slight etching.

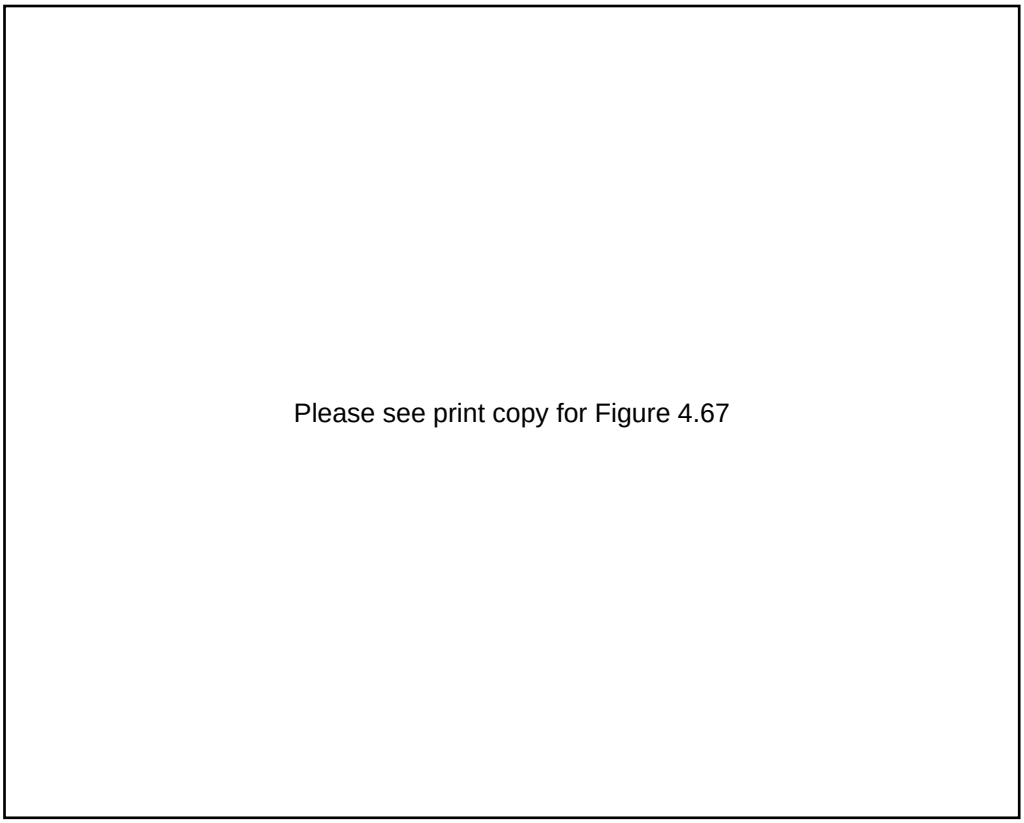

Figure 4-67: TEM image of carbon extraction replica made from steel L9 after annealing at 675 °C in 5% H_2 + 95% N_2 atmosphere for 20 hours and slight etching.

Figure 4-68 shows a typical TEM EDS spectrum of the steels annealed at 675 °C. Comprehensive TEM EDS of the grain boundary precipitates extracted from the steel annealed at 675 °C indicate that the grain boundary precipitates were $MnCr_2O_4$.

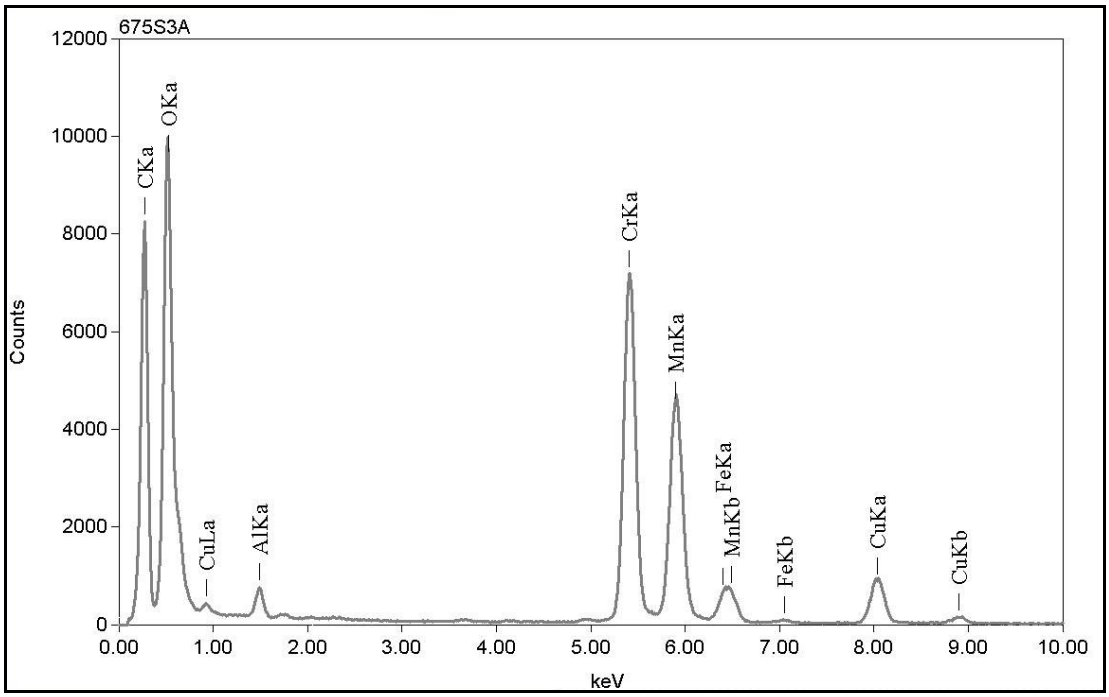

Figure 4-68: TEM EDS of typical particle extracted from surface of steel L3 annealed at 675 °C in 5% H_2 + 95% N_2 atmosphere for 20 hours.

The particle sizes of grain boundary $MnCr_2O_4$ spinel precipitates were measured from the TEM images of carbon extraction replicas using an image analyser. The particle size distribution of the steels annealed at 675 °C is shown in Figure 4-69. Most of the precipitates have a diameter of less than 100 nm. However, the steels with the higher chromium concentrations have a larger percentage of particles greater than 100 nm.

Figure 4-70 to Figure 4-77 show TEM images of carbon extraction replicas from steels annealed at 700 °C in 5% H_2 + 95% N_2 atmosphere.

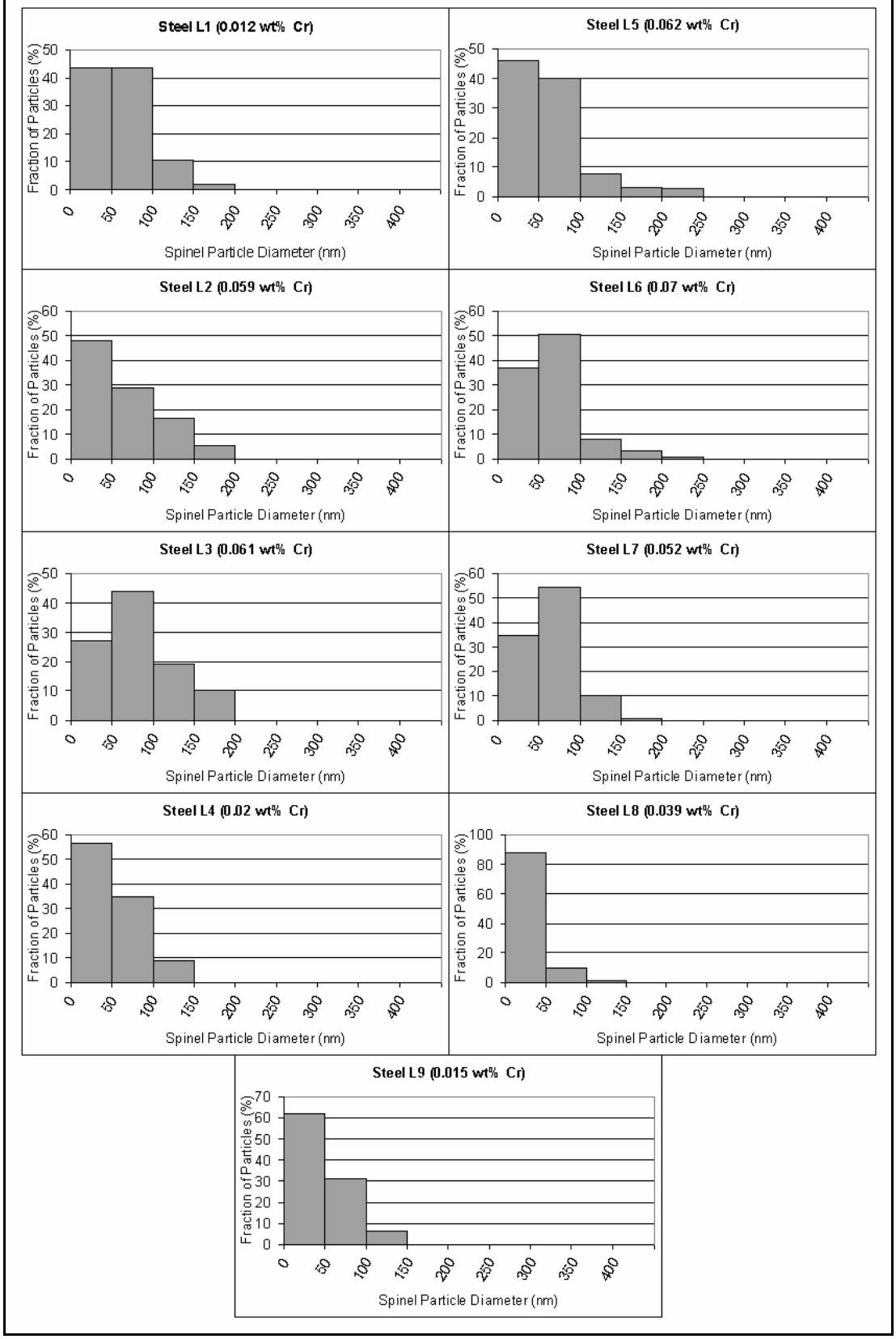

Figure 4-69: Particle size distribution of $MnCr_2O_4$ precipitates extracted from the surface of steels annealed at 675 °C in a 5% H_2 + 95% N_2 atmosphere.

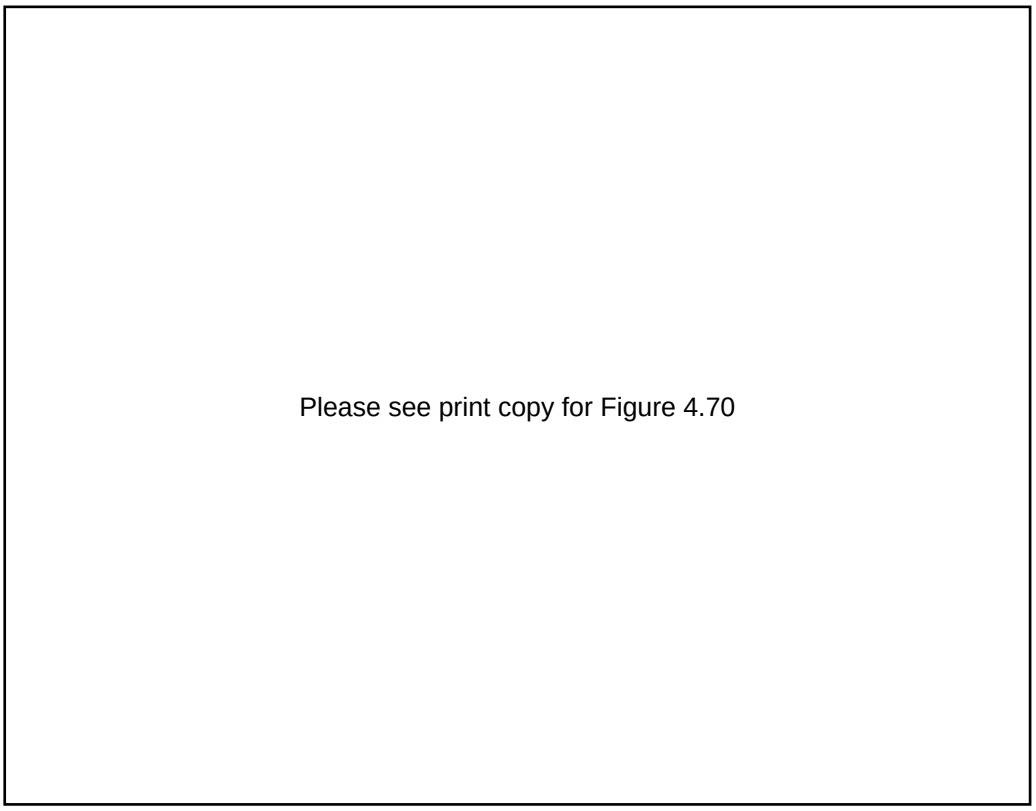

Figure 4-70: TEM image of carbon extraction replica made from steel L1 after annealing at 700 °C in 5% H_2 + 95% N_2 atmosphere for 20 hours and slight etching.

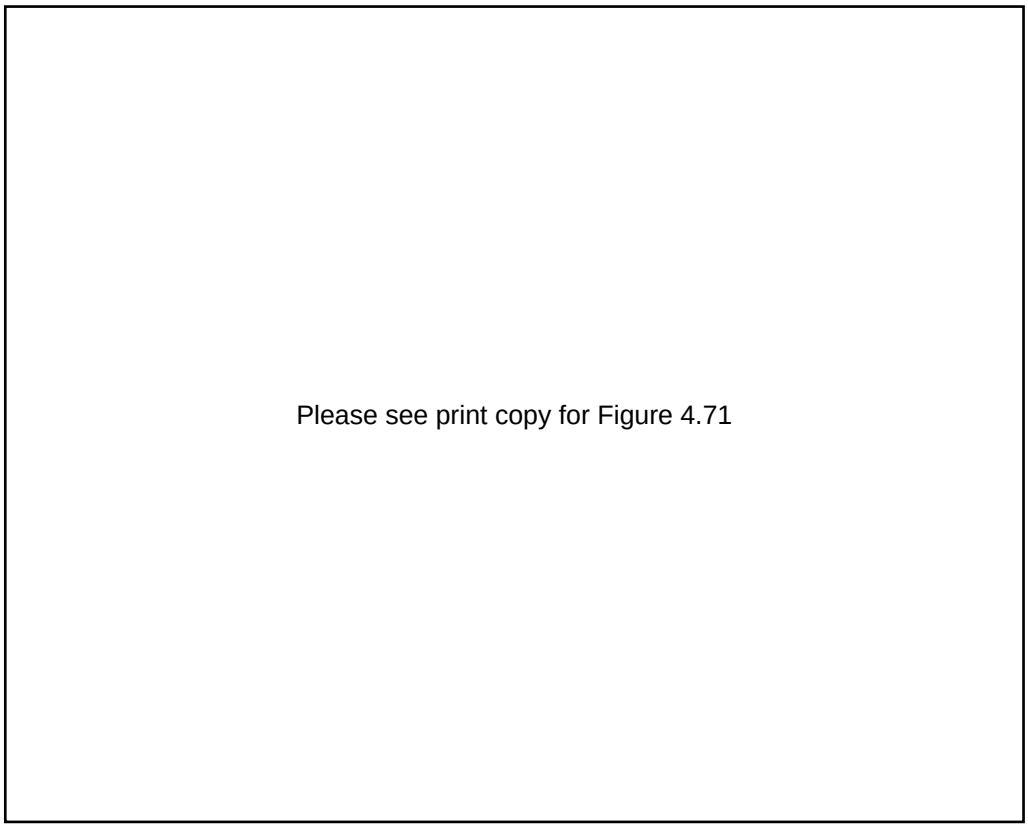

Figure 4-71: TEM image of carbon extraction replica made from steel L2 after annealing at 700 °C in 5% H_2 + 95% N_2 atmosphere for 20 hours and slight etching.

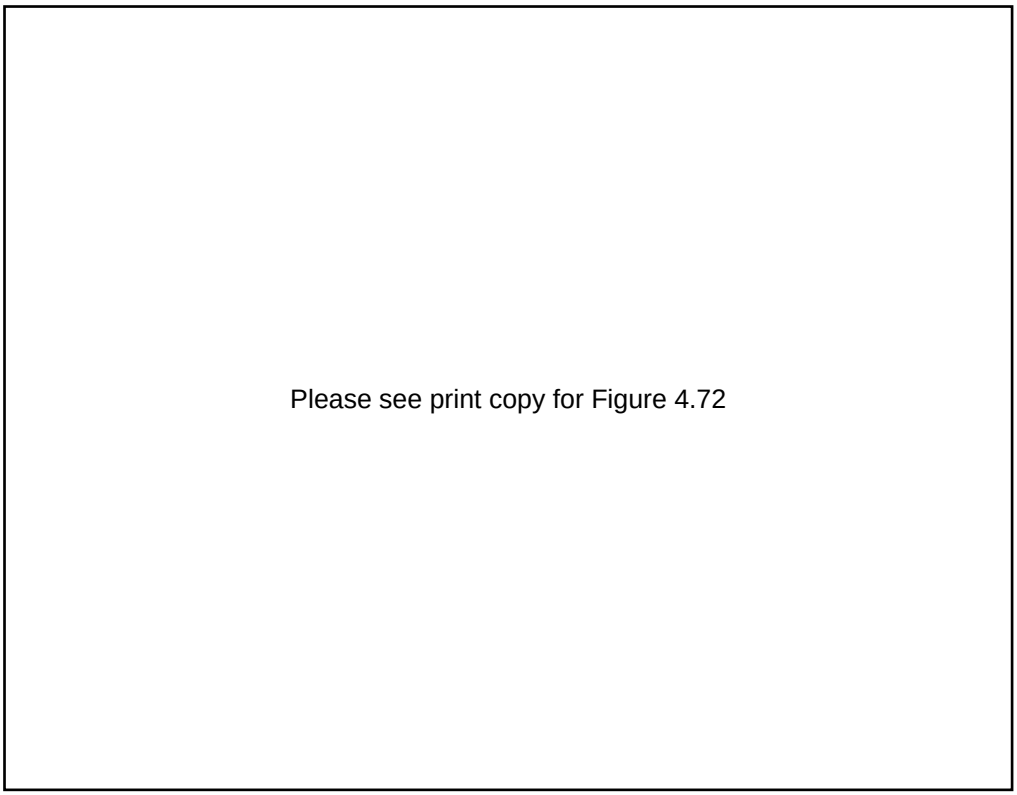

Figure 4-72: TEM image of carbon extraction replica made from steel L3 after annealing at 700 °C in 5% H_2 + 95% N_2 atmosphere for 20 hours and slight etching.

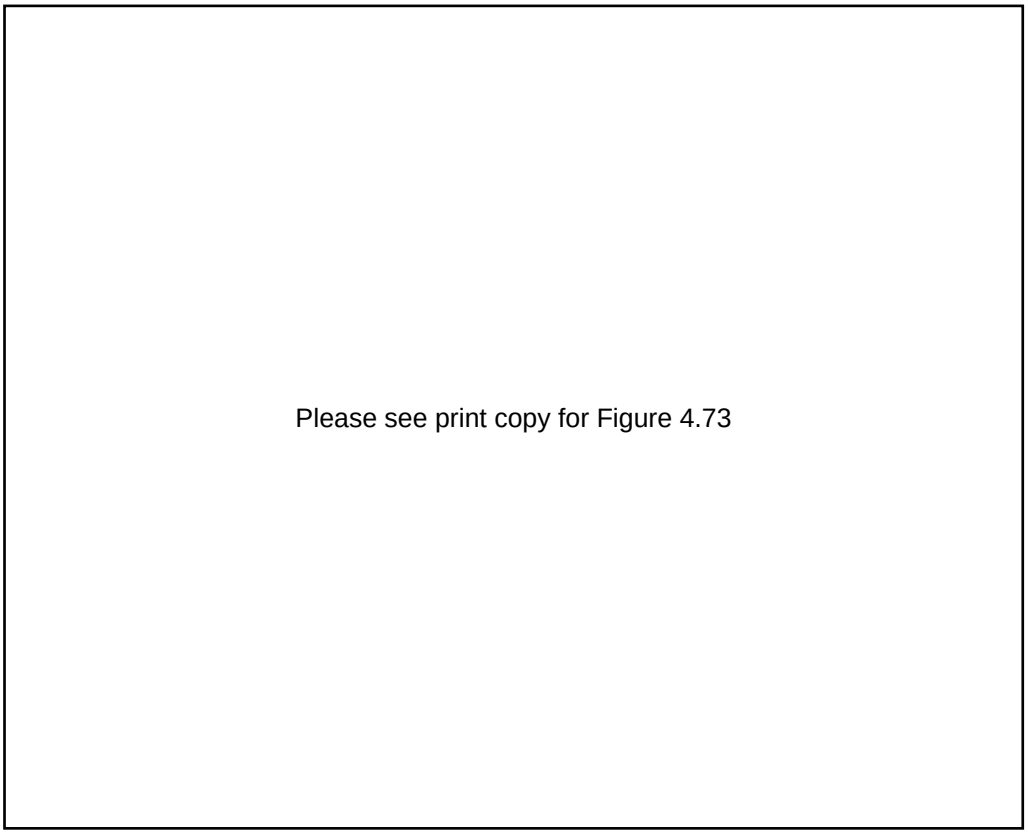

Figure 4-73: TEM image of carbon extraction replica made from steel L4 after annealing at 700 °C in 5% H_2 + 95% N_2 atmosphere for 20 hours and slight etching.

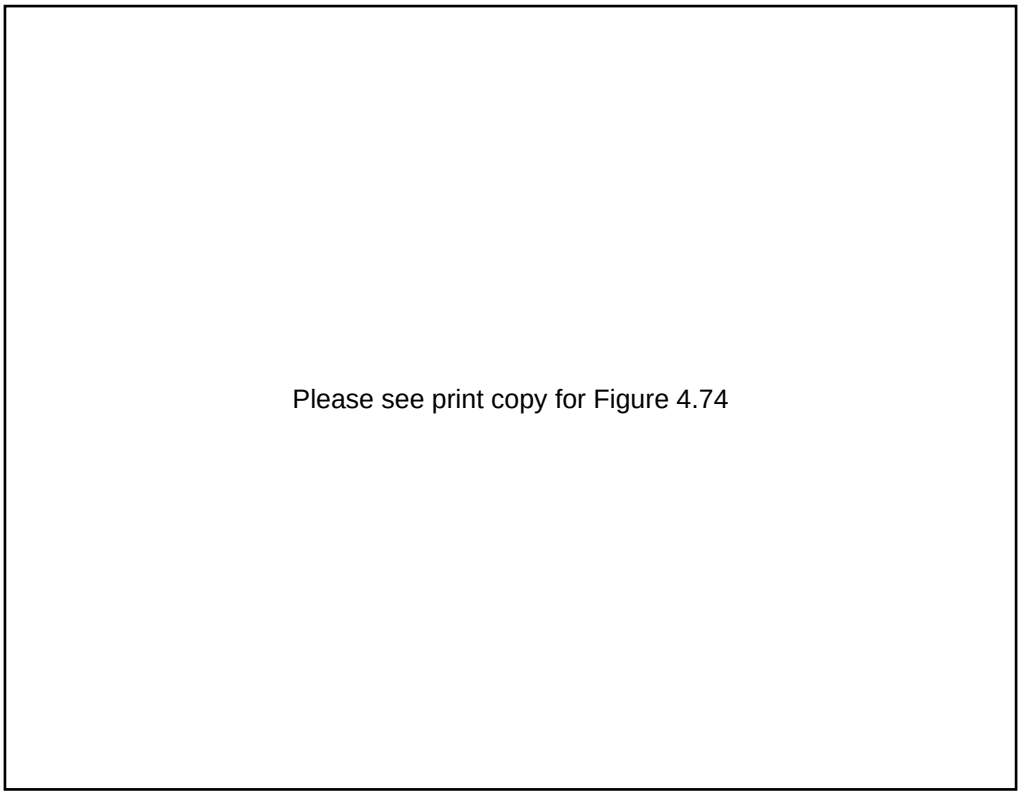

Figure 4-74: TEM image of carbon extraction replica made from steel L5 after annealing at 700 °C in 5% H_2 + 95% N_2 atmosphere for 20 hours and slight etching.

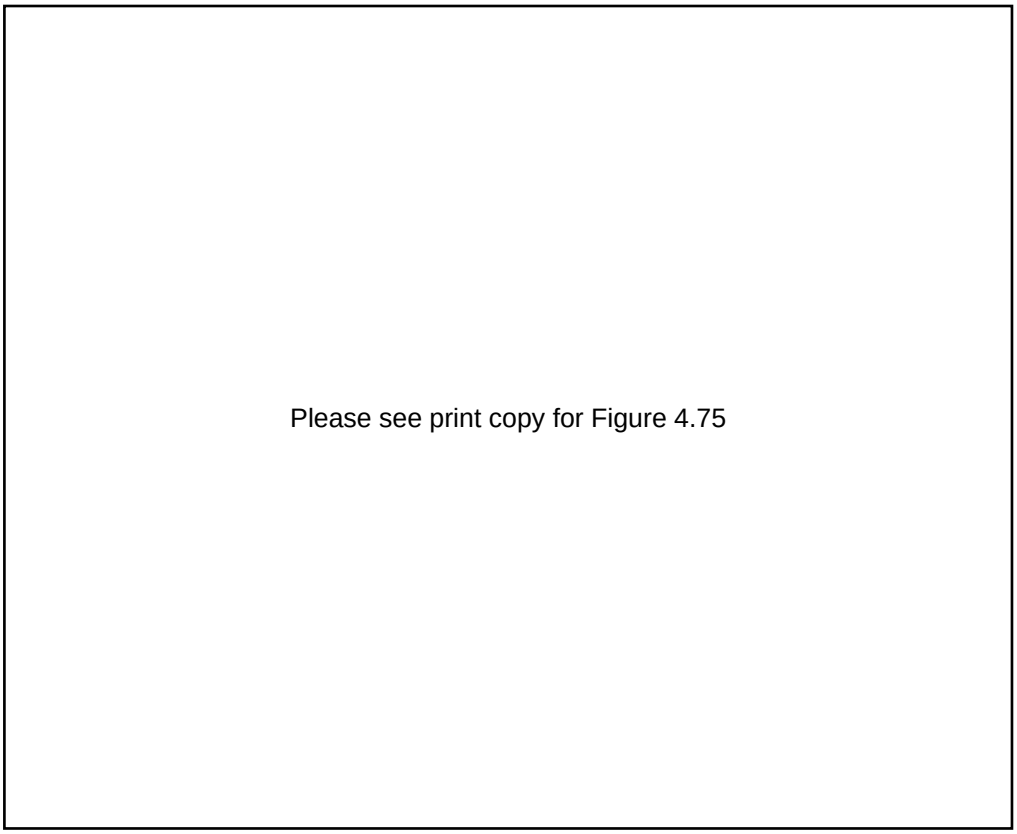

Figure 4-75: TEM image of carbon extraction replica made from steel L6 after annealing at 700 °C in 5% H_2 + 95% N_2 atmosphere for 20 hours and slight etching.

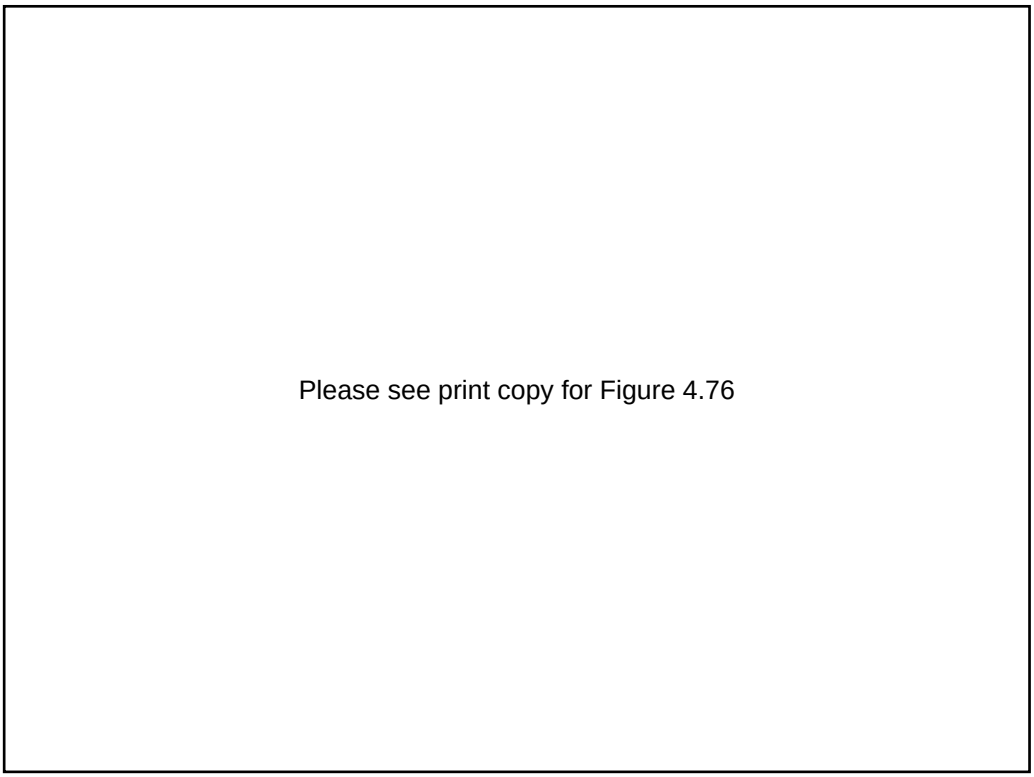

Figure 4-76: TEM image of carbon extraction replica made from steel L8 after annealing at 700 °C in 5% H_2 + 95% N_2 atmosphere for 20 hours and slight etching.

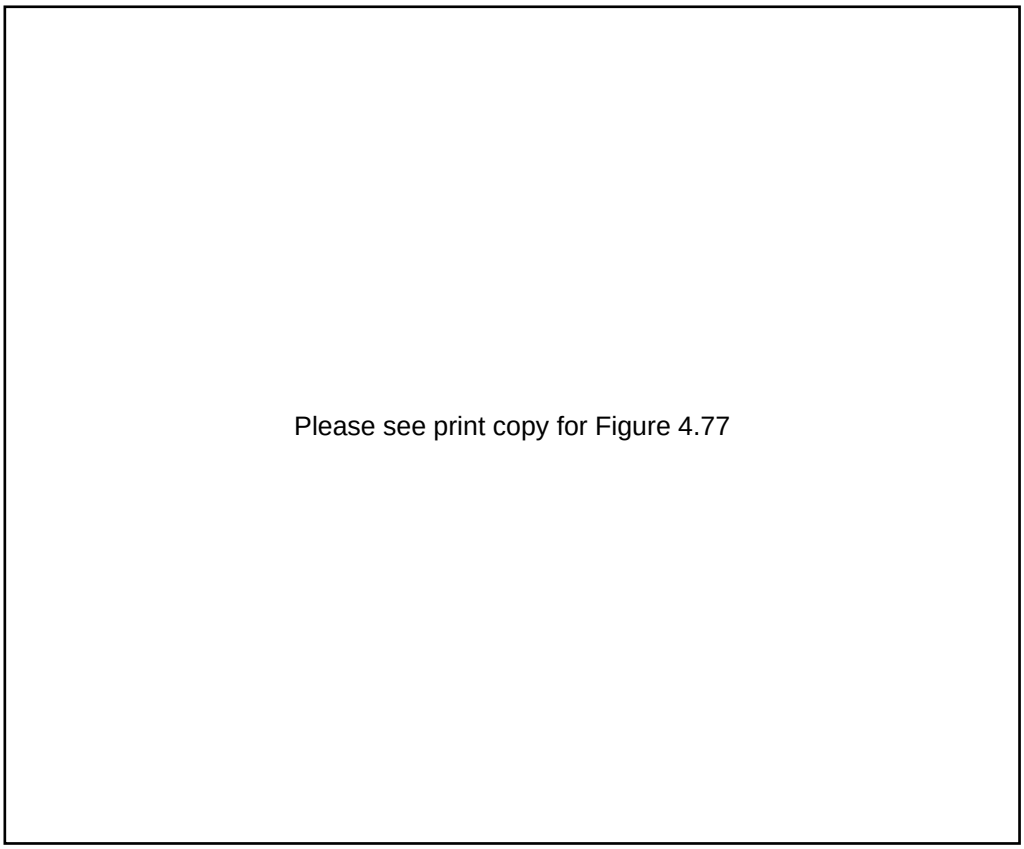

Figure 4-77: TEM image of carbon extraction replica made from steel L9 after annealing at 700 °C in 5% H_2 + 95% N_2 atmosphere for 20 hours and slight etching.

A typical TEM EDS from the steels annealed at 700 °C is shown in Figure 4-78. Clearly the grain boundary precipitates extracted from the steel annealed at 700 °C were $MnCr_2O_4$.

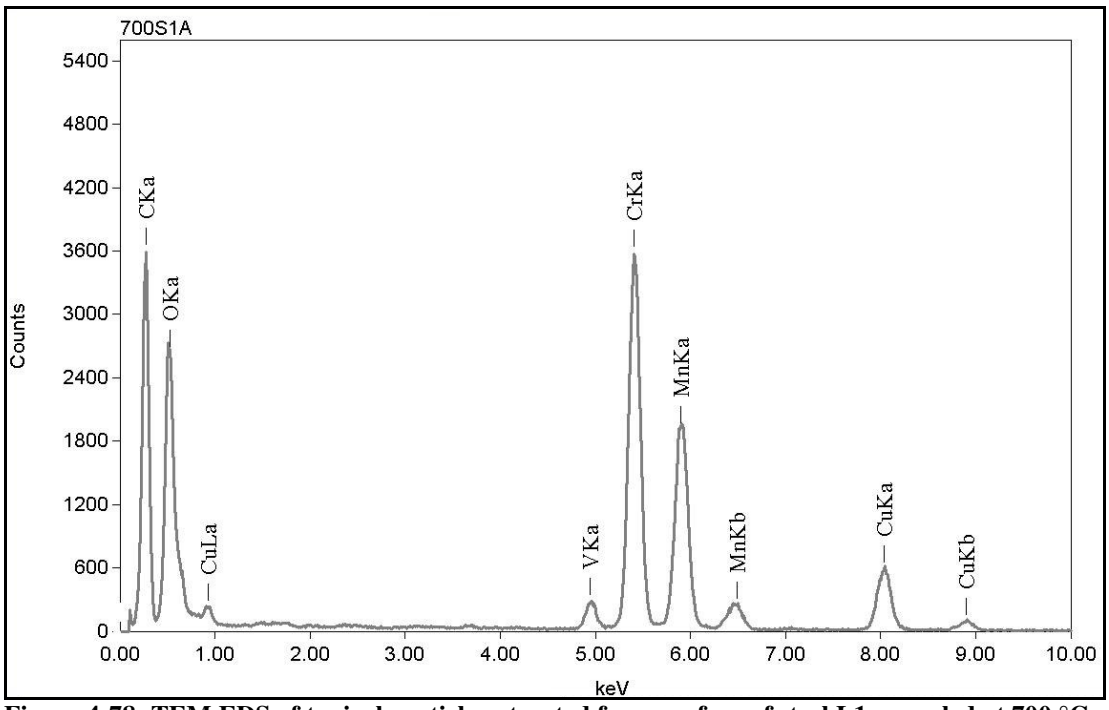

Figure 4-78: TEM EDS of typical particle extracted from surface of steel L1 annealed at 700 °C in 5% H_2 + 95% N_2 atmosphere for 20 hours.

The particle size distribution of the steels annealed at 700 °C is shown in Figure 4-79. Clearly the steels with greater chromium concentration have much larger precipitates. The size of the precipitates is much greater than that observed in the steels annealed at 675 °C with the largest particles having a diameter of about 600 nm.

TEM images of carbon extraction replicas extracted from steels annealed at 750 °C in 5% H_2 + 95% N_2 atmosphere are shown in Figure 4-80 to Figure 4-88.

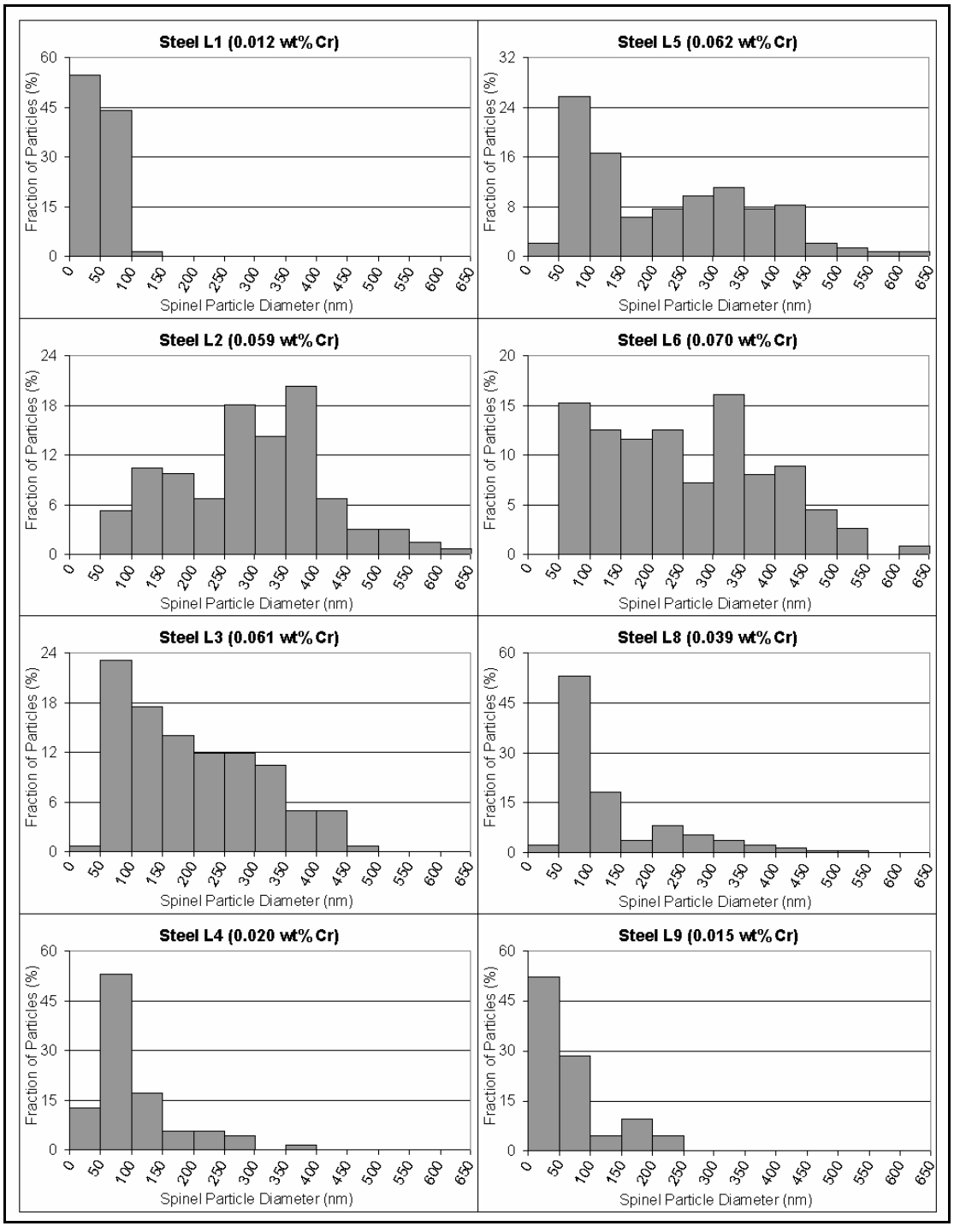

Figure 4-79: Particle size distribution of $MnCr_2O_4$ precipitates extracted from the surface of steels annealed at 700 °C in a 5% H_2 + 95% N_2 atmosphere.

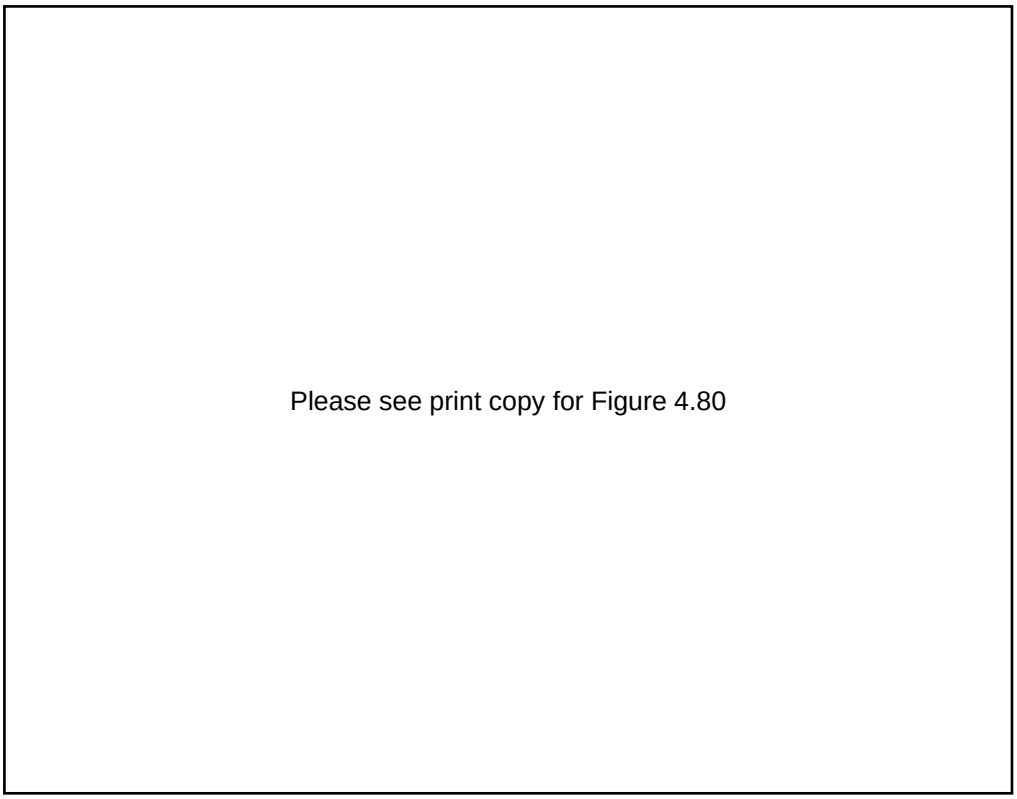

Figure 4-80: TEM image of carbon extraction replica made from steel L1 after annealing at 750 °C in 5% H_2 + 95% N_2 atmosphere for 20 hours and slight etching.

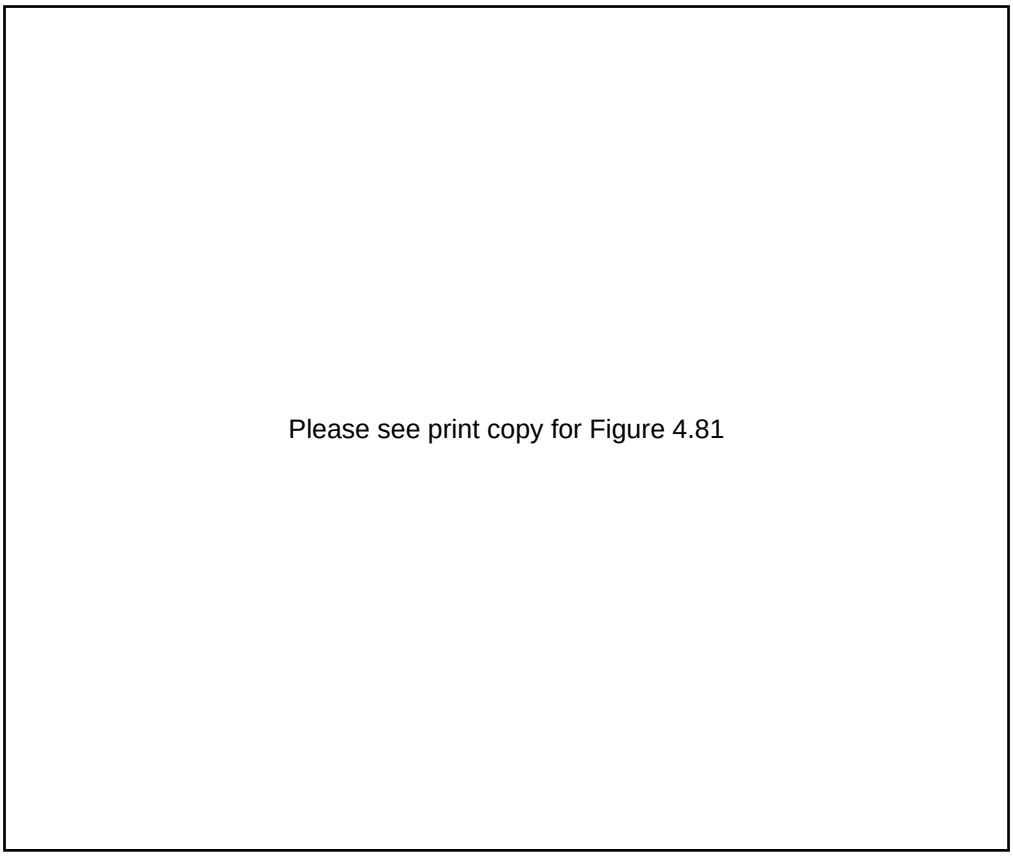

Figure 4-81: TEM image of carbon extraction replica made from steel L2 after annealing at 750 °C in 5% H_2 + 95% N_2 atmosphere for 20 hours and slight etching.

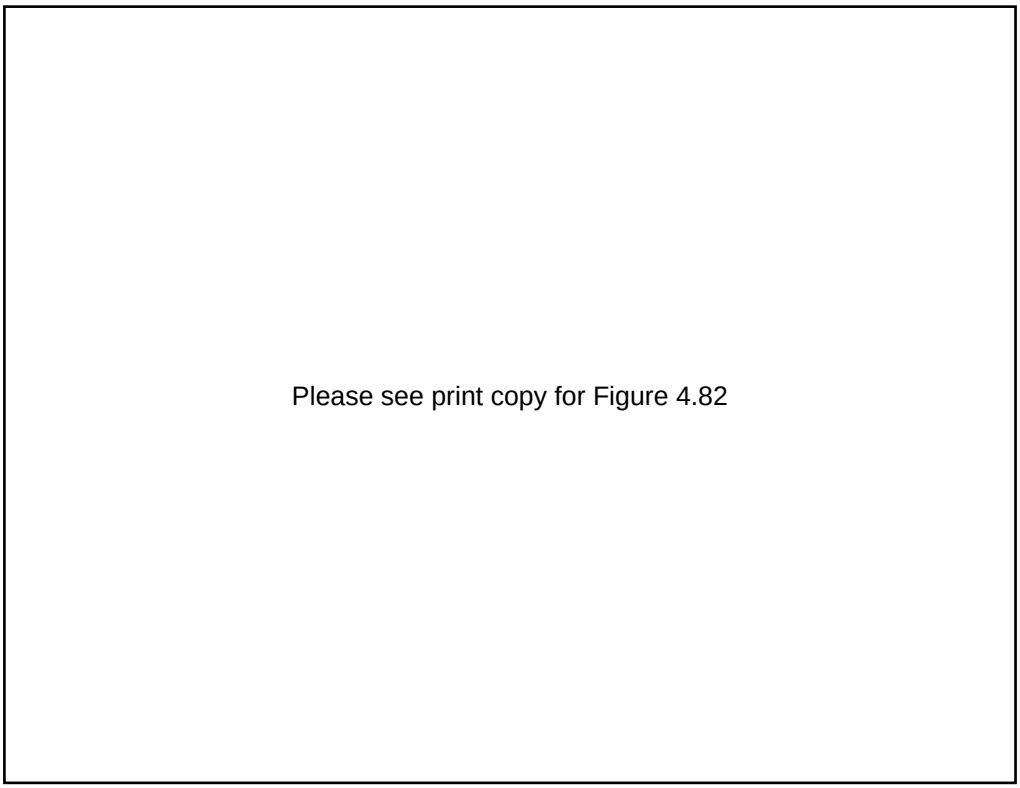

Figure 4-82: TEM image of carbon extraction replica made from steel L3 after annealing at 750 °C in 5% H_2 + 95% N_2 atmosphere for 20 hours and slight etching.

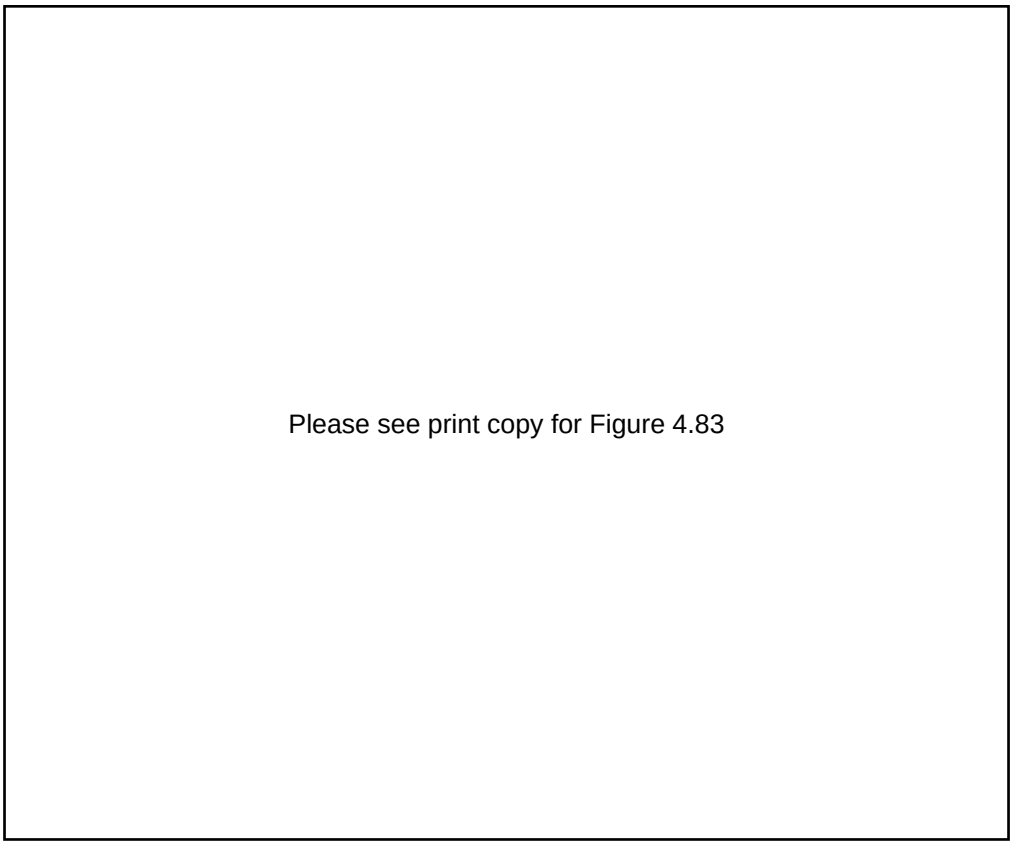

Figure 4-83: TEM image of carbon extraction replica made from steel L4 after annealing at 750 °C in 5% H_2 + 95% N_2 atmosphere for 20 hours and slight etching.

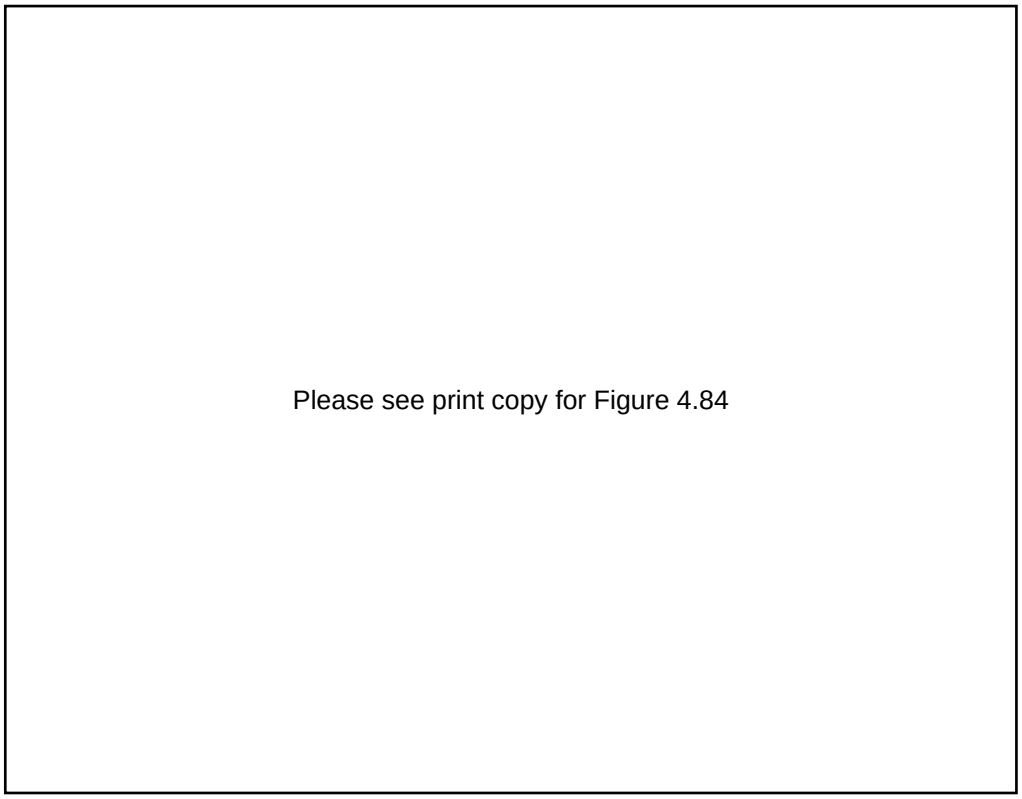

Figure 4-84: TEM image of carbon extraction replica made from steel L5 after annealing at 750 °C in 5% H_2 + 95% N_2 atmosphere for 20 hours and slight etching.

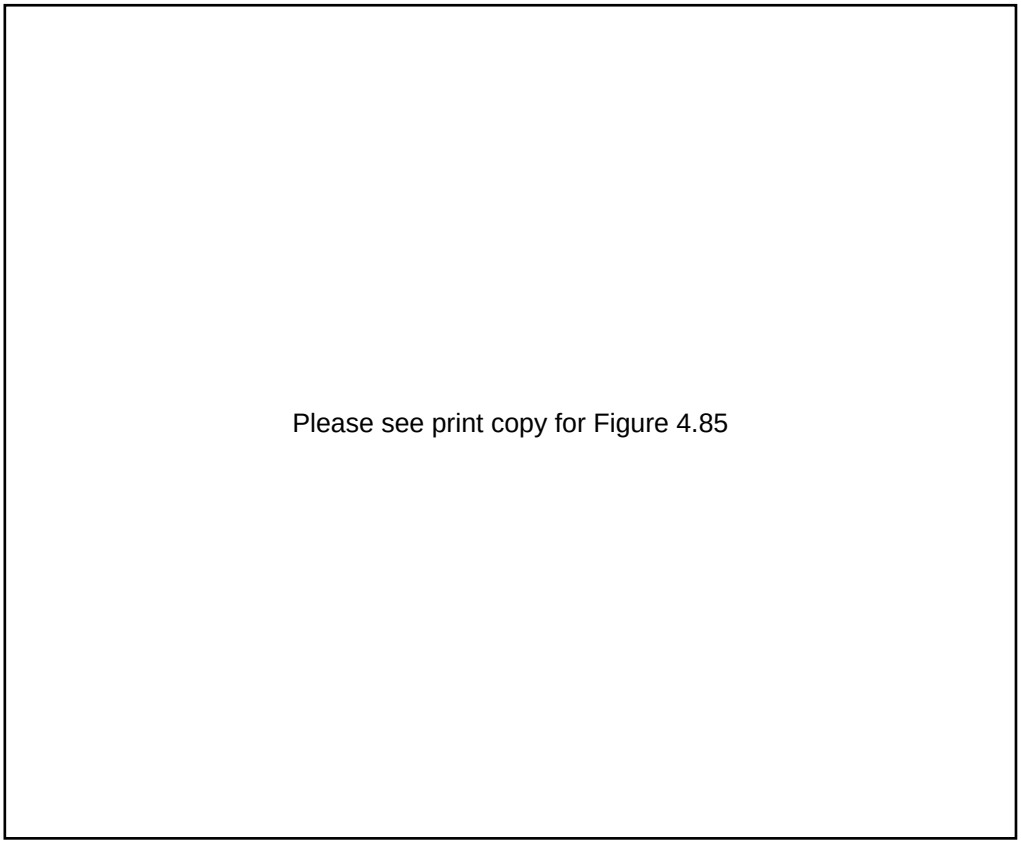

Figure 4-85: TEM image of carbon extraction replica made from steel L6 after annealing at 750 °C in 5% H_2 + 95% N_2 atmosphere for 20 hours and slight etching.

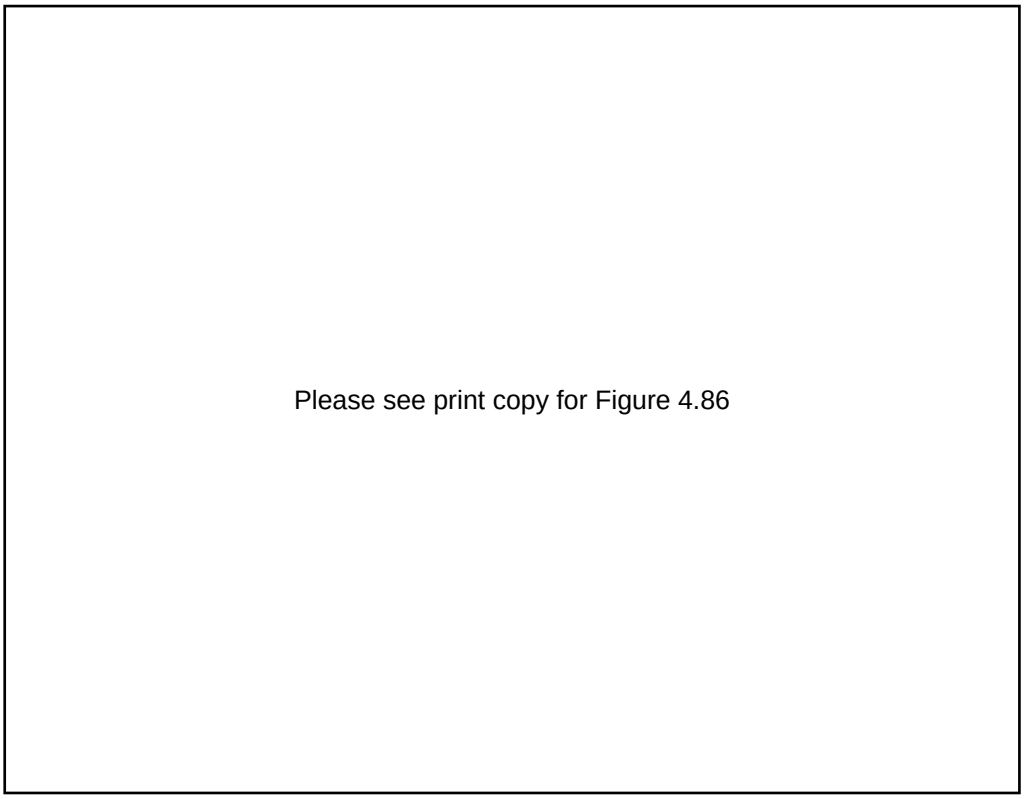

Figure 4-86: TEM image of carbon extraction replica made from steel L7 after annealing at 750 °C in 5% H_2 + 95% N_2 atmosphere for 20 hours and slight etching.

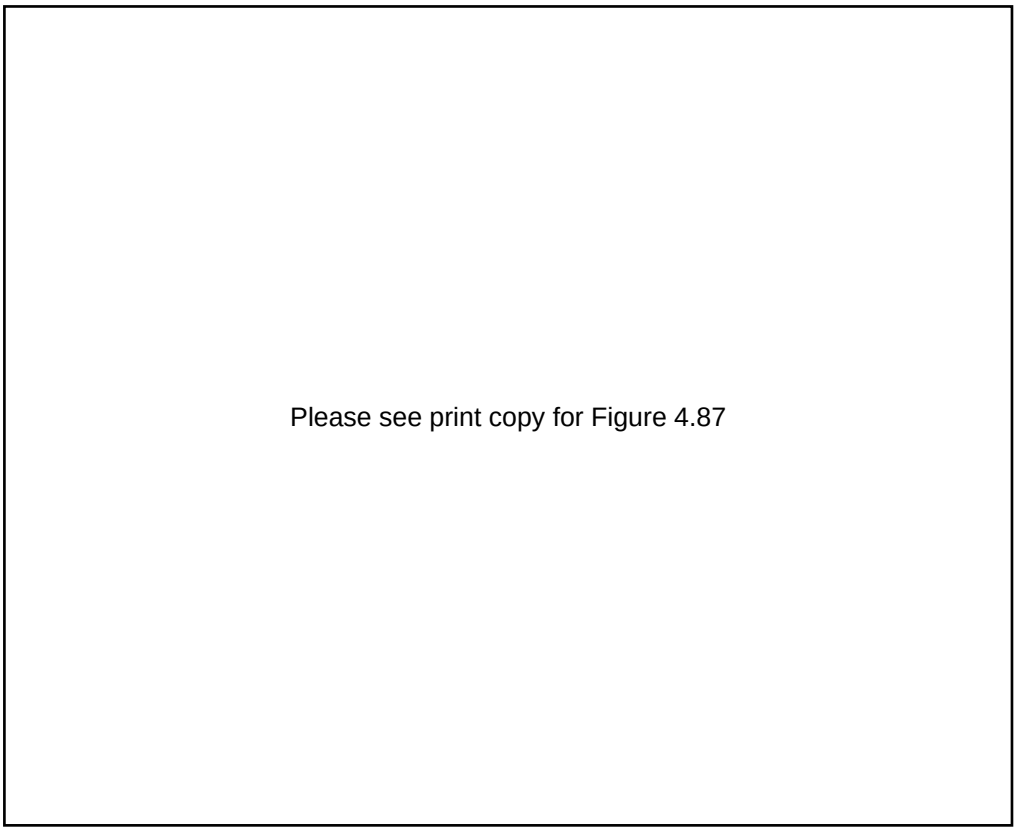

Figure 4-87: TEM image of carbon extraction replica made from steel L8 after annealing at 750 °C in 5% H_2 + 95% N_2 atmosphere for 20 hours and slight etching.

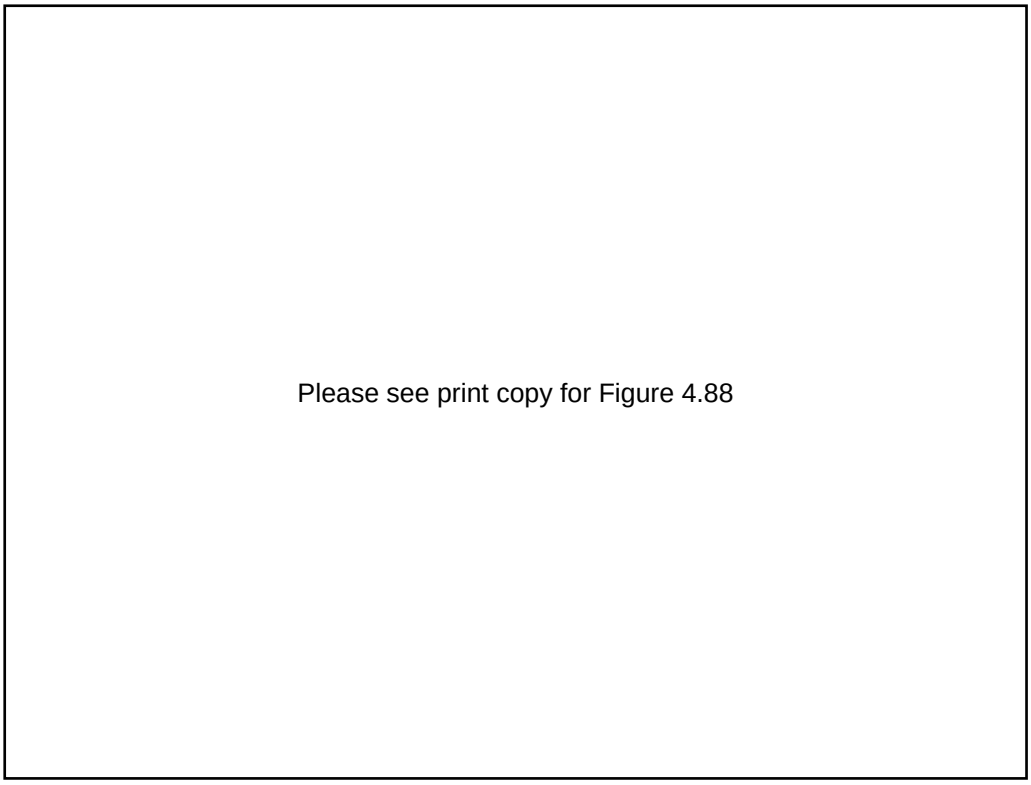

Figure 4-88: TEM image of carbon extraction replica made from steel L9 after annealing at 750 °C in 5% H_2 + 95% N_2 atmosphere for 20 hours and slight etching.

A typical TEM EDS spectrum of grain boundary precipitates from steels annealed at 750 °C is shown in Figure 4-89. Clearly these precipitates were the $MnCr_2O_4$ spinel.

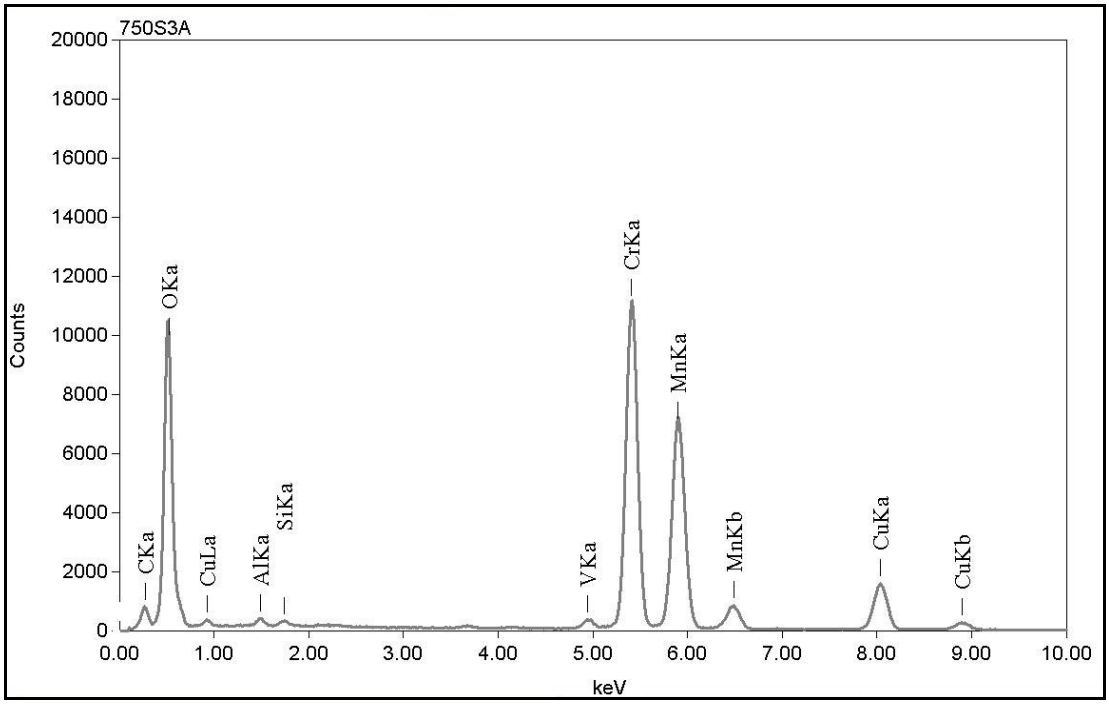

Figure 4-89: EDS spectrum of a typical grain boundary precipitate extracted from the surface of steel L3 annealed at 750 °C in 5% H_2 + 95% N_2 atmosphere for 20 hours

The particle size distribution of the steels annealed at 750 °C is shown in Figure 4-90. Again the steels with higher chromium concentrations have larger precipitates than the steels with lower chromium concentrations. The steels annealed at 750 °C also have some slightly larger particles the largest being about 700 nm.

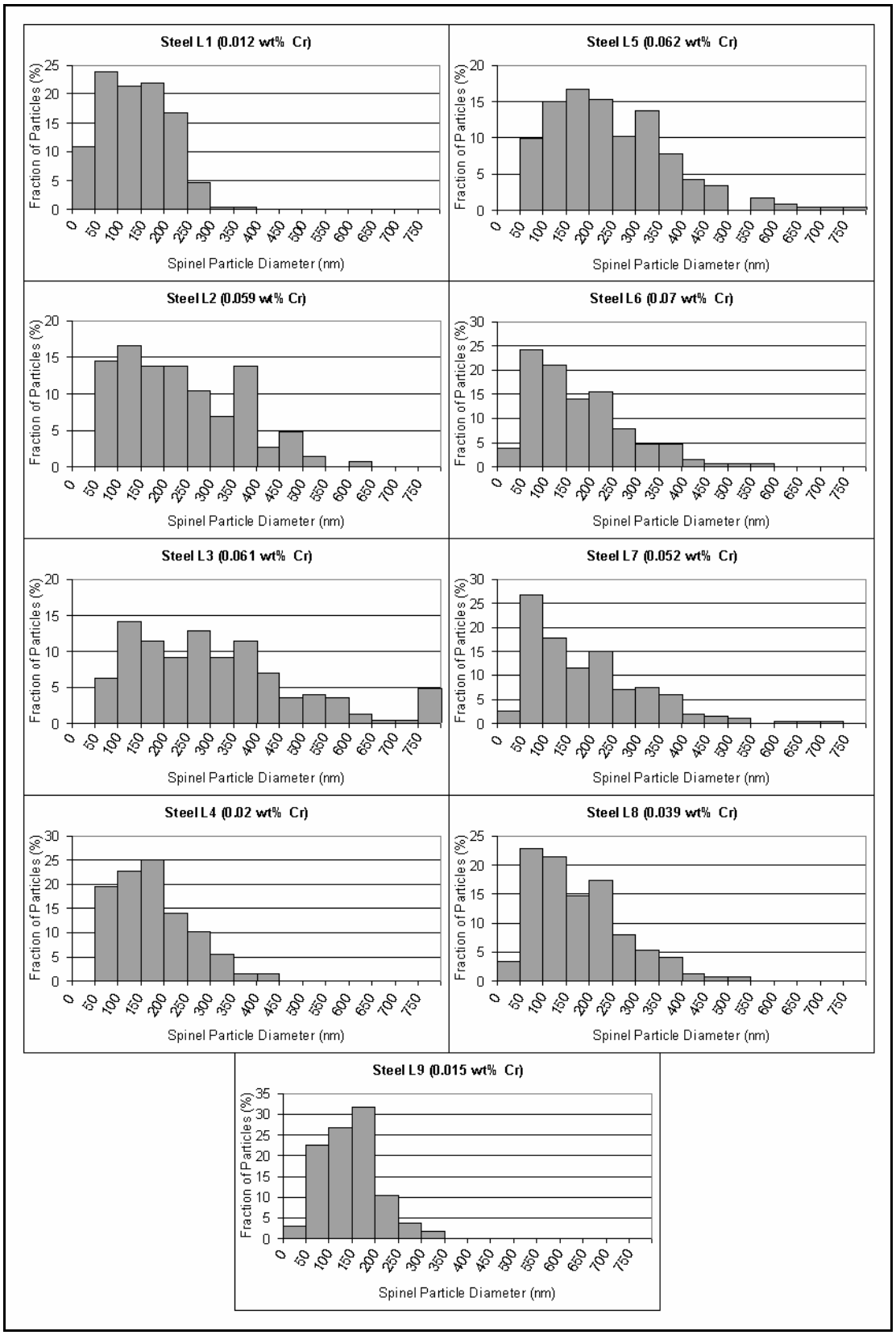

Figure 4-90: Particle size distribution of $MnCr_2O_4$ precipitates extracted from the surface of steels annealed at 750 °C in a 5% H_2 + 95% N_2 atmosphere.

Varying size and shapes of the grain boundary precipitates were extracted from the steel surface however the composition of these precipitates was consistent. X-ray mapping of the carbon extraction replica demonstrates that the composition of the precipitates was homogenous (Figure 4-91). Clearly, the extracted grain boundary precipitates are the $MnCr_2O_4$ spinel.

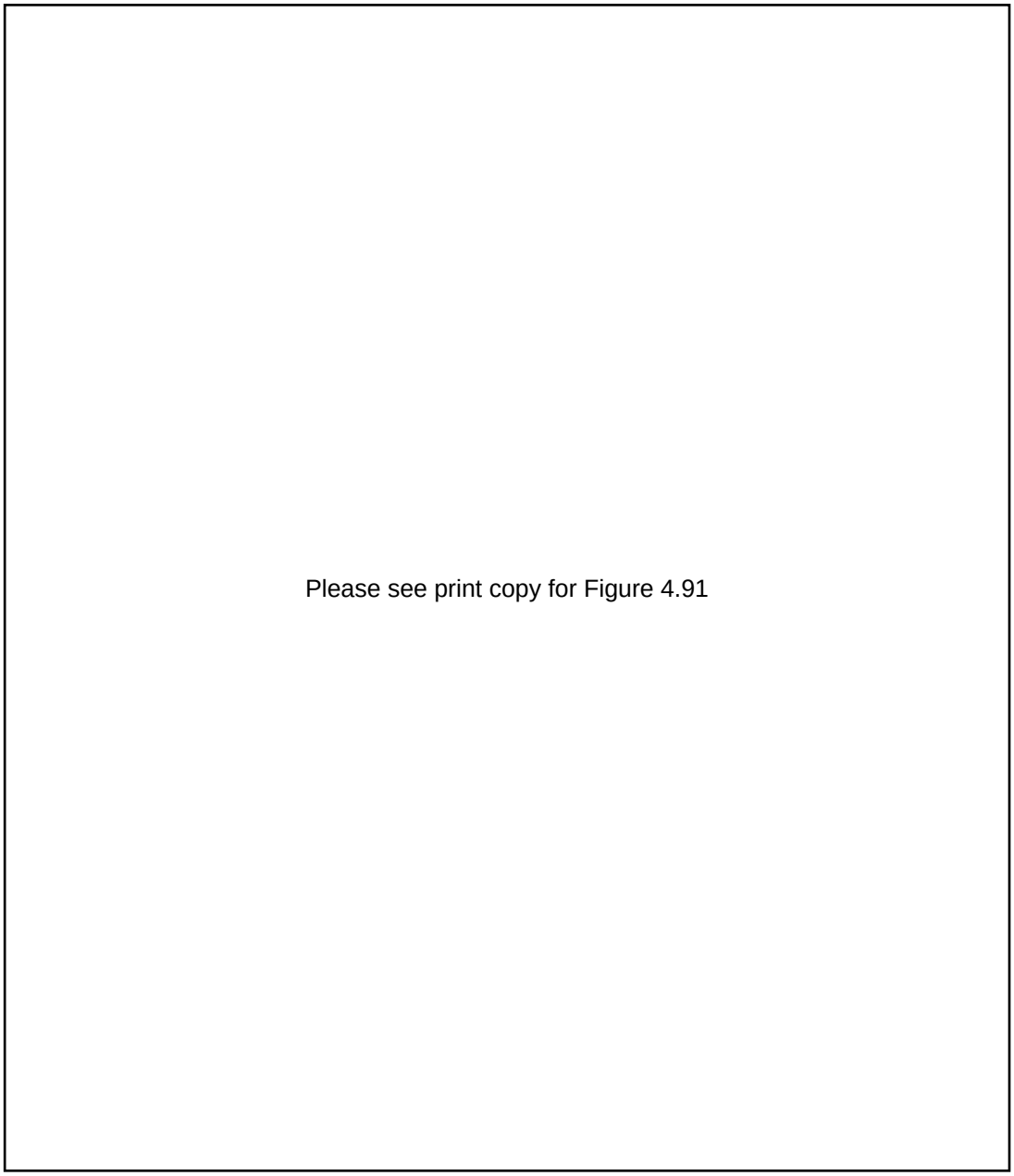

Figure 4-91: X-ray mapping of grain boundary precipitates extracted from the surface of steel L7 annealed at 750 °C in 5% H_2 + 95% N_2 atmosphere for 20 hours.

In addition to the grain boundary precipitates fine precipitates <50nm in diameter were observed on the grain surface (Figure 4-92). Although typical grain boundary precipitates have <1% aluminium, a higher aluminium level was observed in the fine surface precipitates (Figure 4-93). This aluminium seems to replace the chromium in the oxide. In some of the fine precipitates, aluminium has been observed to have up to 50 atomic % of metal in the oxide.

In some of the low chromium steels, particularly steel L1, the vanadium level in the spinel was observed to be much higher, approximately 10 atomic % of metal in the spinel. A TEM EDS spectrum showing the higher ratio of vanadium in the oxide is shown in Figure 4-94. The vanadium seems to replace the chromium in the oxide, as the manganese levels in the spinel remain similar.

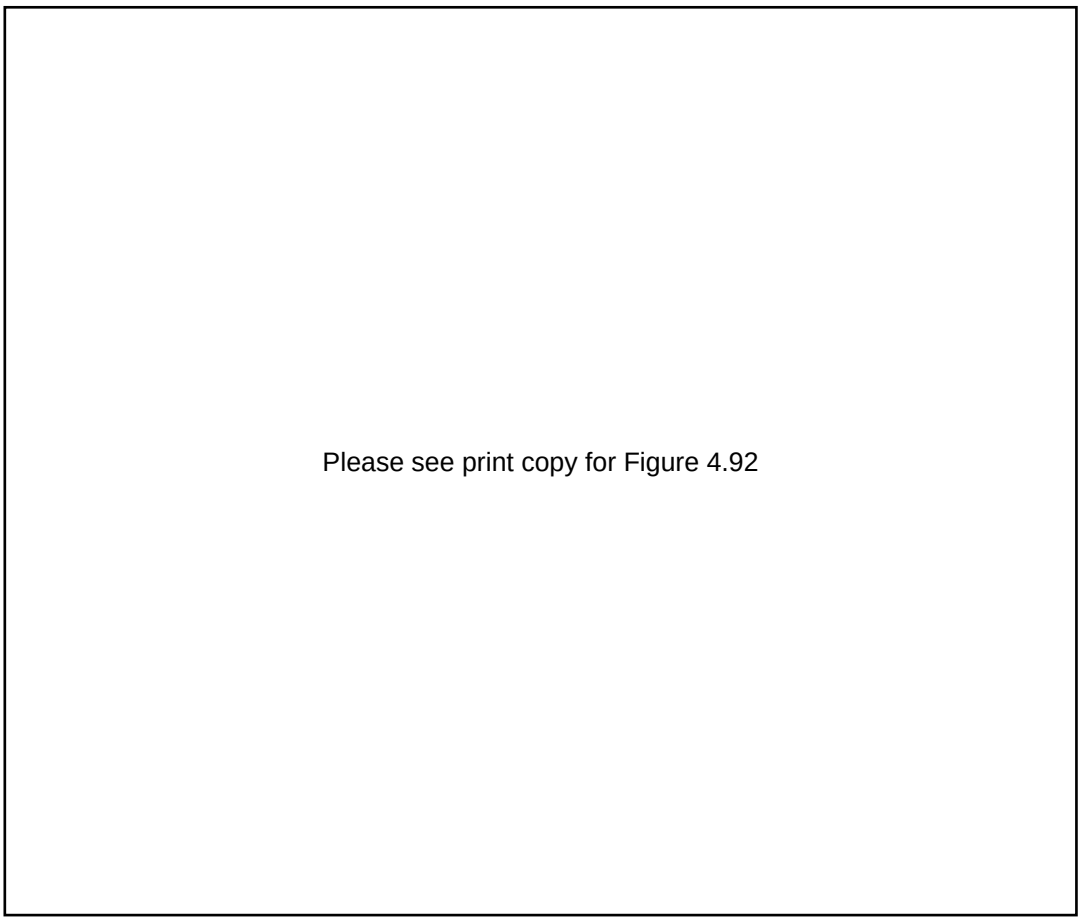

Figure 4-92: TEM image of carbon extraction replica showing grain boundary $MnCr_2O_4$ precipitates and fine precipitates (<50 nm) located on the grain surface.

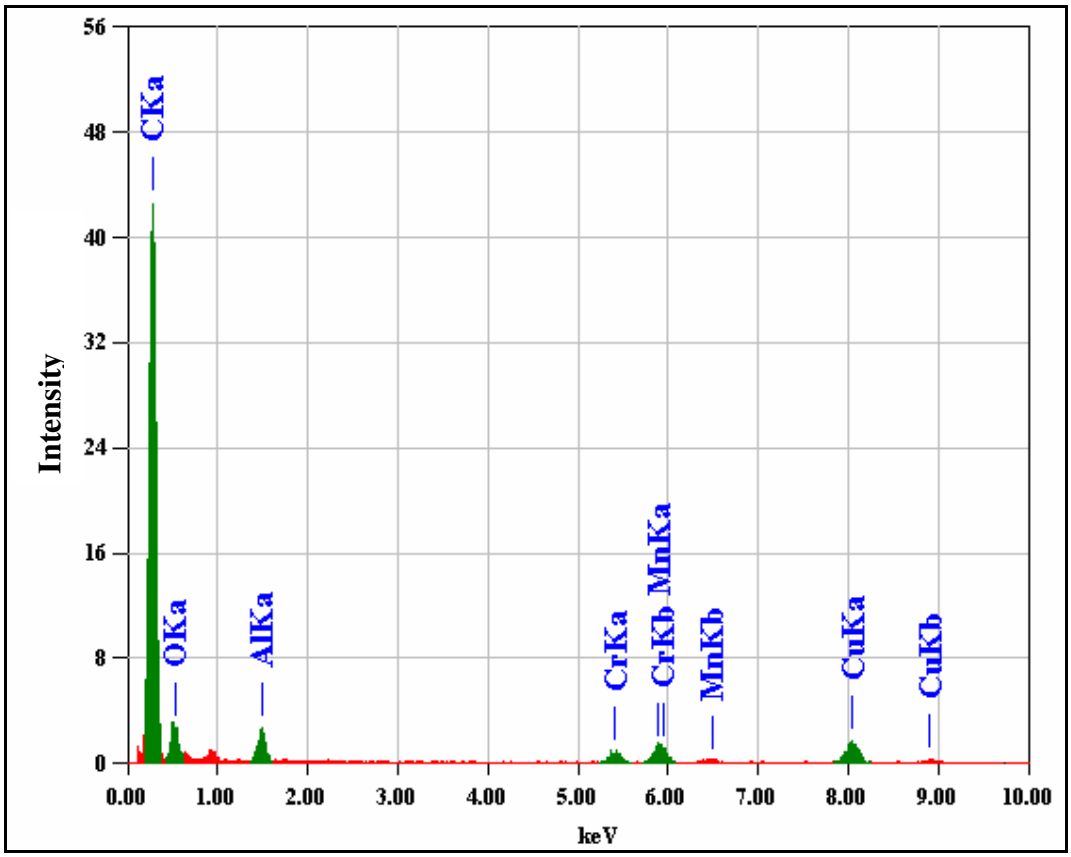

Figure 4-93: TEM EDS spectrum of fine precipitate extracted from the surface of steel L8 annealed at 700 °C in 5% H_2 + 95% N_2 atmosphere for 20 hours.

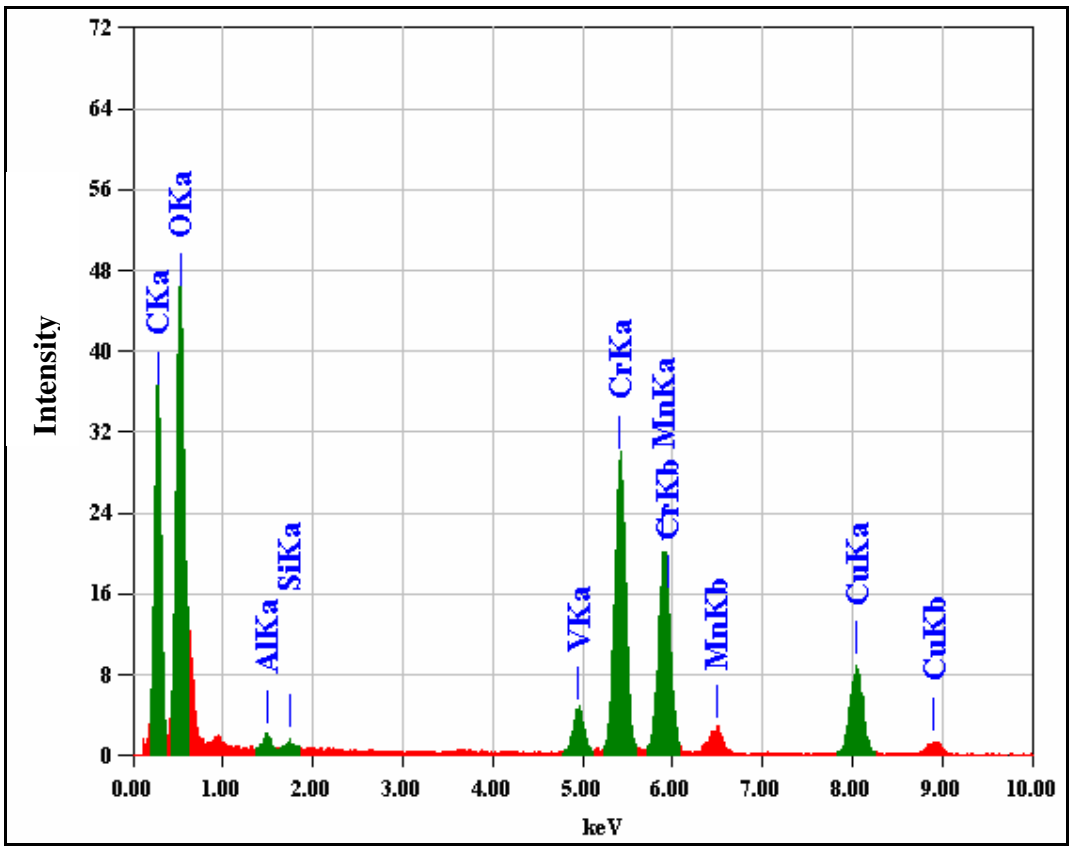

Figure 4-94: TEM EDS spectrum of precipitate extracted from the surface of steel L1 annealed at 700 °C in 5% H_2 + 95% N_2 atmosphere for 20 hours.

Table 4-4 shows the measured mean particle diameter of $MnCr_2O_4$ spinel precipitates extracted on carbon replicas as observed by TEM.

Table 4-4: The mean particle diameter of $MnCr_2O_4$ spinel precipitates extracted on carbon replicas from the surface of steels annealed in 5% H_2 + 95% N_2 atmosphere as observed by TEM.

Temperature (°C)	Steel	Mean Particle Diameter (nm)
675	L1	70
	L2	78
	L3	90
	L4	61
	L5	79
	L6	74
	L7	71
	L8	38
	L9	59
700	L1	52
	L2	324
	L3	227
	L4	124
	L5	260
	L6	288
	L8	171
	L9	85
750	L1	154
	L2	267
	L3	371
	L4	195
	L5	282
	L6	207
	L7	232
	L8	201
	L9	157

The effect of annealing temperature and the chromium level in the steel on the mean particle diameter of $MnCr_2O_4$ spinel precipitates extracted on carbon replicas from the surface of steels annealed in 5% H_2 + 95% N_2 atmosphere is shown in Figure 4-95. At 675 °C the amount of chromium seems to have little effect on the spinel particle size with only a slight increase in the size of particles observed. At 700 °C the effect of chromium on particle size is dramatic. The mean particle size increases dramatically with the chromium level in the steel. At 750 °C the mean particle size

increases with the chromium. However, this increase is not as dramatic as that observed in the sample annealed at 700 °C.

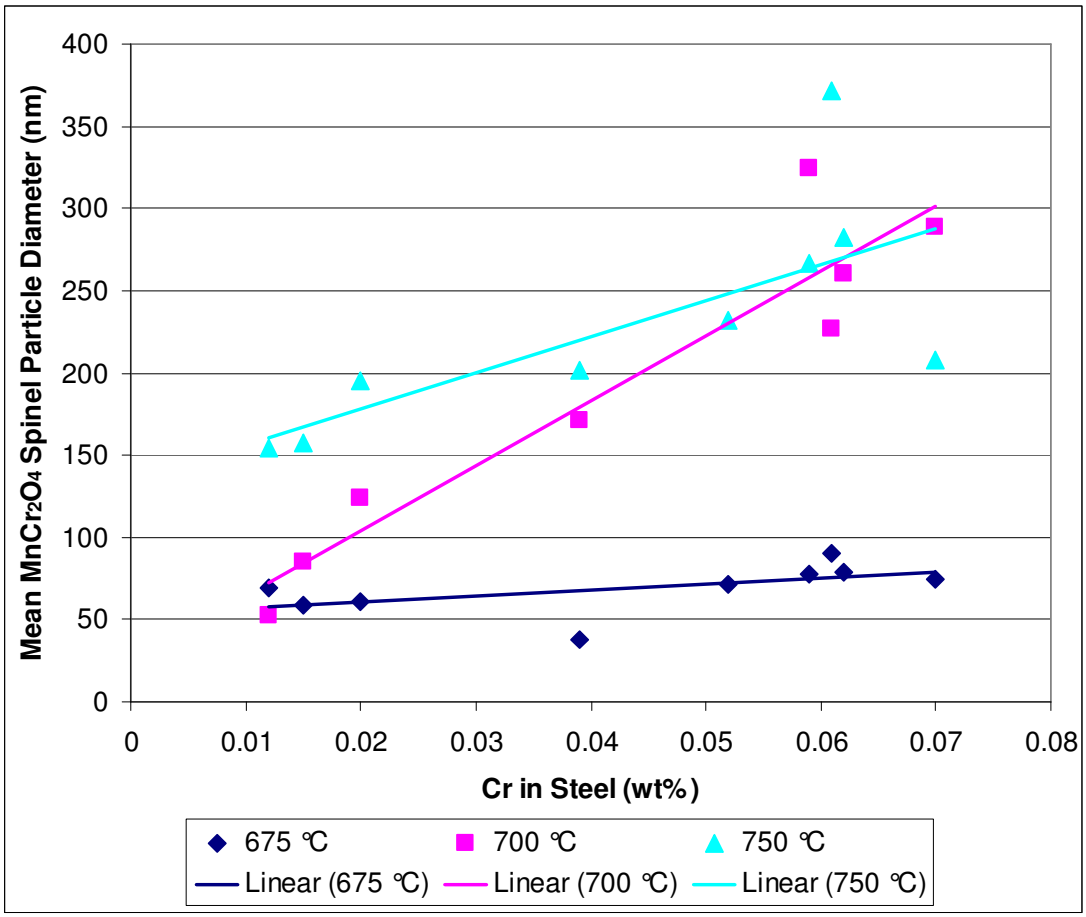

Figure 4-95: The effect of temperature and chromium level in the steel on the mean $MnCr_2O_4$ grain boundary precipitate size observed by TEM.

4.6 Surface Oxides across the Width of Steel Strip

The location of the 'edge defect' caused by grain boundary precipitates is generally restricted to a band near the coil edge. However, the surface precipitates are not restricted to this localised area and are present in a much wider area and extend quite extensively into the middle of the strip. The surface particle size across the width of industrial batch annealed steel strips was measured and the results are presented below.

4.6.1 Coil B1

The composition of coil B1 is designated as steel B1 in Table 3-1. The sample was of blackplate steel strip taken from the seventh wrap into the coil. Figure 4-96 shows backscattered electron images of the surface of coil B1 at different locations from the strip edge which demonstrates the change in the size of the surface oxides. As in the previous section the surface oxide were composed of coarser (MnFe)O and finer $MnCr_2O_4$. The average particle size as a function of the distance from the coil edge is given in Figure 4-97a. The spinel precipitates were much smaller than the (MnFe)O so most of these precipitates measured from backscatter electron images were (MnFe)O. The average particle size for the (MnFe)O precipitates was relatively fine at the very edge of the sample but then quickly increased to a maximum mean particle diameter of 950 nm in the 30 to 70 mm range from the edge. The particle size then decreased with increasing distance from the edge until they could not be resolved by SEM at a distance of about 350 mm from the coil edge. Figure 4-97a also shows the percentage of the surface covered by these precipitates versus the distance from the coil edge. A maximum surface coverage of 3.5% was observed at 70 mm from the coil edge. At 30 - 40 mm from the strip edge although the average particle size was relatively large, the surface coverage was not as high as at 70mm from the strip edge, indicating the particles are more sparsely populated at 30 - 40 mm location.

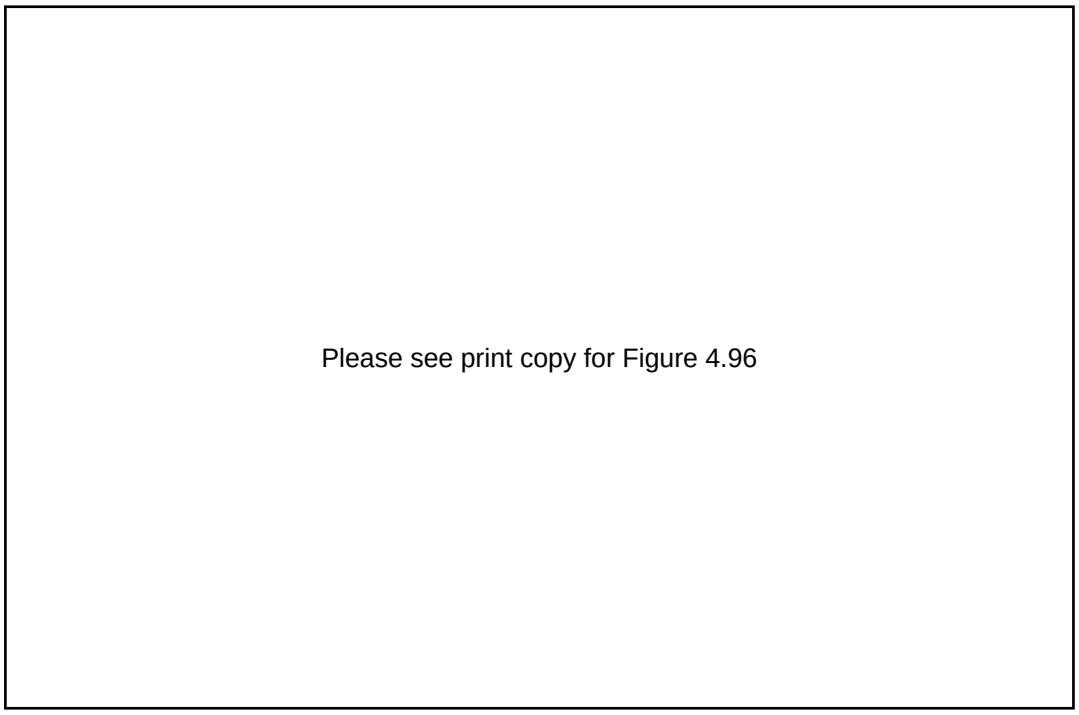

Figure 4-96: Backscatter electron images showing change in (MnFe)O particle size across width of coil B1 a) at the edge, b) 50mm from edge, c) 100mm from edge and d) middle of coil.

Carbon extraction replicas of the etched steel surface were characterised using TEM which showed only the presence of $MnCr_2O_4$ spinel grain boundary precipitates (Figure 4-98). Figure 4-97b shows the mean spinel particle size as a function of the distance from the coil edge. The greatest mean particle diameter of 200 nm for the spinel precipitates was observed at the same location from the coil edge as the maximum particle size and surface coverage of the (MnFe)O precipitates.

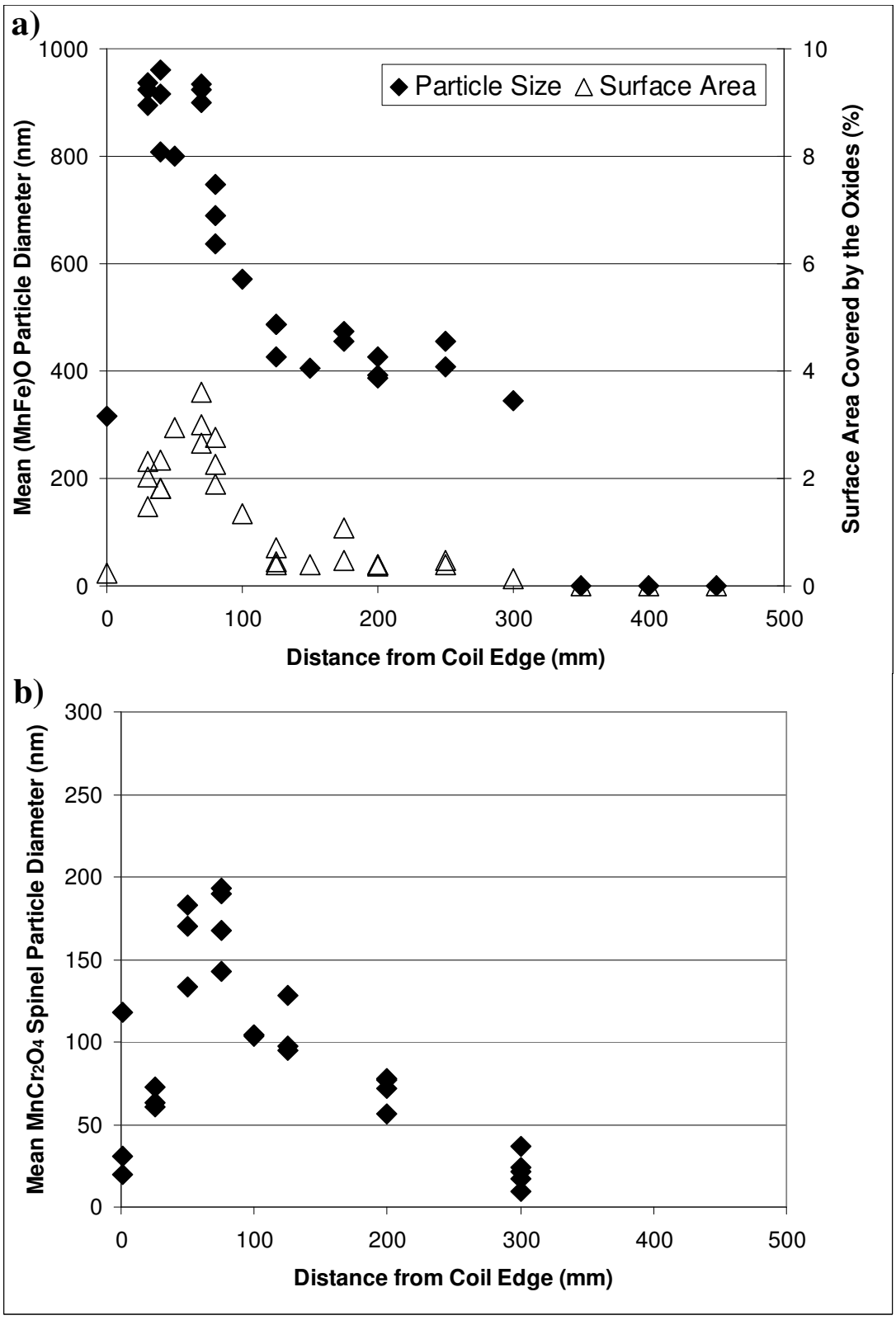

Figure 4-97: a) The distributions of mean particle size and surface area of (MnFe)O oxides observed by SEM, b) Distribution of the mean particle size of $MnCr_2O_4$ spinel precipitates, across width of coil B1

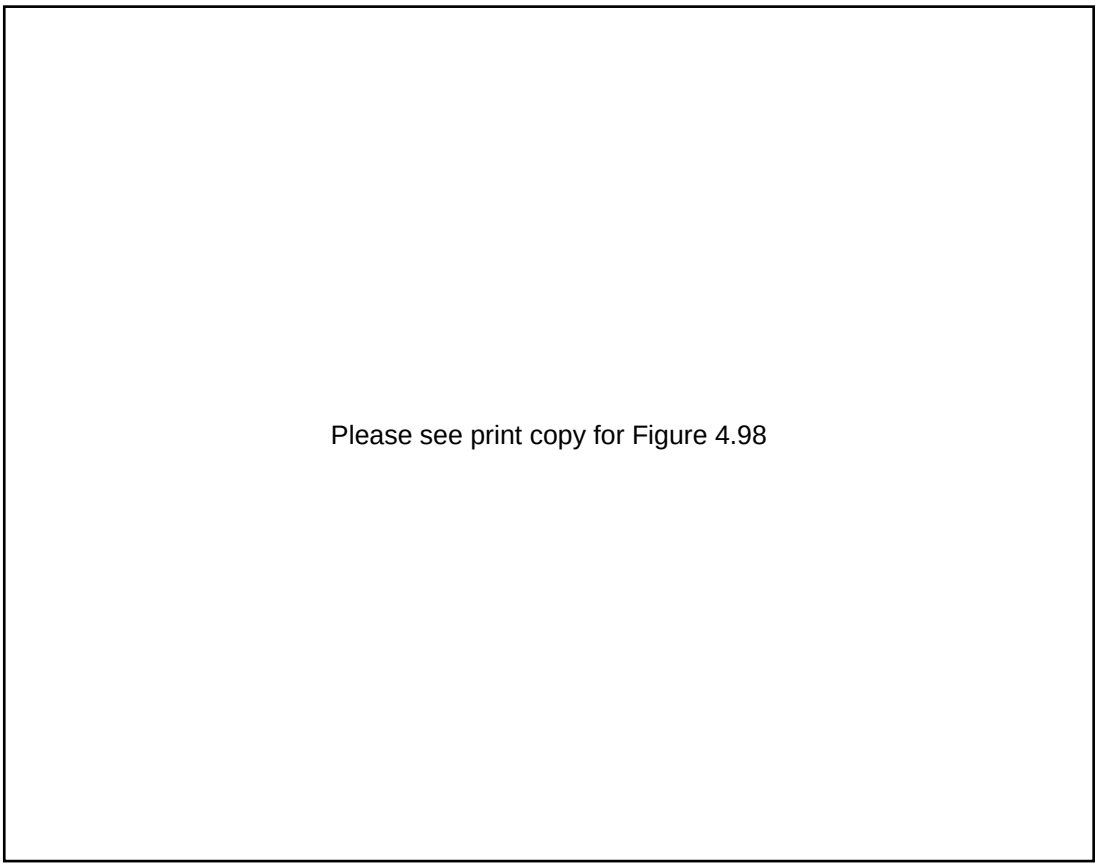

Figure 4-98: TEM image of carbon replica's made of etched steel surface at a) 25 mm b) 50 mm, c) 75 mm and d) 200 mm from edge of coil B1 showing the change in the size of grain boundary $MnCr_2O_4$ spinel precipitates.

Nitrogen Pick-up across Strip

The oxygen potential is difficult to measure across the width of steel sheet's, but may be deduced from the nitrogen pick-up in the steel. The nitrogen level across the width of coil B1 is shown in Figure 4-99. The nitrogen content of coil B1 prior to annealing was about 25 ppm from the heat analysis. The nitrogen content in this sample increased from 20 ppm at the strip edge to 125 ppm at the strip mid width location as shown by Figure 4.55.

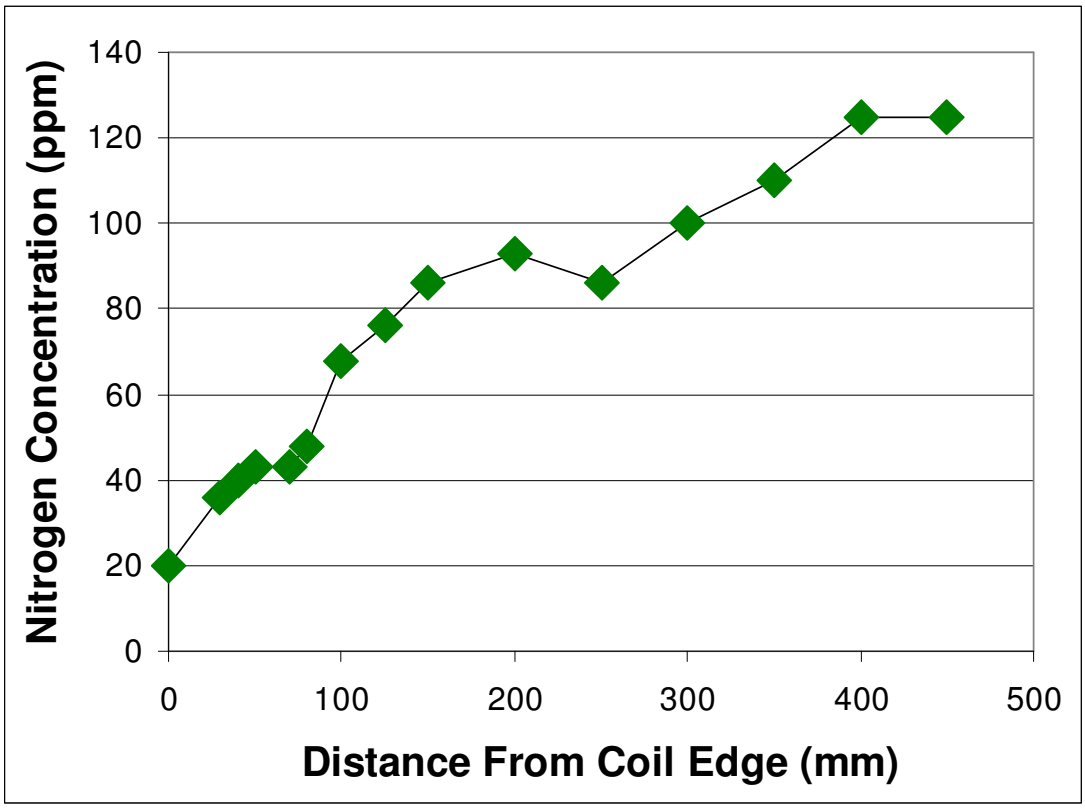

Figure 4-99: The change in nitrogen content in the steel with distance from edge of coil B1.

Cross Section Sample at Coil Edge

A sample taken in the area about 15 mm from the edge of coil B1 was used to prepare a TEM cross-section specimen to investigate the reduction in particle size observed near the coil edge. Figure 4-100 shows a relatively coarse grain boundary precipitate about 300 nm in diameter located 100 nm below the steel surface (A and B) and a fine precipitate about 20 nm in diameter located at about 1500 nm below the surface (C). As shown previously the coarse precipitate is (MnFe)O with a small $MnCr_2O_4$ core region (B).

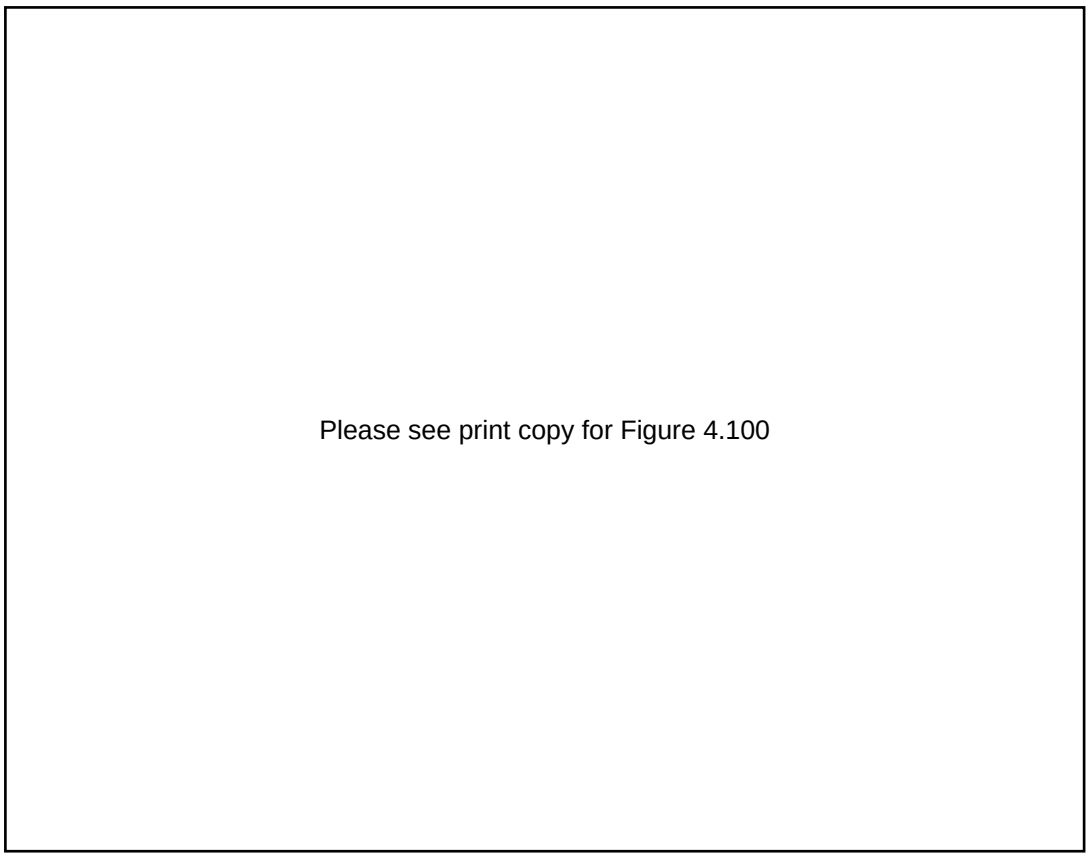

Figure 4-100: TEM images showing grain boundary precipitates below the steel surface. Pt: platinum coating, A, B, C, D: areas analysed by EDS.

Figure 4-101 compares EDS spectra from the fine grain boundary precipitate marked as C to the iron matrix marked as D in Figure 4-100. The spectrum from the area marked C clearly shows additional Cr Kα, Mn Kα and O Kα peaks. The large Fe Kα in the EDS spectrum of the fine particle was mainly due to the iron matrix and the Cr Kα to Mn Kα ratio for precipitate C is very similar to that of $MnCr_2O_4$.

Figure 4-102 is another TEM image of the cross section sample produced by FIB. In this image the grain boundary precipitate (C) is visible as are other grain boundary precipitates further in to the steel. These results demonstrate that at the edge of coil B1 internal oxidation occurs.

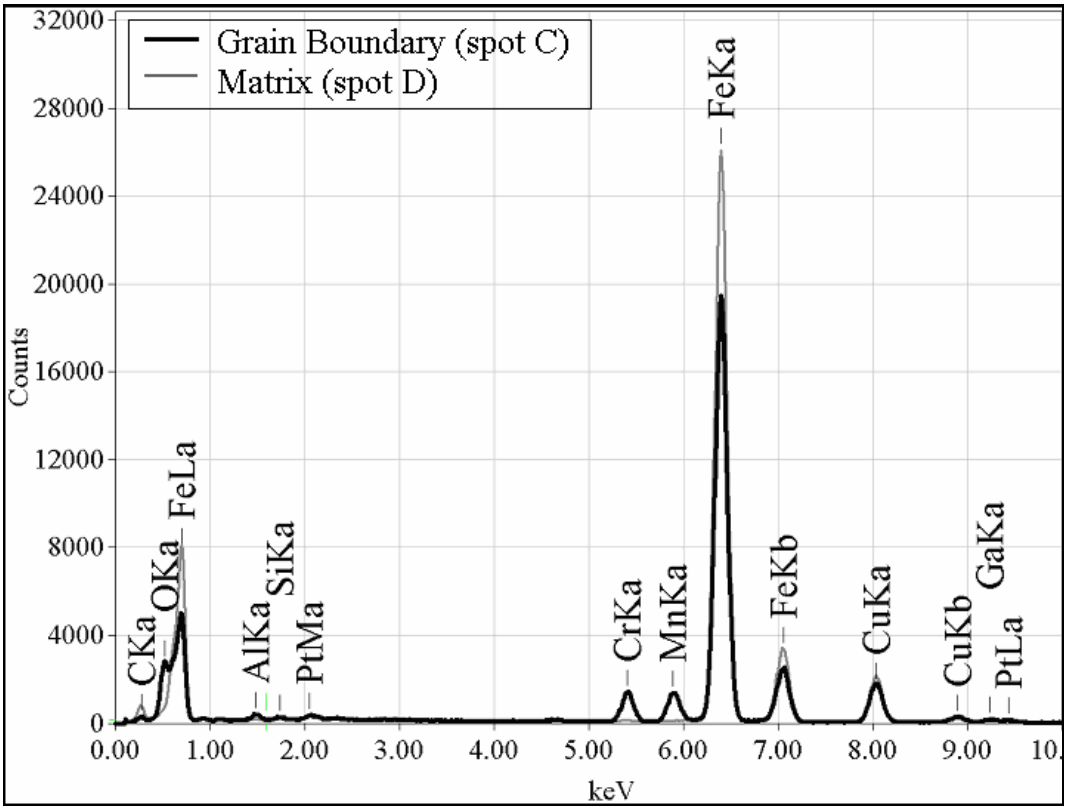

Figure 4-101: Superimposed EDS spectra of grain boundary precipitate (area C in Figure 4-100) and adjacent matrix (area D in Figure 4-100)

Please see print copy for Figure 4.102

Figure 4-102: TEM cross section image showing a series of internal grain boundary precipitates.

4.6.2 Coil B2

Coil B2 was also examined with the sample taken from the seventh wrap into the coil. Uncharacteristically of the 'edge defect' the largest surface oxide particles were observed at the very edge of coil B2. Overall the average oxide particle size was smaller than those observed in coil B1. This coil showed a maximum average particle diameter of (MnFe)O precipitates just below 700 nm in the area of 0 - 25 mm from the coil edge and which decreased to 400 nm in the area from about 75 mm, maintaining this value to a distance of 150 mm from the strip edge, after which no precipitates were observed by SEM (Figure 4-103a). Figure 4-103b shows the size of spinel precipitates versus distance from the coil edge characterised by TEM. The largest average spinel particle diameter of 350 nm was observed at the edge. The diameter then decreased to a distance of 150 mm from the edge, beyond which no grain boundary precipitates were observed.

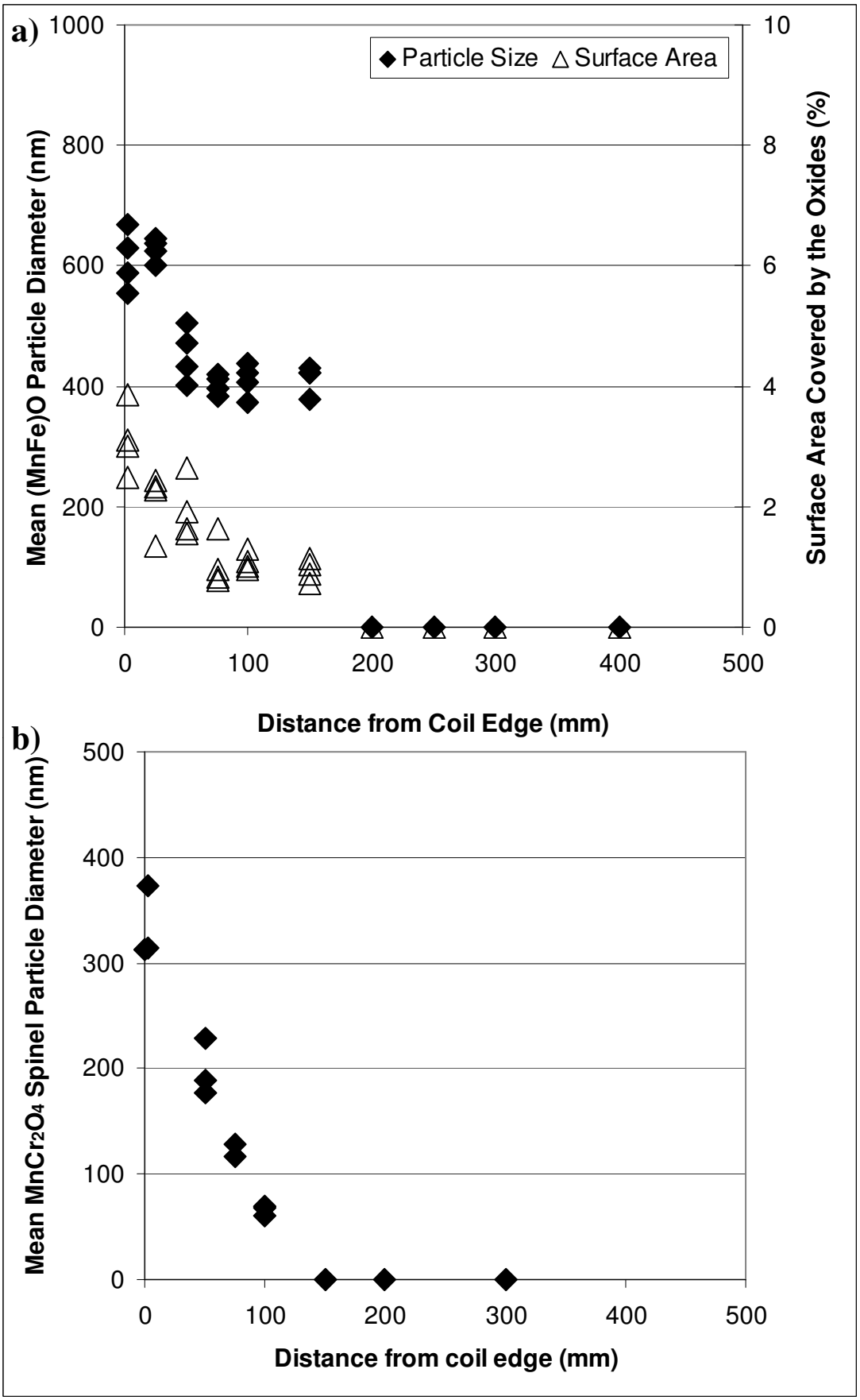

Figure 4-103: a) The distributions of mean particle size and surface area of (MnFe)O oxides observed by SEM, b) Distribution of the mean particle size of $MnCr_2O_4$ spinel precipitates, across the width of coil B2.

4.7 Solid State Reaction of MnO and Cr_2O_3

MnO and Cr_2O_3 oxide powders were annealed together to investigate reactions between these oxides under the annealing conditions. Figure 4-104 is an XRD spectrum of the MnO powders confirming the powder is MnO. Figure 4-105 is an XRD spectrum of the Cr_2O_3 powders confirming the powder is Cr_2O_3. Figure 4-106 is the XRD spectrum of powders after annealing showing only MnO and Cr_2O_3 peaks. Under the annealing conditions in this investigation MnO and Cr_2O_3 powders did not combine to form the $MnCr_2O_4$ spinel.

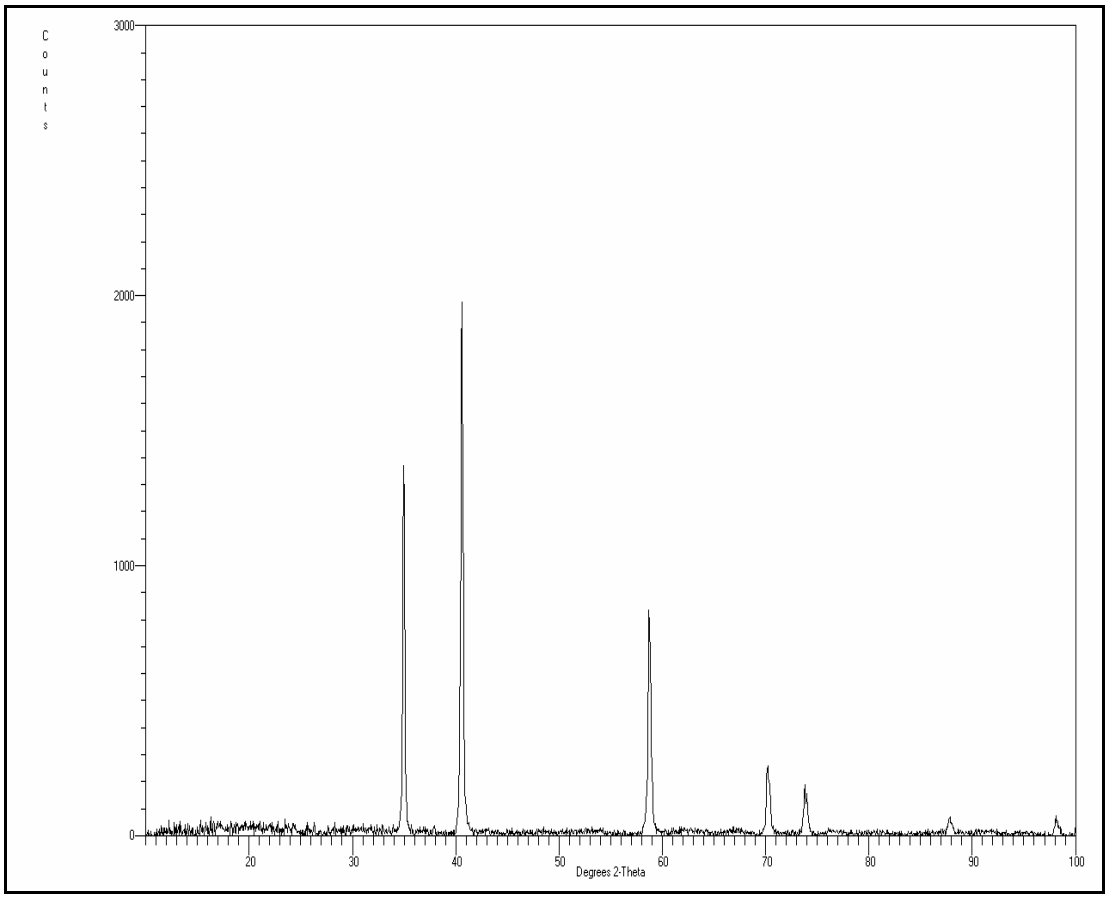

Figure 4-104: XRD trace showing characteristic peaks of MnO before annealing.

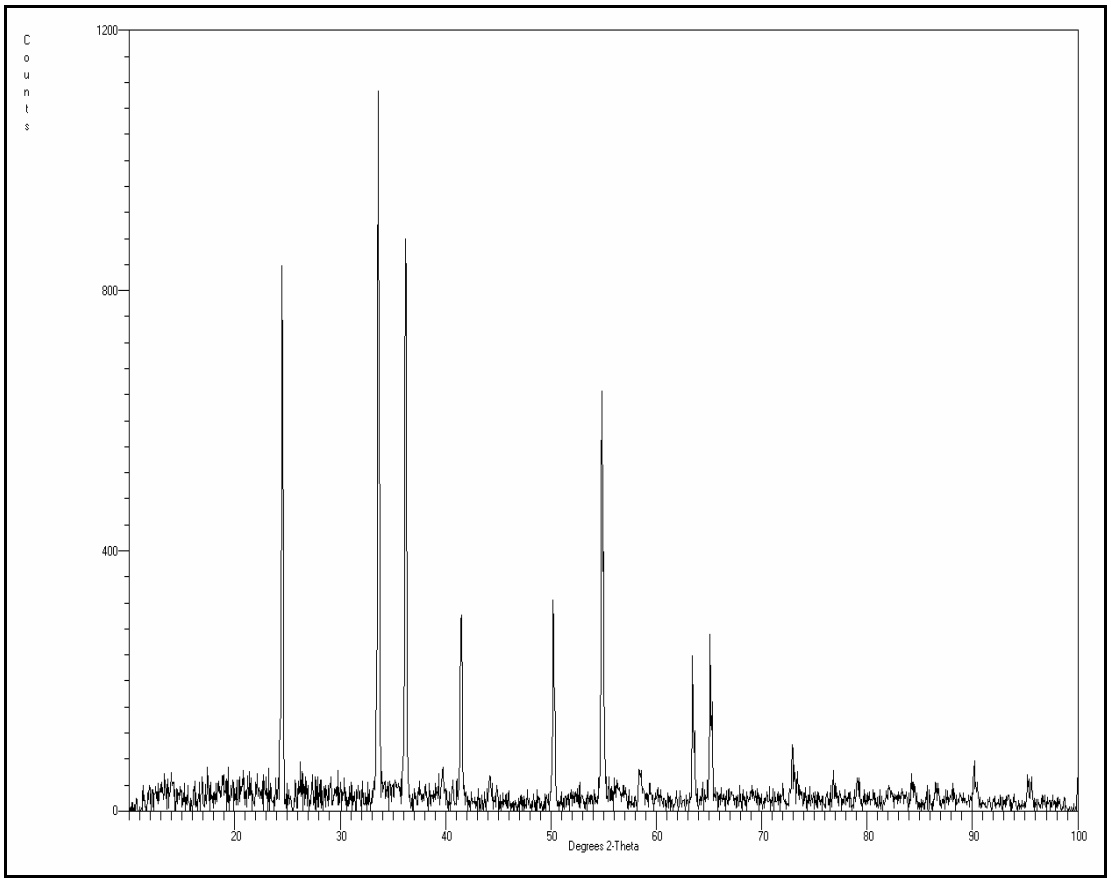

Figure 4-105: XRD trace showing characteristic peaks of Cr_2O_3 before annealing.

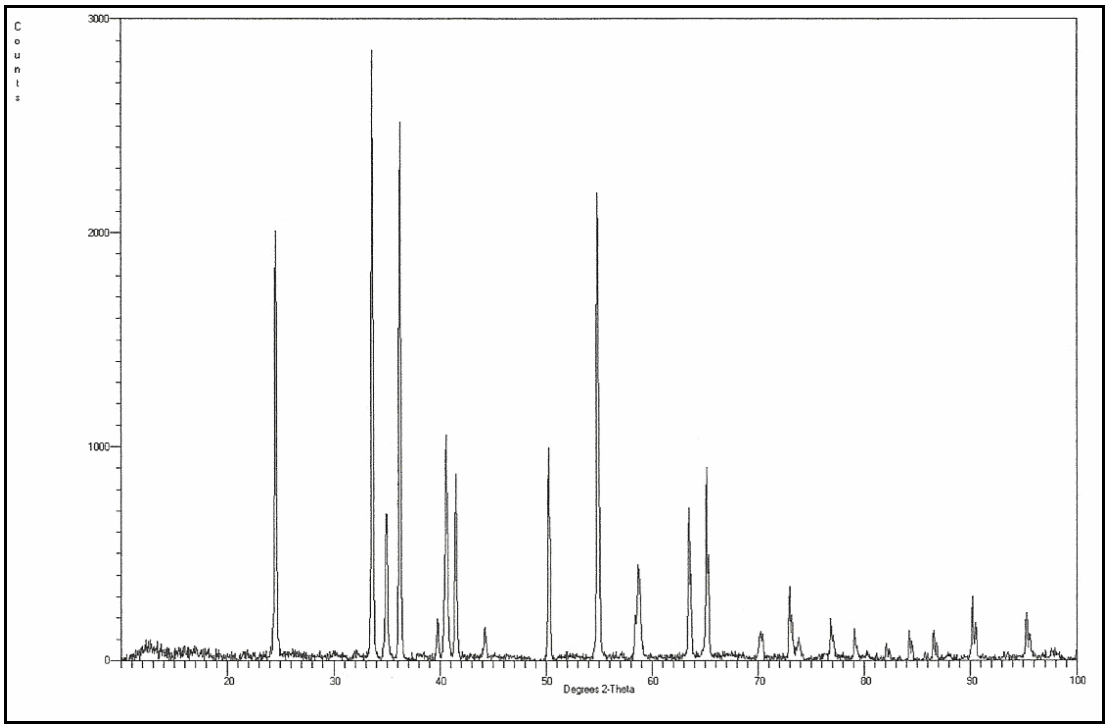

Figure 4-106: XRD trace of mixed oxides after annealing of a 50-50 mixture of MnO and Cr_2O_3 powders annealed at 700 °C under a vacuum of 10^{-2} Torr.

Chapter 5 : Discussion

5.1 Formation of Oxides

The results obtained in this investigation demonstrate that the surface of annealed low carbon strip steel not only contained the $MnCr_2O_4$ spinel but also other oxides, such as (MnFe)O and $Mn(CrAl)_2O_4$. The two major oxides, $MnCr_2O_4$ and (MnFe)O were predominantly located on the steel surface at α-iron grain boundaries.

The 'edge defect' observed in tinplate was caused by the formation of coarse $MnCr_2O_4$ spinel precipitates and thus the result of the selective oxidation of manganese and chromium. The selective oxidation of manganese and chromium can take place during annealing under environments reducing for iron because manganese and chromium have much higher affinities for oxygen than iron. Interestingly the main oxidation products observed in this investigation were (MnFe)O and $MnCr_2O_4$ instead of MnO and Cr_2O_3.

5.1.1 Thermodynamic Consideration

The formation potential of the various oxides observed in this investigation thermodynamically depends on their formation energy at the annealing temperatures. Although for the $MnCr_2O_4$ spinel oxide the free energy of formation, ΔG_f value at 298 K was available [66] the thermodynamic data on the formation of the $MnCr_2O_4$ spinel in the required temperature range was not available in the literature. This however can be deduced from the available thermodynamic data for some well researched similar spinels such as $FeCr_2O_4$, $MgCr_2O_4$, $FeAl_2O_4$, $MnAl_2O_4$ and $MgAl_2O_4$ [67]. By comparing the values of ΔG_f at 298 K and the values of ΔG_f at elevated temperatures of the following spinels, $FeCr_2O_4$, $MgCr_2O_4$, $FeAl_2O_4$, $MnAl_2O_4$ and $MgAl_2O_4$ it was possible to estimate the ΔG_f values for the $MnCr_2O_4$ spinel at elevated temperatures assuming the $MnCr_2O_4$ spinel formed via reaction 5.a and ΔG_f value for the $MnCr_2O_4$ spinel changes with temperature in a similar way to other spinels. Figure 5-1 shows the formation energies of the selected spinels and the estimated formation energy of the $MnCr_2O_4$ spinel as a function of temperature. The

solid lines were obtained from the literature [67] and the dashed lines are either estimated or extrapolated from the experimental ones.

$$Mn + 2Cr + 2O_2 \rightarrow MnCr_2O_4 \qquad (5.a)$$

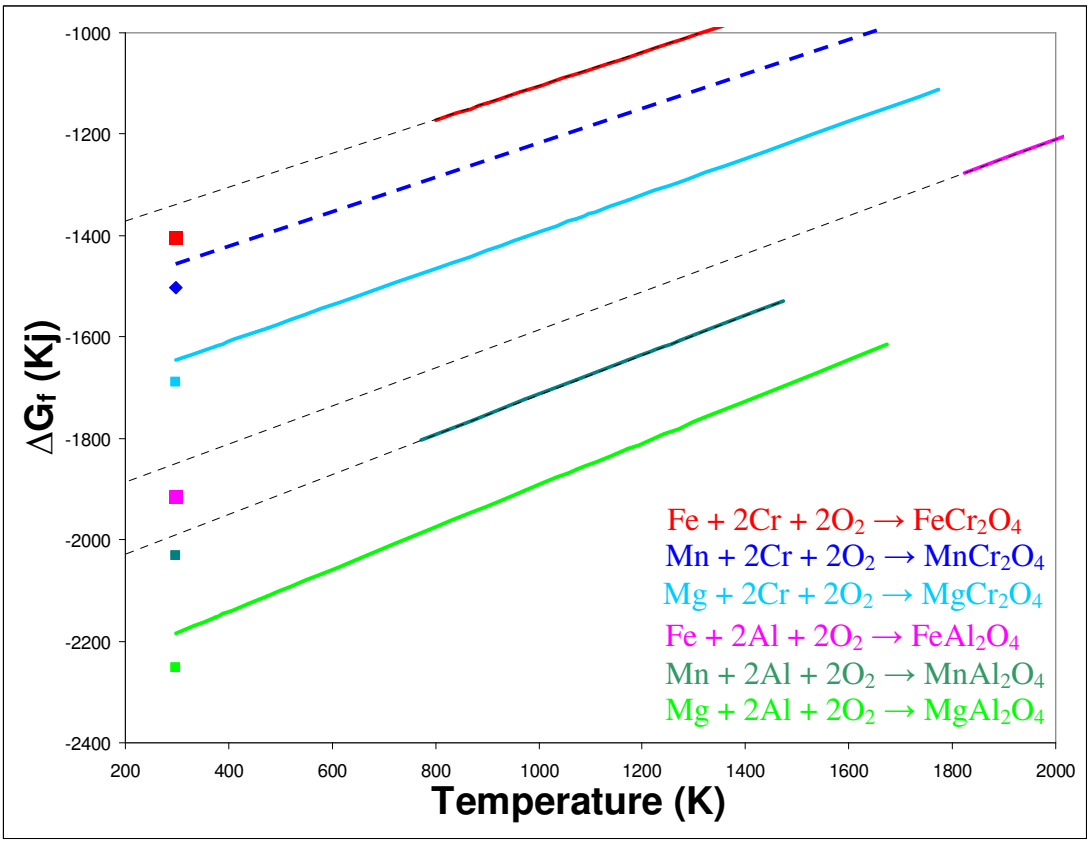

Figure 5-1: The Gibbs energies of formation of selected spinel oxides at 298 K and at elevated temperatures. The solid lines were obtained experimentally and the dash lines are extrapolated from the experimental ones. The dashed blue line indicates the estimated Gibbs energy of formation of $MnCr_2O_4$ spinel.

The deduced formation energy for the $MnCr_2O_4$ spinel is halved and plotted against temperature in Figure 5-2 representing the free energy of reaction 5.b. The free energy of reactions 5.c-5.e forming FeO, MnO and Cr_2O_3 are also plotted against temperature in Figure 5-2.

$$\tfrac{1}{2}Mn + Cr + O_2 \rightarrow \tfrac{1}{2}MnCr_2O_4 \qquad (5.b)$$

$$2Fe + O_2 \rightarrow 2FeO \qquad (5.c)$$

$$2Mn + O_2 \rightarrow 2MnO \qquad (5.d)$$

$$\tfrac{4}{3}Cr + O_2 \rightarrow \tfrac{2}{3}Cr_2O_3 \qquad (5.e)$$

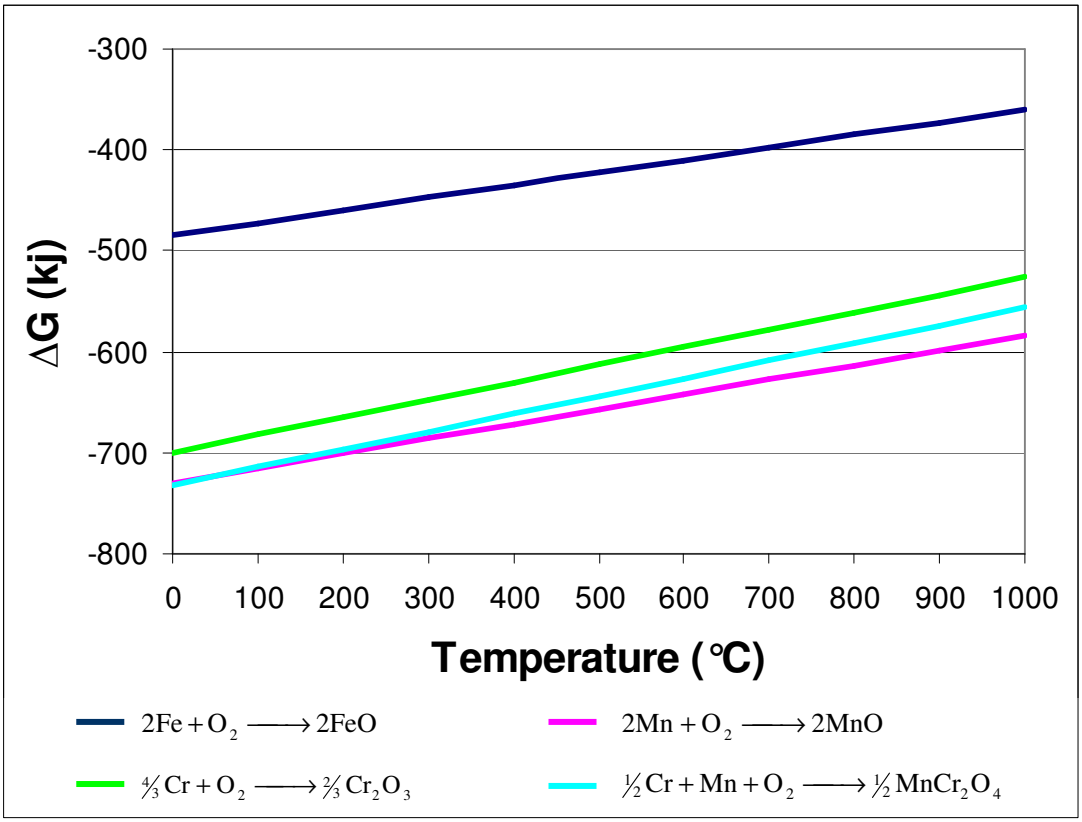

Figure 5-2: The Gibbs energies of selected reactions. The $MnCr_2O_4$ spinel reaction was estimated from the behaviour of similar spinel oxides over the temperature range.

It can be seen that MnO has the most negative formation energy which is followed by $MnCr_2O_4$ in the temperature range 0 -1000 °C. Thus MnO and $MnCr_2O_4$ of the four oxides have the highest potential to form at the annealing temperatures. Since the steels were annealed in 95% N_2 + 5% H_2 gas the water content in the annealing gas is the main source of the oxygen. Hence it is likely that the $MnCr_2O_4$ spinel forms by reaction 5.f.

$$½Mn + Cr + 2H_2O \rightarrow ½MnCr_2O_4 + 2H_2 \qquad (5.f)$$

Figure 5-3 shows the relationship between formation temperature of the four oxides and the water content of the annealing gas in terms of H_2O/H_2 ratio. For a given temperature MnO may form in an annealing gas with much less water content than FeO. All oxides except the FeO have similar formation potentials and MnO has the highest potential followed by $MnCr_2O_4$. If the activities of manganese and chromium

in the steels are taken into account Figure 5-3 is replaced by Figure 5-4 which shows that $MnCr_2O_4$ has the virtually the same formation potential as MnO at 700 °C.

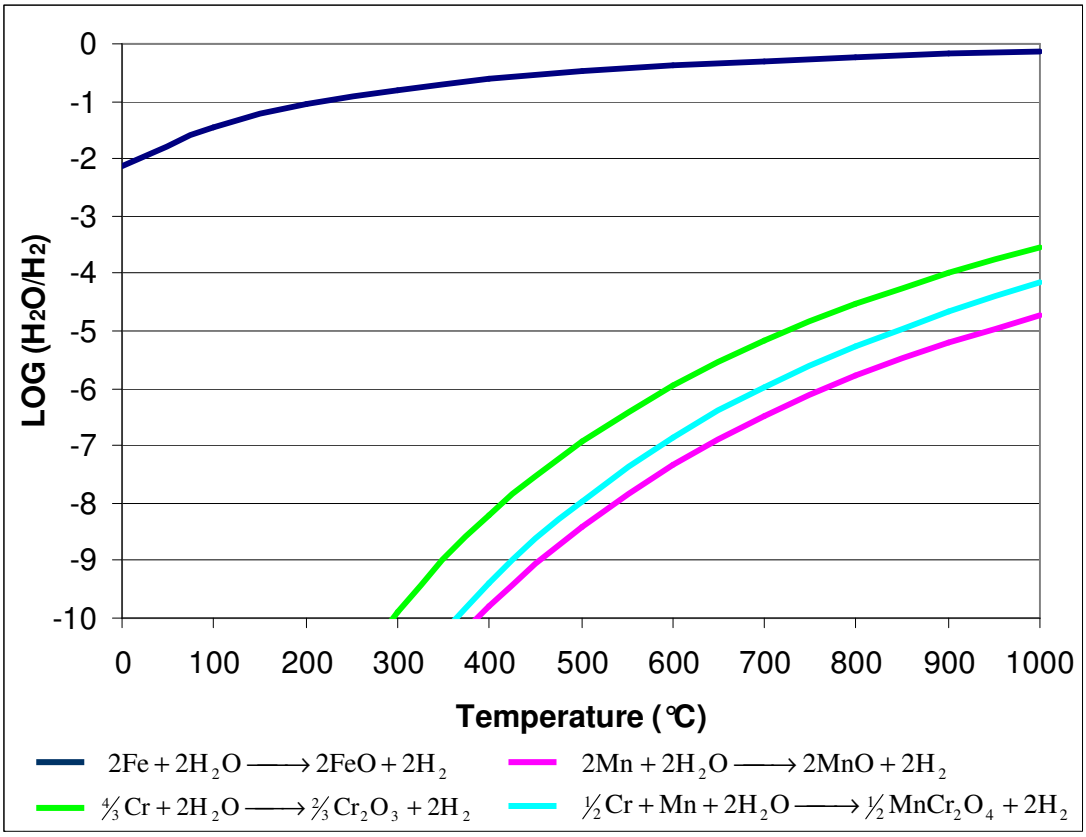

Figure 5-3: The H_2O/H_2 ratio for the formation of selected oxides over the given temperature range. The $MnCr_2O_4$ spinel reaction was estimated from the behaviour of similar spinel oxides.

The water content in the annealing gas is commonly measured by the dewpoint of the gas. The relationship between the dewpoint and the saturation vapour pressure of water of an annealing gas is shown in equation 2.16 [40]. Using this relationship, the dewpoint of hydrogen containing annealing gas can be converted to H_2O/H_2 ratio. Therefore the annealing conditions that represent the laboratory 5% H_2 + 95% N_2 annealing at 700 °C can be obtained and are shown in Figure 5-4.

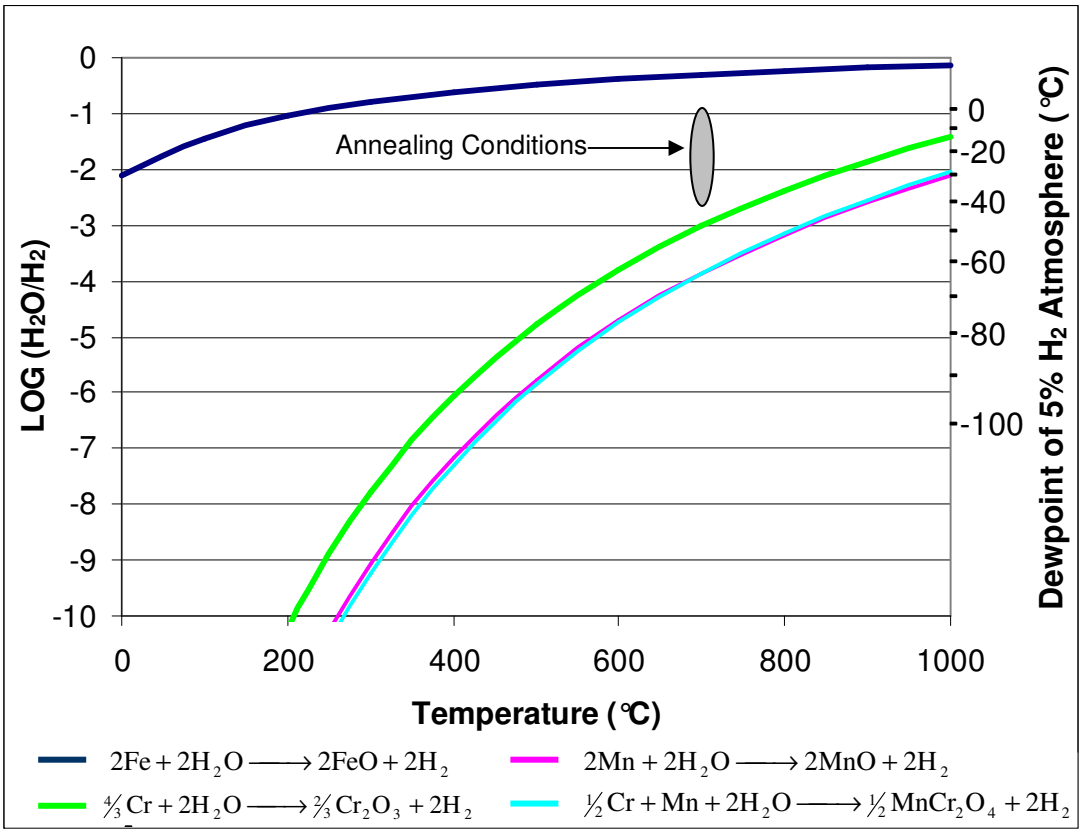

Figure 5-4: The H_2O/H_2 ratio for the formation of selected oxides over the given temperature range considering the activity of manganese (0.24 wt%) and chromium (0.06 wt%) in steel. The annealing conditions represent the 5% H_2 + 95% N_2 annealing at 700 °C simulated in the laboratory. The $MnCr_2O_4$ spinel reaction was estimated from the behaviour of similar spinel oxides.

Under the annealing conditions FeO was not expected to form. The MnO and $MnCr_2O_4$ spinel oxides were more likely to form than Cr_2O_3, which is consistent with what was observed in this investigation. Although it was thermodynamically possible for Cr_2O_3 to form, MnO and $MnCr_2O_4$ have much lower formation energies and are likely to form before Cr_2O_3. As a result chromium may be preferentially oxidised as the $MnCr_2O_4$ spinel. As the formation of $MnCr_2O_4$ spinel consumes most of the chromium in the steels the activity of chromium will be significantly reduced for the formation of Cr_2O_3. Consequently the formation of Cr_2O_3 was completely suppressed. Furthermore, the relative high manganese to chromium ratio also increases the formation potential of the $MnCr_2O_4$ spinel in the steels. Therefore the low formation energy and the high manganese to chromium ratio in the steels in this investigation favour the formation of $MnCr_2O_4$ over Cr_2O_3.

5.1.2 Surface Spinel Oxides

The ternary AB_2O_4 spinel oxide may be represented by the double oxide $AO.B_2O_3$. $MeO.Cr_2O_3$ double oxide, where Me is a bivalent metal, can be produced by fusing Cr_2O_3 with oxides of more strongly basic bivalent metals [68]. Kiessling [51] reported that the Cr_2O_3 can be completely substituted by Al_2O_3 in the $MnO.Cr_2O_3$ double oxide.

In addition to the $MnCr_2O_4$ spinel there were several spinel variants such as $Mn(CrV)_2O_4$ and $Mn(CrAl)_2O_4$, which were observed on the annealed sheet surface. In some of the low chromium steels, particularly steel L1 annealed at 700 °C, the vanadium level in the spinel precipitates was observed to be much higher, approximately 10 atomic % of metal in the spinel. The vanadium replaces the chromium in the spinel and the manganese level in the spinel remains constant. The formation of the complex spinel $Mn(CrV)_2O_4$ maybe considered as the solid solution of MnV_2O_4 in the $MnCr_2O_4$. Presumably the MnV_2O_4 has similar formation potential as the $MnCr_2O_4$. Since vanadium is a trace element in the steels the size and the volume was relative small. In the higher chromium steels the vanadium content in the $Mn(CrV)_2O_4$ precipitates were usually very low less than 2% of the metal in the oxide. However, in the low chromium steels the $MnCr_2O_4$ precipitates were smaller while the size of the MnV_2O_4 was constant and independent of chromium and thus the vanadium to chromium ratio in the spinel increases.

In addition to the grain boundary $MnCr_2O_4$ precipitates fine $Mn(CrAl)_2O_4$ precipitates (<50nm in diameter) were frequently observed on the steel surface but not at grain boundaries. The fine matrix $Mn(CrAl)_2O_4$ precipitates contained substantial aluminium (up to 50 at%) at expense of chromium. This suggests that the chromium at the steel surface was predominantly located at grain boundaries. Away from the grain boundaries the supply of chromium to the steel surface was limited so the $MnCr_2O_4$ precipitates were much finer. Again the formation of the complex spinel $Mn(CrAl)_2O_4$ maybe considered as the solid solution of $MnAl_2O_4$ in the $MnCr_2O_4$ or visa versa. In this case the sizes of the $MnAl_2O_4$ in the $MnCr_2O_4$ are comparable and thus substantial aluminium was observed in these complex spinel particles. The extensive solid solubility between the spinel variants maybe due to the

fact they all have the same crystal structure and similar lattice parameters satisfying the Hume-Rotherey rules for extensive solid solubility between two solids [69].

5.1.3 The $MnCr_2O_4$ Spinel Formation Mechanism

$MnCr_2O_4$ like other spinel oxides usually form at high temperatures by fusion [68]. $MnCr_2O_4$ may also form by the solid-state reaction between MnO and Cr_2O_3 (reaction 5.g) at lower temperatures about 1000 °C at the gas/metal interface when a 430 stainless steel was exposed to oxidation environments [46]. However, at the annealing temperature of 700 °C in this investigation it seems that the $MnCr_2O_4$ spinel can not be produced via the solid state reaction between MnO and Cr_2O_3 either in vacuum, air or under the 5% H_2 + 95% N_2 annealing gas.

$$MnO + Cr_2O_3 \rightarrow MnCr_2O_4 \qquad (5.g)$$

The TEM cross section sample showed fine $MnCr_2O_4$ particles at the grain boundary well below the surface (Figure 4-100) and since neither Cr_2O_3 nor MnO was observed adjacent to the fine $MnCr_2O_4$ particles it is unlikely the formation of $MnCr_2O_4$ in this investigation was via a solid chemical reaction between Cr_2O_3 and MnO. Furthermore, the manganese oxide observed in this investigation contained a small quantity of iron. If the $MnCr_2O_4$ was formed by the solid state reaction of Cr_2O_3 and the (MnFe)O oxide in this investigation it would be expected that iron would also be present in the spinel. However, the $MnCr_2O_4$ spinel oxides contained no measurable iron. This confirms that the $MnCr_2O_4$ spinel observed in this investigation was not the product of the solid-state reaction between the two binary oxides. Alternatively, the ternary spinel may form directly from the oxidation of manganese and chromium. It should be noted however that this direct formation mechanism does not preclude the possibility of corundum type oxide (Cr_2O_3, Al_2O_3) as a precursor.

5.1.4 Mixed Surface Manganese and Iron Oxide (MnFe)O

The manganese oxide observed in this investigation was not pure MnO as it contains a small amount of iron thus it may be written as (MnFe)O. The manganese to iron

ratio in the oxide precipitates was more than 9. Again (MnFe)O can be considered as the solid solution of FeO in MnO as these two oxides have the same crystal structure and similar lattice parameter [44]. However, thermodynamically under the annealing conditions FeO was not expected to form. It is very possible that FeO was present on the steel surface prior to the annealing and it may act as heterogeneous nucleation site for MnO although most of the FeO will be reduced at the annealing temperature by the annealing gas, which was designed to be reducing for iron. The iron present in the manganese oxide might also be explained by localised areas of increased oxygen potential at the manganese oxides formed on the steel surface. Mixed manganese and iron oxides have been observed on the surface of steels in other investigations under similar annealing conditions [25, 41, 45].

5.1.5 Surface Grain Boundary Oxides

The oxides, (MnFe)O and $MnCr_2O_4$, were predominantly located at the grain boundaries which may be explained by grain boundaries acting as fast diffusion paths for the alloying elements to the steel surface [30, 70]. Oxide precipitates were commonly observed at the intersections between the grain boundaries at the free surface when low alloy steel was annealed [22, 23]. The formation of the grain boundary oxides observed in this investigation is illustrated schematically in Figure 5-5. Initially fine (MnFe)O and $MnCr_2O_4$ were formed at the early stage of annealing and as annealing proceeded the (MnFe)O grew much faster than the $MnCr_2O_4$. This was probably due to the higher manganese content compared to chromium content and the higher diffusivity of manganese than chromium in iron at high temperatures [47]. Eventually the smaller $MnCr_2O_4$ particles were capped by the much larger (MnFe)O particles, which is consistent with the fact that the relative heights of the Mn Kα and Cr Kα peaks in the EDS spectra reverse after etching as the etching removes only the (MnFe)O particles (Figure 4-56 and Figure 4-28). This observation was further supported by the TEM results which show the network of the $MnCr_2O_4$ along the grain boundaries was largely preserved but no (MnFe)O on the carbon extraction replicas which were prepared after the etching.

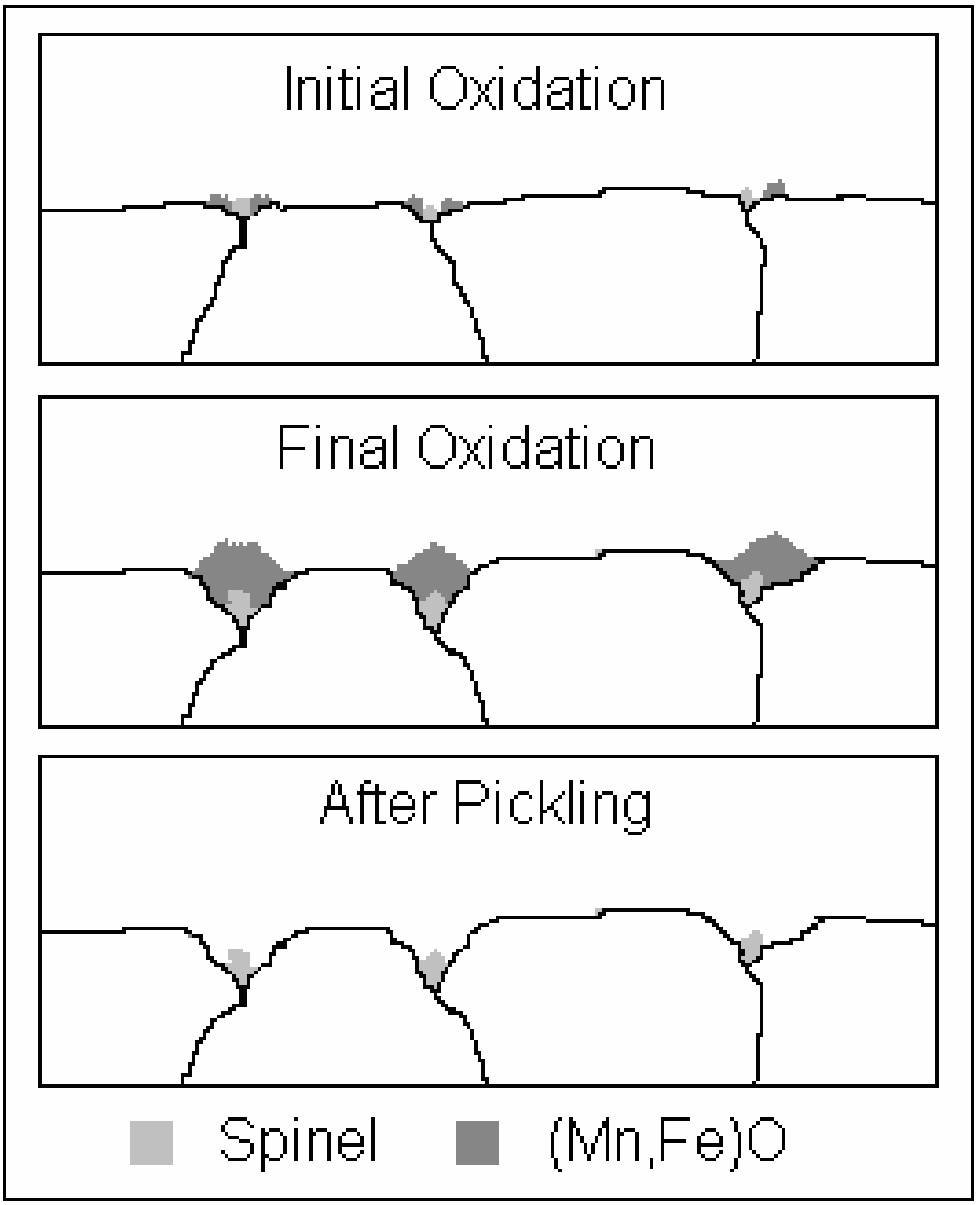

Figure 5-5: Schematic drawings showing the formation of surface grain boundary (Fe,Mn)O and $MnCr_2O_4$ precipitates on low carbon steels annealed at 700 °C in 5% H_2 + 95% N_2 atmosphere.

5.2 Selective Oxidation of Chromium and Manganese

Selective oxidation can be internal or external. Internal oxidation occurs when oxygen dissolves at the surface and diffuses into an alloy and causes precipitation of oxides below the alloy surface. The nucleation of the oxides occurs at a reaction front parallel to the specimen surface. Whether the selective oxidation is external or internal is governed by the inward oxygen diffusion and outward diffusion of the solute [17]. External oxidation occurs when the outward diffusion of the alloying element is large enough to form a continuous oxide layer and stop inward oxygen diffusion and hence prevent internal oxidation [17].

In this investigation selective oxidation predominantly occurred at grain boundaries as they acted as fast diffusion paths. Wagner's [20] theory on selective oxidation will be extended to grain boundary selective oxidation, i.e. selective oxidation of chromium and manganese at grain boundaries can be internal and external. The nature of the selective oxidation will affect the size and distribution of the grain boundary oxides. If the selective oxidation is external then the surface oxides are either coarser in size or larger in volume or both compared to internal selective oxidation.

5.2.1 Effect of Annealing Temperature on Selective Oxidation

Increasing the annealing temperature will reduce the driving force for metals to oxidise, as all metal oxidation reactions are exothermic. However in this investigation increasing the annealing temperature from 675 °C to 750 °C increased the surface oxidation. Grain boundary selective oxidation is strongly related to the inward oxygen grain boundary diffusion and outward alloying element grain boundary diffusion. Temperature affects the diffusion of elements in the steel. From equations 2.10 and 2.11 we know the ratio of alloying element diffusion to oxygen diffusion is given by equation 5.1.

$$\frac{D_X}{D_O} = \frac{D_X' \, e^{\left(\frac{-Q_X}{RT}\right)}}{D_O' \, e^{\left(\frac{-Q_O}{RT}\right)}} \qquad (5.1)$$

The ratio of alloying element grain boundary diffusion to oxygen grain boundary diffusion can be deduced by assuming that the grain boundary diffusion activation energies are half the values for bulk diffusion (Q_o and Q_x) in a single crystal lattice [16]. Therefore equation 5.1 was modified to produce equation 5.2.

$$\frac{D_{X.GB}}{D_{O.GB}} = \frac{D'_X \, e^{\left(\frac{-Q_X}{2RT}\right)}}{D'_O \, e^{\left(\frac{-Q_O}{2RT}\right)}} \qquad (5.2)$$

Equation 5.2 can be rearranged to give equation 5.3.

$$\frac{D_{X.GB}}{D_{O.GB}} = \frac{D'_X}{D'_O} e^{\left(\frac{Q_O - Q_X}{2RT}\right)} \qquad (5.3)$$

The activation energies for bulk diffusion for the alloying elements (Q_X) in this investigation (chromium and manganese) are higher than the activation energy for bulk diffusion of oxygen (Q_O) in α-iron (Table 5.1). Therefore $(Q_O - Q_X)$ will be a negative value meaning increasing the temperature will increase value of $e^{\left(\frac{Q_X - Q_O}{2RT}\right)}$ in equation 5.3 which will increase the ratio of alloying element grain boundary diffusion to oxygen grain boundary diffusion. Hence increasing the annealing temperature will increase the rate of grain boundary diffusion of alloying elements to the surface compared to the rate of oxygen grain boundary diffusion into the steel. Therefore assuming the amount of oxygen at the steel surface is the same increasing temperature will lead to more surface or external grain boundary oxidation.

Table 5-1: Activation energies for bulk diffusion for elements in α-iron [30].

Please see print copy for Table 5.1

However, the annealing temperature will also affect the amount of dissolved oxygen at the steel surface and this must be considered. Huin et al. [40] reported that the

mass concentration of dissolved oxygen on the steel surface is related to the partial pressure of oxygen in the annealing gas and the temperature (equation 2.18). The partial pressure of oxygen in the annealing gas is related to the ratio of H_2O/H_2 and temperature (equation 2.19). By combining equation 2.18 and 2.19 the relationship between the ratio of H_2O/H_2, temperature and the mass concentration of dissolved oxygen on the steel surface can be produced and is shown by equation 5.4

$$\log_{10} C_O^{surf} = 4.00 - \frac{3690}{T} + \log_{10}\left(\frac{p(H_2O)}{p(H_2)}\right) \qquad (5.4)$$

For a given ratio of H_2O/H_2 the mass concentration of dissolved oxygen on the steel surface is temperature related. Increasing the annealing temperature will increase the mass concentration of dissolved oxygen on the steel surface because of the greater dissociation of water vapour at higher temperatures.

Increasing annealing temperature would be expected to increase the surface oxidation if the mode of oxidation remains external in nature. This is caused by the increase in both the diffusion of alloying elements to the surface and the amount of dissolved oxygen at the surface. However, if the temperature is increased beyond this range the mode of oxidation may become internal in nature, which would decrease the surface oxidation since the amount of oxygen at the steel surface will be further increased and the supply of oxygen into the steel becomes dominant. In this investigation the surface oxidation increased with increasing annealing temperature from 675 °C to 750 °C, therefore it is expected that all the oxidation was external in nature.

Mataigne et al. [22] suggested a criteria for the transition between external and internal selective oxidation modes for steels (equation 2.15). This has been adjusted for grain boundary selective oxidation and is shown in equation 5.5

$$\sum_X N_X^o \sqrt{n D_{X.GB} V_{XO_n}} \geq \sqrt{\frac{\pi g^* V}{2}} \sqrt{N_O^S D_{O.GB}} \qquad (5.5)$$

External oxidation should occur when the LHS (left hand side) is greater or equal to the RHS (right hand side). In all other cases internal oxidation should occur. The LHS of equation 5.5 is dependent on the molar fraction of elements in the steel, diffusion of elements in the steel and the molar volume of the oxide. A typical steel in this investigation had 0.06 wt% Cr and 0.24 wt% Mn. This corresponds to a molar fraction of 6.44×10^{-4} and 2.44×10^{-3} for chromium and manganese respectively. As chromium forms $MnCr_2O_4$ in this investigation the molar volume fraction of $MnCr_2O_4$ is used instead of Cr_2O_3 for the chromium supply section of the LHS of this relationship. The molar volume fractions of MnO and $MnCr_2O_4$ are 13.2 cm^3/mole and 45.4 cm^3/mole respectively. The RHS of equation 5.5 is dependent on the alloy molar volume (7.1 cm^3/mole), the critical volume fraction of precipitated oxides which leads to the obstruction of all oxygen inward diffusion (0.3 Rapp's estimate), the molar fraction of dissolved oxygen at the surface, and the grain boundary diffusion of oxygen.

Figure 5-6 shows relationship produced by equation 5.5 graphically. For internal grain boundary oxidation to occur the annealing environment must be above the line and for external grain boundary oxidation below the line. The measured dewpoints of the 5% H_2 + 95% N_2 annealing environment in the temperature range 25 °C – 700 °C are shown in Figure 3-3. The dewpoint varies from -45 °C to 0 °C upon heating. Assuming the dewpoint changes are similar for the other annealing temperatures these dewpoints are converted to a H_2O/H_2 ratio and shown on Figure 5-6. Clearly the laboratory annealing in 5% H_2 + 95% N_2 conditions are below the line in Figure 5-6 hence grain boundary selective oxidation is expected to be external in nature which supports the observations of this investigation.

The increase in surface oxidation observed with increasing temperature can be explained by the increase in alloying element diffusion to the surface combined with the increase in the amount of dissolved oxygen at the surface.

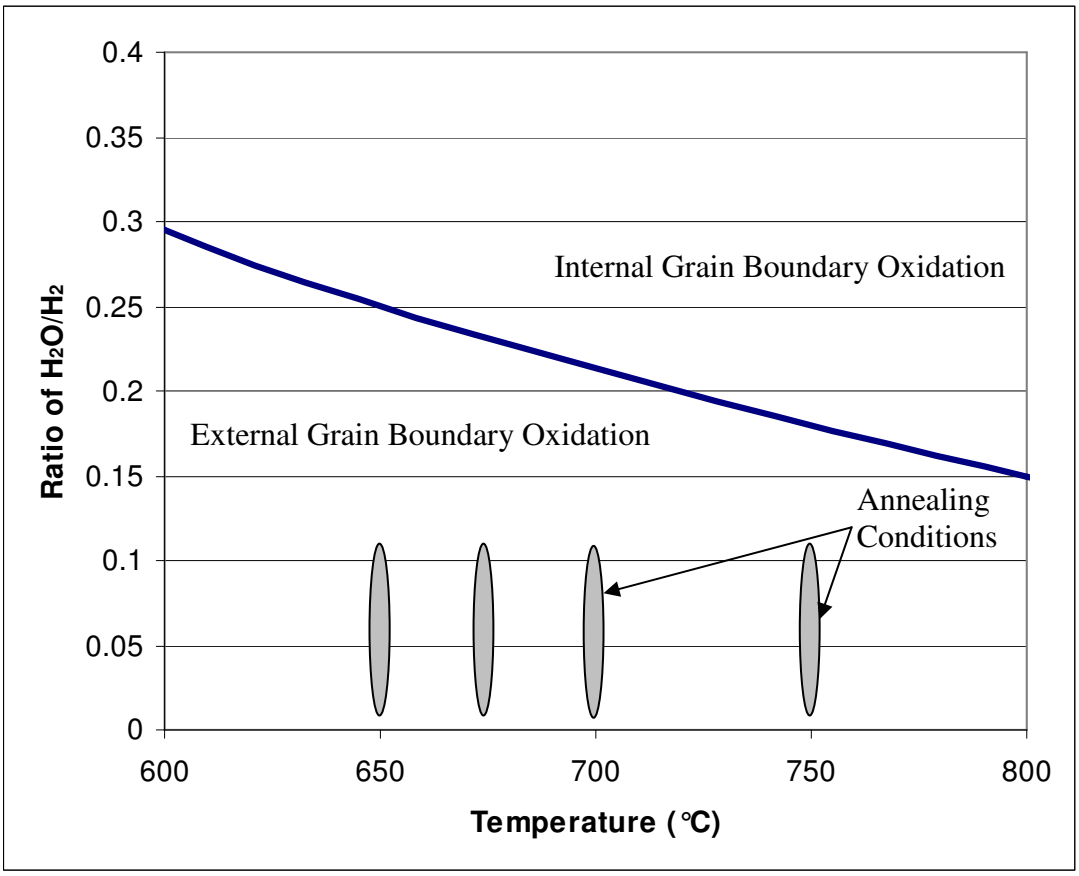

Figure 5-6: The effect of temperature and H_2O/H_2 ratio has on the mode of selective oxidation. The dark eclipses indicate the annealing conditions for the 5% H_2 + 95% N_2 laboratory annealing.

Another effect of increasing the annealing temperature that must be considered is a change in the phase of the steel. Steels annealed at 750 °C may have austenite present at the annealing temperature. According to the iron-carbon phase diagram the most austenite will be present in steels with the higher carbon concentration. In this investigation the steel with the highest carbon level was L9, which contains 0.07 wt% carbon. Using the iron-carbon phase diagram it is expected that at 750 °C for 0.07 wt% carbon the amount of austenite present is less than 10%. This low percentage of austenite does not seem to greatly affect the surface oxidation.

At 650 °C

At this annealing temperature neither (MnFe)O nor $MnCr_2O_4$ surface grain boundary precipitates were observed though they are expected to form according to the earlier thermodynamic calculations (Figure 5-4). It is unclear whether this was due to these oxides not being formed because the activation energy for the oxide formation was

not reached at this temperature or due to the (MnFe)O formed being too fine to be resolved by SEM or the fine $MnCr_2O_4$ not being replicated during the carbon extraction replica technique.

Between 675 °C and 750 °C

(MnFe)O Precipitates

The increase in the annealing temperature from 675 °C to 750 °C increased the surface area covered by (MnFe)O particles (Figure 4-58). The increase was due to the faster diffusion of manganese to the surface and the more dissolved oxygen at the steel surface at higher temperatures. The effect of annealing temperature on the surface enrichment of manganese during annealing has been investigated previously and is in agreement with the findings of this investigation. Hudson et al. [36] demonstrated that increasing the annealing temperature from 580 °C to 730 °C greatly increased the surface enrichment of manganese.

$MnCr_2O_4$ Precipitates

The effect of annealing temperature on the mean $MnCr_2O_4$ spinel precipitates size is shown in (Figure 4-95). The increase in annealing temperature from 675 °C to 700 °C increased the average size of surface grain boundary $MnCr_2O_4$ spinel precipitates in all the steels in this investigation. Increasing the annealing temperature from 700 °C to 750 °C increased the average size of surface grain boundary $MnCr_2O_4$ spinel precipitates of the low chromium steels in this investigation. However, the steels with higher chromium levels either showed no increase in average size or a slight decrease. This was unexpected, however closer investigation of the particle size distribution of these steels that the surface spinel particles were larger in the steels annealed at 750 °C but there was a higher proportion of small grain boundary precipitates as well. At 750 °C the diffusion path for chromium was not limited only on grain boundaries firstly because the higher temperature makes bulk diffusion easier, secondly at this temperature partial phase transformation $\alpha \rightarrow \gamma$ may have occurred which reduces the driving force for the segregation of chromium at grain boundary. The increase in annealing temperature in this investigation increased the surface oxidation of $MnCr_2O_4$. It should be noted however that at an annealing temperature of 675 °C all the steels exhibit a mean spinel particle diameter of less

than 100 nm well below the critical value of 250 nm in diameter for causing the 'edge defect'.

5.2.2 Effect of Steel Composition on Selective Oxidation

The increase of the manganese and chromium contents increased the surface oxidation of the steels by increasing the activities of manganese and chromium. This increase in activities will decrease the amount of oxygen required to form oxides of these elements (equation 2.8). Increasing the concentration of manganese and chromium in the steel will also have the effect of increasing the amount of these elements present at the steel surface and promote external selective oxidation of manganese and chromium. A change in composition in the steel however, will have no effect on the supply of oxygen to the steel surface during annealing. Therefore an increase in alloying elements will increase the supply of alloying elements to the steel surface but not affect the supply of oxygen into the steel therefore increasing external or surface oxidation.

Effect of Manganese Concentration in the Steel

Manganese is one of the major elements in the surface oxides thus increasing the manganese level in the steel increased the surface area of the steel covered by (MnFe)O as shown by Figure 4-58. The increase of the manganese concentration in the steel allows more manganese to diffuse to the steel surface. This observation is consistent with the results reported in the literature that increasing the manganese level in the steel increases the amount of surface manganese oxidation [23, 37, 38].

The average size of (MnFe)O particles on the steel surface annealed at temperatures 675 °C to 750 °C ranged from 600 nm to 1300 nm and was clearly much larger than the critical size (250 nm) for causing the 'edge defect'. However, these precipitates were removed from the surface and hence were not responsible for the 'edge defect'.

Within the composition range of this investigation the manganese content did not seem to have any effect on the $MnCr_2O_4$ spinel oxide in terms of the volume fraction and particle size. This is due to the manganese contents being much higher than chromium contents in the steels. Thus the supply of chromium was the major factor

that governs the $MnCr_2O_4$ spinel particle size and the supply of manganese was not a limiting factor. If the manganese content in the steel was reduced to levels comparable with that of chromium it would be expected that the manganese level in the steel would impact the growth of the $MnCr_2O_4$ spinel particles.

Effect of Chromium Concentration in the Steel

The effect of chromium level in the steel on the $MnCr_2O_4$ spinel is shown in Figure 4-95. An increase of chromium concentration increased the size of surface $MnCr_2O_4$ spinel precipitates. Although this oxide contains both chromium and manganese the manganese level in the steel was much larger than chromium and hence the supply of chromium to the steel surface was the rate-limiting step for surface $MnCr_2O_4$ spinel precipitates. Clearly, increasing the chromium level in the steel will increase the supply of chromium to the steel surface and result in more surface oxidation of chromium. This explains the increase in surface $MnCr_2O_4$ spinel oxide size with increasing steel chromium concentrations.

At the annealing temperatures of 675 °C the increase of the chromium concentration in the steels increases slightly the mean spinel precipitate size. This could be due to the slow rate of chromium diffusion to the surface at this annealing temperature causing less surface oxidation. Furthermore, at 675 °C the average particle size of the $MnCr_2O_4$ spinel precipitates was less than 100 nm, which is well below the critical size of 250 nm to cause the 'edge defect'.

At the annealing temperature of 700 °C the average size of the grain boundary $MnCr_2O_4$ spinel precipitates increases sharply with the content of chromium in the steel. Again the supply of the chromium was the limiting factor for the growth of the $MnCr_2O_4$ spinel at 700 °C. Importantly, at this temperature, the average spinel size was about 250 nm in diameter or larger for the steels with chromium contents higher than 0.05 wt%; and it was less than 200 nm for steels containing less than 0.05 wt% chromium. Therefore at the annealing temperature of 700 °C the 0.05 wt% chromium in the steels seems to be the critical chromium content above which coarse grain boundary $MnCr_2O_4$ precipitates are likely to result in the formation of the surface 'edge defect'.

Steels annealed at 750 °C exhibit a similar relationship. Increasing the chromium in the steel generally increased the mean spinel particle size. At 750 °C the critical value for chromium in the steel to cause the 'edge defect' is 0.04 wt%, lower than at 700 °C.

5.2.3 Effect of Annealing Atmosphere on Selective Oxidation

The effect of the oxygen potential or the H_2O/H_2 ratio of the annealing atmosphere on the selective oxidation of steels is more complex. The high oxygen potential not only encourages more external selective oxidation but also changes the nature of the selective oxidation from external to internal [29]. Consequently there will be an oxygen potential which gives maximum external oxidation and thus the maximum surface grain boundary oxides. Above this critical potential the oxidation becomes internal.

The change in surface oxide particle size of steel samples annealed at different vacuum environments in this investigation demonstrates how the mode of oxidation may have changed (Figure 4-17). The maximum average particle size of about 700 nm observed when the pressure was approximately $1x10^{-3}$ Torr and oxidation was external. At pressures above $1x10^{-3}$ Torr the maximum average particle size was 400 nm to 600 nm which is smaller than that at $1x10^{-3}$ Torr, which suggests that the increased oxygen potential lead to increased oxygen diffusion into the steel. In this case oxidation was partially internal and supply of the alloying elements to the steel surface was the limiting factor for surface oxide growth. At pressures of $1x10^{-5}$ Torr no oxides were formed because of the reduced supply of oxygen.

5.2.4 The 'Edge Defect'

<u>Oxygen Potential and Nitrogen Pick-up</u>

The oxygen potential across the width of batch annealed steel strip may change from the edge to the centre as the strip was tightly wound. The variation may affect the nature of selective oxidation. The oxygen potential across the width of the strip in a tightly wound coil was measured indirectly by measuring the increase in the nitrogen content of the steel which is also known as nitrogen pick-up. Nitrogen pick-up is

related to the dewpoint of the annealing gas [59]. The nitrogen pick-up can also be affected by temperature but can be neglected in this case because it is unlikely that there was a significant temperature variation across the width of the steel strip observed in this investigation due to the small radial distance from the outer wraps of the coil. If a change in temperature was present across the steel strip width, the edges would be expected to be hotter than the coil centre [71]. If this was the case the nitrogen levels at the strip edge would be expected to be higher at the steel edge as increasing temperature increases the degree of nitrogen pick-up [58, 60]. However, the nitrogen levels at the steel edge were lower than the coil centre. This suggests that the change of the nitrogen pick-up across the strip was largely due to the variation of the dewpoint or oxidising potential of the annealing environment across the strip.

The nitrogen pick-up observed in this investigation increased from the edge of the strip to a maximum in the middle of the strip (Figure 4-99). This result is consistent with the results reported by other authors [57, 58] and indicates that the very edge of the strip had the highest oxidising potential and the middle of the strip had the lowest oxidising potential. The oxidising potential at the very edge was effectively that of the annealing gas. The drop of the oxidising potential towards the middle of the strip was likely to be partially due to residual oxygen on the steel surface reacting with carbon in the steel to form carbon monoxide gas. It should be noted that the major oxygen supply was the annealing gas. The very small gap between the wraps traps this carbon monoxide and limits the penetration of the annealing gas.

The ‘Edge Defect’

The variation of the local oxidising potential across the steel strip may lead to different selective oxidation zones across the strip. The very edge of the strip has the highest oxidising potential the same as the annealing gas. If internal oxidation occurs it is more likely to be at the very edge of the strip. In the middle of the strip the oxidising potential is very different from that of the annealing gas and is expected to be at a minimum. In theory the selective oxidation across the strip could be divided into four zones according to their oxidation characteristics: internal grain boundary oxidation, mixed grain boundary oxidation, external grain boundary oxidation and oxidation free, (as shown schematically in Figure 5-7). The internal grain boundary

oxidation zone if it exists is expected to be located closest to the coil edge followed by the mixed and then the external grain boundary oxidation zone. The grain boundary oxidation free zone is most likely located at the centre of the coil. The size and location of these four zones will vary from coil to coil and wrap to wrap. Schematic cross section images of these oxidation zones is shown in Figure 5-8.

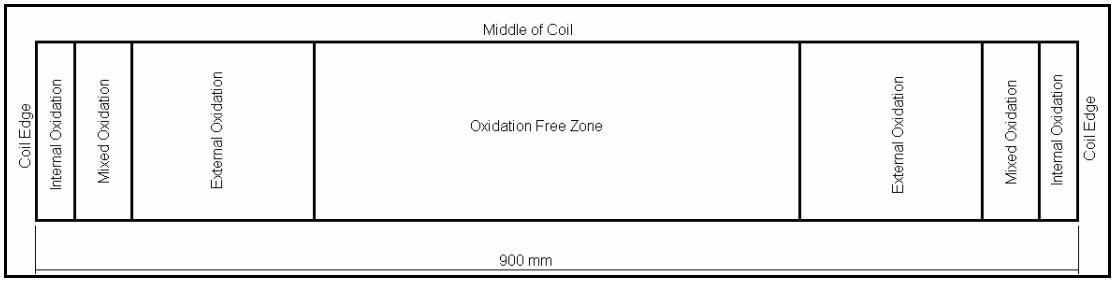

Figure 5-7: Schematic diagram of different zones of grain boundary oxidation present across the coil width.

The internal grain boundary oxidation zone is characterised as a region with no surface oxides and a high oxidation potential. The relative large oxygen supply to the steel surface allows fast grain boundary diffusion of oxygen into the steel where it combines with alloying elements forming oxides below the steel surface.

The external grain boundary oxidation zone is characterised as a region with oxides forming on the surface only. In this zone oxygen penetration in the steel is reduced by the lower supply of oxygen to the steel surface, allowing alloying elements to diffuse through the grain boundaries to the steel surface before they combine with oxygen forming surface oxides. These surface grain boundary oxides block further grain boundary diffusion of oxygen into the steel. As a result grain boundary oxidation is predominantly external. Particles in the external oxidation zone decrease in size and volume as the distance from the coil edge is increased. This decrease is caused by the reduction in the supply of oxygen to the steel surface. This reduction in oxygen supply limits the oxide growth. The area having the maximum surface oxide particles in terms of volume and size is where the grain boundary selective oxidation begins to be entirely external. Between the internal oxidation and external oxidation zones a transition area where mixed internal and external grain boundary oxidation exists. This area of mixed oxidation is characterised by a smaller volume of surface particles compared to the external oxidation zone. The oxidation free zone is

characterised as a region with no surface grain boundary oxides due to the very low oxygen potential.

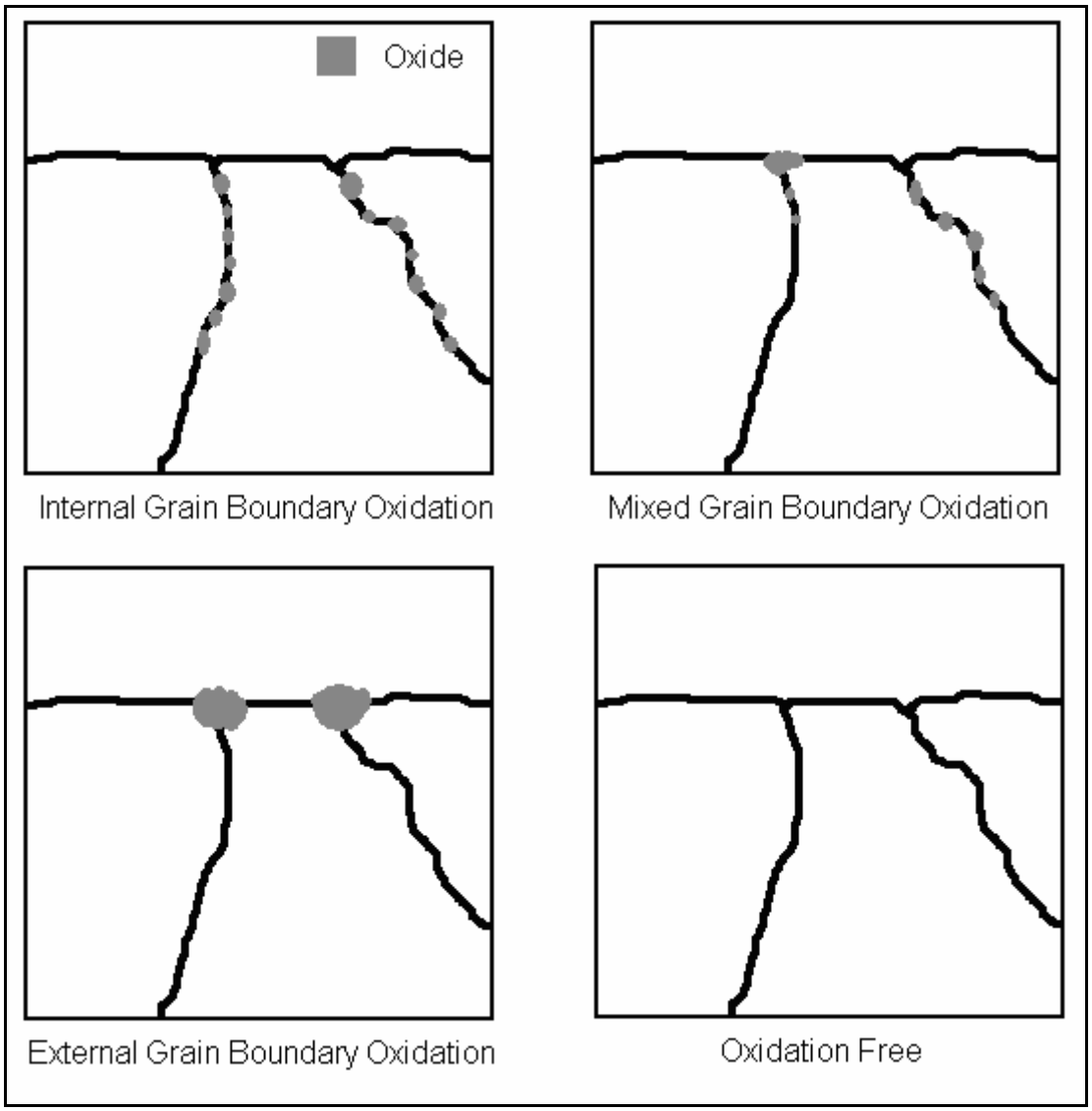

Figure 5-8: Schematic cross section diagrams of each oxidation zone present across the coil width.

The location and width of the grain boundary oxidation zones differ from coil to coil and even from wrap to wrap and this can be explained in terms of the location of the coil in the furnace and the tightness of coil wraps. A change in the tightness of the coil wrapping will change the gap between wraps of the coil. This will affect the penetration of the annealing gas to the centre of the coil and hence the oxygen potential. If a coil is tightly wrapped the penetration of the annealing gas will be limited. The grain boundary oxidation zones mentioned above will be translated towards the edge of the coil and the oxidation free zone will be increased. If a coil is

wrapped loosely, the annealing gas will be able to penetrate across the width of the steel strip. This will lead to increased oxidation and the oxidation zones being extended towards the centre of the coil. The oxidation free zone would be limited in size or not observed in the case of loosely wrapped coils. It has also been observed that the 'edge defect' band can exhibit a wavy pattern, particularly the inner boundary of the band. This formation pattern could be attributed to the influence of poor strip shape, such as edge wave, on the variation in the inter-wrap tightness. The location of the coil in the furnace will affect the temperature the steel reaches, with the coils at the top of a stack generally hotter than coils at the bottom. The annealing temperature will affect grain boundary diffusion and hence the size and location of surface grain boundary oxides and the oxidation zones.

A pure internal grain boundary oxidation zone would be quite difficult in an annealing gas with a nominal dewpoint of -40 °C (Figure 5-6) unless the dewpoint of the annealing gas is very different from the nominal one. Manganese is known to segregate to the surface of steel and this surface manganese would easily oxidise, forming surface oxides meaning pure internal oxidation of manganese would be unlikely.

A change in the dewpoint or oxygen potential of the annealing gas between different annealing cycles could be caused by a variety of reasons, including a small air leak into the furnace, differing quality in the supply of the annealing gas, differing annealing cycles. This change in dewpoint will affect the oxidation zones with an increase in dewpoint shifting the zones towards the centre of the coil and a decrease shifting the zones towards the coil edge. If the dewpoint is maintained at a very low level, selective grain boundary oxidation could be avoided and the whole coil width could be classified as an oxidation free zone. As such the 'edge defect' would be avoided.

Not only does the size of the zones of oxidation change but the size of precipitates in these zones also changes from coil to coil. This may be explained by different steel compositions being more susceptible to selective oxidation. Steels with greater amounts of manganese and chromium will have more free chromium and manganese to form larger oxide precipitates.

Coil B1

Figure 5-9 shows the oxidation across the width of Coil B1 (Figure 4-97) overlayed with the zones of oxidation. At the very edge (2 mm from edge) of coil B1 sample the oxide precipitates were quite fine and sparse on the surface. Thus internal grain boundary oxidation was the predominant mode of oxidation with limited external grain boundary oxidation at this point. As the distance from the coil edge increases the surface oxide size increases, hence grain boundary oxidation was becoming more external in nature. At about 70 mm from the coil edge the maximum external grain boundary oxidation occurred as the maximum surface coverage and particle size were observed. Therefore from the coil edge to 70 mm from the edge mixed grain boundary oxidation must have occurred. In this region the rate limiting step for surface oxide growth was the supply of manganese and chromium to the steel surface. Particles observed in the external oxidation zone decreased in size and volume as the distance from the edge further increased. This decrease was caused by the reduction in the supply of oxygen as shown by the trend of the nitrogen pick-up. At a distance of 350 mm there were no grain boundary oxides detected. Thus the grain boundary oxidation free zone occurred from 350 mm to the centre of the coil. In this zone the reduction in oxygen supply stops grain boundary oxidation. This shows that the change in surface oxidation across the width of this coil can be explained in terms of the different zones of oxidation.

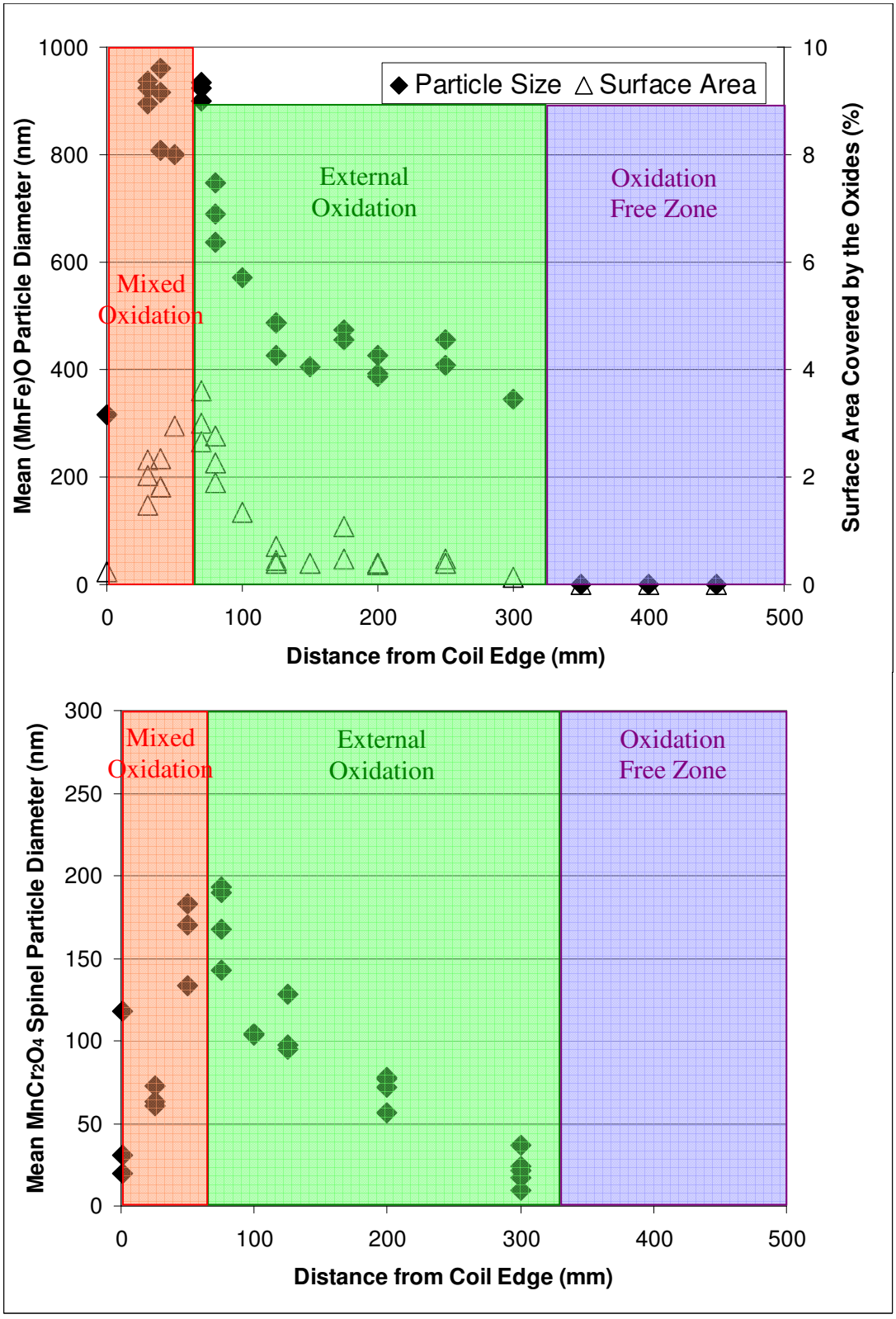

Figure 5-9: The corresponding oxidation zones of coil B1 and a) The distributions of mean particle size and surface area of (MnFe)O oxides observed by SEM, b) Distribution of the mean particle size of $MnCr_2O_4$ spinel precipitates.

Coil B2

Figure 5-10 shows the oxidation across the width of Coil B2 (Figure 4-103) overlayed with the zones of oxidation. The internal grain boundary oxidation zone was not evident. The mixed grain boundary oxidation zone was quite narrow, if it existed at all, as the maximum particle size was observed close to the edge (2 mm from edge). Hence the external grain boundary oxidation zone extended from 2 mm to 200 mm after which no surface grain boundary oxidation was observed and the oxidation free zone was reached. This coil therefore only contained the external oxidation zone and the oxidation free zone. This coil is indicative of a coil that was tightly wrapped causing a reduced supply of oxygen across the coil width.

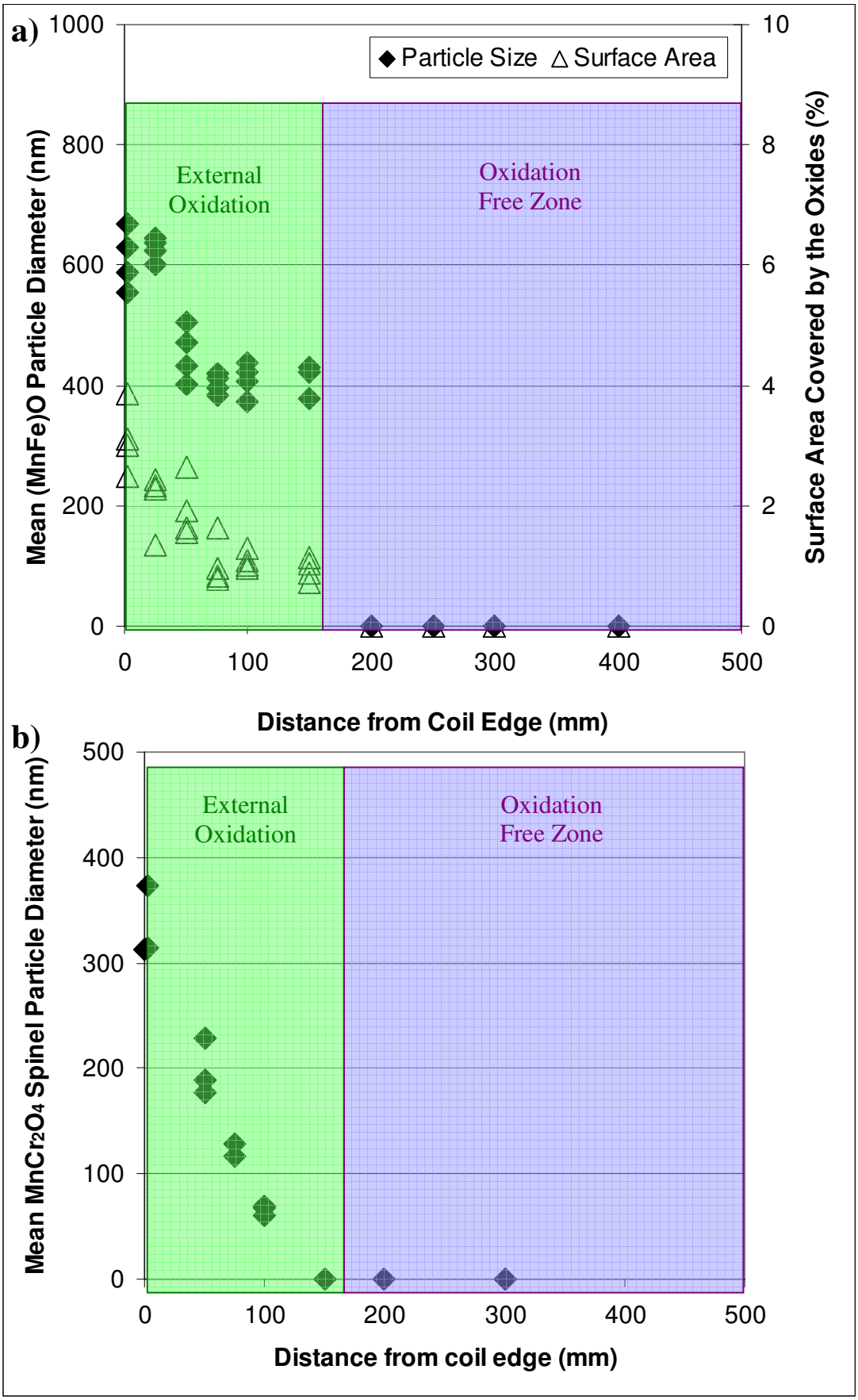

Figure 5-10: The corresponding oxidation zones of coil B2 and a) The distributions of mean particle size and surface area of (MnFe)O oxides observed by SEM, b) Distribution of the mean particle size of $MnCr_2O_4$ spinel precipitates.

Tinplate Coil

The average size of surface spinel precipitates and the nitrogen content as a function of the distance from coil edge for a tinplated coil that exhibited the 'edge defect' is shown in

Figure **5-11** (supplied by Bluescope Steel). The largest average spinel particle size corresponds to the band where the 'edge defect' was observed in the finished tinplate product. The largest mean spinel particle diameter was measured to be 480 nm. As can be seen the nitrogen content was initially very low (25 ppm) at the coil edge and comparable to the level prior to annealing, but there was a significant increase in the nitrogen content across the coil width, with a maximum of 220 ppm at the coil centre. This again identifies that the oxygen was a maximum at the coil edge and decreases towards the coil centre.

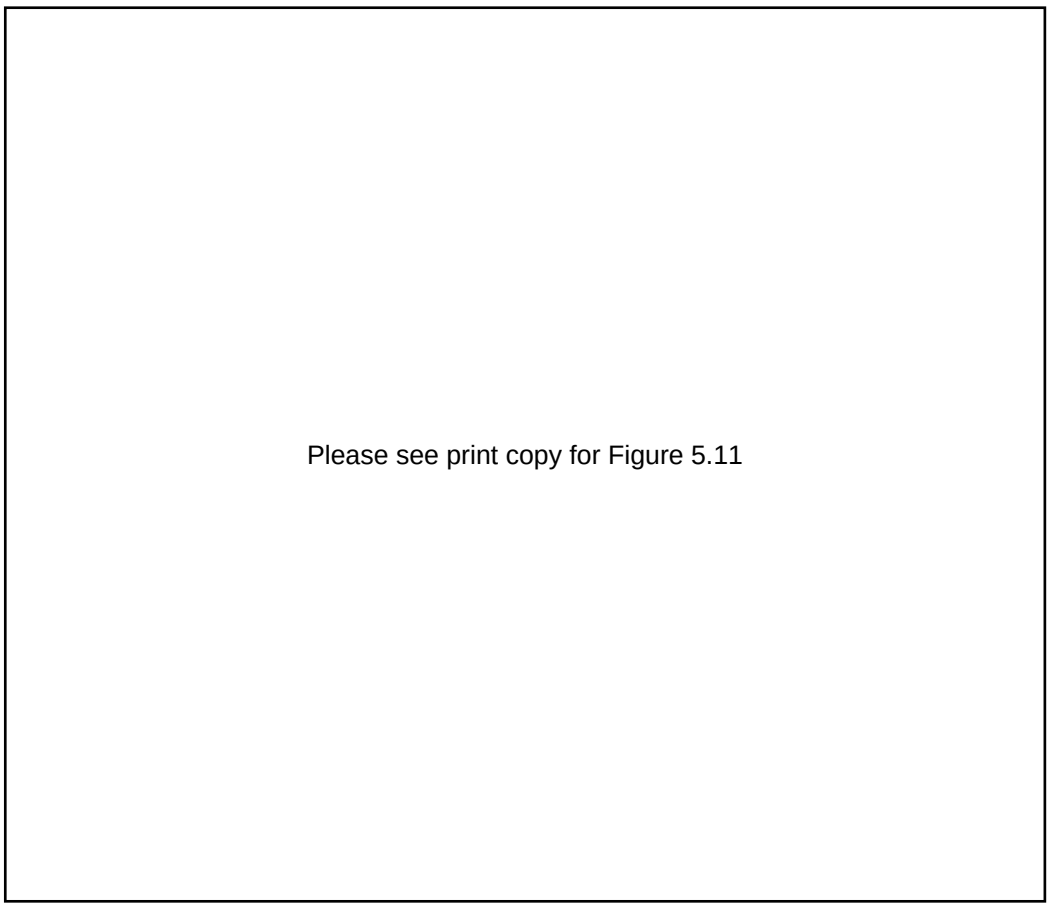

Figure 5-11: Distribution of mean $MnCr_2O_4$ spinel particle sizes and nitrogen concentrations in the steel across the width of a tinplated coil [72].

In this tinplated sample no pure internal oxidation zone was observed. The mixed internal and external grain boundary oxidation zone occurred from the edge till 60 mm from the coil edge where the maximum external grain boundary oxidation occurred. The external oxidation zone extended from 60 - 200 mm after which no oxidation was observed and the oxidation free zone was reached. The change in surface oxidation across the width of this coil can also be explained in terms of the different zones of oxidation supporting this model.

Chapter 6 : Conclusions

- Grain boundary precipitates formed on the surface of low carbon steel during batch annealing in a reducing atmosphere were determined to be (MnFe)O and $MnCr_2O_4$ spinel. These precipitates were formed by the selective oxidation of manganese and chromium.

- The (MnFe)O particles were coarser than the spinel $MnCr_2O_4$ particles. Although the (MnFe)O precipitates contained some iron (less than 10% of the metal in the oxide) they were predominantly manganese oxide. These (MnFe)O precipitates were easily removed from the steel surface by pickling in 8% sulphuric acid and thus they make no contribution to the surface 'edge defect'.

- The surface area covered by (MnFe)O precipitate increased with increasing manganese levels in the steel and with increasing annealing temperatures from 675 °C to 750 °C.

- The spinel $MnCr_2O_4$ precipitates were not easily removed from the steel surface by pickling and are responsible for the 'edge defect' in tinplate when they are larger than a critical size. This critical size is approximately 250 nm in diameter.

- The spinel $MnCr_2O_4$ particles size increased with increasing chromium level in the steels, but was independent of the manganese level in the steels. The spinel $MnCr_2O_4$ particles size increases with increasing temperature. At an annealing temperature of 675 °C the average size of the spinel precipitates was below the critical level to disrupt tinplating for all steels investigated. At 700 °C the critical concentration of chromium in the steel above which the 'edge defect' would be expected was 0.05 wt %. At 750 °C the critical concentration of chromium in the steel above which the 'edge defect' may occur was 0.04 wt %.

- The extent of the region affected by the selective oxidation products across the strip width varied between the samples examined. The size and surface coverage of the particles also varied within the affected region.

- The non-uniformity of the selective oxidation across the strip width can be attributed to the variation in the dewpoint or oxygen potential of the inter-wrap atmosphere across the strip width. The selective oxidation pattern found can be accounted for by the competing processes of internal and external grain boundary oxidation, leading to four different oxidation zones across the strip width: internal grain boundary oxidation, mixed grain boundary oxidation, external grain boundary oxidation and oxidation free.

- The extent of each zone would be a function of the annealing gas temperature and dewpoint, the inter-wrap gap across the coil width, and the manganese and chromium levels of the steel.

Chapter 7 : Recommendations

The recommendations presented in this section outline factors that could reduce the occurrence of the 'edge defect'.

Reducing the annealing temperature from 700 °C to 675 °C would greatly reduce the chances of the 'edge defect' occurring. The trade off with reducing the annealing temperature is the longer annealing times required for re-crystallization hence reducing the productivity of the annealing furnace.

A change in the annealing atmosphere would be effective in reducing the occurrence of the 'edge defect'. Increasing the hydrogen level will reduce the oxidising potential of the annealing gas meaning less selective oxidation would occur. However, increasing the hydrogen in the annealing atmosphere will raise safety concerns due to the explosive nature of hydrogen gas. The annealing atmosphere could also be made less oxidising at the annealing temperature by having a purging step during initial heating. Purging the furnace at approximately 300 °C would be effective in reducing the increase in oxidising potential that occurs in the furnace on heating.

Reducing the chromium level in the steel to 0.04 wt % should be effective in stopping surface graphitization and reducing the likelihood of the 'edge defect'. Such a reduction on one hand reduces the production cost on other hand may reduce the effectiveness of chromium in preventing surface graphitization.

Chapter 8 : References

1. Jessop, K., *Frosty Surface.* Unpublished Document, Australian Iron & Steel PTY. LTD., 1975.

2. Andersson, T. & Smith, U., *New Mechanism for Formation of Carbon Edges on Steel Strip during Annealing.* Metals Technology, 1977. **4**(2): p. 106-114.

3. Inokuti, Y., *Formation of Graphite on the Surface of Cold Rolled Low Carbon Steel Sheet during Annealing.* Transactions ISIJ, 1975. **15**: p. 314-323.

4. Nakamura, T. & Sato, M., *Graphite Pollution Mechanism at the Surface of Steel Sheet during Annealing.* Kobe Steel Research and Development Engineering Reports, 1992. **42**(3): p. 75-78.

5. Maeda, S., Boshoku Gijutsu, 1983. **32**: p. 37.

6. Okamoto, A. & Takahashi, M. in *Symposium Proceedings Japan Institute Metals at Akita*. 1983. p. 197-198.

7. Okamoto, A., *Graphite Formation in High-Purity Cold Rolled Carbon Steels.* Metallurgical Transactions A, 1989. **20A**: p. 1917-1925.

8. Harris, J., Whiteman, J. & Quarrell, A., Iron Steel Institute, 1965. **233**: p. 168-179.

9. Leroy, V., Richelmi, J. & Graas, H., *Graphite Formation on the Surface in Annealed Low Carbon Steel Sheet.* CRM Metallurgical Reports, 1976. **49**: p. 49-58.

10. Van Aken, D., *Decarburization of Steel and Graphitization.* Industrial Heating, 2000. **67**(4): p. 14.

11. Inokuti, Y., *Effect of Third Elements on the Graphite Formation on the Surface of Iron.* Transactions ISIJ, 1975. **15**: p. 324-333.

12. Austin, C. & Norris, B., Transactions ASM, 1942. **30**: p. 425.

13. Austin, C. & Fretzer, M., Transactions ASM, 1939. **27**: p. 18.

14. Saito, K., Journal JIM, 1963. **27**: p. 186-191.

15. Kubaschewski, O. & Hopkins, B.E., *Oxidation of Metals and Alloys*. 2 ed. 1962, London: Butterworths.

16. Kofstad, P., *High Temperature Oxidation of Metals*. 1966, New York: John Wiley & Sons, Inc. 285-292.

17. Birks, N. & Meier, G.H., *Introduction to High Temperature Oxidation of Metals*. 1983, London: Edward Arnold.

18. Evans, H.E., *Oxidation.* Encyclopedia of Materials: Science and Technology, 2001: p. 6574-6579.

19. Douglass, D., *A Critique of Internal Oxidation in Alloys during The Post-Wagner Era.* Oxidation of Metals, 1995. **44**(1-2): p. 81-111.

20. Wagner, C., *Reaktionstypen bei der Oxydation von Legierungen.* Zeitschrift fur Elektrochemie, 1959. **67**(7): p. 772-782.

21. Rapp, R.A., *Kinetics, Microstructures and Mechanism of Internal Oxidation - Its Effects and Prevention in High Temperature Alloy Oxidation.* Corrosion - NACE, 1965. **21**: p. 382-401.

22. Mataigne, J.M., Lamberigts, M. & Leroy, V. *Selective Oxidation of Cold-Rolled Steel during Recrytallization Annealing*. in *Developments In The Annealing of Sheet Steels*. 1991. Cincinnati, Ohio, USA: The Minerals, Metals & Materials Society. p. 511-528.

23. Leijon, W. & Olefjord, I., *Surface State of Batch Annealed Low-Carbon Steel Sheets.* Scandinavian Journal of Metallurgy, 1983. **12**: p. 239-245.

24. Olefjord, I., Leijon, W. & Jelvestam, U., *Selective Surface Oxidation During Annealing of Steel Sheets in H2/N2.* Applications of Surface Science, 1980. **6**: p. 241-255.

25. Servais, J.P., Graas, H. & Leroy, V., *Influence of Heat Treatments on the Surface of Low-Carbon Steels.* CRM Metallurgical Reports, 1975. **44**: p. 29-42.

26. Piehl, C., Toekei, Z. & Grabke, H., *Influence of Chromium Diffusion and Different Surface Finishes on the Oxidation Behaviour of Chromium Steels.* Materials at High Temperature, 2000. **17**(2): p. 243-246.

27. Porter, D.A. & Easterling, K.E., *Phase Transformations in Metals and Alloys*. 1984: Van Nostrand Reinhold Co. Ltd.

28. Fairbank, L.H. & Palethorpe, L.G.W., *Controlled Atmospheres for the Heat Treating of Metals.* Special Report 95, Iron and Steel Institute, 1966. p. 57-69.

29. Lamberigts, M. & Servais, J.P., *Use of XPS to Investigate Surface Problems in ULC Deep Drawing Steels.* Applied Surface Science, 1999. **144-145**: p. 334-338.

30. Grabke, H.J., Leroy, V. & Viefhaus, H., *Segregation on the Surface of Steels in Heat Treatment and Oxidation.* ISIJ International, 1995. **35**(2): p. 95-113.

31. Jyrkas, K. & Paavilainen, J., *Investigation of Surface Segregation on Cold Rolled Steel by Glow Discharge Spectroscopy.* Surface Engineering, 1996. **12**(1): p. 68-76.

32. Lochner, H. *Surface Improvements of Steel Strip Annealed in Ebner HICON/H_2 Batch Furnaces*. in *Developments In The Annealing Of Sheet Steels*. 1991. Cincinnati, Ohio, USA: The Minerals, Metals & Materials Society. p. 427-441.

33. Martinez, C., Cremer, R., Loision, D. & Servais, J.P., *In-situ Investigation on the Oxidation Behaviour of Low Alloyed Steels Annealed Under N_2-5%H_2 Protective Atmospheres.* Materials Technology, 2001. **72**(11-12): p. 508-511.

34. Suzuki, S., Yanagihara, K., Yamazaki, S., Tanaka, K. & Waseda, Y., *SIMS/XPS Characterization of Surface Layers formed in 3 mass% Si-Steel by Annealing in Oxygen at Low Partial Pressure.* Surface and Interface Analysis, 2003. **35**: p. 276-281.

35. Reed-Hill, R.E. & Abbaschian, R., *Diffusion in Substitutional Solid Solution.* Physical Metallurgy Principles, 1994: p. 360-402.

36. Hudson, R., Biber, H., Oles, E. & Warning, C., *Kinetic Studies on Surface Segregation of Manganese during annealing of Low-Carbon Steel.* Metallurgical Transactions A, 1977. **8A**: p. 1713-1719.

37. Feliu, S. & Perez-Revenga, M.L., *Effect of the Presence of Alloying Elements in Interstitial-Free and Low-Carbon Steels on Their Surface Composition after Annealing in Reducing Atmospheres.* Metallurgical and Materials Transactions A, 2004. **35A**(7): p. 2039-2050.

38. Hudson, R., Biber, H., Oles, E. & Warning, C., *Surface Segregation of Manganese In Low-Carbon Steel during Annealing.* Metallurgical Transactions A, 1976. **7A**: p. 1857-1865.

39. Angeli, G., Dienhammer, H., Farderl, J., Angeli, J., Papst, I. & Wolpers, M., *Distribution and Composition of Surface Oxides on High Strength IF-Steels after Recrystallisation Annealing.* 44th MWSP Conference Proceedings, 2002. **40**: p. 825-832.

40. Huin, D., Flauder, P. & Leblond, J.B., *Numerical Simulation of Internal Oxidation of Steels during Annealing Treatments.* Oxidation of Metals, 2005. **64**(1/2): p. 131-167.

41. Vanden Eynde, X., Servais, J.P. & Lamberigts, M., *Thermochemical Surface Treatment of Iron-Silicon and Iron-Manganese Alloys.* Surface and Interface Analysis, 2002. **33**: p. 322-329.

42. Vanden Eynde, X., Servais, J.P. & Lamberigts, M., *Investigation into the Surface Selective Oxidation of Dual-Phase Steels by XPS, SAM and SIMS.* Surface and Interface Analysis, 2003. **35**: p. 1004-1014.

43. Cheron, R., Quillard, X., Roland, J.M. & Roptin, D., *Surface Segregation during Rapid Annealing of a Cold Worked Low Carbon Steel.* Scripta Metallurgica et Materialia, 1994. **31**(4): p. 423-426.

44. Pearson, W., *Handbook of Lattice Spacings and Structures of Metals*. Vol. 2. 1967, Sydney: Pergamon Press.

45. Wayman, M.L. & Gray, J.T., *The Surface Segregation Behaviour of Manganese and Nickel in Iron.* ACTA Metallurgica, 1974. **22**: p. 349-355.

46. Saeki, I., Konno, H., Furuichi, R., Nakamura, T., Mabuchi, K., Itoh, M., *The Effect of the Oxidation Atmosphere on the Initial Oxidation of Type 430 Stainless Steel at 1273 K.* Corrosion Science, 1998. **40**: p. 191-200.

47. Marasco, A.L. & Young, D.J., *The Oxidation of Iron-Chromium-Manganese Alloys.* Oxidation of Metals, 1991. **36**(1/2): p. 157-174.

48. Lille, C. & Jargelius-Pettersson, R.F.A., *Factors Affecting the Oxidation Mode of Stainless Steels.* Materials at High Temperature, 2000. **17**(2): p. 287-292.

49. Chevalier, S., Bonnet, G., Dufour, P. & Larpin, J.P., *The REE: A Way To Improve The High-Temperature Behaviour of Stainless Steels.* Surface and Coatings Technology, 1998. **100-101**: p. 208-213.

50. Stott, F.H., Wei, F.I. & Enahoro, C.A., *The Influence of Manganese on the High-Temperature Oxidation of Iron-Chromium Alloys.* Werkstoffe und Korrosion, 1989. **40**: p. 198-205.

51. Kiessling, R., *Non-metallic Inclusions in Steel*. 2nd ed. Vol. Part 1. 1964, London: The Metals Society. 83-88.

52. Kingery, W., Bowen, H. & Uhlmann, D., *Introduction to Ceramics*. 1976, New York: Wiley.

53. Garner, F.A., Hollengurg, G.W., Sickafus, E., Larson, A.C., Nastashi, M., Yu, N., & Brandt, R.C. *Cation Disorder in High Dose Neutron Irradiated Spinels*. in *Proceedings of Forth Symposium on the Fabrication and Properties of Ceramics for Fusion Energy*. 1994.

54. Miller, A., *Distribution of Cations in Spinels.* Journal of Applied Physics (Supplement), 1959. **30**(4): p. 24S.

55. Muller, R., *The Major Ternary Structural Families*. 1974, Berlin: Springer-Verlag. 41.

56. Lowry, M.L., Hartman, J.E. & Granwalt, J.J. *Examination of Nitrogen Diffusion during Batch Annealing of Cold Rolled, Drawing Quality, Killed Steels*. in *Mechanical Working & Steel Processing XXIII*. 1986. Cleveland, Ohio, USA.

57. Perrin, A.R., Wolosiuk, M. & McLean, A. *Nitrogen in Steel*. in *Mechanical Working & Steel Processing XXIII*. 1986. Cleveland, Ohio, USA.

58. Okuyama, T., Nishimoto, A. & Yoshida, M. *Influence on the Annealing Conditions and Alloying Elements on Nitrogen Pickup in Box Annealing.* in *Mechanical Working & Steel Processing XXIII*. 1986. Cleveland, Ohio, USA. p. 15-22.

59. Nishikida, S., *Nitrogen Absorption in Cold-Rolled Steel Sheets during the Annealing in N_2-H_2 Gas.* Tetsu-To-Hagane, 1981. **67**(5): p. S627.

60. Hudson, R. & Warning, C. *Effect of Box-Annealing Conditions on Nitrogen Pickup In Aluminium-Killed Steel*. in *Mechanical Working & Steel Processing XXIII*. 1986. Cleveland, Ohio, USA.

61. Yao, N. & Wang, Z.L., *Handbook of Microscopy for Nanotechnology*. 2005, Boston: Kluwer Academic Publishers.

62. Reimer, L., *Scanning Electron Microscopy: Physics of Image Formation and Microanalysis*. 2nd ed. 1998, Berlin: Springer.

63. Reimer, L., *Transmission Electron Microscopy: Physics of Image Formation and Microanalysis*. 4th ed. 1997, Beriln: Springer-Verlag.

64. Marcus, H.L., *Auger Electron Spectroscopy.* Encyclopedia of Materials: Science and Technology, 2001: p. 393-398.

65. Sibilia, J.P., *A Guide to Materials Characterization and Chemical Analysis*. 2nd ed. 1996, New York: VCH Publishers.

66. Kubaschewski, O., *Materials Thermochemistry*. 6 ed. 1993, Oxford: Permagon Press.

67. Turkdogan, E.T., *Physical Chemistry of High Temperature Technology*. London. 1980: Academic Press.

68. Remy, H., *Treatise On Inorganic Chemistry*. Vol. 2. 1956, Amsterdam: Elsevier Publishing Company.

69. Askeland, D.R., *The Science and Engineering of Materials*. 3rd ed. 1996, London: Chapman and Hall.

70. Hauffe, K., *Oxidation of Metals*. 1965, New York: Plenum Press.

71. Rovito, A.J., Aiello, W.M. & Voss, G.F., *Batch Anneal Coil Cold Spot Temperature Prediction Using On-line Modelling at LTV.* Iron and Steel Engineer, 1991. **63**(9): p. 31-37.

72. Killmore, C., Laird, S., Wilson, P., Chen, Z. *Investigations into the Formation of Regions of Low Reflectivity on Tinplate Produced by the Batch*

Annealing Route. in *2nd National Steel Conference*. 2003. University of Wollongong, Wollongong, Australia.

Appendix 1: Associated Publications

1. C. Killmore, S. Laird, P. Wilson, Z. Chen, *"Investigations into the formation of regions of low reflectivity on tinplate produced by the batch annealing route"*. in 2nd National Steel Conference. 2003. University of Wollongong, Australia.

2. P.R. Wilson, Z. Chen, *"Characterisation of surface grain boundary precipitates formed during annealing of low carbon steel sheets"*, Scripta Materialia, Volume 53, No. 1, (2005), pp 119–123.

3. P. R. Wilson, Z. Chen, *"Identification of surface precipitates found on the surface of steel annealed for tinplating"*, Microscopy and Microanalysis, Volume 11, Supplement S02, Aug 2005, pp 1990-1991.

4. P. R. Wilson, Z. Chen, C. R. Killmore, S. Laird, *"Selective oxidation of manganese and chromium during annealing of low carbon strip steels"* Advanced Materials Research, Volume 15-17, THERMEC 2006 Supplement, (2007), pp 762-767.

5. P.R Wilson, Z. Chen, *"The effect of manganese and chromium on surface oxidation products formed during batch annealing of low carbon steel strip"*, Corrosion Science, Volume 49, No. 3, (2007), pp 1305-1320.

6. P. R. Wilson, Z. Chen, C. R. Killmore, S. J. Laird, J.G. Williams, *"Surface oxidation across the width of batch annealed low carbon steel strip"*, ISIJ International, Vol 47, No. 1, (2007), pp. 114-121.

List of Tables

Table 2-1: The octahedral site preference energies for various cations in spinels. The values for P are in K.Cal/g-atomic weight. The larger (and the more positive) the values of P, the greater is the preference of the ion for the octahedral site in spinels [55]. 38
Table 3-1: Composition of steels used in this investigation in wt%, balance iron..... 55
Table 4-1: Measured and calculated angles and ratios between diffractions for the zone axes in this investigation. 80
Table 4-2: Possible diffraction groups and point groups for the [001], [011], [$\bar{1}$11] and [013] zone axes. 81
Table 4-3: The mean particle diameter and percentage of the steel surface covered by particles for steels annealed in 5% H_2 + 95% N_2 atmosphere as observed by SEM. 110
Table 4-4: The mean particle diameter of $MnCr_2O_4$ spinel precipitates extracted on carbon replicas from the surface of steels annealed in 5% H_2 + 95% N_2 atmosphere as observed by TEM..... 135
Table 5-1: Activation energies for bulk diffusion for elements in α-iron [30]. 158

List of Figures

Figure 1-1: The tinplate production process for batch annealed steels 2
Figure 2-1: Variation in the reflection intensity of (002) plane of graphite with the relation of the clearance between 2 specimens in slow-cooling at the rate of 30 °C/hour after annealing in vacuo at 700 °C for 15 minutes [3]. 7
Figure 2-2: Schematic diagram of a fractured cementite particle. 8
Figure 2-3: Arrangements of iron atoms on $\{002\}_G$ planes which are coherent with $\{011\}_\alpha$ planes of α–iron matrix [3]. 10
Figure 2-4: The variation in the reflection intensity of (002) plane of graphite for the specimens treated by slow-cooling at the rate of 30 °C/hour and by rapid-cooling after annealing in H_2, 7% H_2 + 93% N_2, N_2, Ar and vacuum at 700 °C for 15 minutes and 6 hours [3]. 12
Figure 2-5: a) Relation between the reflection intensity of (002) plane of graphite and the carbon content in steel in rapid-cooling after annealing in vacuo at 700 °C for 6 hours, b) The variation of the surface coverage of graphite [3]. 14
Figure 2-6: Relation between the reflection intensities of (002) plane of graphite and the concentrations of alloying elements, Ti, Zr, V, Nb, Ta, Cr, Mo, Co, Ni, Cu, Ag, Zn, B and Al after annealing in vacuo at 700 °C for 6 hours [11]. 15
Figure 2-7: Relation between the surface coverage percents of graphite and the concentrations of alloying elements, Ti, Zr, V, Nb, Ta, Cr, Mo, Co, Ni, Cu, Ag, Zn, B and Al after annealing in vacuo at 700 °C for 6 hours [11]. 16
Figure 2-8: a) Relation between the reflection intensity of (002) plane of graphite and the concentration of manganese after annealing in vacuo at 700 °C for 6 hours, b) The relation between the surface coverage and the concentration of manganese [11]. 18
Figure 2-9: Ellingham diagram. The standard free energy of formation of selected oxides as a function of temperature. 21
Figure 2-10: Ellingham diagram. The minimum partial pressure for chromium oxide formation at 700 °C is read from the diagram, $p(O_2) = 10^{-32}$ atm. 22
Figure 2-11: Influence of dewpoint and temperature on metal oxidation in a hydrogen atmosphere [32] 28
Figure 2-12: Rate of surface enrichment in manganese for 0.43 wt% Mn steel annealed in 6% H_2 + 94% N_2 containing 0.013% water vapour (dewpoint -40 °C) [36]. 30
Figure 2-13: Manganese surface enrichment of a steel as influenced by oxygen potential of annealing atmosphere annealed for 7 hours at 732 °C in a 6% H_2 + 94% N_2 atmosphere [36]. 34
Figure 2-14: Expected location of ions in the $MnCr_2O_4$ spinel unit cell. 39
Figure 2-15: Effect of annealing temperature and dewpoint on nitrogen pick-up in cold rolled steel sheet's [59]. 41
Figure 2-16: Schematic drawing of the scanning electron microscope were, BSE = backscattered electrons, SE = secondary electrons, SC = specimen current, EBIC = electron-beam-induced current, X = x-rays and CRT = cathode-ray tube [62]. 44
Figure 2-17: Interaction volume between the electron beam and the specimen in SEM. 45
Figure 2-18: The two basic operations of the TEM imaging system involve A) projecting the diffraction pattern on the viewing screen and B) projecting the image onto the screen. 47
Figure 2-19: Schematic diagram showing the competitive processes of x-ray and auger electron emission [64]. 49
Figure 3-1: Three zoned stainless steel tube furnace. 57
Figure 3-2: Annealing cycle for laboratory annealed steels in 5% H_2 + 95% N_2 gas atmosphere. 57
Figure 3-3: The change in dewpoint of the outgas with annealing time for the 700 °C annealing cycle in 5% H_2 + 95% N_2 gas atmosphere. 58
Figure 3-4: The batch annealing process with: a) coils being stacked and b) being covered. 59
Figure 3-5: The batch annealing process with: a) the furnace being placed on and b) being cooled. 60
Figure 3-6: Leica Stereoscan 440 scanning electron microscope 61
Figure 3-7: JEOL JEM 2011 transmission electron microscope. 62
Figure 3-8: xT Nova NanoLab 200 Dualbeam (FIB). 63
Figure 3-9: Secondary electron image of steel surface showing the position (between the two X marks) from which the sample was cut. The sampling region was plated with platinum, and the groove in front of this region demonstrates where milling was started. 64

Figure 3-10: Secondary electron image of TEM cross-section sample in the process of preparation by focussed ion beam milling. The brighter surface layer is platinum and the darker under layer is part of the steel sheet. A surface and an internal precipitate are still visible in the cross-section of the steel sheet. Dashed white lines indicate where the final cuts were made to allow the specimen to be removed from the base steel. 65
Figure 3-11: Phillips 1370 XRD. 66
Figure 3-12: Example of an image being analysed were individual precipitates were manually traced. 67
Figure 4-1: Band of low reflectivity located near the coil edge of a tinplated sample. 70
Figure 4-2: SEM image of region of low reflectivity showing uneven tin coating caused by surface grain boundary precipitates. Arrow indicates location of Figure 4.3 EDS spectrum. 71
Figure 4-3: Typical SEM EDS spectrum of dark region in Figure 4.2 (tinplated) indicated by arrow in Figure 4.2. 71
Figure 4-4: SEM image of 'edge defect' mounted at an angle of 20 degrees from the parallel, polished and etched in nital. 72
Figure 4-5: TEM image of carbon replica sample showing precipitates extracted from steel surface. .73
Figure 4-6: A typical TEM EDS spectrum of the grain boundary precipitates showing that the main constitutes are chromium, manganese and oxygen. 73
Figure 4-7: Kikuchi map produced from a surface grain boundary precipitate. 74
Figure 4-8: Schematic Kikuchi map for a FCC crystal extending over two standard triangles, □ depicting zone axes shown in Figure 4-7. 75
Figure 4-9: a) Convergent beam diffraction pattern of the [011] zone axis with a whole pattern symmetry of 2mm, (b) Indexed nano-diffraction pattern of the [011] zone axis. 76
Figure 4-10: a) Convergent beam diffraction pattern of the [$\bar{1}$11] zone axis with a whole pattern symmetry of 3m, (b) Indexed nano-diffraction pattern of the [$\bar{1}$11] zone axis. 77
Figure 4-11: a) Convergent beam diffraction pattern of the [013] zone axis with a whole pattern symmetry of m, (b) Indexed nano-diffraction pattern of the [013] zone axis. 78
Figure 4-12: Indexed nano-diffraction pattern of the [001] zone axis. 79
Figure 4-13: Secondary electron image of the surface of steel L2 annealed at 700 °C in an air pressure of $1x10^{-1}$ for 6 hours. 83
Figure 4-14: Secondary electron image of the surface of steel L2 annealed at 700 °C in an air pressure of $3x10^{-2}$ for 6 hours. 83
Figure 4-15: Secondary electron image of the surface of steel L2 annealed at 700 °C in an air pressure of $8x10^{-4}$ for 6 hours. 84
Figure 4-16: Secondary electron image of the surface of steel L2 annealed at 700 °C in an air pressure of $1.7x10^{-5}$ for 6 hours. 84
Figure 4-17: The change in mean particle diameter of precipitates measured by SEM with annealing air pressure when annealed at 700 °C for 6 hours. 85
Figure 4-18: Typical SEM EDS of precipitates on steel surface. 85
Figure 4-19: Secondary electron image of the surface of steel L2 annealed at 700 °C in an air pressure of $1x10^{-2}$ for 72 hours. 86
Figure 4-20: XRD spectrum of steel L2 annealed at 700 °C in an air pressure of $1x10^{-2}$ for 72 hours showing the (111), (200) and (200) peaks of FCC crystal structure with a=0.43 nm. 87
Figure 4-21: Secondary electron image of the surface of steel B1, 40 mm from coil edge. 88
Figure 4-22: SEM EDS of precipitate on surface steel B1, 40 mm from coil edge. 88
Figure 4-23: TEM images showing grain boundary precipitates below the steel surface. Pt: platinum coating, A, B, C, D: areas analysed by EDS. 89
Figure 4-24: EDS spectrum of area B in Figure 4-23. 90
Figure 4-25: EDS spectrum of area A in Figure 4-23. 90
Figure 4-26: Indexed selective area diffraction pattern of manganese and oxygen rich precipitate. The zone axis is $[101]_{FCC}$. 91
Figure 4-27: SEM image of steel surface after pickling in 8% sulfuric acid for 2 seconds. 93
Figure 4-28: SEM EDS of dark region shown in Figure 4-27. 93
Figure 4-29: Secondary electron image of the surface of steel L8 annealed at 650 °C in 5% H_2 + 95% N_2 for 20 hours. 94
Figure 4-30: Backscatter electron image of the surface of steel L1 after annealing at 675 °C in 5% H_2 + 95% N_2 for 20 hours. 95
Figure 4-31: Backscatter electron image of the surface of steel L2 after annealing at 675 °C in 5% H_2 + 95% N_2 for 20 hours. 95

Figure 4-32: Backscatter electron image of the surface of steel L3 after annealing at 675 °C in 5% H_2 + 95% N_2 for 20 hours. 96
Figure 4-33: Backscatter electron image of the surface of steel L4 after annealing at 675 °C in 5% H_2 + 95% N_2 for 20 hours. 96
Figure 4-34: Backscatter electron image of the surface of steel L5 after annealing at 675 °C in 5% H_2 + 95% N_2 for 20 hours. 97
Figure 4-35: Backscatter electron image of the surface of steel L6 after annealing at 675 °C in 5% H_2 + 95% N_2 for 20 hours. 97
Figure 4-36: Backscatter electron image of the surface of steel L7 after annealing at 675 °C in 5% H_2 + 95% N_2 for 20 hours. 98
Figure 4-37: Backscatter electron image of the surface of steel L8 after annealing at 675 °C in 5% H_2 + 95% N_2 for 20 hours. 98
Figure 4-38: Backscatter electron image of the surface of steel L9 after annealing at 675 °C in 5% H_2 + 95% N_2 for 20 hours. 99
Figure 4-39: Backscatter electron image of the surface of steel L1 after annealing at 700 °C in 5% H_2 + 95% N_2 for 20 hours. 99
Figure 4-40: Backscatter electron image of the surface of steel L2 after annealing at 700 °C in 5% H_2 + 95% N_2 for 20 hours. 100
Figure 4-41: Backscatter electron image of the surface of steel L3 after annealing at 700 °C in 5% H_2 + 95% N_2 for 20 hours. 100
Figure 4-42: Backscatter electron image of the surface of steel L4 after annealing at 700 °C in 5% H_2 + 95% N_2 for 20 hours. 101
Figure 4-43: Backscatter electron image of the surface of steel L5 after annealing at 700 °C in 5% H_2 + 95% N_2 for 20 hours. 101
Figure 4-44: Backscatter electron image of the surface of steel L6 after annealing at 700 °C in 5% H_2 + 95% N_2 for 20 hours. 102
Figure 4-45: Backscatter electron image of the surface of steel L8 after annealing at 700 °C in 5% H_2 + 95% N_2 for 20 hours. 102
Figure 4-46: Backscatter electron image of the surface of steel L9 after annealing at 700 °C in 5% H_2 + 95% N_2 for 20 hours. 103
Figure 4-47: Backscatter electron image of the surface of steel L1 after annealing at 750 °C in 5% H_2 + 95% N_2 for 20 hours. 103
Figure 4-48: Backscatter electron image of the surface of steel L2 after annealing at 750 °C in 5% H_2 + 95% N_2 for 20 hours. 104
Figure 4-49: Backscatter electron image of the surface of steel L3 after annealing at 750 °C in 5% H_2 + 95% N_2 for 20 hours. 104
Figure 4-50: Backscatter electron image of the surface of steel L4 after annealing at 750 °C in 5% H_2 + 95% N_2 for 20 hours. 105
Figure 4-51: Backscatter electron image of the surface of steel L5 after annealing at 750 °C in 5% H_2 + 95% N_2 for 20 hours. 105
Figure 4-52: Backscatter electron image of the surface of steel L6 after annealing at 750 °C in 5% H_2 + 95% N_2 for 20 hours. 106
Figure 4-53: Backscatter electron image of the surface of steel L7 after annealing at 750 °C in 5% H_2 + 95% N_2 for 20 hours. 106
Figure 4-54: Backscatter electron image of the surface of steel L8 after annealing at 750 °C in 5% H_2 + 95% N_2 for 20 hours. 107
Figure 4-55: Backscatter electron image of the surface of steel L9 after annealing at 750 °C in 5% H_2 + 95% N_2 for 20 hours. 107
Figure 4-56: EDS of typical grain boundary precipitates observed by SEM. 108
Figure 4-57: The effect of annealing temperature and manganese level in the steel on the mean particle diameter of surface particles formed during annealing in 5% H_2 + 95% N_2 atmosphere as observed by SEM. 111
Figure 4-58: The effect of annealing temperature and manganese level in the steel on the percentage of the surface covered by surface particles formed during annealing in 5% H_2 + 95% N_2 atmosphere as observed by SEM. 111
Figure 4-59: TEM image of carbon extraction replica made from steel L1 after annealing at 675 °C in 5% H_2 + 95% N_2 atmosphere for 20 hours and slight etching. 112
Figure 4-60: TEM image of carbon extraction replica made from steel L2 after annealing at 675 °C in 5% H_2 + 95% N_2 atmosphere for 20 hours and slight etching. 113

Figure 4-61: TEM image of carbon extraction replica made from steel L3 after annealing at 675 °C in 5% H_2 + 95% N_2 atmosphere for 20 hours and slight etching. 113
Figure 4-62: TEM image of carbon extraction replica made from steel L4 after annealing at 675 °C in 5% H_2 + 95% N_2 atmosphere for 20 hours and slight etching. 114
Figure 4-63: TEM image of carbon extraction replica made from steel L5 after annealing at 675 °C in 5% H_2 + 95% N_2 atmosphere for 20 hours and slight etching. 114
Figure 4-64: TEM image of carbon extraction replica made from steel L6 after annealing at 675 °C in 5% H_2 + 95% N_2 atmosphere for 20 hours and slight etching. 115
Figure 4-65: TEM image of carbon extraction replica made from steel L7 after annealing at 675 °C in 5% H_2 + 95% N_2 atmosphere for 20 hours and slight etching. 115
Figure 4-66: TEM image of carbon extraction replica made from steel L8 after annealing at 675 °C in 5% H_2 + 95% N_2 atmosphere for 20 hours and slight etching. 116
Figure 4-67: TEM image of carbon extraction replica made from steel L9 after annealing at 675 °C in 5% H_2 + 95% N_2 atmosphere for 20 hours and slight etching. 116
Figure 4-68: TEM EDS of typical particle extracted from surface of steel L3 annealed at 675 °C in 5% H_2 + 95% N_2 atmosphere for 20 hours. 117
Figure 4-69: Particle size distribution of $MnCr_2O_4$ precipitates extracted from the surface of steels annealed at 675 °C in a 5% H_2 + 95% N_2 atmosphere. 118
Figure 4-70: TEM image of carbon extraction replica made from steel L1 after annealing at 700 °C in 5% H_2 + 95% N_2 atmosphere for 20 hours and slight etching. 119
Figure 4-71: TEM image of carbon extraction replica made from steel L2 after annealing at 700 °C in 5% H_2 + 95% N_2 atmosphere for 20 hours and slight etching. 119
Figure 4-72: TEM image of carbon extraction replica made from steel L3 after annealing at 700 °C in 5% H_2 + 95% N_2 atmosphere for 20 hours and slight etching. 120
Figure 4-73: TEM image of carbon extraction replica made from steel L4 after annealing at 700 °C in 5% H_2 + 95% N_2 atmosphere for 20 hours and slight etching. 120
Figure 4-74: TEM image of carbon extraction replica made from steel L5 after annealing at 700 °C in 5% H_2 + 95% N_2 atmosphere for 20 hours and slight etching. 121
Figure 4-75: TEM image of carbon extraction replica made from steel L6 after annealing at 700 °C in 5% H_2 + 95% N_2 atmosphere for 20 hours and slight etching. 121
Figure 4-76: TEM image of carbon extraction replica made from steel L8 after annealing at 700 °C in 5% H_2 + 95% N_2 atmosphere for 20 hours and slight etching. 122
Figure 4-77: TEM image of carbon extraction replica made from steel L9 after annealing at 700 °C in 5% H_2 + 95% N_2 atmosphere for 20 hours and slight etching. 122
Figure 4-78: TEM EDS of typical particle extracted from surface of steel L1 annealed at 700 °C in 5% H_2 + 95% N_2 atmosphere for 20 hours. 123
Figure 4-79: Particle size distribution of $MnCr_2O_4$ precipitates extracted from the surface of steels annealed at 700 °C in a 5% H_2 + 95% N_2 atmosphere. 124
Figure 4-80: TEM image of carbon extraction replica made from steel L1 after annealing at 750 °C in 5% H_2 + 95% N_2 atmosphere for 20 hours and slight etching. 125
Figure 4-81: TEM image of carbon extraction replica made from steel L2 after annealing at 750 °C in 5% H_2 + 95% N_2 atmosphere for 20 hours and slight etching. 125
Figure 4-82: TEM image of carbon extraction replica made from steel L3 after annealing at 750 °C in 5% H_2 + 95% N_2 atmosphere for 20 hours and slight etching. 126
Figure 4-83: TEM image of carbon extraction replica made from steel L4 after annealing at 750 °C in 5% H_2 + 95% N_2 atmosphere for 20 hours and slight etching. 126
Figure 4-84: TEM image of carbon extraction replica made from steel L5 after annealing at 750 °C in 5% H_2 + 95% N_2 atmosphere for 20 hours and slight etching. 127
Figure 4-85: TEM image of carbon extraction replica made from steel L6 after annealing at 750 °C in 5% H_2 + 95% N_2 atmosphere for 20 hours and slight etching. 127
Figure 4-86: TEM image of carbon extraction replica made from steel L7 after annealing at 750 °C in 5% H_2 + 95% N_2 atmosphere for 20 hours and slight etching. 128
Figure 4-87: TEM image of carbon extraction replica made from steel L8 after annealing at 750 °C in 5% H_2 + 95% N_2 atmosphere for 20 hours and slight etching. 128
Figure 4-88: TEM image of carbon extraction replica made from steel L9 after annealing at 750 °C in 5% H_2 + 95% N_2 atmosphere for 20 hours and slight etching. 129
Figure 4-89: EDS spectrum of a typical grain boundary precipitate extracted from the surface of steel L3 annealed at 750 °C in 5% H_2 + 95% N_2 atmosphere for 20 hours 130
Figure 4-90: Particle size distribution of $MnCr_2O_4$ precipitates extracted from the surface of steels annealed at 750 °C in a 5% H_2 + 95% N_2 atmosphere. 131

Figure 4-91: X-ray mapping of grain boundary precipitates extracted from the surface of steel L7 annealed at 750 °C in 5% H_2 + 95% N_2 atmosphere for 20 hours. 132
Figure 4-92: TEM image of carbon extraction replica showing grain boundary $MnCr_2O_4$ precipitates and fine precipitates (<50 nm) located on the grain surface. 133
Figure 4-93: TEM EDS spectrum of fine precipitate extracted from the surface of steel L8 annealed at 700 °C in 5% H_2 + 95% N_2 atmosphere for 20 hours. 134
Figure 4-94: TEM EDS spectrum of precipitate extracted from the surface of steel L1 annealed at 700 °C in 5% H_2 + 95% N_2 atmosphere for 20 hours. 134
Figure 4-95: The effect of temperature and chromium level in the steel on the mean $MnCr_2O_4$ grain boundary precipitate size observed by TEM. 136
Figure 4-96: Backscatter electron images showing change in (MnFe)O particle size across width of coil B1 a) at the edge, b) 50mm from edge, c) 100mm from edge and d) middle of coil. 138
Figure 4-97: a) The distributions of mean particle size and surface area of (MnFe)O oxides observed by SEM, b) Distribution of the mean particle size of $MnCr_2O_4$ spinel precipitates, across width of coil B1 139
Figure 4-98: TEM image of carbon replica's made of etched steel surface at a) 25 mm b) 50 mm, c) 75 mm and d) 200 mm from edge of coil B1 showing the change in the size of grain boundary $MnCr_2O_4$ spinel precipitates. 140
Figure 4-99: The change in nitrogen content in the steel with distance from edge of coil B1 141
Figure 4-100: TEM images showing grain boundary precipitates below the steel surface. Pt: platinum coating, A, B, C, D: areas analysed by EDS. 142
Figure 4-101: Superimposed EDS spectra of grain boundary precipitate (area C in Figure 4-100) and adjacent matrix (area D in Figure 4-100) 143
Figure 4-102: TEM cross section image showing a series of internal grain boundary precipitates. 143
Figure 4-103: a) The distributions of mean particle size and surface area of (MnFe)O oxides observed by SEM, b) Distribution of the mean particle size of $MnCr_2O_4$ spinel precipitates, across the width of coil B2. 145
Figure 4-104: XRD trace showing characteristic peaks of MnO before annealing. 146
Figure 4-105: XRD trace showing characteristic peaks of Cr_2O_3 before annealing. 147
Figure 4-106: XRD trace of mixed oxides after annealing of a 50-50 mixture of MnO and Cr_2O_3 powders annealed at 700 °C under a vacuum of 10^{-2} Torr. 147
Figure 5-1: The Gibbs energies of formation of selected spinel oxides at 298 K and at elevated temperatures. The solid lines were obtained experimentally and the dash lines are extrapolated from the experimental ones. The dashed blue line indicates the estimated Gibbs energy of formation of $MnCr_2O_4$ spinel. 149
Figure 5-2: The Gibbs energies of selected reactions. The $MnCr_2O_4$ spinel reaction was estimated from the behaviour of similar spinel oxides over the temperature range. 150
Figure 5-3: The H_2O/H_2 ratio for the formation of selected oxides over the given temperature range. The $MnCr_2O_4$ spinel reaction was estimated from the behaviour of similar spinel oxides. 151
Figure 5-4: The H_2O/H_2 ratio for the formation of selected oxides over the given temperature range considering the activity of manganese (0.24 wt%) and chromium (0.06 wt%) in steel. The annealing conditions represent the 5% H_2 + 95% N_2 annealing at 700 °C simulated in the laboratory. The $MnCr_2O_4$ spinel reaction was estimated from the behaviour of similar spinel oxides. 152
Figure 5-5: Schematic drawings showing the formation of surface grain boundary (Fe,Mn)O and $MnCr_2O_4$ precipitates on low carbon steels annealed at 700 °C in 5% H_2 + 95% N_2 atmosphere. 156
Figure 5-6: The effect of temperature and H_2O/H_2 ratio has on the mode of selective oxidation. The dark eclipses indicate the annealing conditions for the 5% H_2 + 95% N_2 laboratory annealing. ...161
Figure 5-7: Schematic diagram of different zones of grain boundary oxidation present across the coil width. 167
Figure 5-8: Schematic cross section diagrams of each oxidation zone present across the coil width. 168
Figure 5-9: The corresponding oxidation zones of coil B1 and a) The distributions of mean particle size and surface area of (MnFe)O oxides observed by SEM, b) Distribution of the mean particle size of $MnCr_2O_4$ spinel precipitates. 171
Figure 5-10: The corresponding oxidation zones of coil B2 and a) The distributions of mean particle size and surface area of (MnFe)O oxides observed by SEM, b) Distribution of the mean particle size of $MnCr_2O_4$ spinel precipitates. 173
Figure 5-11: Distribution of mean $MnCr_2O_4$ spinel particle sizes and nitrogen concentrations in the steel across the width of a tinplated coil [72]. 174